

***Establishing species-specific 3D liver microtissues for
repeat dose toxicology and advancing in vitro to in
vivo translation through computational modelling***

Jonathan Arthur Kyffin

A thesis submitted in partial fulfilment of the requirements of

Liverpool John Moores University

For the degree of Doctor of Philosophy,

July 2018

This research programme was carried out in collaboration with

Syngenta Ltd

Table of Contents

Table of Contents	2
Declaration	6
Acknowledgments	7
Publications	9
Abbreviations	10
Abstract	13
Chapter 1: General Introduction	15
1.1 Research motivation	16
1.2 Introduction to the liver	18
1.3 Structure of the liver	18
1.3.1 Parenchymal cells of the liver	20
1.3.2 Non-parenchymal cells of the liver	21
1.3.3 Hepatic stellate cells (HSCs)	22
1.3.4 Liver sinusoidal endothelial cells (LSECs)	23
1.3.5 Kupffer cells (KCs)	23
1.3.6 Biliary epithelial cells (BECs)	23
1.4 Functions of the liver	24
1.4.1 Metabolism	24
1.4.2 Synthesis	24
1.4.3 Biotransformation and Excretion	25
1.5 <i>In vitro</i> liver models utilised for hepatotoxicity prediction	26
1.5.1 Primary Human Hepatocytes (PHH)	29
1.5.2 Hepatic-derived Cell Lines	33
1.5.3 Co-cultures	38
1.5.4 3D liver microtissues	41
1.5.5 <i>In vitro</i> to <i>in vivo</i> extrapolation (IVIVE)	55
1.6 Mathematical modelling of the liver	61
1.7 Biological and mathematical motivation	71
1.8 Thesis aims and objectives	73
1.9 Thesis outline	73

Chapter 2: Characterisation of a functional primary rat hepatocyte spheroid model.....	76
2.1 Introduction.....	77
2.1.1 Aims of experimental characterisation	78
2.2 Materials and methods	79
2.2.1 Production of liquid-overlay plates	79
2.2.2 Primary rat hepatocyte isolation and culture	80
2.2.3 Spheroid formation	81
2.2.4 Phase contrast microscopy.....	81
2.2.5 Histological analysis	82
2.2.6 Immunohistochemical analysis	82
2.2.7 Ultrastructural analysis of hepatocytes via Transition electron microscopy	83
2.2.8 Immunofluorescent analysis of spheroids	83
2.2.9 Analysis of transporter functionality.....	84
2.2.10 Quantification of albumin production.....	84
2.2.11 Quantification of urea secretion	85
2.2.12 Oxygen consumption rate analysis.....	85
2.3 Results	87
2.3.1 Optimisation for size-controllable spheroid production.....	87
2.3.2 Effect of initial cell seeding number on spheroid size and morphology	88
2.3.3 Histological analysis of spheroids.....	91
2.3.4 Nuclear staining of spheroid sections	94
2.3.5 Immunohistochemical analysis	97
2.3.6 Ultrastructural analysis of hepatocytes	103
2.3.7 Cellular polarisation in spheroids.....	104
2.3.8 Secondary structure formation in spheroids	105
2.3.9 Analysis of transporter functionality.....	107
2.3.10 Urea quantification.....	108
2.3.11 Albumin quantification.....	109
2.3.12 Oxygen consumption rate analysis.....	110
2.4 Chapter discussion	111
2.5 Conclusion.....	115

Chapter 3: Mathematical modelling of oxygen diffusion through primary rat hepatocyte spheroids	117
3.1 Biological motivation.....	118
3.1.1 Aims of the chapter.....	120
3.1.2 Modelling background	121
3.1.3 Modelling oxygen diffusion.....	124
3.2 Mathematical methods.....	125
3.2.1 Numerical methods.....	127
3.3 Fixed boundary oxygen profile simulations	129
3.3.1 Parameter values.....	129
3.3.2 Oxygen concentration conversion.....	130
3.3.3 Single parameter value simulations	131
3.3.4 Literature OCR value simulations.....	133
3.3.5 Experimentally-derived spheroid radii simulations	134
3.3.6 Spheroid-specific OCR value simulations	138
3.3.7 Analysis of experimental OCR measurements	139
3.3.8 Radially-coupled OCR simulations.....	142
3.4 Oxygen profile simulations with non-fixed boundary conditions.....	144
3.4.1 Oxygen profile simulations with varying incubator oxygen supply.....	153
3.5 Proposed optimal culture conditions for maintenance of sinusoidal oxygen gradients.....	156
3.5.1 Normalised error function for optimisation fitting.....	158
3.6 Chapter discussion	166
3.7 Conclusion.....	170
Chapter 4: Mathematical modelling of xenobiotic transport through hepatocyte spheroids	172
4.1 Biological motivation.....	173
4.1.1 Aims of mathematical modelling of solute diffusion in PRH spheroids	175
4.1.2 Background on porous media modelling	175
4.2 Porous media modelling equations	178
4.3 Model parameterisation	179
4.3.1 Voronoi tessellation	184
4.3.2 Physicochemical characteristics of chosen xenobiotics	200

4.4	Xenobiotic transport simulations.....	207
4.5	Simulation results.....	209
4.5.1	Transport of APAP.....	209
4.5.2	Transport of vinblastine	214
4.5.3	Transport of fluorouracil	216
4.5.4	Transport of larger particles.....	221
4.6	Chapter discussion	227
4.7	Conclusion.....	230
Chapter 5: Concluding discussion		232
5.1	Chapter summaries	234
5.2	Key research outputs.....	238
5.3	Future work.....	239
5.4	Concluding statement	240
Chapter 6: Appendix.....		241
6.1	Appendix	242
Bibliography		252

Declaration

I, Jonathan Kyffin, confirm that the work presented in this thesis is my own. The material contained within this thesis has not been presented, nor is currently being presented, either wholly or in part for any other degree or qualification. Where information has been gathered from other sources, I can confirm that this has been indicated in the thesis.

Acknowledgments

I would firstly like to thank Maxine, Awel and Parveen who maybe saw that small glimmer of a researcher in me and encouraged me to go for this project. I am forever grateful for the opportunities you gave me whilst working as a technician.

I would like to thank Steve for your expert supervision and guidance throughout the duration of this project. I will never forget the phrase “just chuck it in a see what happens”. It has certainly proved a productive approach to research. Thank you Steve for the change of Universities (and departments!) in the middle of the project, which, whilst at first may have seemed like a mild inconvenience, has actually proved rather fruitful now in hindsight. It has enabled me to rightfully assume the title of “pseudo mathematician”. Jack of all trades, master of.....well I think we can stop there.

Thank you Jean and Domingo for moving on to better things and allowing Parveen to come along for the ride.

To my supervisory team - Steve, Parveen, Pratibha, Richard and Joe you have all made this a fantastic experience. I remember before starting the PhD, everyone in the lab used to say, as long as you have a good supervisor it doesn't matter about the project because it changes so many times from start to finish. I certainly landed on my feet with such a fantastic and knowledgeable team around me. Parveen, your laboratory expertise have been invaluable. Thank you for listening to my rants and being the voice of reason when I needed it. Joe, I love your uncertain optimism from our weekly meetings, something I will sorely miss. Thank you all for giving me so much time and putting in the effort to drag me over the finish line.

I would also like to thank my industry supervision team from Syngenta Ltd. led by the supreme advice of Dr Pratibha Mistry. Pratibha, you certainly gave me the kick up the jacksie when I needed it and for that I am truly thankful. Richard, your pondering and ever thoughtful approach to this project is something I have very much appreciated. I

would like to thank Syngenta for their sponsorship for the project alongside the BBSRC who have funded my research.

To team Webb lab UK- Ross, Darren, Chanty, Sneddo, Terry-lad and Adam. After moving from UoL to LJMU I was extremely apprehensive about starting over again after one and a half years, but you guys have made coming into work thoroughly enjoyable, if not terribly unproductive at times. Thank you all for the coffee and laughs!

I must thank the guys from UoL; Harriet, Áine, Jo, Agnès (guapa), Sophie, Jon, and Vicky, your expertise have been such a help. I had so much fun coming in to work and spending time with you guys. You all made the experience something special.

To ITM stores - Mick the grafter, your expert and sometimes not-so-expert knowledge of the horse racing made my time in UoL stores a joy. Mark, I will never forget the countless lunchtimes jamming on the guitar to gypsy jazz. If only everyone knew how truly gifted and talented you are as a musician and composer.

To my family - Ben and Katie, "how do you like them apples!" All I can say is that cream always rises to the top. Mum and dad, thank you for all of the support you have given me over the last 28 years, and especially the last 6. I can't believe how much life has changed in that time, from not knowing where my life was going and working in a pub, to completing this thesis seems worlds apart.

To my wife and best friend, I love you - who would have thought when we met 10 years ago in college that we would be here now? A lot has changed in that time - a house, marriage, 2 beautiful kids (the perfect parent to child ratio by the way). You truly have been the unshakable foundation of my life. Through so many highs, and some pretty big lows, your love and commitment has been the thing that has kept me going. From encouraging me to apply for jobs and pushing me to achieve my potential; your belief in me has made me believe in myself. I dedicate this thesis to you.

Publications

Kyffin, J.A., et al., *Impact of cell types and culture methods on the functionality of in vitro liver systems – A review of cell systems for hepatotoxicity assessment*. *Toxicology in Vitro*, 2018. **48C**: p. 262-275.

Kyffin, J.A., et al., *Characterisation of a functional primary rat hepatocyte spheroid model* (submitted for publication July 2018, *Toxicology in Vitro*).

In vitro liver zonation of primary rat hepatocytes. (Co-authored journal article submitted August 2018).

Kyffin, J.A., et al., A combined *in vitro* and *in silico* approach to understand solute transport in primary rat hepatocyte spheroids. *Manuscript in prep* (2018)

Abbreviations

ADRs – Adverse drug reactions
3D – 3 dimensional
2D – 2 dimensional
PRH – Primary rat hepatocytes
LOT – Liquid-overlay technique
OCR – Oxygen consumption rate
ECM – Extracellular matrix
TNF α - Tumour necrosis factor α
IL-1 β – Interleukin 1 β
NPCs – Non-parenchymal cells
HSCs – Hepatic stellate cells
LSECs – Liver sinusoidal endothelial cells
KCs – Kupffer cells
BECs – Biliary epithelial cells
APPs – Acute phase proteins
PHH – Primary human hepatocytes
CYP – Cytochrome P450 monooxygenases
VCM - Vinyl chloride monomer
PCLS – Precision cut liver slices
DILI – Drug induced liver injury
HIFs – Hypoxia-inducible factors
ALB – Albumin
CAR – Constitutive androstane receptor
PXR – Pregnane X receptor
APAP – Acetaminophen
LDH – Lactate dehydrogenase
DAH – Differential adhesion hypothesis
ATP – Adenosine triphosphate
CMFDA - 5-chloromethylfluorescein diacetate

DPP IV – Dipeptidyl peptidase 4
PCR – Polymerase chain reaction
MDR1 – Multidrug resistance protein 1
BSEP - Bile salt export pump
MRPs – Multidrug resistance-associated proteins
P-gp – P-glycoprotein
OATP2 - Organic anion transporting polypeptide 2
ULA – Ultra-low adhesion
OUR – Oxygen usage rate
IVIVE – *in vitro* to *in vivo* extrapolation
AFP – Alpha fetoprotein
PK – Pharmacokinetic
PBPK – Physiologically based pharmacokinetic
MIPK - Model-independent pharmacokinetic
ALF – Acute liver failure
DNA – Deoxyribonucleic acid
HBSS – Hanks' balances salt solution
HEPES - 4-(2-hydroxyethyl)-1-piperazineethanesulfonic acid
EDTA - Ethylenediaminetetraacetic acid
FBS – Fetal bovine serum
PBS – Phosphate buffered saline
PFA – Paraformaldehyde
BSA – Bovine serum albumin
GSMF - Glutathione-methylfluorescein
IF – Immunofluorescence
IHC – Immunohistochemical
SD – Standard deviation
BAL – Bioartificial liver
PDE – Partial differential equation
ODE – Ordinary differential equation

PI – Propidium iodide

OG – Octyl gallate

IV – Intravenous

RTP – Room temperature and pressure

TEM – Transisiotn electron microscopy

VT – Voronoi tessellation

SMILES - Simplified molecular-input line-entry system

Abstract

The scientific basis of xenobiotic safety is complicated because of the variance in predictability of the primary and secondary pharmacology of foreign chemical substances, as well as variability in individual susceptibility within the population [1]. Despite a wealth of research into this field, our understanding of the mechanisms underpinning the occurrence of adverse effects from xenobiotics remains limited [2]. Adverse drug reactions (ADRs) represent a major encumbrance to the development of new therapeutics with approximately 21% of drug attrition attributed to toxicity during the development process [3].

The *in vivo/ex vivo* use of animals in science, and in particular drug development, is a global practice and the main purposes of animal experiments are; (i) to gain basic biological knowledge, (ii) for fundamental medical research, (iii) for the discovery and development of drugs, vaccines and medical devices, and (iv) for the toxicity testing of xenobiotics/drugs [4]. However, with there being species-species differences in mechanistic responses, it is difficult to assess results in animal trials and translate these findings in order to predict the *in-vivo* response in humans [5]. Current *in vitro* model systems developed to assess ADRs have a number of down falls including; (i) the isolating procedure of primary hepatocytes, (ii) their cost, (iii) inter-donor differences, (iv) limited availability, (v) as well as increasing ethical pressure to implement the 3R's (Replacement, Reduction and Refinement) in research [6]. The emphasis on producing a relevant and representative *in vitro* model for hepatotoxicity has therefore expanded.

The aim of this thesis is to characterise a novel 3D microtissue model that, in the future, aims to provide a better *in vitro* platform to assess liver toxicity after repeat-dose exposure to xenobiotics. This is particularly important because the processes of hepatotoxicity manifest themselves over several hours and even days, and therefore *in vitro* models need to be able to comprehensively assess toxic potential for repeat-dose scenarios as well as chronic exposures. Computational modelling is implemented to

allow translation of results and to better bridge the gap between *in vitro* and *in vivo* approaches and to exploit the knowledge gained from experimental work.

Chapter 1 is a critical review of culture techniques and cell types that are used during the development stages of xenobiotic discovery. A number of *in vitro* models are evaluated with regards to the determination of hepatotoxic potential of compounds. This review has been previously published [7]. Chapter 1 also includes an introduction to mathematical modelling of hepatic clearance and other pharmacokinetic approaches.

Chapter 2 describes the experimental characterisation of a primary rat hepatocyte (PRH) spheroid model. The application of the liquid-overlay technique (LOT) [8] with PRH results in the production of viable and reproducible microtissues, amenable for high-throughput investigations. I show that our *in vitro* system mimics the *in vivo* cellular morphology, exhibiting both structural and functional polarisation, along with active and functional transporters.

Chapter 3 describes the construction of a mathematical model of oxygen diffusion for my experimental *in vitro* spheroid system. This model is utilised to predict oxygen profiles within the spheroids and to propose optimised operating conditions in order to recapitulate healthy sinusoidal oxygen tensions. This optimisation is based on initial cell seeding densities and experimentally derived oxygen consumption rates (OCR).

Chapter 4 describes the construction of a mathematical model to predict the diffusion of xenobiotics based on their inherent physicochemical properties. The *in silico* system incorporates specific parameters from the experimental spheroid system including paracellular transport features, namely tortuosity and pore fraction properties. The model describes how these spatiotemporal characteristics vary over the duration of the culture period and what effect these have on the transport of xenobiotics.

Chapter 1: General Introduction

1.1 Research motivation

Syngenta are the world's third largest seed company that specialise in the innovation and manufacture of novel seed and crop protection products including fungicides, herbicides and pesticides. The main ethos of the company stems from the challenge of how to feed an ever growing population in a sustainable way. This main principle drives the continual development of new technologies through the collaborative efforts of scientific research. These research collaborations enable Syngenta to critically evaluate all aspects of product safety and in turn ensures that these much-needed products reach the market.

As new products are developed, a number of xenobiotics are examined and assessed not only with regards to their safety for eventual consumers, but also in terms of safety for users and the environment. These product safety analyses influence the design and selection of optimal new chemistry, traits and formulations for the development of novel products. This in combination with the use of sound scientific evidence ensures that these products and technologies are safe for both humans and the environment. As such, Syngenta outsource numerous research projects in order to strengthen their collaborative research efforts with leading academic experts, and also to facilitate the development of these required technologies.

In order to be able to determine xenobiotic safety appropriately, it is vital that relevant and suitable means to test novel products are in place. In terms of novel xenobiotics, a key component of their intrinsic safety relies on the ability to elucidate the metabolism and physicochemical kinetics of the compounds, and also the toxic potential of subsequent metabolites. This is not only true for plant agrochemicals but also for other industries including pharmaceuticals, cosmetics and industrial chemicals.

As product safety assessments of xenobiotics relies heavily on the ability to discern their metabolism and toxicity potential, our understanding of the liver plays a vital role in this process. As the liver is the organ responsible for the majority of metabolism of both endogenous and foreign substances, this project will focus on the characterisation of a

novel *in vitro* model that may aid in the elucidation of xenobiotic toxicity potential, as well as the development of *in silico* systems to facilitate the translatability of these results.

As Syngenta are interested in the impact of xenobiotics on the environment as well as consumers and users, they have previously implemented the use of *in vitro* and *in vivo* rodent models. However, as the desire to implement the refinement, reduction and replacement of animals within scientific research is ever increasing, I will look at the utilisation of primary rat hepatocytes in a high-throughput platform as an *in vitro* model of choice in line with these principles.

The main aim of the development of this *in vitro* model is to facilitate the reduction in the number of cycles and also the cycle time between test and analysis phases of Syngenta's product development programme. The *in vitro* model may also potentially be used to reduce the number of initial/early stage compounds that reach later-stage testing by identifying xenobiotics that exhibit toxicity (see **Figure 1-1**). In order to achieve this, a robust and in-depth characterisation of the model must first be undertaken.

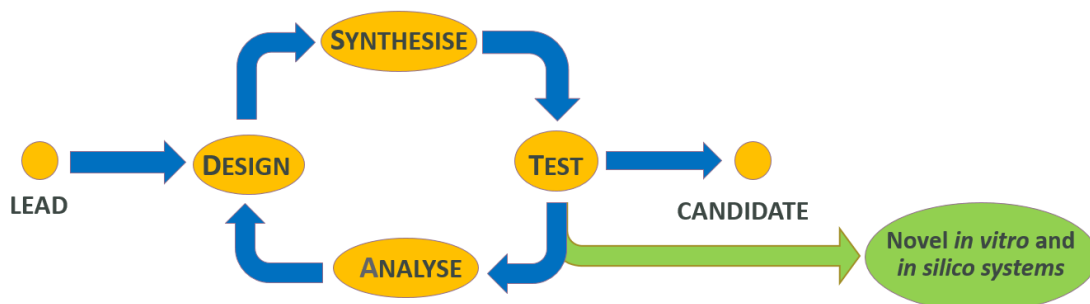


Figure 1-1- Schematic illustrating Syngenta's research and development cycle. An initiative is taken for a new product (Lead), where early chemicals are designed and synthesised and then tested and analysed at various stages. One of the main aims of this research is to develop and characterise an *in vitro* model that can be implemented to reduce the number of cycles, the overall cycle time and the number of chemicals that pass through cycles.

1.2 Introduction to the liver

The liver is the largest solid organ in the body, and weighs between 1.8kg and 1.3kg (on average) in men and women respectively. The liver performs a number of vital roles within the body including; metabolism and detoxification of drugs, protein synthesis, as well as playing an important role in digestion, immunity and the control of blood glucose levels.

1.3 Structure of the liver

The entirety of the liver is made up of a number of functional units, often described as “classical lobules” which are anatomically hexagonal in microarchitecture. The human liver contains about one million of these lobules. There are two other ways to visualize the 2D microarchitecture of the liver which are, the portal lobule and liver acini (see **Figure 1-2**).

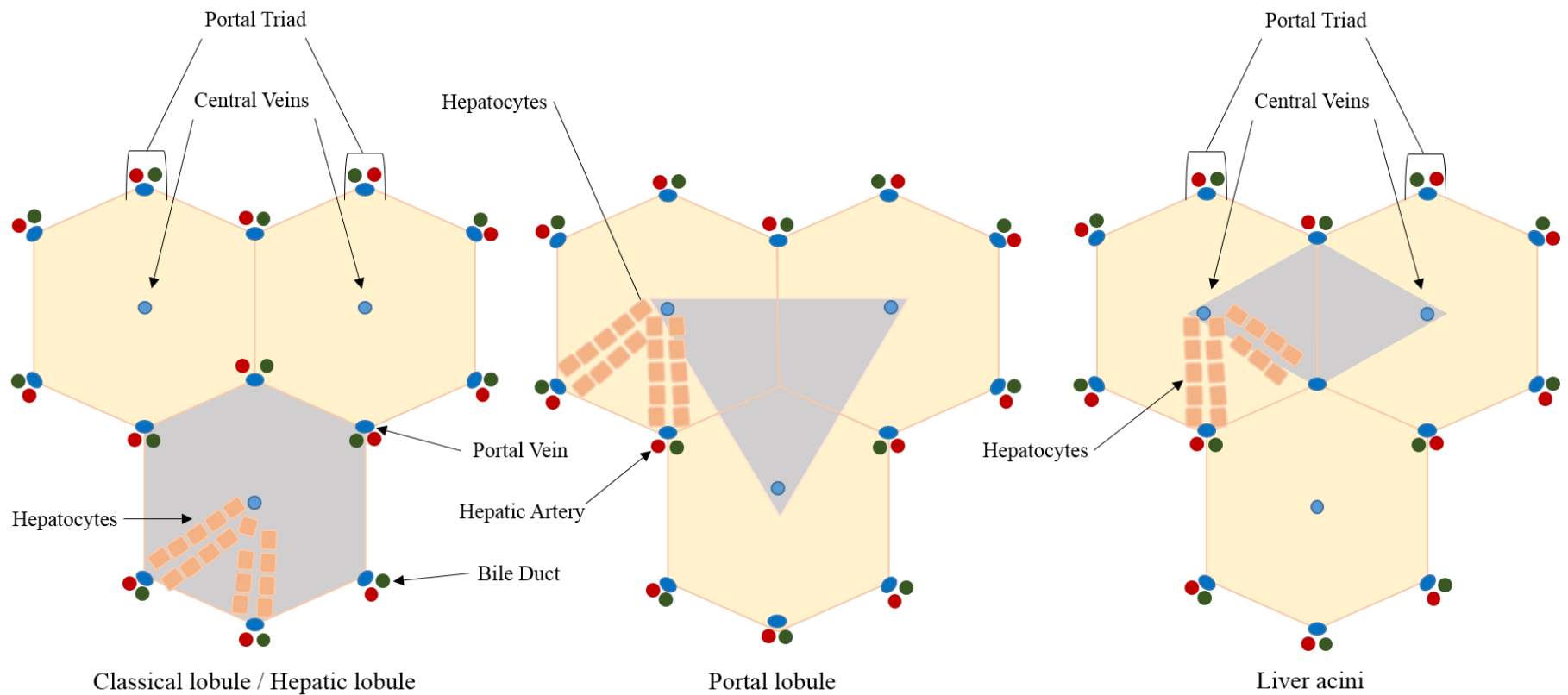


Figure 1-2 – A schematic diagram of the multiple functional units of the liver. The portal triad consists of the portal vein (blue oval), the hepatic artery (red) and the bile duct (green). The central veins are represented by the blue circles. The grey shaded areas show the functional units of the liver from multiple perspectives.

1.3.1 Parenchymal cells of the liver

The major constituent cell type of the liver is the highly specialized hepatocyte, a parenchymal cell which makes up to 80% of the entire liver mass and performs the majority of the liver functions including synthetic activities, drug detoxification and metabolic functions [9]. Hepatocytes are unique in their proliferative capabilities *in vivo* and this inherent capacity allows the liver to regenerate following injury [10].

In vivo hepatocytes are functionally polarized and have a sinusoidal and a canalicular terminus. Hepatocytes are organized into plates which are one cell thick in mammals, and are separated via fenestrated capillaries called the sinusoids which allow blood to perfuse along the vascular channels. The inlet (periportal zone), which is made up from the portal triad, and the outlet (pericentral zone) of the hepatic lobule, are exposed to gradients of oxygen, nutrients, hormones, metabolites etc. which is caused by cellular uptake along the sinusoids. This variability of exposure to oxygen and hormones etc. gives rise to zonation whereby cells along the sinusoids have varying levels of gene and enzyme expression and also metabolic competence [11] (see **Figure 1-3**).

The oxygen gradient within the sinusoid regulates the spatial expression of a number of specific genes [12]. For example, these genes encode specific carbohydrate metabolizing enzymes such as pyruvate carboxykinase 1, glucokinase and liver pyruvate kinase. These spatially expressed genes are mediated via oxygen-responsive transcription factors e.g. hypoxia-inducible factors (HIFs) [13].

Hofman *et al.* [14] described how hepatocytes take up substances such as bile salts via the basolateral membrane and subsequently excrete them across the canalicular membrane into the bile canaliculi where they move into the bile ductules. Protein and lipid components are specifically separated in the distinctive plasma membrane domains and thus, functional transport in hepatocytes is dependent on this highly polarized arrangement of the cells [15].

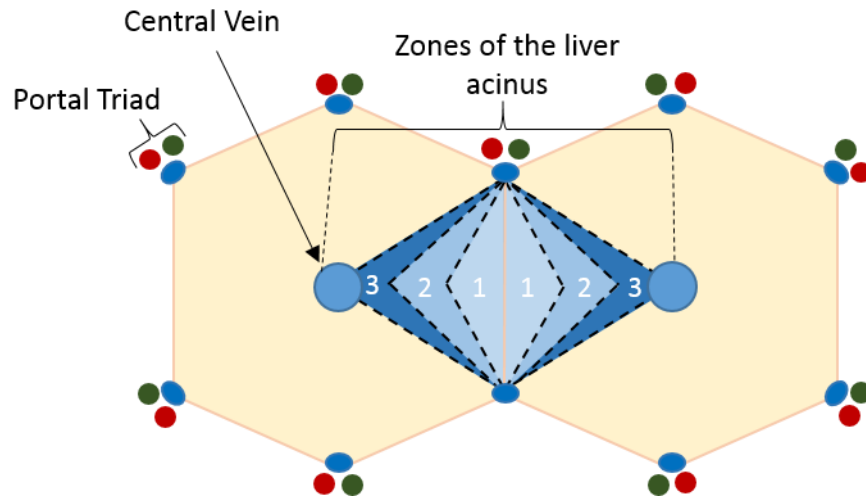


Figure 1-3 – A diagram illustrating zonation of the liver acinus. Within the periportal zone (1), oxygen rich blood from the hepatic artery (red) mixes with nutrient rich blood from the portal vein (blue oval) and moves along the sinusoid towards the central vein (blue circle) in the pericentral zone (3). Bile moves in the opposite direction and drains into the bile duct (green). The expression of most genes appears to be determined by dynamic factors within the blood such as oxygen and hormone gradients which exist due to uptake along the sinusoid.

1.3.2 Non-parenchymal cells of the liver

The remaining liver mass of around 20% is made up of a number of non-parenchymal cells (NPCs) such as; Hepatic stellate cells (HSCs), Liver sinusoidal endothelial cells (LSECs), Kupffer cells (KCs) acting as in-situ macrophages, biliary epithelial cells (BECs), and immune cells such as lymphocytes and leukocytes [16]. (See **Figure 1-4** for microarchitectural arrangement of parenchymal and non-parenchymal cells).

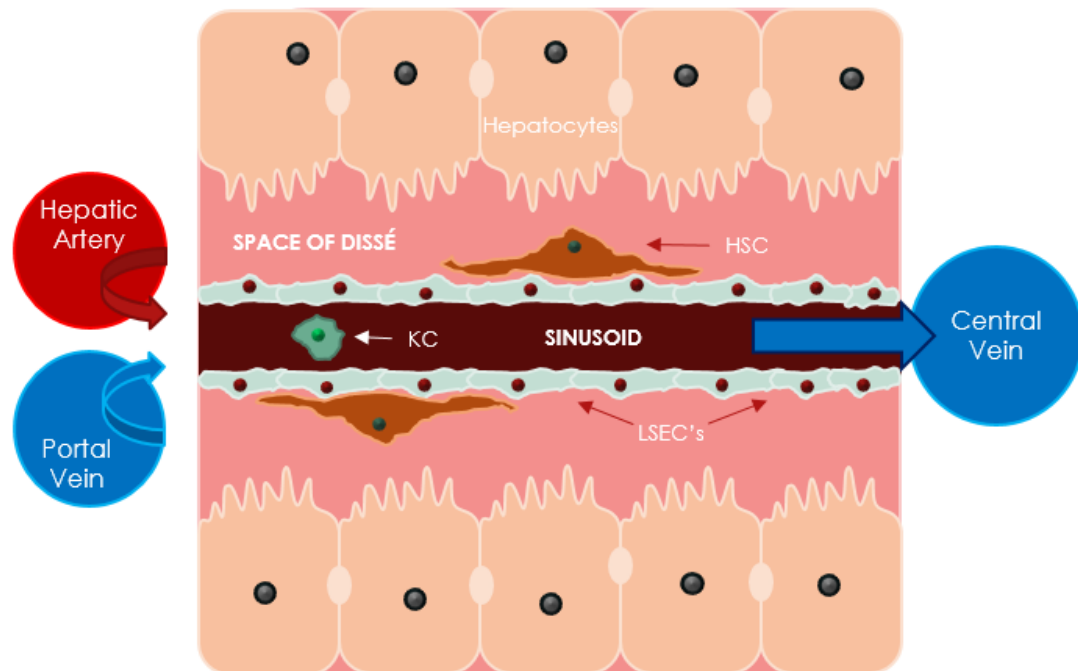


Figure 1-4 – A schematic representation of the spatial distribution of parenchymal and non-parenchymal cells within the liver acinus.

1.3.3 Hepatic stellate cells (HSCs)

HSCs are located in the perisinusoidal space of Dissé within the liver formed between the hepatocytes and the LSECs. These cells store up to 80% of retinoids in the whole body, and under normal conditions these quiescent cells play a vital role in retinoid homeostasis [17]. Under disease conditions (e.g. hepatic fibrosis) the inflammatory immune cells secrete cytokines and growth factors which in turn activates the HSCs. HSCs subsequently start to produce large amounts of extracellular matrix (ECM) components including collagen and adhesive glycoproteins such as fibronectin, as well as proteoglycans [18].

1.3.4 Liver sinusoidal endothelial cells (LSECs)

In the 1970's Wisse described LSECs as specialised endothelial cells with distinct features such as open fenestration as well as a lack of a basement membrane [19]. Wisse also described the atypically high amounts of endocytic vesicles and postulated that these cells were involved in protein uptake from the blood passing through the sinusoid.

The literature has a number of conflicting opinions regarding the functions of these specific cells. However, it is accepted that LSECs play a scavenger role whereby they clear soluble macromolecules (e.g. hyaluronic acid and collagen α -chains) and colloids. This is in contrast to Kupffer cells, another identified type of scavenger cell, which is involved in the uptake of particulate matter [20].

1.3.5 Kupffer cells (KCs)

KCs are bone marrow-derived monocyte cells acting as *in-situ* macrophages [21]. These cells act as a scavenger cell ingesting particulate matter, degraded red blood cells and endotoxins. When activated by liver damage, KCs synthesize and secrete the pro-inflammatory cytokine, tumour necrosis factor α (TNF α) as well as interleukin-1 β (IL-1 β) [22]. Roberts and colleagues also demonstrated that TNF α from KCs activated LSECs leading to the deposition of fibrin in liver tissue [22]. Although the role of KCs has yet to be fully elucidated, it is thought that KCs may be the primary site of toxic response and also a secondary target responsive to toxic signals received by the parenchymal cells.

1.3.6 Biliary epithelial cells (BECs)

BECs line the biliary tracts and are often targets of liver damage (e.g. cholestatic liver disease), and are a subject of intense NPC research [15]. BECs constitute between 3-5% of the cells within the liver [23]. However, these cells are critical to the formation of the biliary components and the transport of bile into the duodenum. Although there is a relatively small percentage of BECs within the liver, they can account for up to 40% of total bile secretions in humans [24].

1.4 Functions of the liver

The liver has a number of vitally important functions which include metabolism and excretion. With regards to endogenous liver metabolism, there are a several main categories including carbohydrate, lipid and protein metabolism.

1.4.1 Metabolism

As well as endogenous metabolism, the liver is responsible for the metabolism and excretion of xenobiotics. The vast majority of molecules that enter the body are lipophilic and therefore, excretion of these substances is difficult. In this case, the liver converts these substances into more water-soluble substances by increasing the polarity of the compounds, thereby facilitating excretion.

It is by no surprise that the main constituent cell of the liver, the parenchymal hepatocyte, carries out the majority of metabolism. The biotransformation of substances including xenobiotics is a multistep process.

The liver breaks down lipids into their component parts and subsequently excretes them as lipoproteins. The liver also has the role of cholesterol production which is essential for plasma membrane fluidity and permeability.

1.4.2 Synthesis

The liver is responsible for synthesising a number of substances including; ECM proteins such as collagen, which are extremely important in liver function, acute phase proteins (APPs), clotting factors, and carrier proteins such as albumin etc. Albumin is the most abundant plasma protein and functions to bind to lipid-soluble toxins in order to excrete them, as well as playing an important role in maintaining oncotic pressure [25].

1.4.3 Biotransformation and Excretion

1.4.3.1 Phase I Metabolism

Phase I metabolism involves the metabolic modification of the xenobiotic via one of three modification processes. These include oxidation, reduction or hydrolysis but xenobiotics may also be modified via cyclization or decyclization. These reactions serve to introduce reactive and polar groups to the parent compound, thereby increasing the molecules polarity for subsequent modification. With most small drug molecules being relatively lipophilic, phase I modifications involve the conversion of these hydrophobic molecules into more water soluble compounds. Phase I metabolism mainly involves the oxidation of xenobiotics which are catalysed via the Cytochrome P450 monooxygenases (CYP450s). CYP450s are the most predominant drug metabolising enzyme present in the human body, and these enzymes account for up to 90% of all xenobiotic metabolism [26].

1.4.3.2 Phase II Metabolism

Phase II metabolism involves the conjugation of the phase I metabolites, i.e. modification of the functional groups that were incorporated into the parent compound during phase I metabolism. In humans, glycine and glutamine are the most common amino acids involved in conjugation reactions. The most common phase II reactions are glucuronidation, which involves the addition of glucuronic acid via UDP-glucuronosyltransferases (UGTs), and sulphation which involves combining with sulphate via sulphotransferases (SULTs) [27].

1.4.3.3 Phase III Elimination

Phase III metabolism encompasses the transporter mechanisms for xenobiotic metabolites. Interestingly, this process does not have to occur sequentially after phase I or phase II as the name implies. Recent studies have shown that a number of specific transporter proteins can mediate the transport of unmodified xenobiotics before they

are metabolised by phase I and II enzymes, as well as their subsequent phase I and II metabolites [28].

This process involves the active transport of these unmodified parent compounds and metabolites via a number of membrane transporters such as, multidrug resistance-associated proteins (MRPs), P-glycoprotein (P-gp), and organic anion transporting polypeptide 2 (OATP2) [27].

The above processes all contribute to the detoxification and subsequent elimination of many xenobiotic compounds.

1.5 *In vitro* liver models utilised for hepatotoxicity prediction

The main aim of an *in vitro* liver model is to be able to capture relevant and useful end points, such as assessing the toxicity potential of novel xenobiotics, identify possible ADRs and modifications in transporter functionality. For example, simple vesicle models can be used to investigate the uptake and efflux properties of specific transporters, demonstrating that *in vitro* models do not necessarily have to fully recapitulate the natural *in vivo* microenvironment in order to be utilised successfully [29].

Further to that, there are a number of *in vitro* liver models that differ depending on their culture conditions and conformations, cell types used and other additional culture parameters. These platforms include isolated primary hepatocytes, hepatic-derived cell lines and precision cut liver slices. Conventional cellular model systems such as simple monolayer cultures are easier to manipulate in the laboratory and are much more widely accepted ethically than the use of animal models. However, immortalised cell lines and 2D hepatocyte cultures may be less representative of the *in vivo* liver.

For certain compounds and other endpoint analyses, a more complex model that recapitulates the *in vivo* microenvironment more closely is required. As such, more complex approaches including 3D culture platforms, co-culture models and systems that

incorporate flow parameters such as bioreactor technologies, may prove to be better suited to capture these end points.

The ongoing and continual development of 3D cell culture technology has meant that several technologies have been established to culture cells in these more complex environments. These include matrix-free systems for some cells, but also include the addition of hydrogels and scaffold technologies, and also the more recently established stem cell-derived hepatocyte-like cells and liver organoids [30-33]. Another degree of complexity in these systems has been introduced with the inclusion of fluid-flow to emulate sheer stress and nutrient exchange seen *in vivo* as a way to improve functionality and relevance [34, 35].

The use of animal models in research aids the development of our scientific understanding of basic and more complex cellular processes in both humans and animals. As a number of key cellular processes are conserved between species, animals provide an appropriate model by which to test and develop novel compounds across multiple industries. There are various ethical implications with regards to using animals in research, and to address these concerns the development of more representative *in vitro* and *in silico* models has accelerated. However, it is clear that in order to develop these alternative models accurate data and parameters are required, and thus the need for animal studies is apparent. (see **Figure 1-5** for an overview of *in vitro* models utilised for hepatotoxicity investigations).

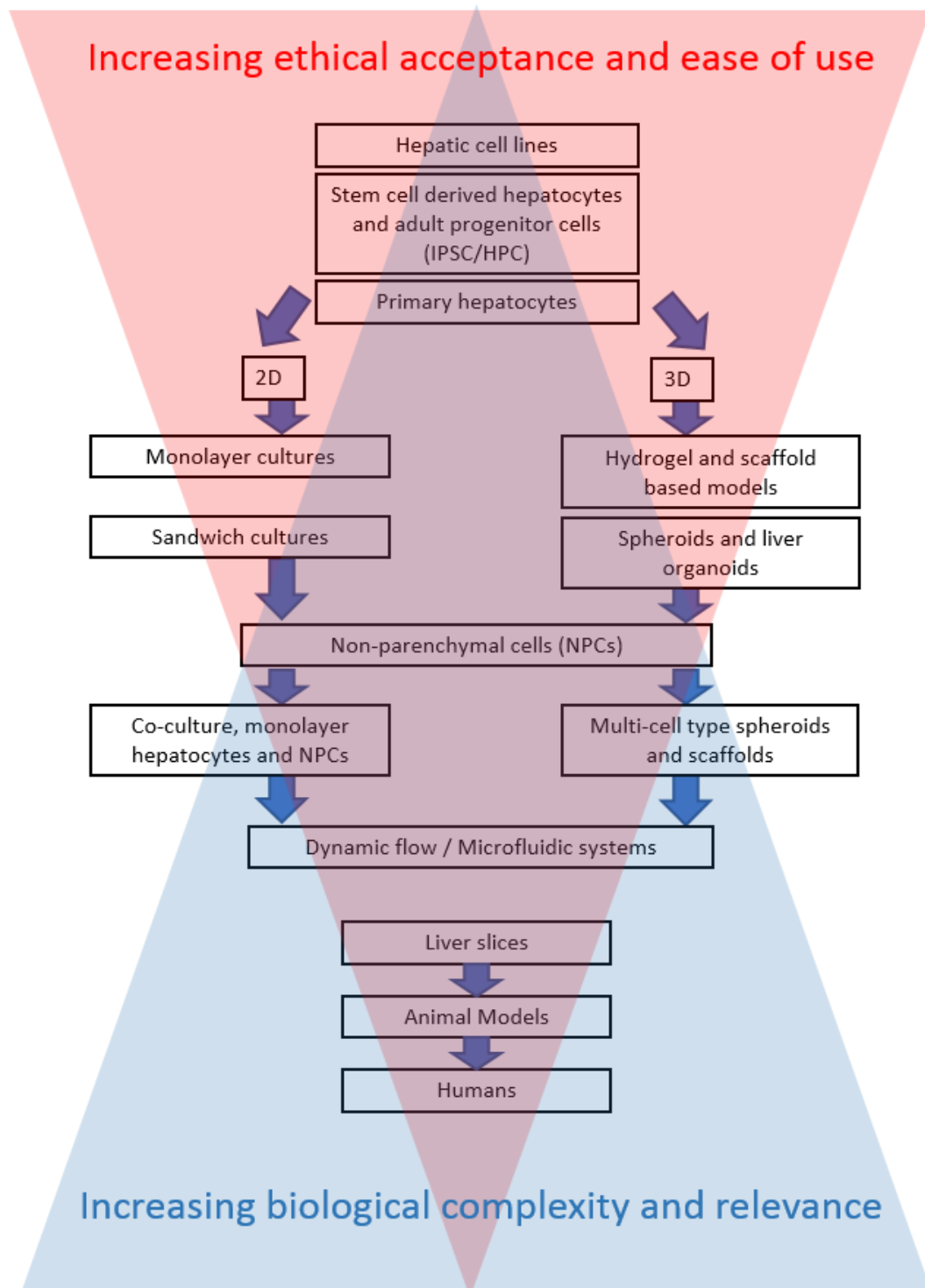


Figure 1-5- Schematic of commonly used liver models. These model can be ranked by their complexity and subsequent relevance to humans, and also by their ethical status. Some in vitro liver models are far more ethically accepted compared with others.

Figure 1-5 shows the multitude of liver models that differ in their translational relevance to humans. Systems vary from complex animal models that present significant ethical challenges alongside species variation, and primary human hepatocytes (PHH) that, although deemed more relevant, suffer from inter-donor variability, rapid dedifferentiation *in vitro*, along with sparse availability. On the other end of the spectrum are the more conventional cellular models that are easier to manipulate in the laboratory and are much more ethically accepted. However, these immortalised cell line models are less representative of the *in vivo* liver. Sandwich cultured hepatocytes retain more *in vivo*-like properties, including polarised excretory function, enhanced morphology and viability of hepatocytes compared to monolayer cultures. However these models still lack complex cellular interactions and the 3D microenvironment. Cells can be grown in a 2D monolayer setting or the more complex 3D conformation, with 3D set-ups considered to be more representative of the native liver *in vivo*. The complexity of both 2D and 3D models can be further increased with the addition of NPCs, producing a more representative model via the adoption of a multicellular system, and the addition of flow with some systems incorporating highly complex microfluidic devices.

1.5.1 Primary Human Hepatocytes (PHH)

PHH in monolayer cultures are generally considered the gold standard *in vitro* model for drug metabolism and toxicity investigations [36, 37]. When isolated effectively, PHH demonstrate a number of favourable characteristics such as phase I and II metabolic enzyme activity, expression of liver-specific transporters, glucose metabolism, ammonia detoxification, as well as urea secretion and albumin production [38]. However, there are a number of problematic issues with this system; (i) loss of liver-specific function/dedifferentiation (PHHs lose their specific-liver function rapidly *in vitro*, including Cytochrome P450 (CYP) expression, and are therefore unsuitable for long-term and repeat-dose studies) [15, 39]; (ii) the isolation procedure of hepatocytes is technically difficult (with limited availability of tissue and considerable inter-donor variability that impacts on the reproducibility of end point measurements) [40]; (iii) classical

2D/monolayer cell culture does not recapitulate the complex 3D *in vivo* microenvironment. Despite this, PHH *in vitro* are still widely used despite the difficulties associated with culturing, isolating, cost, inter-donor variation, acquisition etc. Much research has therefore been conducted using cryopreserved hepatocytes, hepatic-derived cell lines and other alternatives.

Research has demonstrated that one way to improve and retain hepatocyte phenotype is to culture cells in a 3D conformation [41-43]. Mammalian cells *in vivo* grow in a 3D setting, therefore, 2D cell cultures are ineffectual at recreating a microenvironment that is representative of this native *in vivo* configuration [43]. 2D cultures fail to maintain phenotypic characteristics over the duration of the culture period [44]. Other strategies to improve PHH function and survival *in vitro* include the use of growth factors, cytokines and other supplementation within the growth media [45]. However, research has shown that one of the most successful techniques in retaining hepatocyte function has been their co-culture with other cell types including NPCs [46-48].

Since many toxic responses *in vivo* are mediated by complex interplay amongst a multitude of cell types, the predictive capabilities of isolated hepatocytes are limited and therefore, there is a need to establish models that integrate NPCs within the culture platform [49]. Research has shown that intricate hepatocyte-NPC interactions affect the response after exposure to specific compounds. An example of this is vinyl chloride monomer (VCM), which is metabolically activated within hepatocytes causing hepatocellular cancer [50]. However, a long-term effect of VCM is that it gives rise to haemangiosarcoma, a rare tumour that arises from the LSECs [51]. Furthermore, toxic responses are not only mediated by the association of the cells within these multiplexes, but also by the complex 3D interaction involving NPCs and the extracellular matrix (ECM) which is believed to be crucial in regulating and maintaining hepatic function *in vivo* [52].

The differences between cells grown on flat culture surfaces versus novel 3D formats such as extracted ECM attachment surfaces, has been documented since the early 1970's [53]. With decades of research being conducted since then, the compelling similarities of

in vivo morphologies and behaviours of cells grown in 3D environments have been well demonstrated [54]. Consequently, it is widely agreed that culturing cells in 3D provides a much more *in vivo*-like platform and this format is extensively used in an array of disciplines within scientific research such as: cancer medicine/tumour-immune system interactions regenerative medicine and tissue fabrication technologies, and in the field of toxicology [15, 55-57].

There are certainly a number of *in vitro* pharmacological models that have been developed to assess uptake, metabolism and detection of undesired effects, along with a vast number of publications that have addressed a number of desirable endpoints. However, only a small fraction of these models will inevitably become standardised industrial tools [58]. In part this is due to the specific internal requirements of industries and their capacity to incorporate these emerging technologies into their existing experimental framework. Industry screening comprises a battery of models that address single end points and in combination make up the tools for xenobiotic safety evaluations. Even though it is widely accepted that 3D cell culture provides a more representative and *in vivo*-like model, with large sets of historical data at their disposal, and potential difficulties in comprehensive characterisation and automation of novel 3D models, the widespread adoption of these 3D platforms into the already well-established battery of screening tools remains a challenge [59].

1.5.1.1 Precision cut liver slices (PCLS)

There are a number of desirable characteristics attributed to liver slices when compared with other *in vitro* liver models. Unlike primary cell isolations, liver slices do not require incubation with proteolytic enzymes and therefore, cell-cell interactions and other cellular components remain largely undisrupted. The maintenance of this microarchitecture also provides a more *in vivo*-like model. Additionally, with many *in vitro* systems, the conditions of isolation vary from species to species; counter to this, a reproducible, standardised procedure is used to prepare and incubate liver slices from

different species making this model particularly suitable to perform inter-species studies [60].

Liver slices have been utilised extensively in the field of hepatotoxicity and drug induced liver injury (DILI) investigations with the main advantage of this system being that the liver microarchitecture remains intact with all liver cell types being present, along with zone specific CYP450 activity [60]. Human liver tissue can either be obtained from excised tissue removed during surgical procedures such as a partial hepatectomy or from the non-transplanted donor tissue [61]. Such liver slices have been utilised as an *in vitro* method for the prediction of human specific toxicity by toxicogenomics and proteomic investigations. However, human liver slices used from different donors, many of whom have underlying conditions, result in the introduction of inter-individual variability. This in turn means that reproducibility of the investigations can be difficult to achieve [15].

Animal tissue on the other hand, is more readily available and can be controlled via perfusion methods using preservation solutions or simple buffers [15]. It has been shown that albumin production and phase II enzyme expression remain relatively stable for a period of up to 96 hours in culture, with studies typically lasting between 30 minutes and 5 days using rat liver slices [62-64]. The main limitation with using freshly cut liver slices is their longevity, meaning that repeat-dose studies cannot be achieved with this model beyond 5 days. Inter-individual variability has also been seen in liver slices taken from different rats within a strain [65, 66].

The literature has shown that the long-term conservation of metabolic competence for *in vitro* models is difficult to achieve, but it has been reported that metabolic capacity is better preserved in human liver slices when compared to PHH [61, 67]. However, conflicting reports have demonstrated that xenobiotic metabolism in liver slices is impaired after 24 hours of culture [68]. Research has demonstrated good *in vitro-in vivo* correlations for the qualitative metabolism of xenobiotics in liver slices obtained from multiple species. However, Lerche-Langrand *et al.* suggest that the use of liver slices may be limited to identifying low- and high-clearance compounds [60].

Despite their short-term viability, liver slices have been used extensively over the years to investigate metabolism and toxicity of a number of xenobiotics. Olinga *et al.* showed that in human liver slices, all hepatocytes within the slice had an equal rate of metabolism of lidocaine [67]. Elferink and colleagues further evaluated the utility of human liver slices as an *in vitro* platform for the prediction of human-specific toxicity by toxicogenomics [69]. They found that human liver slices retained a relatively stable protein expression of transporters and enzymes that are involved in drug metabolism during a 24 hour culture period.

Liver slices have also been used in conjunction with bioreactor platforms such as the multiwell plate platform engineered by CN BIO Innovations [34]. This combined approach has been utilised as a means of increasing the complexity and representativeness of the liver slice platform as, fluid shear stress has been shown to improve liver-specific functional output [70]. Liver slices are placed into multiwell chambers of the plate and the media flow is controlled by a pneumatic underlay. This bioreactor is produced from polystyrene and has two connected chambers, one for the media reservoir, and the second is the reactor chamber. This reactor chamber can be used for culturing liver slices (as well as for the culture of isolated hepatocytes) with polycarbonate scaffolds [71]. This engineered platform enables the cells or liver slices to be cultured in an environment close to that of the *in vivo* liver. The system incorporates media flow, oxygen gradients and shear stresses. The experimental set up is able to recapitulate oxygen gradients similar to that seen within the liver sinusoid (145 μM to 50 μM at a flow rate of 0.25 ml/minute) [71]. Hepatocytes cultured using this system have improved longevity when compared with conventional monolayer cultures. However, liver slices utilised in this platform are still not able to provide a model for repeat-dose toxicity studies due to their short term culture longevity and viability.

1.5.2 Hepatic-derived Cell Lines

To overcome some of the aforementioned limitations with PHH (1.5.1), immortalized hepatic-derived cell lines have been utilised extensively. Cell lines previously used in

toxicological investigations include; HepG2, C3A, HepaRG and Huh7 [72-75]. Use of these cell lines inherently overcomes the issue associated with inter-individual variability of primary hepatocytes, and these cells are characterised by having a relatively stable phenotype, ease of manipulation in the laboratory along with unlimited life-span [72, 76]. The main limitation with utilising these cell lines is that they generally possess reduced metabolic competence due to lack of expression of key metabolising enzymes [77].

1.5.2.1 HepG2

Since its isolation in the 1970's, extensive work has been carried out in the fields of toxicological and pharmacological assessment using the HepG2 cell line [62]. These cells possess a number of attractive characteristics such as: (i) nuclear transcription factor (Nrf2) expression, which is essential for drug metabolism and toxicity response [78]; (ii) availability, unlimited growth and the absence of inter-donor variation ensuring reproducible results [79]; and (iii) it is an easy-to handle cell line with uncomplicated culture protocols [80]. Research has targeted the development of classical monolayer formats to more complex 3D models including spheroids, with HepG2 spheroids showing markedly different gene expression when compared to monolayer cultures [81]. Chang *et al.* revealed that significantly more genes related to ECM, cytoskeleton, and cell adhesion were expressed in monolayer cells, whilst genes involved in liver-specific functions of xenobiotic and lipid metabolism were upregulated in HepG2 spheroids [81]. In addition, more genes involved in the cell cycle and regulation of growth and proliferation were upregulated in monolayers (**Table 1**). For example, CYP1A1 and ALB (albumin) expression was approximately 10 and 2-fold higher respectively, in 3D spheroid cultures when compared with monolayers, whilst COL1A1 (alpha 1 type-1 collagen) and GSPG2 (versican) expression was approximately 70 and 11-fold higher respectively, in monolayer cultures when compared with 3D spheroids.

	Number of Genes	Number of Genes
Category	Monolayer	Spheroids
Total	250	210
Extracellular matrix	10	0
Cytoskeleton	10	5
Cell adhesion	21	4
Cell cycle	13	7
Growth/proliferation	25	10
Xenobiotic metabolism	0	6
Lipid metabolism	4	11
Apoptosis/cell death	11	12
Signal transduction	26	20
Transcription	20	21

Table 1 – Number of genes upregulated by at least 2-fold in HepG2 monolayers or spheroid as determined by microarray analysis [81].

It has been demonstrated that, with the lack of appropriate levels of CYP expression when compared to PHH, HepG2 cells do not fully represent the phenotype of *in vivo* hepatocytes and therefore the detection of many hepatotoxic compounds utilising the HepG2 cells line is inaccurate, and for non-liver specific toxins this model is ineffectual [82]. It is, however, still the case that 2D cultures of hepatic-derived cell lines are valuable in the early stages of safety assessments, and liver cell lines can still provide a convenient and pragmatic tool for early screening and drug safety assessment [15, 83].

1.5.2.2 C3A

C3A cells are a sub-clone of the HepG2 cell line that demonstrate more advantageous characteristics compared with the parent cells. C3A cells are selected for their contact-inhibited growth characteristics, increased albumin production and alpha fetoprotein production, alongside their ability to proliferate and thrive in glucose-deficient media [84]. These characteristics have made C3A cells a more representative model for hepatotoxicity studies with a number of researchers utilising this cell type in 3D culture systems [76].

1.5.2.3 HepaRG

The HepaRG cell line is another hepatocellular carcinoma-derived cell line that has been of interest over the last decade [85]. It is a human cell line that exhibits a number of attractive qualities and unique features when compared to the more commonly used HepG2 cells [74]. HepaRG cells have been shown to express a number of phase II enzymes and membrane transporters comparable to freshly isolated or cultured PHH [77, 80, 86]. HepaRG cells, when seeded at low density, acquire an elongated undifferentiated morphology. They then actively divide and after having reached confluence, form typical hepatocyte-like colonies surrounded by biliary epithelial-like cells [74]. In addition, the literature has reported enhanced CYP450 expression along with improved liver-specific functionality [15, 74, 77, 85].

Guillouzo *et al.* demonstrated that the HepaRG cell line was more sensitive to metabolism-mediated toxicity when compared with HepG2 cells [74]. They found that HepaRG cells expressed various CYPs (1A2, 2B6, 2C9, 2E1, 3A4) and the nuclear receptors, constitutive androstane receptor (CAR) and pregnane X receptor (PXR), at levels comparable to those found in cultured PHH, and much increased when compared to the expression levels in HepG2 cells. HepaRG cells also expressed phase II enzymes, apical and canalicular ABC transporters and basolateral solute carrier transporters, albumin, haptoglobin, as well as aldolase B which is a specific marker of adult hepatocytes. The findings of Guillouzo *et al.* demonstrate that HepaRG cell models have the potential to replace PHH models for xenobiotic metabolism and toxicity studies [74]. McGill *et al.* [87] concluded that HepaRG cells are a useful model to study mechanisms of APAP hepatotoxicity in humans. They found that HepaRG cells that were exposed to varying concentrations of APAP resulted in glutathione depletion, APAP-protein adduct formation, mitochondrial oxidative stress, peroxynitrite formation, mitochondrial dysfunction, and lactate dehydrogenase (LDH) release. This analysis indicated that these key mechanistic propagators of APAP-induced cell death were the same as in the *in vitro* rodent models and cultured primary mouse hepatocytes.

Gerets *et al.* carried out a comprehensive assessment of the HepaRG cell line investigating mRNA levels and CYP activity in response to a number of inducers [77]. This study characterised PHH, HepG2 and the novel HepaRG cell lines in direct comparison with each other. All of the cells in this investigation were cultured in a monolayer multiwell format and were compared with regard to their metabolism and potential to detect hepatotoxicity. Gerets *et al.* concluded that HepG2 cells in this 2D environment responded weakly to the different inducers (β -naphthoflavone, phenobarbital and rifampicin), when compared with PHH and the HepaRG cells at the gene expression and CYP activity levels, whilst HepaRG cells appeared to be most suitable for these induction studies. However, HepaRG cells were not as predictive for hepatotoxicity as PHH and were more comparable to HepG2 cells [77].

One of the main limitations with the HepaRG cell line as a model for hepatotoxicity investigations is the long culture procedure that is required. HepaRG cells are seeded at low densities and after a period of 14 days, these cells differentiate into hepatocyte-like and biliary epithelial-like cells. This pre-differentiation culture phase incurs cost and also time when compared to more commonly used cell lines such as HepG2/C3A cells. Specialist culture media and supplements are required for the entirety of the culture procedure and licensing is required to culture the cells meaning the cost of culturing the HepaRG cells can be as much as one hundred times more expensive than the more commonly used cell lines. As a research tool this means that availability to all researchers is limited. However, terminally differentiated, commercially available cryopreserved HepaRG cells can be obtained [88].

1.5.3 Co-cultures

It has been demonstrated that culturing hepatocytes with other cell types increases their longevity and functionality [89]. The culturing of hepatocytes with NPCs has been investigated since the late 1970's and is still being intensively researched [90]. The predictive capabilities of isolated PHH can be limited [49]. Therefore, in order to represent the multicellularity of the liver, culturing primary hepatocytes with NPCs is an important facet for *in vitro* cellular models [58]. Prior research has demonstrated that culturing primary hepatocytes with NPCs not only increases liver-specific functionality, but also improves the longevity of the cultures [47, 48, 91]. Whilst there is a wealth of research regarding co-culture models in a 2D format, the emphasis has shifted to producing 3D co-cultures where not only multiple cell types can interact but they can grow in a physiologically relevant manner [58]. **Figure 1-6** highlights various methods for producing co-culture models of hepatocytes that incorporate multiple NPCs within the model.

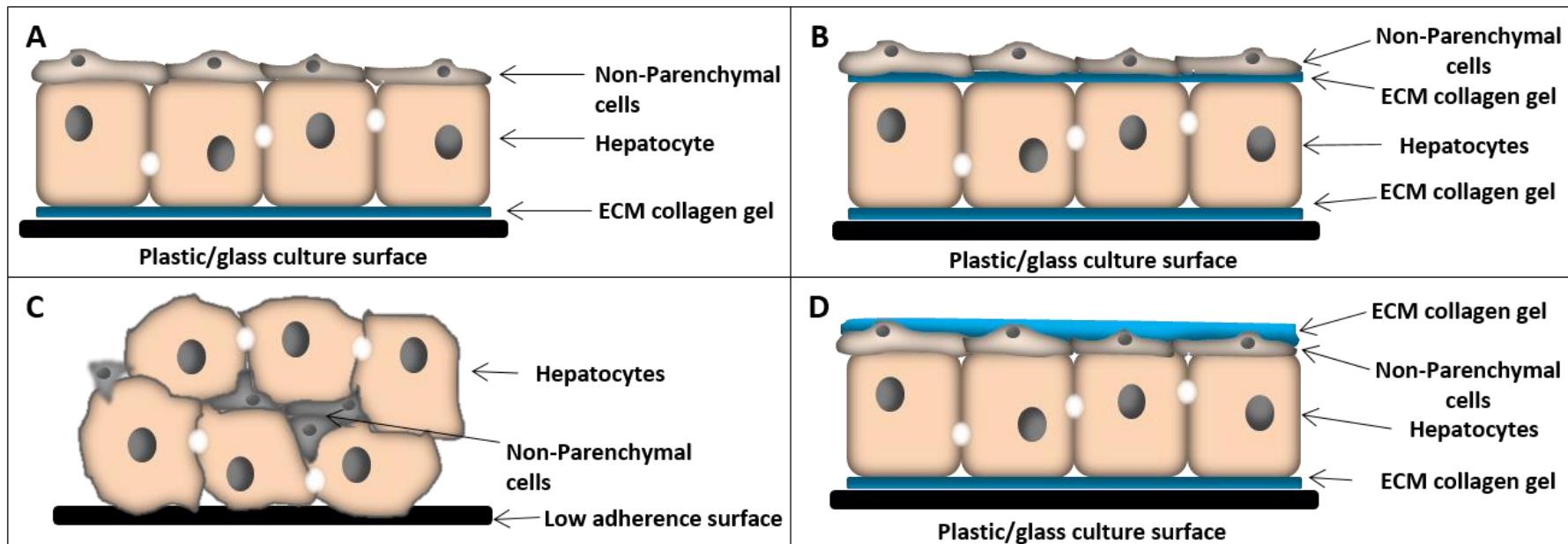


Figure 1-6 - Schematic of a selection of in vitro co-culture liver models. (A) shows hepatocyte cultures that have been grown on a collagen coated surface and then overlaid with NPCs. (B) demonstrates the much-utilised sandwich culture method whereby hepatocytes are cultured between two layers of collagen and then subsequently overlaid with NPCs. (C) demonstrates the structural formation of hepatocyte spheroids including NPCs. In this conformation there are multiple and direct cell-cell contacts between the parenchymal cells and the NPCs. There are a number of methods for culturing hepatocyte spheroids, however it is becoming more common to utilise low-attachment surfaces. (D) Sandwich culture whereby NPCs are in direct contact with the hepatocytes and then subsequently sandwiched between two layers of collagen matrix.

Research has shown that hepatocyte function and stability is improved regardless of whether the secondary cells used are primary or not. Bhandari *et al.* showed that when culturing PRH with murine 3T3 fibroblasts, there was a reciprocal relationship whereby the cellular interactions in the co-cultures ensured survival and increased stability and function of both cell types [46]. Thomas *et al.* further expanded the work of Bhandari and colleagues by producing a co-culture model where activated rat SCs were cultured with isolated PRH in a spheroid model [48]. This co-culture spheroid model displayed bile canaliculi-like structures, complex ECM within the spheroid and, when compared with monoculture spheroids, superior cytochrome P450 functionality.

Peters *et al.* were able to demonstrate that PRH co-cultured with rat liver epithelial cells displayed higher levels of albumin secretion and the longevity of CYP enzyme activity was enhanced when compared to conventional PRH monolayer cultures [92]. It was concluded that this co-culture model was the most applicable method for investigating cytokine-mediated induction of acute-phase proteins, due to there being a threefold increase in fibrinogen secretion in comparison with monolayer cultures.

Kang *et al.* produced a model system whereby PRH and LSECs were cultured on the opposite sides of a transwell membrane, allowing prolonged viability for a period of up to 39 days, as well as the stable presence of hepatocyte-specific differentiation markers [93]. Dedifferentiation of primary hepatocytes is a commonly discussed limitation of classical *in vitro* liver platforms. However, the model system developed by Kang and colleagues showed that PRH maintain this differentiated status for an extended period as verified by mRNA expression of albumin, transferrin, and hepatocyte nuclear factor 4 [93].

KCs have been the focus of much research and it is accepted that this NPC plays a role in the development of DILI. Jemnitz *et al.* produced a 2D co-culture model of PRH and KCs and concluded that the hepatocyte-KC co-culture model provided a good platform for the prediction of chemical hepatotoxic potential [94]. KCs have also been shown to detect hepatocyte stress and damage from model hepatotoxins *in vitro*, leading to the release

of cytokines [95]. Hepatocytes cultured in isolation are not able to capture this release of inflammatory response, further strengthening the view that co-culture and, in particular, co-culture with KCs may increase the sensitivity of *in vitro* liver models to DILI and specific hepatotoxins [95].

BECs line the biliary tracts and are often targets of liver pathologies such as cholestatic liver disease and because of this, BECs have been the subject of much NPC research [15]. Auth *et al.* developed a model where hepatocytes were co-cultured with BECs and demonstrated substantially increased protein synthesis and urea production [96]. Hepatocytes in isolation exhibited low levels of CYP450 activity; however, in co-culture with BECs, CYP450 activity remained stable for up to 3 weeks. Auth and colleagues concluded that co-culture of human hepatocytes with BECs restored the synthetic and metabolic liver function *in vitro* [96].

1.5.4 3D liver microtissues

1.5.4.1 Spheroids

3D cultures of hepatocytes and hepatic-derived cell lines is a rapidly developing field, whereby researchers and bioengineers endeavour to capture the complexity of the microenvironment with a view to improving the liver-specific functionality, longevity and relevance of the cultured cells [62]. The recent progress in 3D *in vitro* liver spheroid models may improve the ability to predict hepatotoxicity of novel compounds, in part owing to the better recapitulation of the native physiology of the liver [97]. It has been shown that the re-establishment of cellular polarisation is critical in maintaining gene expression and hepatocyte-specific function [98]. With 2D cultures of hepatocytes unable to model the multiple apical and basolateral membranes of the *in vivo* hepatocytes, it is crucial that liver models are capable of restoring this highly-complex microenvironment. There are now a number of 3D liver approaches which help restore this highly-complex microenvironment including hydrogel [30, 57, 99, 100] and scaffold based technologies [101], as well as the production of “hepatospheres” or liver spheroids

[102]. For the latter, techniques to produce spheroids have become progressively more refined and accessible, and they are being increasingly utilised to assess areas such as xenobiotic penetration, metabolism and hepatotoxicity [103].

The basic underlying principle for the production of spheroids is that monodispersed cells (isolated cells from fresh tissue or cell lines) are capable of reforming a 3D configuration via self-reaggregation if adhesion to the substrate in which they are being cultured in is prevented [104]. According to the prevalent theory of self-assembly, in the absence of external influences, cells will self-organize into a spherical conformation as a result of specific local interactions amongst the cells themselves [99]. In conjunction with this, the differential adhesion hypothesis (DAH) states that tissues are treated as liquids composed of mobile cells whose varying degrees of surface adhesion causes them to reorganize spontaneously in order to minimize their free energy [105]. Thus, cells will migrate to be near other cells of comparable adhesive capacity in order to maximize the strength of the bonds between them. This in turn produces a more thermodynamically stable structure [99].

One of the main advantages of culturing cells in a spheroid is the increased cell-cell interactions and cell-ECM interactions when compared to 2D monolayer culture [43]. The majority of cells are in close contact with each other and are able to communicate and produce their own ECM. Cells within a spheroid have virtually 100% of their surfaces in contact with neighbouring cells unlike a 2D monolayer. On this basis, cells in a spheroid conformation mimic much more closely the cells natural *in vivo*-like state. **Figure 1-7** illustrates the differences between monolayer cells and cells grown in a 3D spheroid model.

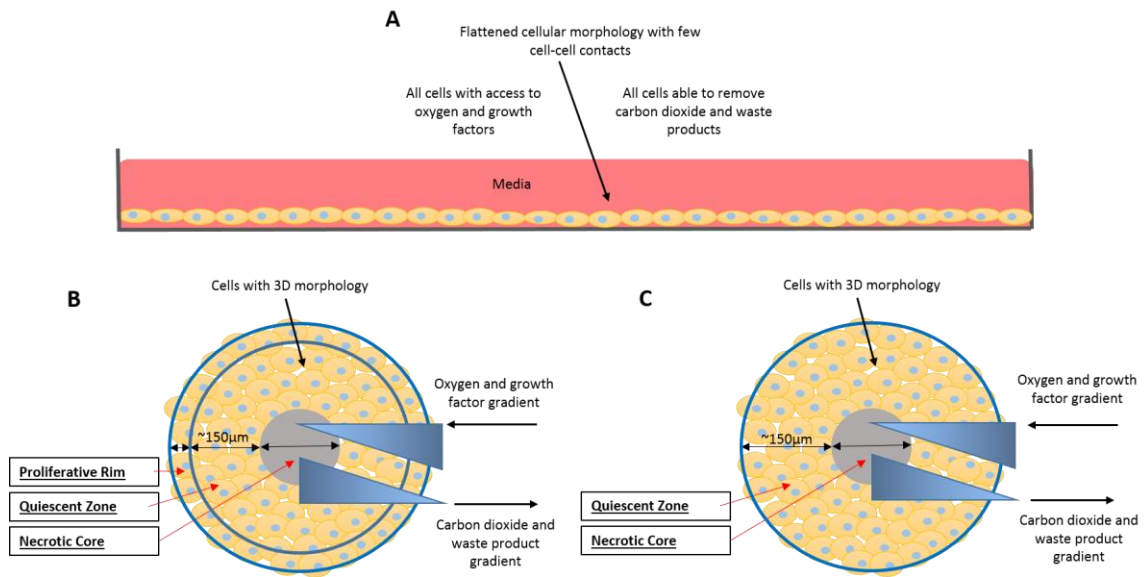


Figure 1-7 - Comparison of monolayer cells and cells cultured in a spheroid. (A) Monolayer cells become flattened, have very few cell-cell contacts, unlimited access to the media as well as ease of waste product expulsion into the media. (B) Proliferative cell lines grown within the spheroid have numerous cell-cell contacts, do not become flattened and retain an *in vivo*-like morphology. Cells on the periphery of the spheroid proliferate and have greater access to media and can remove waste products easier than those cells situated in the centre of the spheroid. These cells have less access to the nutrients within the media and less access to oxygen due to an oxygen diffusion gradient. Waste products may also accumulate in this central area, and potentially this may cause necrotic regions. Over the duration of the culture period, the size of the spheroid can increase dramatically. (C) Non-proliferative cells such as PHH/PRH grown within a spheroid again have numerous cell-cell contacts and retain an *in vivo*-like morphology. Similar nutrient and solute gradients form within the spheroids. However, as there is no proliferative rim, the overall size of the spheroid remains relatively constant over-time, reducing the formation of necrotic areas due to hypoxia.

A number of hepatic-derived cell lines have been utilised extensively in research including; C3A, HepG2, HepaRG and Huh7 [43, 76, 106, 107]. These cell lines are capable of forming 3D liver spheroids and the resultant models are most commonly being used in the early stages of assessing xenobiotic safety [15]. HepG2 cells cultured as a spheroid model show the morphological characteristics of hepatocyte-like cells, as well as the formation of bile canalicular-like structures. HepG2 spheroids also exhibit a highly compact structure with tight cell-cell interactions [108]. Studies by Li *et al.* and Ramaiahgari *et al.* have assessed a number of key functional outputs including; (i) cellular interactions as shown by E-cadherin, electron microscopy, β 1-integrin and β -catenin that are indicative of polarity; (ii) epithelial characteristics (CK7/8); and (iii) proliferative capabilities (Ki-67) [43, 100]. Wrzesinski and colleagues, along with others, have also investigated end points such as albumin and urea production, and metabolic competence via CYP activity (CYP1A1, CYP1A2, CYP3A4, & CYP7A1) [73, 76, 100]. These studies have conclusively elucidated that spheroids, and perhaps in general, 3D cultures of the HepG2 cell line show enhanced liver-like functionality when compared to the more traditional 2D cultures. However, it is widely accepted that with their low metabolic competence [15], HepG2 spheroids may be limited in their use as a model for toxicological investigations and may underestimate the toxicity potential of compounds [80].

The formation of bile canalicular-like structures within HepG2 spheroids has been increasingly investigated in recent years [100, 109]. Much of the work has shown the formation of these structures but further investigation into whether or not they are functional in producing bile salts and their subsequent transport is required [15]. It has been shown in work previously undertaken with the HepG2 and C3A cell, that there are several quantifiably useful end points such as albumin, urea secretion and ATP content that can be used to confirm *in vitro* 3D liver model phenotype lines [43, 108, 109]. Recently, Gaskell *et al.* demonstrated secondary structure functionality in C3A spheroids via the transport of 5-chloromethylfluorescein diacetate (CMFDA) by the canalicular transporter MRP2 [76]. This line of investigation has yet to be fully characterised in primary hepatocyte spheroids and would help strengthen the case that 3D spheroid

cultures may be better placed to assess hepatobiliary transporter-based compounds. Nevertheless, HepG2 or C3A cells have poor metabolic competencies when compared with PHH in 2D and this is one of the main limitations with these commonly used cell lines [79].

There are a limited number of publications using HepaRG cells in a 3D liver microtissue model [15]. However, with the accumulation of studies detailing more comparable functionality to that of PHH and improved functionality when compared with the more commonly used cell lines such as HepG2 and C3A cells in 2D culture, it is anticipated that a 3D HepaRG model may bridge the gap between conventional monolayer cultures and *in vivo* physiology [74, 77, 85, 110].

Gunness *et al.* reported the production of 3D organotypic cultures using HepaRG cells via the high-throughput hanging drop method [111]. They were able to maintain the cultures for 3 weeks and showed conservation of high liver-specific function for the duration of culture via phase I enzymes (CYP3A4, CYP2E1), transporter activity (MRP2), expression of liver-specific proteins (albumin, urea) and response to a number of drugs (APAP, troglitazone and rosiglitazone). In order to assess whether the 3D HepaRG cultures were a more appropriate model to study drug toxicity, 2D HepaRG cultures were set up in parallel with the 3D cultures over 3 weeks. 3D HepaRG cultures showed higher sensitivity for APAP and troglitazone toxicity, and the 3D cultures maintained high levels of liver-specific functionality, including phase I enzyme and transporter activity, and also production of liver-specific proteins including albumin and urea. These investigators therefore suggested that these 3D organotypic HepaRG cultures provide a suitable *in vitro* tool for assessment of drug-induced hepatotoxicity [111].

HepaRG cells when cultured differentiate into hepatocyte-like cells and biliary-like cells and it has been demonstrated that bile canalicular-like structures form throughout 3D models [112]. The fact that the HepaRG cell line differentiates into two distinguishable cell types means that the resultant cultures are intrinsically co-cultures in nature. Compared with the more commonly used hepatic-derived cell lines, HepaRG cells

possess many more advantages with regards to specific functional output, formation of secondary structures, upregulated metabolic capacity and this makes them much more comparable to PHH [77, 86, 113].

The main advantage of 3D models, and in particular the spheroid model, is that very few cells are required to produce a functional spheroid [15]. For example, we have demonstrated that a functional PRH spheroid can be produced from as little as 2000 cells/well on a 96-well plate (LOT).

PRH spheroid models are well characterised and have been used since the 1980's [42]. These spheroids have been shown to have a smooth outer surface with numerous pore-like openings leading to secondary structures shown to be similar to bile canaliculi [41]. Cells within the spheroid have also shown polarisation by IHC staining of apical HA4 and basolateral HA321 membrane bound proteins [41], and dipeptidyl peptidase 4 (DPP IV) by immunohistochemical staining as an apical membrane marker [114]. Earlier studies have focussed on characterising the cellular morphology and polarity in conjunction with the formation of bile canaliculi [41, 115]. However, more recent work has involved examining intra-cellular interactions and communication along with oxygen concentration and gradients throughout the spheroids [109, 116, 117].

Due to metabolism and uptake of numerous solutes by hepatocytes, the composition of blood changes as it flows along the sinusoids from the periportal zone to perivenous zone. Concentration gradients of substrates, products and hormones are formed and subsequently drive liver zonation [118]. This sinusoidal zonation is extremely important to discuss when looking at hepatotoxic potential of xenobiotics. If we look at APAP toxicity for example, glucuronidation, the dominant pathway of phase II conjugation at high and prolonged APAP concentrations (>5 mM), has been shown to be more rapid in perivenous cells than in periportal cells. Prolonged exposure to high concentrations of APAP damages perivenous cells expressing higher levels of CYP2E1 than periportal cells [119]. This demonstrates that perivenous hepatocytes exhibit increased APAP vulnerability and extensive glutathione depletion when compared with periportal cells,

and emphasises the importance of being able to recapitulate liver-specific zonation and solute gradients *in vitro*.

As one of the circulating signals, oxygen plays an important role in modulating zonation along the liver sinusoid. The partial pressure of oxygen is approximately 60 to 65 mm Hg (84-91 $\mu\text{mol/L}$) in the periportal blood and falls to about 30 to 35 mm Hg (42-49 $\mu\text{mol/L}$) in the perivenous blood [120, 121]. Research utilising liver spheroids has become progressively more interested in the physiological oxygen tension along the sinusoid, with increasing focus on trying to experimentally recapitulate oxygen profiles within 3D liver models.

Oxygen demand and concentration throughout the *in vitro* spheroid models remains an interesting topic of research because it is desirable that all the cells remain viable and free from necrosis. The literature describes that spheroids with a diameter of greater than 150 μm form a necrotic core due to hypoxia and lack of nutrients (see **Figure 1-7**) [32]. For an *in vitro* model used in cancer medicine for example, necrosis is a desirable characteristic because; larger tumour spheroids are characterised by an external proliferating rim, an internal quiescent zone, and a necrotic core resembling the cellular heterogeneity of solid *in vivo* tumours [122]. However, for a model that attempts to recapitulate the *in vivo*-like liver microenvironment, this is an undesirable characteristic. Being able to determine the oxygen diffusion and consumption within spheroids, and using this information to mimic the oxygen profile seen within the liver sinusoid would provide a more accomplished model than classic monolayer culture, and a more comparable one to that of the liver *in vivo*. In the field of 3D tumour cell culture, research has been dedicated to the quantitative description of tumour vascular networks whilst the consideration of oxygen consumption has been largely neglected. Whilst oxidative respiration in standard 2D cell culture has been widely studied, this aspect of characterisation has been lacking with 3D *in vitro* liver models [123].

Sakai *et al.* demonstrated that PRH cultured as spherical multicellular aggregates provided a more useful model than the traditional monolayer culture [109]. Using

quantitative polymerase chain reaction (PCR) it was shown that PRH rapidly lost expression of a number of liver-specific genes when cultured in monolayer from day 1 to day 5. In contrast, PRH spheroid cultures conferred higher levels of expression of these liver-specific genes when compared to the monolayer cultures for a period of up to 10 days. These results suggested that PRH cultured as spheroids acquire intercellular organisation that may permit maintenance of metabolic competence [102, 109].

As outlined previously, PHH are still considered by many to be the gold standard as an *in vitro* tool for DILI and toxicity investigations [37]. Despite the number of limitations with primary cells, spheroid systems can be produced from a low cell number, therefore a large number of spheroids can be produced from a small fraction of a single liver isolation/cell suspension [15]. It is also important to reiterate that hepatocytes isolated from different donors display marked variations in gene expression levels, and thus may respond differently in hepatotoxicity investigations. However, 3D spheroid culture enables the production of spheroids utilising cells from a single donor or pooled hepatocytes. The advantage of utilising pooled hepatocytes is that the resultant spheroids may better predict average population drug responses and conversely, spheroids produced from single donors allows for more direct *in vivo* variability comparisons [124].

Messner *et al.* characterised a multi-cell type spheroid system incorporating PHH and liver-derived NPCs [125]. This system was shown to be functional for a period of up to 5 weeks, demonstrating that longevity of the cultures is vastly improved compared with the conventional monolayer or sandwich cultures of PHH. Secondary structure formation was confirmed in these spheroids via immunohistochemical staining for the apical transporters MDR1 and BSEP, demonstrating functional polarisation of hepatocytes within the spheroids. In addition, these co-culture spheroids displayed improved longevity, stable albumin production over the duration of culture period and with KCs showed responsiveness to inflammatory stimuli. In these investigations, Messner and colleagues were able to incorporate both the 3D microenvironment and multiple cell

types within a single model, producing a more representative *in vitro* tool for the assessment of DILI [125]. These 3D, multicellular models show promise for drug discovery investigations as the much improved longevity and viability of the cells will enable the assessment of long-term effects of compounds over repeat-dose scenarios; an area initially highlighted as a limitation of many of the current commercially available *in vitro* liver models.

A more recent study carried out by Bell *et al.* produced PHH spheroids using ultra-low attachment plates [126]. Primary spheroids in this instance were cultured for a period of up to 5 weeks in serum-free culture medium. Primary spheroids have shown to decrease in size over the culture period alongside increasing expression of E-cadherin, suggesting that the cells within the spheroid model are becoming more tightly incorporated via spheroid compaction [127]. MRP2 staining revealed the formation of bile canaliculi-like structures throughout the spheroid body over the 35 day culture period, indicative of stable functional polarisation of hepatocytes [126]. A direct comparison can subsequently be made between the multi-cell spheroids produced by Messner *et al.* and the monoculture spheroids by Bell and colleagues. Interestingly, both researchers demonstrate improved longevity of up to 5 weeks in culture compared to conventional models via stable albumin production over the duration of the culture period. This demonstrates that co-cultures of NPCs and PHH within this spheroid model may not be essential for improving the longevity. However, the co-culture spheroid models with the inclusion of KC place themselves well to investigate immune-mediated toxicities, whereas a monoculture hepatocyte spheroid model may be inadequate for capturing this specific end point analysis. Both models demonstrate preserved hepatic phenotypes and long-term functionality for investigations into chronic toxicity assays and repeat-dose studies.

There are a number of techniques that have been implemented for the production of PHH and PRH spheroids including, spinner vessels and orbitally shaken flasks [35]. However, limitations of these systems include the inability to control spheroid size,

difficulties with manipulation in the lab as well as these systems requiring relatively high cell numbers. Scaffold-free systems that allow the formation of size controllable primary cell spheroids has currently only been performed using a hanging-drop system as described by Kelm and Fusseneger and the use of ULA plates described by Bell *et al.* [126, 128].

Sufficient supply of oxygen to the cells is crucial for a functional 3D *in vitro* model trying to recapitulate the liver microenvironment. Primary hepatocytes have a relatively high metabolic activity compared with their hepatic cell-line counterparts, and thus, primary hepatocytes have a high oxygen turnover which can be up to ten times greater than other types of non-proliferative cells [129]. Increased levels of albumin and urea production, along with other liver-specific functions have been seen to correlate with higher oxygen uptake rates (OUR) of hepatocytes [129]. The idea that increased functional output increases the oxygen demand on the cells suggests that, even the basic set up of *in vitro* liver models needs to be accurately determined to allow sufficient oxygen to diffuse through the media and into the cells. It also outdates the idea that spheroid diameter is the most crucial factor in determining the formation of central necrosis. It is much more likely that the combination of specific cellular OUR, along with proliferative characteristics and the experimental set up are equally as important.

1.5.4.2 Scaffold and Hydrogel Technology

In recent years it has been shown that the cellular microenvironment contributes to the spatially and temporally intricate signalling domain that directs cell phenotype, and thus the idea that cellular scaffolds serve simply as a vehicle with which to assess the expression of specific genes and subsequent functionality has become outdated [57]. Tibbitt *et al.* concluded that a cell can no longer be thought of as a single entity defined by its genomic material, but must also be regarded in the context of the ECM, soluble growth factors, hormones, and other molecules that regulate organ formation and function [57]. It is better understood that the extracellular microenvironment

coordinates intracellular signalling cascades that influences phenotype by altering gene and subsequent protein expression [130, 131].

Spheroids can be produced by embedding hepatocytes into non-adhesive hydrogels [132]. Spheroids form via the process of cellular self-assembly, and the cells that self-assemble into spheroids have been shown to achieve increased gene expression and retention of the native cell phenotype when compared to 2D cultures [99, 128]. Even though spheroids have been shown to form without scaffolds and hydrogels, not all cell lines are able to form spheroids via self-aggregation and thus, the 3D microtissue system required is heavily dependent on the cell type being utilised [133].

Lee *et al.* were able to produce functional encapsulated spheroids using Huh7 cells [107]. These encapsulated spheroids were functional for a period of up to 3 weeks and the microenvironment in which they were cultured could be adapted depending on the stiffness of the hydrogels [107]. In this case, an *in vitro* model representative of normal liver could be generated by utilising low stiffness hydrogels, and cirrhotic liver by increasing the stiffness of the gels. Lee *et al.* also demonstrated that spheroids cultured within the low stiffness hydrogels had the highest rates of proliferation, albumin secretion and CYP450 expression over the culture period.

Another way in which hepatocytes can be cultured to mimic the 3D microenvironment is the use of scaffolds produced from either natural or synthetic material [15]. Natural scaffold systems are thought to allow for biocompatibility with the cells, with the scaffold itself mimicking the native ECM and conferring multiple cell-ECM interactions. However, these natural liver-derived scaffolds are inherently variable leading to difficulties with experimental reproducibility. Decellularised human livers are considered the ideal ECM alternative because both the 3D microarchitecture and biological features of the native liver are preserved. However, human donor livers are in short supply as decellularised scaffolds, and the intrinsic inter-donor differences means that reproducibility of experiments can be difficult [134]. This limitation can be overcome with the use of synthetic scaffold systems and, similarly to hydrogels, they can be purposely engineered

to allow for specific 3D conformations and cell-specific scaffolds [135, 136]. Hepatocytes have been shown to have an affinity for galactose residues such that scaffold systems presenting galactose on their surfaces allows for improved hepatocyte adhesion leading to an improved functional system [137, 138].

An example of synthetic scaffolds that has been increasingly used within the field of 3D cell culture is the Alvetex® (Reinervate), which has been produced from cross-linked polystyrene. This system has been shown to be biocompatible and the manufacturing of the scaffold has shown little batch-to-batch variation allowing for more reproducible experimental data [31]. The scaffold is engineered into thin (200 µm) membranes that are able to fit into conventional multiwell plate plasticware. Knight *et al.* reported that cells seeded on to the scaffold system are able to form close cell-cell interactions and cellular differentiation, allowing the formation of thin tissue-like cultures [31]. Furthermore, the HepG2 cell line has been shown to have improved liver-specific functionality when cultured with the Alvetex® scaffold including higher viability over the culture period and the formation of bile canaliculi within the tissue-like cultures [139]. Rat hepatocytes have also been cultured using the Alvetex® scaffold system and have been shown to retain their native cuboidal morphology along with much improved viability when compared with conventional monolayer cultures. These 3D cultures display gene expression associated with phase I, II and III drug metabolism under basal conditions along with increased sensitivity to APAP toxicity [140].

One of the main limitations with the hydrogel technologies is that there is poor mass transfer of nutrients, oxygen, xenobiotics and cell retrieval is more difficult [15]. Cell retrieval difficulties have been previously described by Godoy and colleagues, developing the idea that downstream analysis becomes much more challenging with reduced cell numbers. This potentially remains a major caveat of hydrogel systems, as altering the hydrogel stiffness may impact the ability to dissociate cells from the gels themselves. However, with the development of more simplistic methods, the utilisation of non-adhesive hydrogels reduces cell-substrate interactions, thereby increasing the important

cell-cell interactions which are vital for retaining functionality as well as the driving process of self-assemble [99]. One of the main advantages of using non-adhesive hydrogels for the production of 3D microtissues is that hundreds of spheroids can be produced with a single pipetting step. This in turn means that the hydrogel method may lend itself to long-term, repeat-dose toxicological investigations [99].

1.5.4.3 Liver Organoids

Organoids are 3D culture models in which adult stem cells and their progeny grow and are able to recapitulate the natural physiology of the cells *in vivo*. Organoids have been successfully derived from a number of organ systems for both animals and humans [141]. “Organoid” is a term that, in the past, was used interchangeable for *in vitro* spheroid models. However, the term organoid refers to “stem cell-derived” self-organising organoids [142]. Organoids can be produced from two types of stem cells which include; pluripotent stem cells (PSCs) such as embryonic stem cells (ESCs) or induced pluripotent stem cells (iPSCs), and organ-specific adult stem cells (ASCs) such as hepatic progenitor cells (HPCs), which are tissue-specific resident stem cells. Organoid systems have the potential to aid in the development of personalised medicine/treatment strategies and have previously been utilised to investigate a number of disease models [142, 143]. As with hepatic-derived cell lines, 2D culture of PSCs is relatively amenable within the laboratory. However, long-term culture of PSCs with maintenance of stem cell characteristics is a limiting factor [144]. Additionally, 2D cultures fail to produce *in vivo* cell polarisation and intricate cellular interactions, and cannot recapitulate the complex 3D microenvironment as seen *in vivo* [54]. As with hepatic-derived cell lines and primary isolated cells, 3D culture of PSCs has become a rapidly developing field in order to overcome the limitations of monolayer cultures. Huch *et al.* developed a 3D culture system of HPCs that demonstrated long-term genetically stable expansion (>1 year) [33, 145]. The organoid models were derived from both Lgr5+ cells (mouse) and EpCAM+ (normal human liver) ductal cells. It was shown that the original phenotypic epithelial architecture of the cells were maintained and that organoids were differentiated *in vitro*

toward hepatocyte-like and cholangiocyte-like cells [142]. Additionally, upon transplantation of the Lgr5⁺ organoid into impaired mouse livers, this propagated the formation of functionally mature hepatocytes [145].

Takebe *et al.* demonstrated the formation of vascularised, functional human liver organoids from human iPSCs via transplantation of liver buds created *in vitro* (iPSCs-LB) [146]. The researchers were able to show the formation of functional vasculatures that stimulated the maturation of iPSCs-LB into tissue that highly resembled the adult liver. Metabolically competent iPSC-derived tissue demonstrated liver-specific functionality including increased albumin production and human-specific drug metabolism [146]. Commercially available iPSCs have also been used as an *in vitro* tool for the assessment of hepatotoxic potential with Sirenko *et al.* demonstrating this with a large number of identified toxic compounds [147]. The researchers used iCell[®] hepatocytes (Cellular Dynamics International [CDI], Madison WI) which are human iPSC-derived hepatocytes cultured in a 2D multi-well plate platform. The researchers demonstrated that high-content automated screening assays using iPSC-derived hepatocytes were feasible, and additionally this model provided useful information about the potential mechanisms of toxicity. These results suggest that this *in vitro* liver model may be well placed to assess drug and xenobiotic safety. Although this model does show promise, it is clear that monolayer cultures of iPSCs are not representative of the liver *in vivo* and the toxic potential of compounds was assessed over a 72-hour period only. Generation of 3D iPSCs may allow for repeat-dose of xenobiotics and it would be interesting to see the potential of this model in assessing chemicals with unknown toxicity and other novel xenobiotics.

3D organoid systems provide an *in vitro* platform that is highly representative of the *in vivo* physiology of liver cells, and have developed our understanding of disease development and progression. Liver organoids have also demonstrated accurate recapitulation of disease pathways *in vivo*. Although much of the research to date concerning liver organoid systems are focused on the developing field of personalised

medicine, these 3D *in vitro* tools position themselves equally to be utilised within the field of xenobiotic safety and drug toxicity investigations. PSCs have been shown to be a promising model to assess hepatotoxicity in acute treatments, and also in response to chronic drug exposure and repeated-dose investigations, potentially overcoming some of the shortfalls of more commonly used hepatic-derived cell lines [36, 148]. See **Table 2** for a summation of the advantages and limitations of the multiple cell types and culture platforms that have been described.

1.5.5 *In vitro* to *in vivo* extrapolation (IVIVE)

We have previously described a number of *in vitro* cell models. However, it is becoming more apparent that quantitative analyses of the various *in vitro* liver models is necessary to aid in demonstrating their potential for hepatotoxicity investigations compared to more qualitative measures such as physiological and functional improvements of the cell models. Many reviews have detailed improved physiological and metabolic status of 3D and co-culture *in vitro* liver models. However, few have combined this with IVIVE as a quantitative classification tool for the different models. IVIVE refers to the transposition of experimental results or data *in vitro* to predict phenomena *in vivo*. Extrapolation of intrinsic clearance (CL_{int}) measurements using hepatocytes to give predicted *in vivo* clearance ($CL_{in vivo}$) involves a well-established ‘two-step’ mechanistic approach. Firstly, the physiological scaling from cell to whole liver and secondly the subsequent modelling of extraction from blood by the liver [15]. There have been a number of investigations that have compared *in vitro* liver model CL_{int} as a means to develop the predictive capabilities with regards to xenobiotic safety assessments.

Suspensions of PRH have been shown to provide a more accurate estimation of CL_{int} rate when compared to conventional PRH monolayer cultures [149]. Griffin *et al.* investigated the incubation of seven compounds in both suspensions and monolayer cultures, and the CL_{int} was obtained via metabolite formation or substrate depletion analysis [149]. However, the main limitation with this *in vitro* system was that cells rapidly dedifferentiated *ex vivo* in suspension, whereas often the processes of hepatotoxicity

manifest themselves over several hours. Therefore, hepatocytes in suspension are unable to maintain viability for the time necessary to capture the development of toxicities for some xenobiotics. As such the assessment of long-term or repeat-dose investigations with this *in vitro* model will in turn be ineffectual.

Research utilising rat microsomes, hepatocytes and liver slices have indicated adequate accuracy with the aforementioned two-step mechanistic approach [150]. However, more recent investigations have demonstrated that rates of drug metabolism and CL_{int} were found to be lower in rat liver slices than in isolated rat hepatocytes [151]. Other research has indicated that this two-step IVIVE mechanistic approach leads to under-prediction of human *in vivo* clearance when utilising human hepatocytes and microsomes [152].

Although much of the work to date has particularly focused on suspensions and 2D cultures of cryopreserved and primary isolated hepatocytes, more recent publications have analysed the prospective competence of the more novel HepaRG hepatic-derived cells [153]. Zanelli and colleagues compared intrinsic clearance of 26 drug compounds in both cryopreserved hepatocytes and the more novel HepaRG cell line [153]. The CL_{int} of the compounds was determined via substrate depletion and the results showed that there was a direct correlation of CL_{int} for both cryopreserved hepatocytes and HepaRG cells (scaled to whole body) for the range of compounds used.

Co-culture bioprinted systems have also been analysed to investigate their potential for hepatotoxicity studies. An example of this is the Hepregen system which is a collagen micro patterned substrate system where hepatocytes are seeded onto a feeder layer of a secondary cell type. When compared to human microsomes, and PHH suspensions, the Hepregen system allowed for longer incubations with 27 known liver-metabolised compounds and was able to generate a greater proportion of the major human metabolites normally found *in vivo* [154].

Bioreactors and 3D cultures are rapidly becoming incorporated within industry and research as improved predictive platforms for xenobiotic safety assessments. Sivaraman

et al. demonstrated this by using a 3D bioreactor system to analyse the functionality of PRH spheroids [155]. This system was developed as it allowed the formation of heterotypic cell interactions, shear stresses via flow, and an *in vivo* liver-like microarchitecture. Toxicity testing utilising this bioreactor system included studies showing that clearance rates of compounds with known liver metabolism were comparable to those obtained *in vivo* [49, 62].

Table 2- Advantages and limitations of cell lines and culture methods used in vitro liver models.

<u>Cell Type</u>	<u>Advantages</u>	<u>Limitations</u>
HepG2	<p>Unlimited source of cells.</p> <p>Repeatability of experiments is more achievable.</p> <p>Easy-to-handle in laboratory with simplistic culture methods.</p> <p>No inter-donor differences.</p> <p>Some expression of liver-specific enzymes.</p>	<p>Low metabolic competence and rapid loss of expression of liver-specific enzymes/transporters.</p> <p>Loss of cellular polarity. Absence of NPCs.</p>
C3A (HepG2/C3A)	<p>Selected for strong contact inhibited growth characteristics.</p> <p>High albumin production, alpha fetoprotein (AFP) production and ability to thrive in glucose deficient media.</p>	<p>Low metabolic competence and rapid loss of expression of liver-specific enzymes/transporters. Loss of polarity.</p> <p>Absence of NPCs.</p>

<p>HepaRG</p>	<p>Improved liver-specific functionality when compared with the commonly used HepG2 and C3A cells in 2D culture.</p> <p>More comparable to PHH for phase I & II, gene and transporter expression.</p>	<p>More complex culturing methods when compared to more commonly used hepatic cell lines.</p> <p>Expensive consumables required for extended culture periods.</p>
<p>Primary hepatocytes (human, rat)</p>	<p>Improved metabolic competence and more physiologically relevant compared to hepatic-derived cell lines.</p> <p>Availability of cryopreserved hepatocytes. Full expression of liver-specific enzymes.</p> <p>Good transferability of data for <i>in vitro</i> to <i>in vivo</i> models. Historical human data for numerous drugs allows for direct comparison with <i>in vitro</i> models.</p>	<p>Limited availability for researchers and inter-donor variability.</p> <p>Short-term culture time.</p> <p>Rapid loss of expression of liver-specific enzymes.</p> <p>Difficult isolation and subsequent culturing processes.</p> <p>Limitations can be partially overcome by 3D culturing.</p>
<p>Stem cell based approaches</p>	<p>Stem cells proliferate extensively <i>in vitro</i> and can differentiate into hepatocytes. This provides a stable source of hepatocytes for multiple investigations. iPSCs/HPCs have the potential to establish genotype-specific cells, increasing the predictivity of toxicity assays.</p>	<p>Dedifferentiation concerns after the long-term culture of PSCs.</p> <p>Few thorough investigation in toxicological applications. Complex reprogramming steps (iPSCs.)</p> <p>Variability in phenotype between preparations.</p>

	Potential to develop personalised medicine and hepatotoxicity investigations.	Expensive when compared with other hepatic-derived cell lines.
<u>In vitro Approach</u>	<u>Advantages</u>	<u>Limitations</u>
Monolayer cultures	<p>Simplistic culture methods and low set-up costs. Good repeatability of experimental data.</p> <p>Can incorporate NPCs improving overall functionality and longevity.</p>	<p>Cannot recapitulate the complex 3D microenvironment.</p> <p>Lack of <i>in vivo</i>-like cellular morphology. Poor gene and subsequent protein expression profiles. Loss of cell polarity.</p>
Sandwich cultures	Sandwich cultured hepatocytes retain more <i>in vivo</i> -like properties, including polarised excretory function and enhanced morphology and viability of hepatocytes compared to monolayer cultures.	Sandwich cultures lack complex cellular interactions and the 3D microenvironment. The expression of genes responsible for many liver-specific functions decreases over time.
Co-Culture	<p>Multi-cellular environment with direct cell-cell interactions mimicking natural environment.</p> <p>Positive reciprocal effect with improved functionality and longevity.</p> <p>Recovery of cellular polarity</p>	<p>Limited availability of NPCs with difficult isolation procedures.</p> <p>Batch to batch variability between NPCs.</p>

	Co-culture models can be; 2D, sandwich cultures, and 3D cultures such as spheroids.	Differentiation status and viability are varied depending on culture conditions.
Scaffold and Hydrogels	Formation of cellular interactions and representation of native ECM. Improved functionality and sensitivity to APAP. Ability to mimic pathologies via stiffness variation.	Limitations with regards to mass transfer of oxygen and nutrients. Limitations with cell retrieval and subsequent analysis. Poor culture longevity
3D	Recapitulation of 3D microenvironment and ECM properties. Well established cellular interactions leading to improved gene and protein expression. Establishment of cellular polarity. Can incorporate NPCs improving overall functionality and longevity.	More complicated methods of culture. The literature has extensively discussed the formation of necrotic regions within 3D cellular models due to reduced oxygen diffusion to cells within the 3D mass.
Spheroids	Multicellular environments recapitulating native 3D microenvironment. Cell-cell interactions and natural production of ECM. Spheroids can be produced with hepatic cell lines and primary hepatocytes. Maintain liver-specific functionality over longer periods of time. Enhanced CYP450 and transporter expression.	Spheroids have a limited size due to formation of necrotic cores (~150µm). Limitations of oxygen and nutrient diffusion through multicellular aggregates. Comprehensive investigation with regards to optimal spheroid size for specific cell types has yet to be done including cell-specific and model-specific OUR.

	<p>Formation of secondary structures (bile canalicular-like structures).</p> <p>Cellular polarity is recovered. Along with maintenance of native cuboidal morphology.</p>	<p>More work needs to be done to improve basis for high-throughput system.</p>
Liver slices	<p>Maintains multicellularity (all NPCs) in appropriate proportions and complex 3D microenvironment.</p> <p>Can be incorporated into flow systems to allow shear stresses.</p>	<p>Short term culture periods meaning liver slices are unsuitable for repeat-dose investigations.</p> <p>Specialised equipment and technical expertise required.</p>

1.6 Mathematical modelling of the liver

The majority of earlier studies focussing on mathematical modelling of the liver has focused on pharmacokinetic (PK) modelling. This type of modelling can be subcategorised in to three distinct groups which are: simple compartmental models, physiologically based pharmacokinetic (PBPK) models, and the more recently emerging model-independent pharmacokinetic (MIPK) systems.

1.6.1.1 Compartmental modelling

Compartmental modelling is a pragmatic, experimentally-derived approach where compartments do not necessarily have a distinct physiological or anatomic basis [156]. Usually this modelling approach uses single or multiple compartments and although this approach is relatively uncomplicated when compared with more complex systems, many useful quantities (i.e. C_e , V_d , C_{max} etc.) can be determined by comparing large numbers of historical and clinical data sets with predicted values [157].

1.6.1.2 Physiologically based pharmacokinetic modelling

The concept of PBPK modelling was first introduced in 1937 by Toerell et al. [158]. PBPK models increase the complexity of the simple compartmental modelling approach by classifying the aforementioned compartments as specific anatomic spaces [159]. PBPK models are also made more complex than the simple compartmental PK models by incorporating experimentally-determined organ-to-organ transfer and flow rates along with acquired blood and tissue concentration ratios [160].

1.6.1.3 Model independent pharmacokinetic modelling

MIPK modelling is an *in silico* technique and is based solely on mathematical evaluations [161]. MIPK modelling avoids the use of potentially unverified kinetic parameters, and is less complex in comparison to PBPK approaches. This approach of mathematical modelling provides useful information regarding clearance, adsorption and elimination rates etc. However, specific information such as drug distribution cannot be obtained. Model-independent systems are sometimes referred to as 'Black box' models. This approach provides an empirical and stochastic method for the study of complex systems [162]. This type of modelling requires assumptions that, while the input concentration of a drug to a region (e.g arterial concentrations) and the output concentration from that region (e.g venous concentrations) can be measured, the specific features that affect the dynamics of drug transport, uptake and extraction within the region are unknown. Consequently, the region in question is treated as a 'black box'. Thus, these simplistic methodologies disregard the physiological and physicochemical information [162].

1.6.1.4 Hepatic clearance modelling

Mathematical modelling of aspects of the liver has been conducted for decades, with much of the literature reporting on metabolic clearance of xenobiotics in the form of hepatic drug clearance models [163-165]. Clearance within the liver is described as the volume of the perfusing blood that is effectively cleared of drug per unit time [166]. Therefore, clearance relates the concentration of drug entering the liver and the rate of

drug displacement. Despite the fact that total clearance is defined as the cumulative sum of all the eliminating organs of the body, an understanding of hepatic clearance is critically important as the liver is the major metabolising site [167].

Hepatic drug clearance models initially take one of two forms: the “well stirred model”, which describes the liver as a well stirred compartment, with the liver concentration of the drug in equilibrium with that in the blood e.g. see [168]; and the “parallel-tube” model which describes the liver as being composed of a number of identical and parallel tubes along which drug concentration decreases progressively in the direction of blood flow, due to its elimination by hepatic enzymes [169]. Generally the “parallel-tube” model predicts that the steady-state drug concentration following a constant rate oral administration increases with an increase in hepatic blood flow [170]. The “well stirred” model on the other hand predicts that this parameter is not sensitive to changes in hepatic blood flow [170].

Various assumptions are made for both types of mathematical models. One such assumption relates to whether the drug is bound or unbound. Bound drug is associated with either plasma or blood cell elements [156]. Typically, these type of models include a parameter that describes the ratio of the free concentration of drug to that of the bound concentration. This specific parameter is useful as only unbound drug can interact with enzymes or target receptors. Also within these models, there are intrinsically located eliminating liver enzymes whose activity can be defined using Michaelis-Menten kinetics, namely the maximum velocity (V_{max}) and Michaelis-Menten constant (K_m) [163]. Michaelis-Menten kinetics describe the concept that increasing the concentration of a substrate indefinitely does not increase the rate of an enzyme-catalysed reaction beyond a certain threshold. This threshold is reached when, for example, the substrate molecules completely saturate the enzyme's active sites [171]. V_{max} then represents the rate of the enzymatic reaction under these conditions. The parameter K_m introduces the idea of the binding affinity of enzymes to specific substrates [171]. It describes the substrate concentration at which half the enzyme's active sites are occupied by the

substrate. A high K_m means that a lot of substrate must be present to saturate the enzyme, thus the enzyme has low affinity for the substrate. On the other hand, a low K_m means that only a small amount of substrate is required to saturate the enzyme, indicating a high affinity for the substrate.

In terms of clearance of a compound in the liver, by Fick's principle, the rate of removal of the drug from the blood into the liver (v) is given by the difference between the incoming concentrations of drug (C_{in}) and outflowing drug concentration (C_{out}) in the blood, multiplied by the hepatic blood flow (Q). This loss of drug from the blood is equal to the summation of uptake of drug into the liver, the rate of metabolism in the liver, and the biliary excretion [172]. At steady state, the net rate of change of drug in the liver is 0, and v then equals the sum of the rates of metabolism and biliary excretion. Therefore, by definition, at steady state hepatic clearance (CL) can be defined as,

$$CL = \frac{v}{C_{in}} = \frac{Q(C_{in} - C_{out})}{C_{in}} = QE, \quad (1-1)$$

where E , is the steady-state hepatic clearance ratio.

Related to this, there is an additional concept that is introduced within these model systems referred to as intrinsic clearance (CL_{int}). This parameter attempts to measure the intrinsic enzymatic activity of hepatocytes, independent of hepatic blood flow and binding. Both compartmental modelling approaches, namely parallel tube and well stirred models, provide useful information. However, it is clear that for xenobiotics with either very high or very low extraction ratios, no distinction can be made between the models for clearance with respect to changes in either blood flow, drug binding within the blood, or intrinsic clearance [163]. Pang and Rowland concluded that to distinguish between these compartmental models, investigations looking at the changes in the features of hepatic clearance including hepatic blood flow, drug binding within blood,

and intrinsic clearance are required to see how these will affect the extraction ratio and clearance of xenobiotics with intermediate extraction ratios [163].

PBPK modelling has been used to aid the prediction of the pharmacokinetic characteristics of xenobiotics in humans and other animal systems via the utilisation and implementation of clinical and preclinical data [173]. PBPK modelling has also been used to investigate the effects of physiological variables such as age, sex, ethnicity, and disease status [174]. PBPK modelling attempts have also been used to assess the risk factors associated with multiple drug interactions [175].

PBPK models have a number of advantages over more simplistic compartmental models due to the inclusion of verifiably derived parameters and the ability to alter these parameters to represent physiological changes, e.g. perhaps due to disease pathologies and even to aid in the prediction of species-species differences. PBPK models provide robust estimates for classically described pharmacokinetic parameters such as clearance rates etc. and provide a quantitative mechanistic framework by which known drug-specific parameters can be used to predict the plasma as well as organ concentration–time profiles over time [156]. PBPK models can also be used for estimating variable responses in disease profiles by extrapolating a dose in healthy volunteers to one in a disease population by incorporating relevant organ-level specific physiological properties that may affect the functionality and dynamics of the target organ [156]. PBPK modelling therefore provides a more representative *in silico* system when compared to classic compartmental modelling due to its more representative structure and intensive use of experimentally derived data [176].

1.6.1.5 Modelling oxygen diffusion and consumption

Pharmacokinetic modelling typically aim at the clinical end of toxicology (i.e. dealing with *in vivo* data and modelling predictions). An alternative approach focusses on *in vitro* modelling aspects, with a particular focus on modelling oxygen diffusion and availability/cellular respiration in novel 3D *in vitro* systems [177, 178]. The supply of

oxygen to tissue cultures and the subsequent turnover of oxygen via cellular respiration is an extremely important factor to consider when developing new *in vitro* cellular models, and is an extensively underappreciated problem [179] .

In recent years, oxygen supply has been intensely investigated in microfluidic devices [180], alongside the development of extracorporeal devices as a means of treatment for acute liver failure (ALF) [181]. The main limitation with the development of *in vitro* liver systems that incorporate fluid flow, such as bioreactor models or even simplistic perfusion devices, is the supply of oxygen to the hepatocytes. The main parameter that needs to be elucidated for these studies is the oxygen consumption rate (OCR) also described previously as the oxygen usage rate, (OUR) by the cultured cells [34, 182]. There have been a number of approaches to determine this experimental parameter, for a number of culture techniques including conventional monolayer cells, sandwich cultures, spheroid models and microfluidic or bioreactor platforms.

Additionally, there have been numerous approaches for the replacement of liver function in patients with ALF, with whole liver transplantation being the most successful [183]. One of the more promising approaches that incorporates both *in silico* modelling and *in vitro* engineering is the development of a bioartificial liver which consists of functional hepatocytes cultured within platforms such as hollow fibre bioreactors, or microfluidic devices [184, 185]. For example, Rotem and colleagues developed a simple perfusion system based on a T-75 cell culture flask where hepatocytes were cultured and overlaid with collagen, with specific oxygen inlet and outlet channels and separate oxygen sensing probe attachments [181].

The oxygen concentration at the inlet and outlet channels were determined using an oxygen electrode with the average OCR calculated from a simple mass balance equation, namely,

$$OCR = k(P_i - P_o)Q/n, \quad (1-2)$$

where k is the solubility of oxygen under 21% oxygen and atmospheric pressure, P_i and P_o are the measured partial pressures of oxygen at the inlet and outlet respectively, Q is the volumetric flow rate, and n is the total amount of cellular DNA (μg) in the T-75 flask.

In order to determine the effect of the flow rate on the OCR, the researchers also carried out a number of experiments where the flow rate was varied between 1 and 8 ml/min. This work particularly demonstrated that oxygen can quickly become a limiting nutrient, negatively impacting on both the viability of the hepatocytes and the liver-specific functionality of the cells. Optimised operating conditions for the *in vitro* platform are therefore imperative for oxygen supply to remain appropriate and within the normoxic ranges required by the cells [181].

Yarmush *et al.* [186] conducted a similar investigation (implementing equation (1-2) but substituting cell number instead of normalising the data to DNA). These researchers demonstrated that hepatocyte OCR increased during the first day and then remained approximately constant in the sandwich culture for up to 12 days. They further utilised the experimentally derived OCR values by developing a simple mathematical model to describe the functional response of the hepatocytes to variations in cell densities, depth of medium, and external oxygen tensions. The transport and consumption of oxygen within the culture dish was described with a diffusion-reaction equation in one dimension, namely;

$$\frac{\partial^2 P}{\partial x^2} = 0, \quad (1-3)$$

with boundary conditions,

$$-D \frac{\partial P}{\partial x} = \frac{V_{max}\rho P}{k(K_m + p)} \quad \text{at} \quad x = \delta, \quad (1-4)$$

$$P = P_s \quad \text{at} \quad x = 0, \quad (1-5)$$

where P is the partial pressure of oxygen in the liquid media (mmHg), P_s is the partial pressure of oxygen at the gas-liquid interface, K_m is the partial pressure at which the oxygen uptake rate is half-maximal, V_{max} is the maximal specific oxygen uptake rate derived experimentally (OCR), ρ is the cell density, δ is the depth of liquid, x is the variable distance from the air-liquid surface to the cell surface, and D represents the diffusivity of oxygen in the liquid media.

The results from this model coupled with cell culture observations demonstrated the need for optimised culture conditions. For this specific culture platform, cell attachment time and variations in media depth, external oxygen partial pressure etc. were shown to play a pivotal role in the subsequent functionality of the hepatocytes and their longevity. These investigations were consistent with the observations by Rotem and colleagues and suggest the requirement of precise and optimised operating conditions in order to maintain hepatocyte cellular functionality.

1.6.1.6 Mathematical modelling of spheroids

There are a number of notable mathematical modelling examples with regards to 3D spheroid systems [177, 187, 188]. A large number of mathematical modelling approaches have looked at tumour spheroids, the growth dynamics of the tumour cells, and the subsequent effect on drug diffusion and metabolism [177, 188, 189]. The majority of these models describe the tumour growth based on mass balance principles for cells and reaction–diffusion equations for interacting chemicals, such as growth factors [188]. There are a number of considerations that these models take into account such as;

tumour cell dynamics including, motility, proliferation and cell death, and they also assess the effect these spatio-temporal changes with regards to diffusing xenobiotics or particles.

Byrne *et al.* provide an in-depth review of how these types of mathematical models utilise reaction-diffusion equations to predict the distribution within the tumour of the diffusing solute or xenobiotic [188]. Integro-differential equations are often used to describe the changes in the tumours volumetric growth rates via proliferation and cell death. A number of these models have been able to reproduce experimentally observed characteristics such as the three specific zones associated with tumour cell spheroid models (e.g. necrotic, quiescent, proliferative, see **Figure 1-7**).

Ward *et al.* describe a mathematical model where the spheroid contains live cells which generate volume changes due to specific cellular birth and death events [187]. The equations utilised in this model have a multiphase form, with variables for the volume fraction of live tumour cells and a volume fraction for cellular material, with a no-void condition connecting the two. The authors use a combination of analytical approaches (asymptotic) and simulations to study drug dosing of the tumour spheroids. The researchers conclude that this modelling approach provides good qualitative agreement with experimental observations with regards to the dependence of cell survival on the drug dosage and treatment duration and on the initial spheroid size.

The modelling such as that used by Ward *et al.* use what is described as a continuum approach, i.e. variables track the density of cells rather than the individual cells themselves [177, 187]. An alternative approach is known as cellular automaton, where the individual cells are tracked rather than the cell densities. An early example of this cellular automata modelling approach was constructed by DÜchting and Vogelsaenger [190], who used it to investigate the effects of both radiation therapy and chemotherapy on tumour growth dynamics. More recent publications have implemented cellular automata modelling, for example, to investigate the effects of both oxygen and pH on tumour growth and morphology [191]. The researchers in this instance placed particular

emphasis on the impact of pH regulatory mechanisms and what effect these had on cellular pH gradients and subsequent tumour morphology. Such approaches have been applied to spheroids to explore features such as self-aggregation and self-sorting [192, 193]. The differential adhesion hypothesis (DAH) as discussed previously (1.5.4.1), describes how cells will specifically arrange themselves as a result of specific local adhesion characteristics. The premise is simple and states that cells with similar adhesive capacity will co-localise with cells expressing high adhesion potential sorting to the centre of a spheroid, and cells with a lower adhesion potential sorting to the periphery [194]. This poses an interesting question with regards to co-culture spheroids produced from multiple cell types, as these specific local adhesion potentials may produce a model whereby the correct multiplex of cells is present in a 3D microtissue, but not in a conformation that allows the specific cell-cell interactions as seen *in vivo*.

Although there are a large number of publications within the literature assessing the diffusion and metabolism of anti-cancer drugs on tumour cell spheroids, there is limited research on the mathematical modelling of liver spheroids produced from non-proliferative cells such as primary isolated hepatocytes. There are some publications that have looked at oxygen diffusion within liver spheroid systems with the most recent and notable example of this is by Aleksandrova *et al.* [178]. These researchers utilise a Michaelis-Menten equation to describe the rate of oxygen consumption by the cells and assume that the oxygen consumption in the spheroid is constant and equal to V_{max} . For the steady state distribution of oxygen in the spheroid the researchers also assume spherical symmetry within the model. This mathematical approach was combined with experimental cell viability analysis (immunofluorescent viability staining) as a means of model validation. I will also look to derive spheroid-specific parameters from my experimental characterisation work and implement these values to facilitate a robust mathematical modelling prediction of oxygen gradients within the microtissues.

Spheroids hold potential with regards to improving the representativeness of *in vitro* liver models for the assessment of hepatotoxicity. Conventional monolayer cultures are

unable to replicate a number of the required complexities seen *in vivo* and therefore their utility is limited. Previous mathematical models utilising tumour cells have assessed the diffusion distance of xenobiotics and shown that the relatively short diffusional path in monolayer cultures is unrepresentative of *in vivo* tumours. However, spheroid systems provide a more realistic *in vitro* platform where the xenobiotic has to diffuse through multiple zones consisting of functionally different cells before localising to the core [194]. *In vitro* and *in silico* models based on tumour spheroids have also been able to identify the effects of micro-architectural characteristics on xenobiotic transport profiles. These include cellular compaction (as demonstrated by isolated hepatocyte spheroid models) [126], specialised cell-cell junctions [195], and intercellular interactions with high interstitial fluid pressure that can provide a physical barrier to limit drug diffusion [196].

In order to increase the utility of *in vitro* and *in silico* models, it is clear that a reciprocal approach whereby *in vitro* models, either complex bioreactors or microfluidic devices or more simplistic 3D culture platforms, are set up with the optimised operating conditions. This optimisation step would benefit from mathematical modelling to assess key features such as, media flow rates, depth of media, OCR, and the incorporation of tissue-specific micro-architectural features that may impact on solute diffusion and subsequent metabolism.

1.7 Biological and mathematical motivation

As the need for more predictive *in vitro* liver models increases, emerging 3D and bioreactor technologies have started to become increasingly utilised for xenobiotic hepatotoxicity assessments [197]. The incorporation of shear stress and fluid-flow in bioreactor models and microfluidic devices has been shown to improve functionality as described previously [34, 70]. These more complex 3D *in vitro* models and bioreactor technologies have the potential to capture more of the intricate physiological aspects of the liver *in vivo* such as the solute and oxygen gradients of the liver sinusoid, and thus, may be able to better recapitulate the microenvironment of the native liver [3]. It has become clear that collaborative investigations between tissue engineers, toxicologists,

applied mathematicians etc. whereby a more detailed assessment of the *in vitro* liver model set up is analysed, has focused the development of 3D model systems and complex bioreactor models. The incorporation of features including the cellular microarchitecture, diffusion barriers, growth dynamics, shear stress and fluid-flow etc. will enable the further development of both representative *in vitro* and *in silico* models. While many of these systems show encouraging results, only a small number have provided extensive data that demonstrates the added value for hepatotoxicity investigations for human liver.

Industry, along with academia are continually developing a multitude of 3D *in vitro* liver models for toxicological investigations. Prior to these model systems being incorporated and utilised for compound screening investigations, a pragmatic schedule of detailed evaluation and subsequent validation is needed to show relevant pharmacological and toxicological end points. To date, liver organoids and spheroid models in particular show good promise for assessment of hepatotoxicity. Furthermore, solute gradients including oxygen, have been identified as key physiological characteristics that play a vital modulating role for liver zonation and subsequent gene expression and metabolism [118]. Recent focus of *in vitro* liver models has been directed at trying to capture these gradients in a physiological fashion [178]. Multidisciplinary approaches in the development of more complex *in vivo*-like models will better aid human relevant translational research and yield diagnostic advances that will reduce the risk of hepatotoxic potential at pre-clinical and clinical levels. Approaches such as quantitative systems pharmacology will play a pivotal role in this development and further comprehension of *in vitro* model systems utilised for xenobiotic safety investigations for researchers and across industry.

To date, no 3D *in vitro* liver primary cell model has been fully characterised experimentally or optimised to recapitulate sinusoidal oxygen tensions for extended culture periods. Liver spheroid systems have been extensively characterised with regards to metabolic competence and liver-specific functionality. However, there has been no reported system that remains devoid of necrosis for extended culture periods, allowing

for potential repeat-dose toxicology investigations. As such, a functional *in vitro* liver spheroid model that remains devoid of necrosis for extended culture periods, and that is able to replicate the sinusoidal oxygen tensions as seen *in vivo*, would provide an experimental model to better understand the intricacies of xenobiotic transport, diffusion and metabolism in a more representative way.

1.8 Thesis aims and objectives

The aim of this thesis is to produce a novel 3D microtissue model that can be cultured for extended periods whilst remaining devoid of necrosis. It is hoped that an extensive experimental characterisation will show that this model may be suitable for repeat-dose assessments during hepatotoxicity investigations. This is of particular interest to Syngenta as agrochemical exposure scenarios are inherently repeat exposures, and consequently in order to identify and confirm product safety, *in vitro* and *in silico* modelling approaches need to be representative and suitable to these applications.

I will employ various mathematical modelling techniques to aid the *in vitro* model optimisation, in order to better bridge the gap between *in vitro* and *in vivo*. The key outcome from my mathematical modelling is to be able to predict the optimal spheroid size that maintains liver oxygen gradients for as long as possible. As experimental derivation of these parameters is difficult, I will use the mathematical modelling alongside experimental data in order to answer this question. This reciprocal *in vitro* and *in silico* modelling will be used to determine key information that will be used to assess the appropriateness of the resultant model. In order to make these predictions the initial laboratory characterisation work is imperative in order to derive the experimental sizes of PRH spheroids and how this changes over time, and also the model-specific oxygen consumption rates of the cells.

1.9 Thesis outline

In Chapter 1, I critically evaluate a number of culture techniques and cell types that are used during the development stages of xenobiotic discovery. In particular I

comprehensively describe the multiple *in vitro* models that are utilised across industry sectors, for the evaluation of hepatotoxic potential of compounds. This introductory review demonstrates the future potential of spheroid systems in the wider field of *in vitro* liver models, and as a potential high-throughput tool that may be well placed to facilitate the screening of early-stage xenobiotics.

In Chapter 2, I describes an in-depth experimental characterisation of a primary rat hepatocyte (PRH) spheroid model. The application of the liquid-overlay technique (LOT) coupled with a non-proliferative cell type, namely primary isolated rat hepatocytes, results in the formation of a reproducible microtissue model. The 96-well plate format lends itself to potential high-throughput and repeat-does investigations. This *in vitro* system replicates the cellular morphology as observed *in vivo*, exhibiting both structural polarisation (demonstrated by F-actin), functional polarisation (as shown via P-gp and MRP2 staining), along with active and functional MRP2 transporters. Immunohistochemical analysis along with basic histology and transition electron microscopy also demonstrates that the spheroid model does not develop central necrotic cores.

Chapter 3 describes the construction of a mathematical model of oxygen diffusion for my specific experimental *in vitro* spheroid system. The model utilises experimentally-derived OCR values for varying initial seeding cell densities to predict oxygen profiles within the spheroids. This model is further developed, and implemented, to derive optimised operating conditions for the *in vitro* model over the duration of an extended 31 day culture period, to maintain both the periportal and pericentral oxygen tensions as observed in the *in vivo* sinusoid.

Finally, Chapter 4 describes the development of a mathematical model based on porous media modelling to describe the diffusion and transport of various xenobiotics. A number of xenobiotics are analysed and multiple physical and chemical properties are derived including molecular size and weight, spherical radius, pKa, LogD_{7.4}, etc. The model utilises specific experimentally-derived parameters from the characterised

spheroid model, including potential barriers to compound diffusion such as, tortuosity and volumetric porosity. The model describes how spheroid compaction and potential stratification of peripheral cells impacts on the characteristics of paracellular transport, and what effect this has on the subsequent transport of xenobiotics.

Chapter 5 highlights the conclusions of the thesis along with the pertinent novel contributions of the work that has been carried out. My extensive experimental characterisation provides insight into the morphology and functionality of the hepatocytes within the spheroid model, and focuses on the prevention of necrotic regions within the spheroids which is a major problem originally highlighted in the thesis aims. The results show that the culturing of PRH with the LOT allows for the production of an *in vitro* liver model that remains devoid of central necrotic zones. This result alone demonstrates that this model may be better suited for long-term assessments and repeat-dose investigations, not only for agrochemicals but also for pharmaceuticals, cosmetics, industrial chemicals etc. The use of mathematical modelling has provided key information that allows for the culturing of PRH spheroids with specific operating conditions, namely the incubator oxygen concentration, that maintains *in vivo*-like sinusoidal oxygen gradients within the spheroids for as long as possible. This novel contribution demonstrates that for my specific spheroid model, there is no single optimal size/cell seeding density required to capture *in vivo* oxygen gradients. Also, these results help rebut the idea that spheroids larger than 150 μm will become necrotic due to the inability of oxygen to diffuse beyond this threshold. This historical literature-derived value is too generalised and I suggest that in order to determine optimal spheroid size, model specific sizes, oxygen consumption rates and growth characteristics need to be taken into account. All of these results demonstrate the added value that could be gained from the implementation of the *in vitro* system for early-stage xenobiotic screening, and long-term, repeat-dose investigations.

Chapter 2: Characterisation of a functional primary rat hepatocyte spheroid model

2.1 Introduction

The determination of xenobiotic safety is crucial and affects numerous industries, such as pharmaceuticals, agrochemicals, industrial chemicals, cosmetics and environmental contaminants, and therefore robust systems for xenobiotic assessment are required [7]. DILI, one of the most common forms of ADRs, is the main reason for the withdrawal of xenobiotics from the market [198, 199]. DILI is a common side effect of many xenobiotics and is a considerable encumbrance in the field of drug discovery. The reactions involved are complicated and often require interactions between the multiplex of parenchymal hepatocytes and non-parenchymal cells, such as SCs, KCs and LSECs. DILI represents a vast spectrum of manifestations: (i) the impairment of mitochondrial function, (ii) inflammation and lethal effects of immune response, (iii) cell death via necrosis and (iv) apoptosis, and pathologies including microvesicular steatosis and cholestasis [200].

Freshly isolated PHH are currently considered the “gold standard” for an *in vitro* model to assess hepatocyte function and hepatotoxic potential of compounds [201]. However, there are a number of limitations to these models including: the absence of the 3D microenvironment, failure to capture the complexities of multicellularity, inter-donor differences, diminished viability for the study of long-term effects and limited availability to all researchers [15]. In addition, PHH rapidly lose liver-specific functionality and undergo rapid dedifferentiation [202].

In vitro liver models that possess favourable predictive DILI capabilities are therefore imperative during the preliminary stages of drug development in order to aid candidate selection for early research compounds [203]. Many *in vitro* liver cell models, including 2D systems, utilised for xenobiotic safety assessments, suffer from major limitations arising from a lack of preservation of physiological phenotype and metabolic competence. To circumvent some of these limitations there has been increased focus on producing more representative 3D models. It has been shown that culturing primary hepatocytes (both human and rat) and hepatic cell lines (C3A, HepG2, Huh7 and HepaRG), in a 3D conformation has a profound effect on improving liver-specific functionality, cellular

morphology and phenotype, metabolic competence, and toxicological response when compared to conventional 2D/monolayer cultures [43, 76, 97].

There are multiple methods for the generating 3D liver models including hydrogel and scaffold based technologies [30, 99], as well as the production of hepatospheres [102] or liver spheroids. There are also a number of 3D spheroid culture protocols both for monocultures of hepatocytes and cell lines and also cultures including secondary or multiple cell types, all of which vary according to individual practices [76, 103, 125, 126]. Spheroids have the potential to be used for both long-term and repeat-dose investigations, with many platforms allowing for high-throughput analysis for pre-clinical and non-clinical investigations.

One of the main limitations from using a number of these previously described protocols such as rocked and spinner flask methods in particular, is that the resultant spheroids vary considerably in size. This size variation of spheroids makes the direct comparison of results difficult. An additional limiting factor with the implementation of other systems such as the specialised hanging-drop method [125], is the cost implications e.g. a 96-well plate of InSphero spheroids can cost in excess of £1000. These systems are extremely expensive and thus, are not a feasible option to all researchers and industry sectors.

2.1.1 Aims of experimental characterisation

The aim of my initial work is to construct a size controllable, 3D hepatic spheroid model using freshly isolated PRH by implementing a more cost-effective method for production. The liquid-overlay technique (LOT) is used in combination with freshly isolated cells whereby PRH cultured using this experimental platform, spontaneously self-assemble in to 3D microtissues. PRH are chosen for the production of spheroids because the isolation of rat hepatocytes has become a relatively routine procedure with good repeatability of experimental results, along with the culture procedures of PRH being well documented and characterised. Also, a number of industry sectors (including Syngenta) use rodents as model species to investigate the toxic potential of environmental compounds.

PRH do not proliferate *ex vivo* and thus, it is hypothesised that the size of the spheroids will remain relatively constant over the duration of the culture period. This is in contrast to hepatic-derived, human cell lines that proliferate *in vitro* and form 'classic' tumour-like spheroids characterised by regions of necrosis. A scaffold-free protocol for spheroid production is implemented to negate the adverse effects of manufactured or decellularised scaffolds and other ECM components. These protocols have been shown to be reproducible and high-throughput. The experimental procedures subsequently described are implemented to fulfil a comprehensive and robust characterisation the spheroid structure and functionality. The sizes of spheroids and compaction characteristics over the duration of the culture period will be implemented within subsequent mathematical modelling as spheroid-specific sizes at certain culture times will be extremely important due to previously reported compaction. I will also analyse the oxygen consumption rates (OCR) of the spheroids over a number of time points as an additional model-specific parameter. This parameter has been identified as crucial for my mathematical modelling predictions of oxygen gradients within the PRH spheroid system, and unlike previous attempts to model spheroid oxygen gradients, I do not wish to rely on literature-derived values as the variation in reported values seems to be extensive. I hypothesise that PRH spheroids will display *in vivo* characteristics including direct cell-cell contacts, cellular polarisation, 3D cellular morphology, and formation of functional secondary structures throughout the spheroid.

2.2 Materials and methods

2.2.1 Production of liquid-overlay plates

Spheroids were produced using the liquid-overlay technique (LOT) as previously described [8]. A solution of 1.5 % agarose (high gelling temperature $42 \pm 1.5^\circ\text{C}$ - Sigma A3768) in serum-free Williams' medium E was produced. The solution was autoclaved and subsequently, 100 μl of the solution was added to each well of a flat-bottomed 96-well plate. Plates were left for 30 minutes for agarose to fully solidify. Lids were placed back onto 96-well plates and the plates were inverted and stored at 4°C for 2 weeks to

allow for appropriate hydration prior to cell seeding. (See **Figure 2-1** for experimental plate layout for LOT plates).

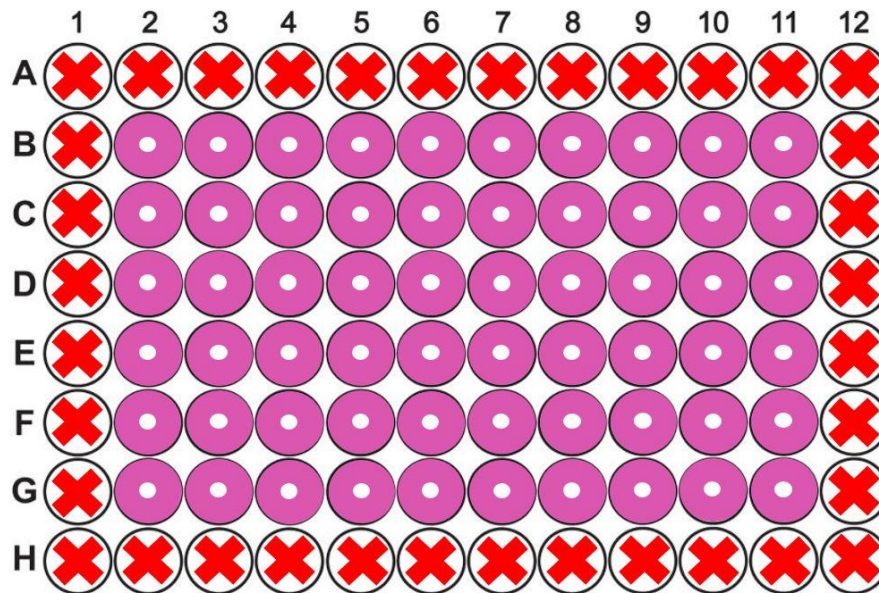


Figure 2-1 Spheroid culture plate layout. Red crosses indicate the wells that were not used for culturing spheroids. White circles indicate the cultures spheroids.

Figure 2-1 shows the spheroid culture plate layout. When culturing the PRH spheroids in 96-well plates, only the inner 60 wells were used, as the outer wells had inconsistencies in spheroid formation and cell density due to a boundary/evaporation effect [204].

2.2.2 Primary rat hepatocyte isolation and culture

Hepatocytes were isolated from the whole liver of adult male Wistar rats, weighing between 175 -200 g, by a modified two-step collagenase perfusion technique described originally by Seglen [205]. Briefly, the rat liver was perfused through the portal vein with $\text{Ca}^{2+}/\text{Mg}^{2+}$ -free HBSS containing 10 mM glucose, 10 mM HEPES, and 0.3 mM EDTA followed by HBSS containing 0.05% collagenase type IV (Sigma C5138). The cell suspension was spun down at 50 g for 2 min. After three washes, hepatocytes were resuspended in Williams' medium E, supplemented with 10% FBS, 10,000 units/ml

penicillin, 10 mg/ml streptomycin, 2 mM L-Glutamine, 10 µg/ml insulin, 5.5 µg/ml transferrin, 6.7 ng/ml selenium and 100 nM dexamethasone (this will hereafter be referred to as supplemented media) under standard culture conditions. Cell viability was determined using the trypan blue exclusion method where 40 µl of the cell suspension was transferred to a 0.5 ml Eppendorf tube with 10 µl of trypan blue stain. 10 µl of the resultant cell suspension was loaded onto a haemocytometer and cells were counted (both total and viable). Isolated cell populations with >85% viability used for the subsequent spheroid cultures.

2.2.3 Spheroid formation

LOT plates were pre-warmed in an incubator at 37°C for 30 min prior to cell seeding and then left to air dry in laminar flow cabinet in order to remove condensation from plate lids. PRH were then seeded at 2000, 3000, 4000 and 5000 cells per well (inner 60 wells of 96-well plate. See **Figure 2-1**) in 100 µl of supplemented media. 200 µl of sterile PBS was added to the outer wells to create an evaporation barrier. Plates were briefly pulse spun in a plate spinner at 100 g for 90 seconds and incubated for 72 hours to allow spheroid formation. After this time, media was changed twice weekly where 50 µl was removed and replenished with another 50 µl of supplemented media. Spheroids were cultured for up to 31 days. 2000 cells were chosen as the lower limit for PRH spheroid formation as determined by previous work, and spheroids did not form with seeding less than 2000 cells. Additional seeding densities were chosen to analyse the effect of increasing cell number on spheroid diameter, cellular morphology and subsequent downstream analysis.

2.2.4 Phase contrast microscopy

Spheroid diameter was analysed via light microscopy utilising a phase-contrast microscope (ECLIPSE TS100/100-F, Nikon). Images were taken at 4x magnification using a digital camera head (DS-Vi1, Nikon) and a stand-alone controller and display unit (DS-L3, Nikon). The maximum spheroid diameter was measured from these images using in-built

microscope software. 3 measurements were taken per spheroid and the average value was subsequently derived ($n=3$ in triplicate).

2.2.5 Histological analysis

Spheroids were washed in PBS, fixed for 1 hour in 4% paraformaldehyde (PFA) and embedded in 2% agarose (low EEO) in 4% PFA before being subjected to routine histological processing and finally paraffin wax embedded. 5 μm sections were cut using a Leica RM2235 microtome (Leica microsystems) and stained with Haematoxylin and Eosin (H&E).

2.2.6 Immunohistochemical analysis

Sections were dewaxed, rehydrated through a series of alcohol dilutions, and endogenous peroxidase neutralised with 3% hydrogen peroxide in methanol for 20 minutes. Antigen retrieval was achieved by using 0.01M Tri sodium citrate buffer (pH 6) at high temperature. After blocking with normal goat serum for 20 minutes at room temperature, sections were incubated with primary antibodies at a 1:50 dilution for Ki67- abcam CK19- abcam and cleaved-caspase 3, and a 1:500 dilution for Vimentin, for 1 hour at room temperature. Secondary antibody and avidin-biotin complex (ABC) provided with Vectastain Elite ABC kit (Vector labs, Peterborough, United Kingdom) were used in accordance with the manufacturer's instructions. Finally, 3,3'-diaminobenzidine tetrahydrochloride (DAB; Vector labs) was used to visualise peroxidase activity and the sections were counterstained with haematoxylin, dehydrated, and mounted in DPX. Light microscope images were taken using an Olympus BX51 microscope and Colour view Illu camera with associated Cell^D software (Olympus soft imaging solutions, GmbH, Münster, Germany). (Vimentin and cleaved-caspase 3 staining was conducted by the Veterinary pathology department, Leahurst campus, University of Liverpool).

2.2.7 Ultrastructural analysis of hepatocytes via Transition electron microscopy

Spheroids were fixed in fresh 2.5% glutaraldehyde in 0.1 M phosphate buffer, overnight at 4°C. Spheroids were then washed in 0.1 M phosphate buffer twice with 30 minute intervals at 4°C. Secondary fixation was carried out in 2% OsO₄ for 2 hours at room temperature and pressure (RTP) and then washed in 0.1 M phosphate buffer. Dehydration occurred through a graded ethanol series. Infiltration was accomplished by a 50/50 mixture of Propylene oxide/Araldite resin. Specimens were embedded in Araldite Epon for 6-8 hours at RTP and then placed in fresh Araldite Epon for 48-72 hours at 60°C. Ultrathin sections (approximately 70-90 nm) sectioned by Reichert Ultracut E ultramicrotome and stained by 3% aq. uranyl acetate and Reynold's lead citrate for 5 minutes. Sections were examined using a FEI Tecnai Transmission Electron Microscope at an accelerating voltage of 80 Kv. Images were taken using a Gatan digital camera (Work carried out by the Biomedical Sciences Electron Microscopy Unit, The University of Sheffield).

2.2.8 Immunofluorescent analysis of spheroids

Spheroids were transferred to flat-bottomed 96-well plates, washed three times in PBS and subsequently fixed in 4% PFA for 1 hour at 4°C. Spheroid were incubated in a permeabilization buffer (0.5% Triton X-100 in Tris-buffered Saline with 0.5% Tween20 (TBST)) overnight at 4°C and then blocking buffer (0.1% Triton X-100, 3% BSA in TBST) for 2 hours at room temperature. Primary antibodies P-glycoprotein (P-Glycoprotein anitbody [EPR10364-57] ab170904) and Multidrug resistance protein-2 (MRP2 antibody (M2III-5) ab15603) were diluted 1:50 in 0.1% Triton X-100, 1% BSA in TBST and spheroids were incubated with primary antibodies overnight at 4°C. Spheroids were then washed 3 times for 1 hour in 0.1% Triton X-100 in TBST and then incubated with secondary Alexa Fluor 568 donkey anti-mouse (for MRP2) and Alexa Fluor 568 donkey anti-rabbit (for P-gp) (Thermo Fisher Scientific) diluted to 1:1000, with Hoechst diluted to 1:5000 and Phalloidin 680 diluted to 1:250 in 0.1% Triton X-100, 1% BSA in TBST overnight at 4°C. Spheroids were then washed twice for 1 hour in 0.1% Triton X-100 in TBST and then

mounted onto a microscope slide with ProLong Gold antifade mountant (Thermo Fisher Scientific). Maximum intensity projection images were taken using a Zeiss Axio Observer microscope with Apoptome platform using 10x and 40x oil objective.

2.2.9 Analysis of transporter functionality

Spheroids were incubated with 5 μ M 5-chloromethylfluorescein diacetate (CMFDA-Thermo Fisher Scientific), a fluorescent cell tracker which has been shown to be cell permeable until it is converted by cytosolic esterases into glutathione-methylfluorescein (GSMF), an auto-fluorescent substrate that is transported by MRP2 [206]. Spheroids were incubated with CMFDA for 2 hours at 37°C. Spheroids were subsequently washed 3 times in PBS and prepared for IF as previously described (2.2.8).

2.2.10 Quantification of albumin production

Albumin production was quantified in spheroid media supernatant samples using Rat Albumin ELISA Kit (Abcam) following the manufacturer's protocol. Supernatant samples were collected 4 days after media changes over the 31 day culture period and stored at -80°C until analysis. All incubations were performed at room temperature. Albumin standards were prepared and 50 μ l added to the wells of a pre-coated 96-well plate, along with samples for analysis, and incubated for 1 hour. The plate was washed 5 times with 200 μ l wash buffer and incubated with 50 μ l of biotinylated albumin antibody for 30 min. The plate was washed as previously described and incubated with 50 μ l SP conjugate for a further 30 min. Again the plate was washed and incubated with 50 μ l Chromagen solution for 20 min then 50 μ l stop solution added. The absorbance was read at 450 nm using a microplate reader (Thermo Scientific Varioskan Flash). The albumin concentration in the samples was calculated using values obtained from the standard curve and normalised to initial cell number.

2.2.11 Quantification of urea secretion

Urea secretion from spheroid supernatant samples were quantified using a Urea Assay Kit (Abcam), according to the manufacturer's protocol. Supernatant were collected 4 days after media changes over 31 days of culture and stored at -80 °C until analysis. Urea standards were prepared and 50 µl added to the wells of a 96-well plate, along with samples for analysis, and incubated with 50 µl urea reaction mix for 1 hour at 37 °C, protected from light. The absorbance was read at 570 nm using a microplate reader (Thermo Scientific Varioskan Flash). Urea concentration in the samples was calculated using values obtained from the standard curve and normalised to initial cell seeding number.

2.2.12 Oxygen consumption rate analysis

OCR was analysed using Seahorse XF technology. Seahorse XF technology is a system that utilises oxygen sensing probes to determine the rate at which cells are consuming oxygen (basal respiration). This system can be used for both monolayer and spheroid systems. It is commonly used for analysing extracellular acidification rates; however, it is well suited to determine the OCR of our experimental system. Briefly, the sensor cartridge from the extracellular flux assay kit was hydrated in XF calibrant at 37 °C in a non-CO₂ incubator overnight. For spheroid analysis, the Seahorse spheroid microplate was coated with Cell-Tak (200µl in 2.8 ml 0.1 M sodium bicarbonate), incubated for 1 hour at 37 °C, washed twice with 200 µl sterile H₂O and left to air-dry. Seahorse medium was prepared using 25 mM glucose, 2 mM L-glutamine and 1 mM in base medium minimal DMEM (Seahorse). The pH was adjusted to 7.4 and warmed to 37 °C. 175 µl Seahorse medium was then added to the spheroid microplate and spheroids were transferred into the centre of each well, one at a time. The outer wells of the Seahorse culture plates were filled with 175µl media and used to calculate background readings (see **Figure 2-2** for plate layout). Spheroids were incubated for 1 hour in a non-CO₂ incubator prior to analysis. Spheroid OCR analysis was then performed using Seahorse XFe96 Extracellular Flux Analyser and Wave software which analyses OCR. Data was analysed using Seahorse XF Test Report

Characterisation of a functional primary rat hepatocyte spheroid model

Generator and data normalised to initial cell seeding number. A minimum of 6 spheroids was analysed for each experiment.

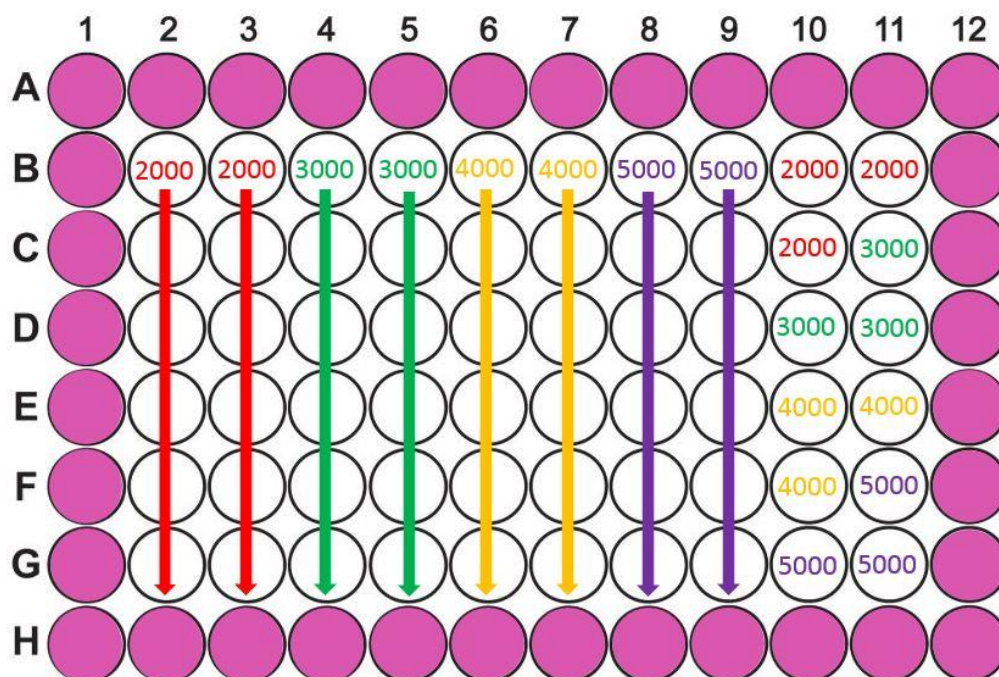


Figure 2-2– Seahorse plate set-up for spheroid OCR analysis. All outer wells of the seahorse spheroid plate were used as background readings. 2000-cell spheroids were transferred from culture plates to seahorse plates in lanes 2B-G, 3B-G, 10B-C and 11B. 3000-cell spheroids in lanes 4B-G, 5B-G, 10D and 11C-D. 4000-cell spheroids were in lanes 6B-G, 7B-G, 11E and 10E-F. 5000-cell spheroids were in lanes 8B-G, 9B-G, 10G and 11F-G.

2.3 Results

2.3.1 Optimisation for size-controllable spheroid production

In the initial stages of experimentation I compared spheroid formation utilising two different techniques; the LOT and ultra-low adhesion (ULA) plates. It was noted that spheroids grown on the ULA plates had an irregular morphology in comparison to those grown utilising the LOT. ULA spheroids were also less spherical, not as compact and had a less well-defined membrane around the periphery of the spheroids (see **Figure 2-3**). All further experimentation was carried out on spheroids that had been produced using the LOT.

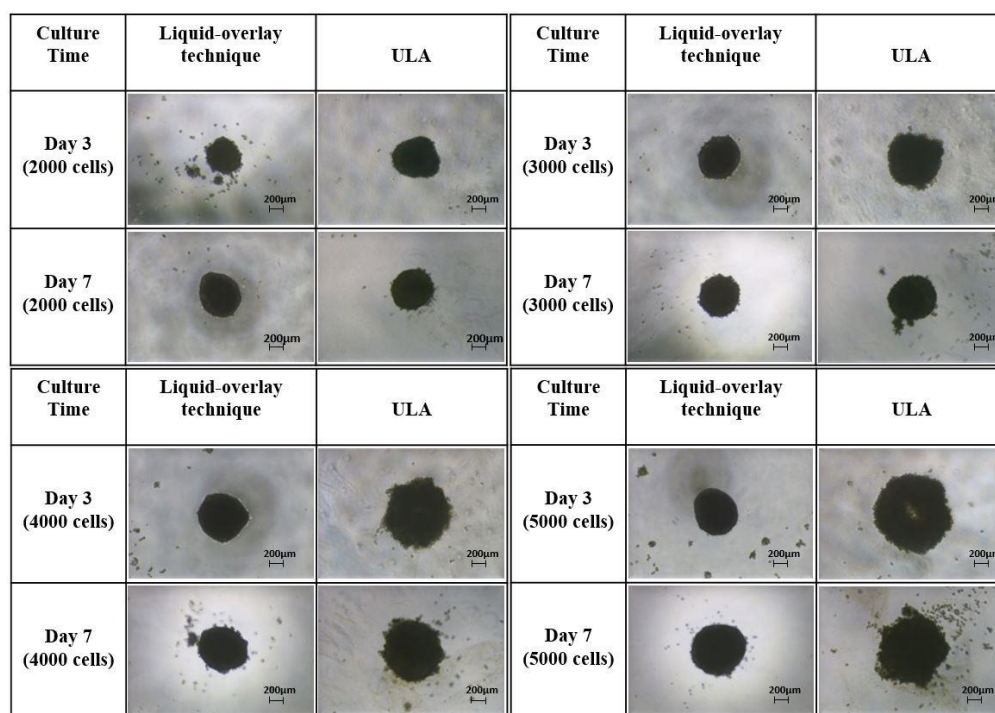


Figure 2-3- Formation and morphology of spheroid produced using the liquid-overlay technique (LOT) or ULA plates for different initial seeding cell numbers. Figure 2-3 shows phase-contrast images (4x magnification) of spheroids produced using 2000, 3000, 4000 and 5000 PRH cells at day 3 and day 7. Scale bar = 200 µm.

2.3.2 Effect of initial cell seeding number on spheroid size and morphology

To determine how the number of PRH initially seeded affected spheroid morphology and size, spheroids were produced by seeding 2000, 3000, 4000 and 5000 cells and monitored over 31 days. The initial seeding density resulted in spheroids of varying sizes, with all cells initially seeded aggregating to form one uniform single spheroid within 3 days. Spheroids produced from the seeding of 2000 cells reduced in diameter over the 31 day culture period from $353 \pm 18.95 \mu\text{m}$ to $212.5 \pm 22.36 \mu\text{m}$. 3000 cell spheroids reduced in diameter over the culture period from $400 \pm 15.38 \mu\text{m}$ to $256 \pm 14.56 \mu\text{m}$, whilst 4000 and 5000 cell spheroids reduced in diameter of the culture period from $423 \pm 21.91 \mu\text{m}$ to $276 \pm 20.3 \mu\text{m}$ and $467 \pm 26.46 \mu\text{m}$ to $278 \pm 20.64 \mu\text{m}$, respectively. All spheroids remained relatively uniform in shape over the duration of the 31 day culture period (**Figure 2-4 (A)**). **Figure 2-4 (B)** shows the mean diameter of PRH spheroids plotted against culture time. Linear regression analysis was used to produce best fit lines.

A

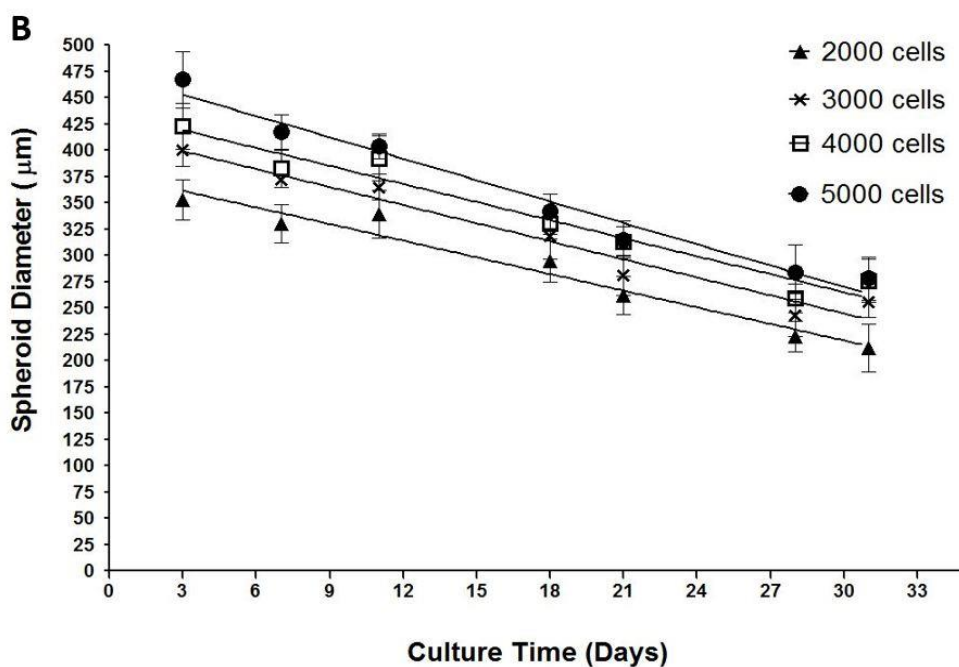
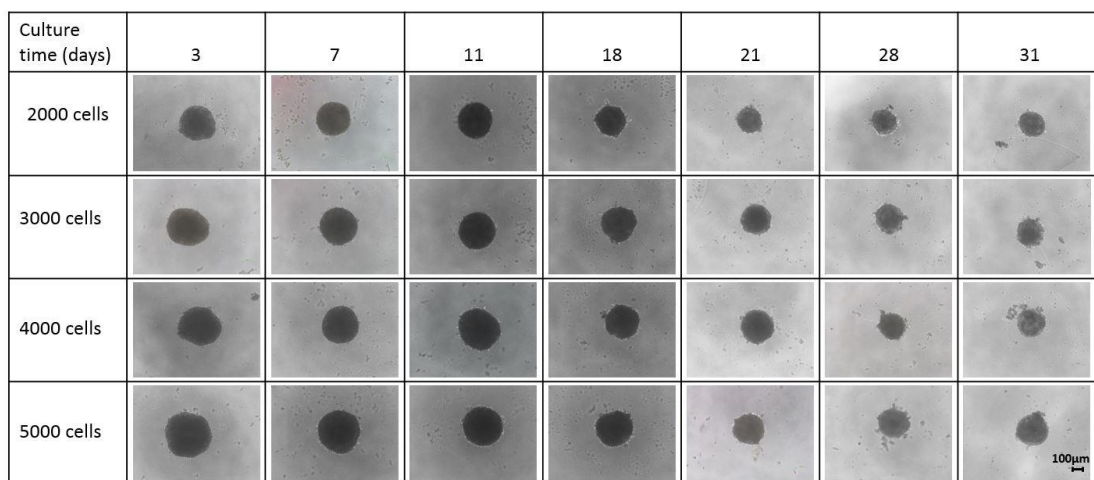


Figure 2-4 - Effect of initial cell seeding density on spheroid size and morphology. Spheroids were produced from seeding 2000, 3000, 4000 and 5000 PRH per well in 100 µl complete Williams' medium e and cultured for up to 31 days. (A) phase-contrast images of spheroids taken at time points (3, 7, 11, 18, 21, 28 and 31 days). Scale bar = 100 µm. (B) compaction of spheroids / reduction of spheroid diameter over 31-day culture period. Data are represented as mean ± standard deviation (n=3 in triplicate). Straight lines represent linear regression analysis using Graphpad Prism. The R² values for linear regression lines were 0.96, 0.96, 0.95 and 0.97 for 2000, 3000, 4000 and 5000 cell spheroids respectively.

2.3.2.1 Statistical analysis of spheroid compaction.

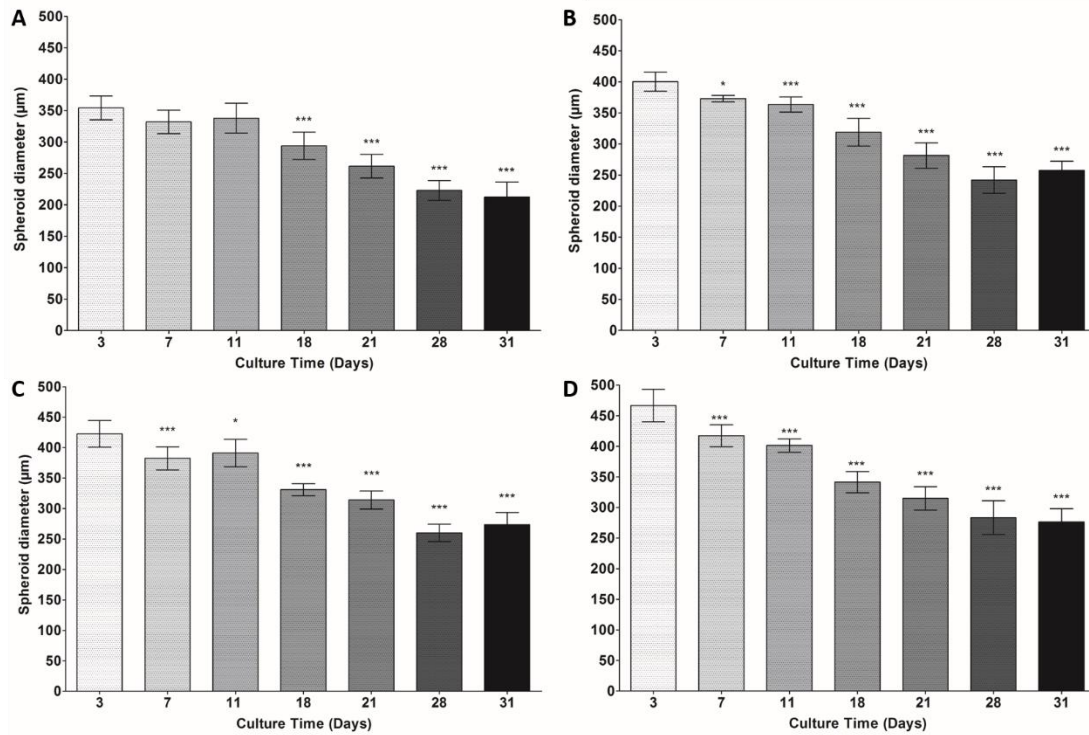


Figure 2-5 – Statistical analysis of spheroid compaction over culture time. There was a time dependent decrease in spheroid diameter up to 31 days in culture. **Figure 2-5 (A)** describes the decrease in spheroid diameter for 2000-cell spheroids, **(B)** for 3000-cell spheroids, **(C)** for 4000-cell spheroids and **(D)** for 5000-cell spheroids. For 2000-cell spheroids, days 18, 21, 28 and 31 were considered statistically significantly smaller when compared to day 3. All other spheroid diameters for 3000, 4000 and 5000-cell spheroids were considered statistically significantly smaller compared to day 3 spheroids, by One-way ANOVA *P value <0.05 and ***P value <0.001.

2.3.3 Histological analysis of spheroids

Haematoxylin and Eosin (H&E) staining was performed on spheroids with an initial cell seeding density of 5000 cells over 21 days of culture to assess cell morphology and cellular arrangement (**Figure 2-6**). H&E staining revealed a compact internal cellular arrangement with a defined outer perimeter of cells. Cells within the spheroid had close cell-cell interactions, however, the outer perimeter of cells increased in thickness over the duration of the culture period (See **Figure 2-7** for statistical analysis). It was also noted that over the duration of the culture period, staining consistent with the formation of central areas of necrosis was not observed. As previously mentioned, it was also noted that spheroids were encapsulated by an uninterrupted cell layer at the periphery (**Figure 2-8**). It is entirely possible that these cells may represent the mesothelial cells lining the external surface of the liver *in vivo* similar to the Glisson membrane as previously described [42] .

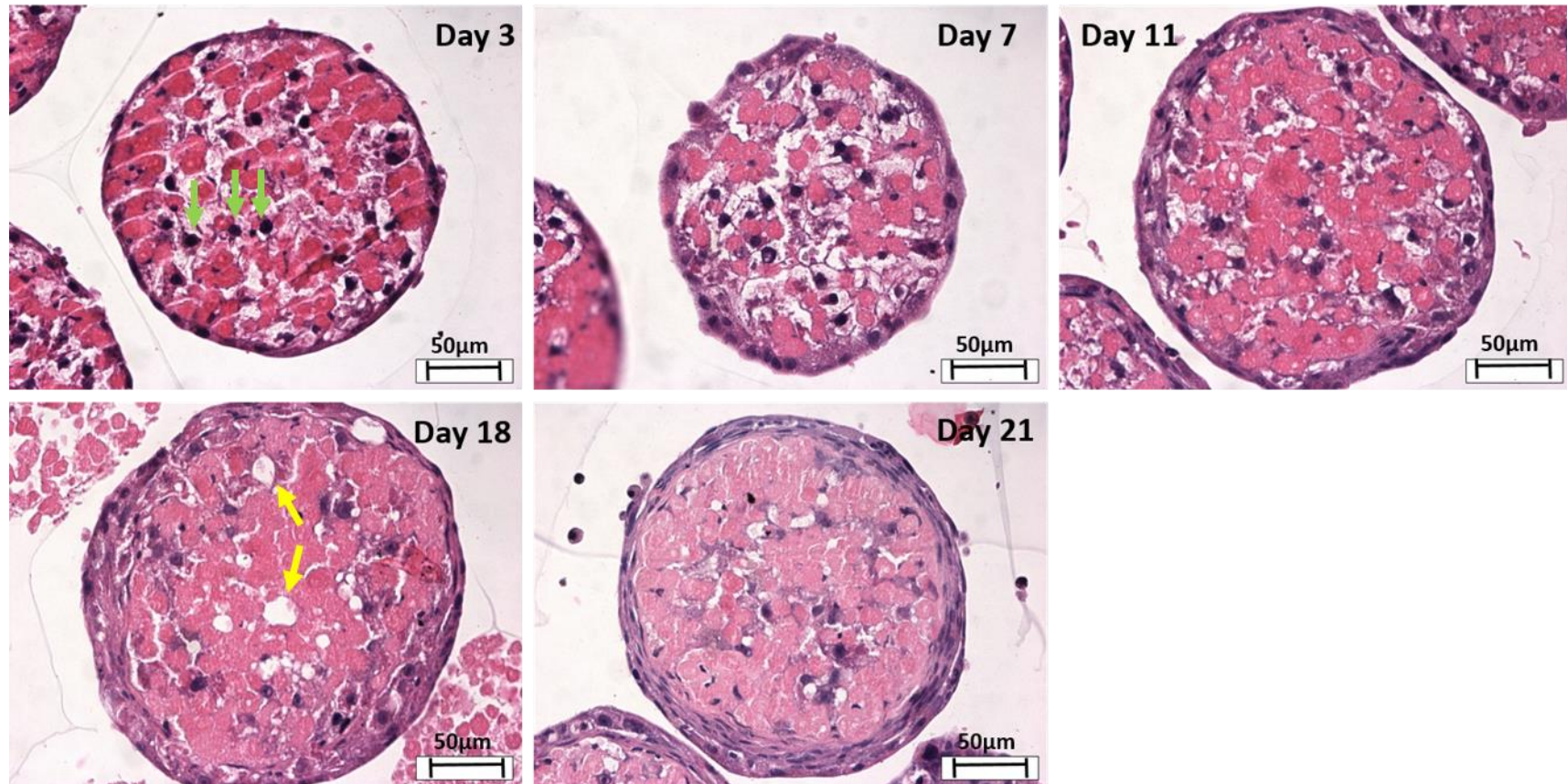


Figure 2-6 – Spheroid internal structure and morphology. Spheroids were created on liquid-overlay plates seeded at 5000 cells per well in 100 µm and fixed at day 3,7,11,18, and 21 of culture, paraffin embedded, sectioned and stained with H&E. Green arrows indicate cell nuclei (purple staining), yellow arrows show vacuoles within the spheroids, and intense pink staining indicates cell cytoplasm (eosinophilia). Images represent mid-sections through the spheroids at 40x magnification. Scale bar = 50 µm.

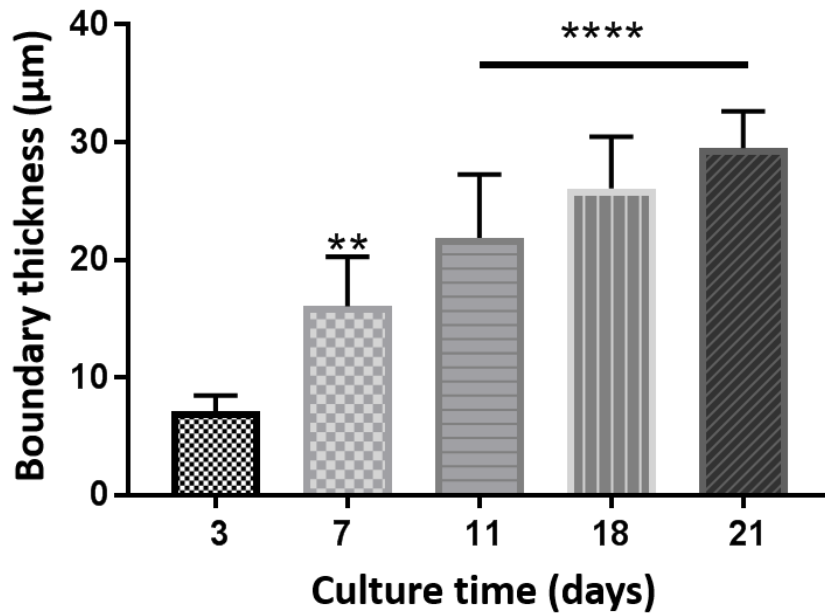


Figure 2-7 - Graph describing spheroid cell perimeter thickness. ImageJ was used to quantify cell-perimeter thickness over time. There was a time dependent increase in cell perimeter thickness up to 21 days in culture. For the calculation, six areas along the perimeter were measured per spheroid. All spheroid cell perimeters were considered statistically significantly thicker compared to day 3 spheroids by One-way ANOVA ** P value <0.0022 and **** P value <0.0001 .

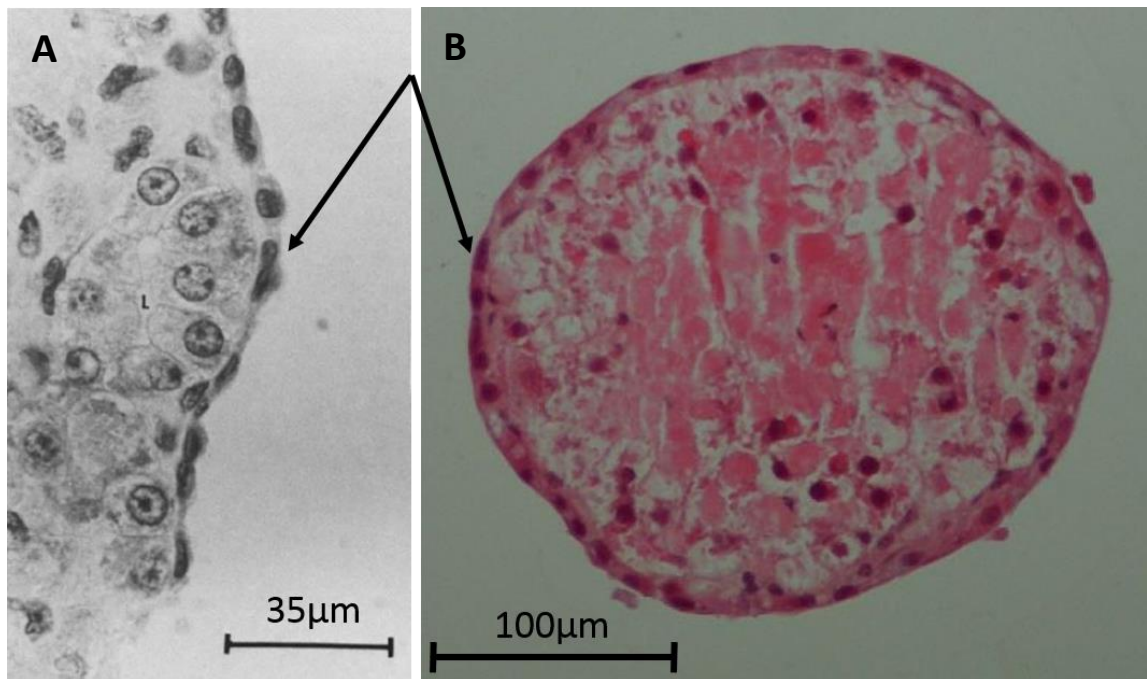


Figure 2-8 – Encapsulated spheroid morphology at the microtissue boundary. (A) a photomicrograph of the edge of a H&E stained section of a 200 µm rat liver cell spheroid at day 11 [42], and (B) a phase contrast image of a H&E stained, 5000-cell PRH spheroid at day 11 (40x magnification), showing the presence of elongated cells forming an encapsulated spheroid with a distinct boundary. Arrows show elongated cell nuclei within peripheral cells. Scale bar = 35 µm and 100 µm respectively.

2.3.4 Nuclear staining of spheroid sections

The internal structure of the spheroids was analysed using immunofluorescent analysis. This was conducted to assess the viability of cells within the spheroids. Sections cut at 5 µm thickness from 5000-cell spheroids were stained with Hoechst over 21 days of culture. Nuclear staining was visualised to assess cellular arrangement within the spheroid (**Figure 2-9**). Sections from the same blocks as in **Figure 2-6** were analysed for direct comparison. H&E stained sections displayed some areas of intense eosinophilic staining and subsequently made nuclear staining difficult to determine. Immunofluorescent analysis was required to better visualise nuclear staining and cellular arrangement within

Characterisation of a functional primary rat hepatocyte spheroid model

the spheroid over the culture period. DAPI stained sections revealed viable central hepatocytes and no presence of a necrotic core.

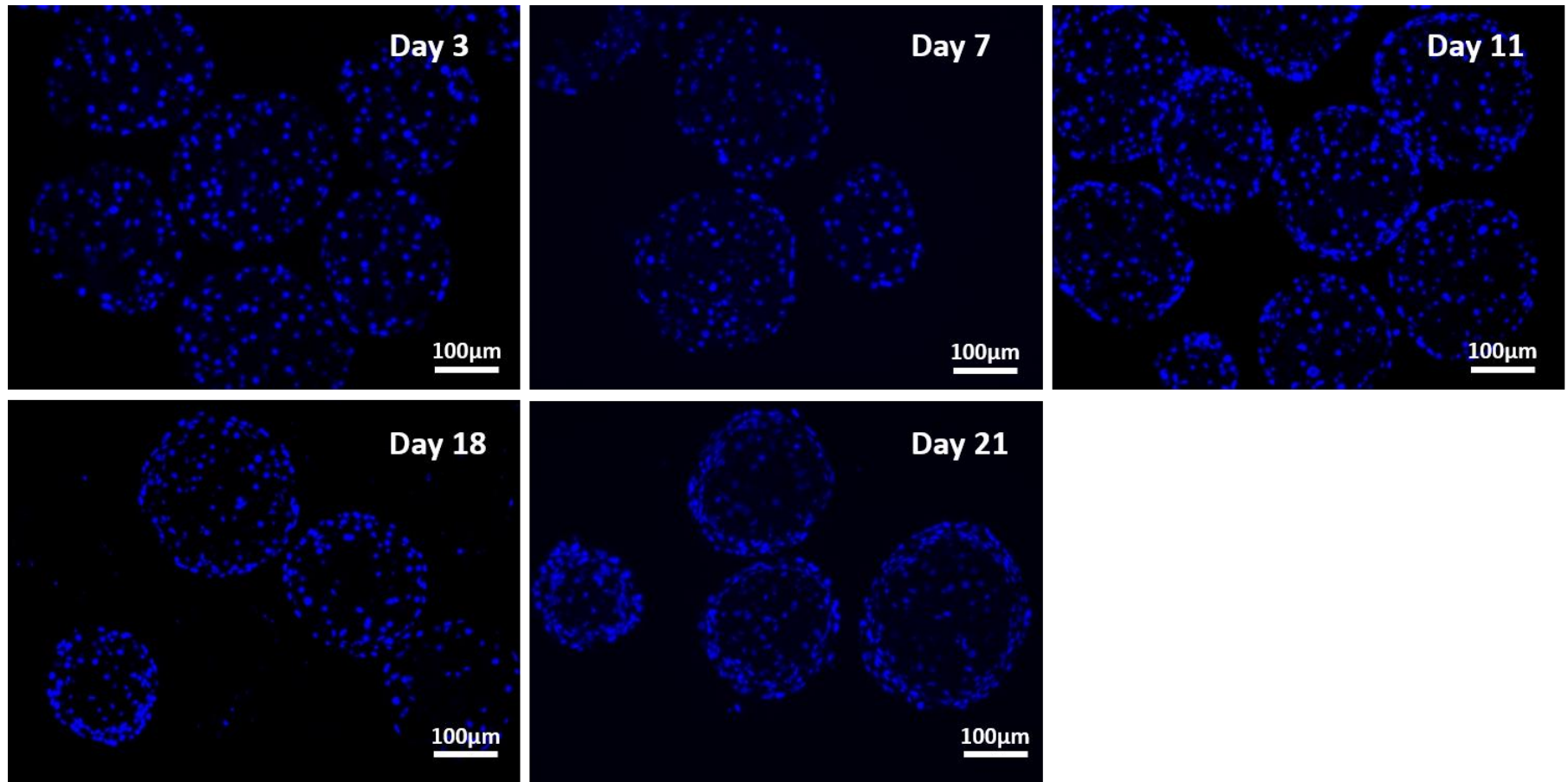


Figure 2-9 - Cellular morphology and nuclear distribution within spheroids. Spheroids were created on liquid-overlay plates from 5000 cells per well and fixed at day 3, 7, 11, 18, and 21 of culture, paraffin embedded, sectioned and stained with Hoechst to stain for cell nuclei. Images represent mid-sections through the spheroids at 20x magnification. Scale bars = 100 µm.

2.3.5 Immunohistochemical analysis

The internal structure of the spheroids was analysed using immunohistochemical analysis (IHC). These experiments were conducted to determine if there were multiple different cell types present within the spheroids and to assess cellular phenotypes. CK19 staining was performed on spheroids with initial cell seeding number of 5000 cells over 11 days culture period, as a specific stain for biliary epithelial cells (BECs) (**Figure 2-10**). This was done to assess if there was a secondary cell type present from the initial hepatocyte isolation procedure that may have been forming this encapsulated boundary. Positive control slides were produced from pancreatic ductal carcinoma samples which have been shown to highly express CK19. CK19 staining showed negative staining for this BECs marker within the spheroid samples.

Ki67 staining was performed on spheroids with initial cell seeding number of 5000 cells over 11 days culture period to assess the potential proliferative characteristics of the cells encapsulated at the boundary (**Figure 2-11**). This was done to assess if there was a proliferative cell type present from the initial hepatocyte isolation procedure that may have been forming this encapsulated boundary. Positive control slides were produced from breast carcinoma samples which have been shown to highly express Ki67 (Sheffield Diagnostic Oral Pathology department). Ki67 staining revealed negative proliferative characteristics of these boundary cells and similarly throughout the entire microtissue.

Vimentin staining was performed on 5000-cell spheroids over 21 days of culture. Vimentin has been shown to positively stain for mesothelial cells and as such this stain was chosen to determine whether or not the cells on the boundary of the spheroids were mesothelial in phenotype (**Figure 2-12**). Positive control slides were produced from rat liver sections which stained positively for mesothelial cells throughout the tissue but also specifically at the boundary of the samples indicating the presence of this mesothelial lining. Vimentin staining showed positive staining over the culture period for mesothelial cells, however, this staining was increasingly constrained to the peripheral cells within the spheroids as the culture time increased.

Characterisation of a functional primary rat hepatocyte spheroid model

5000-cell spheroids were additionally stained over 21 days of the culture period with cleaved-caspase 3 which is an apoptotic cell marker (**Figure 2-13**). This staining was done to assess the presence of cell death and as a means to support the findings of the histological analysis whereby I assert that PRH spheroids are devoid of the central necrotic core. Positive control slides were produced from rat liver sections. Cleaved-caspase 3 staining showed some cell death at early culture time (apoptosis). However, later samples showed negative staining for apoptosis within the spheroids.

CK19 Positive control

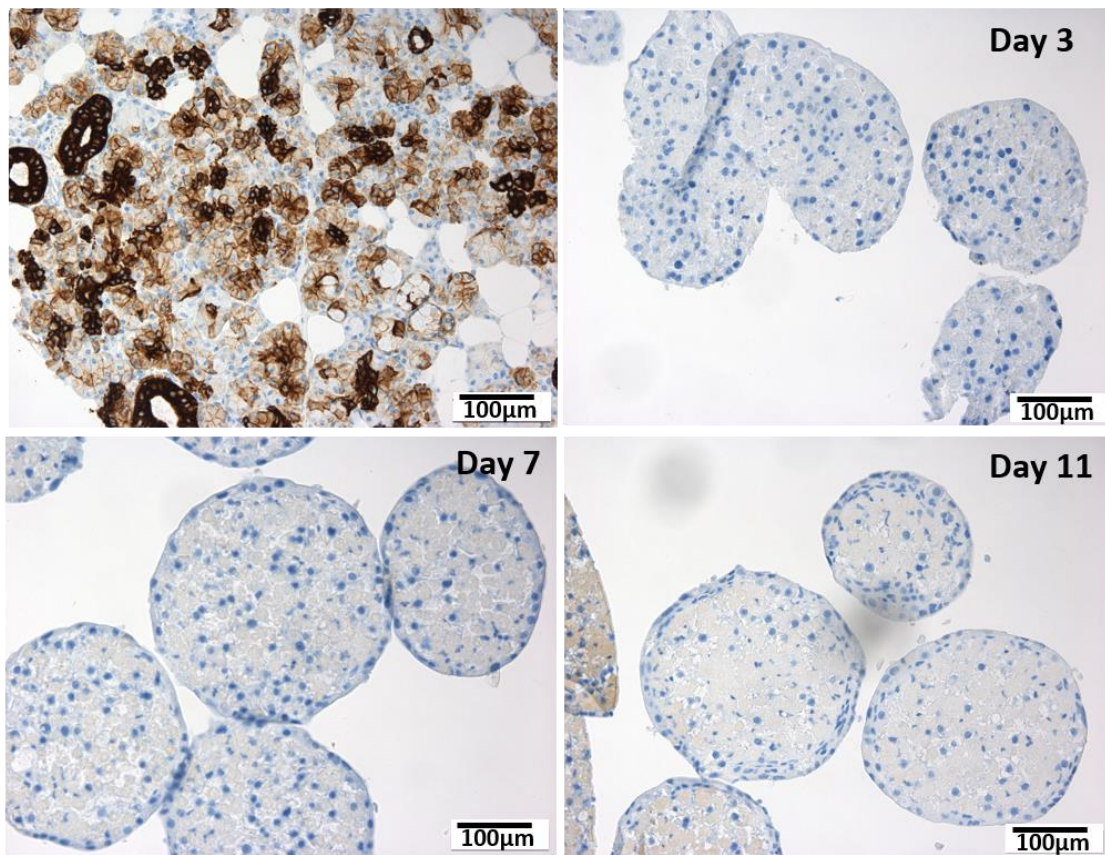


Figure 2-10 – CK19 staining for boundary cell characteristic analysis. Spheroids were created on liquid-overlay plates from 5000 cells per well and fixed at day 3, 7 and 11 of culture, paraffin embedded, sectioned and stained with CK19. Slides were counterstained with haematoxylin (blue) to stain for cell nuclei. Intense brown staining shows the presence of CK19. Images represent mid-sections through the spheroids at 20x magnification. Scale bars = 100 µm.

Ki67 Positive control

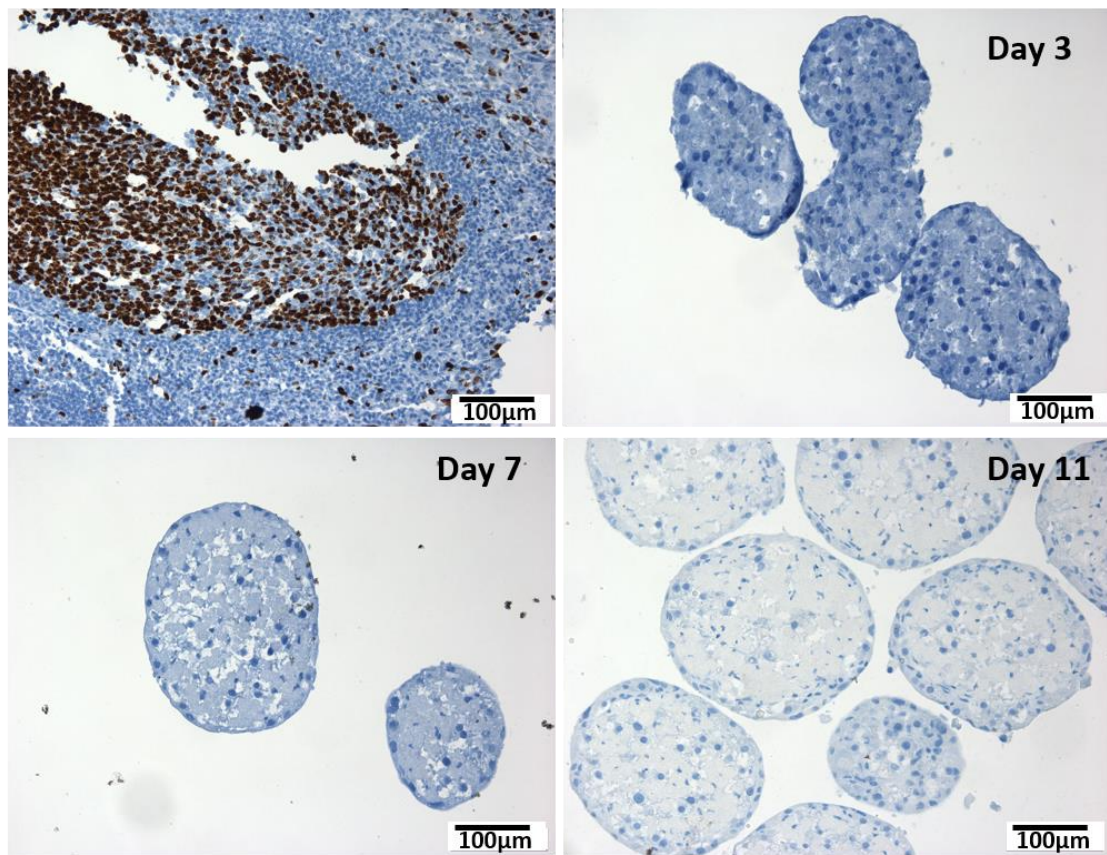


Figure 2-11 – Ki67 staining for boundary cell characteristic analysis. Spheroids were created on liquid-overlay plates from 5000 cells per well and fixed at day 3, 7 and 11 of culture, paraffin embedded, sectioned and stained with Ki67. Slides were counterstained with haematoxylin (blue) to stain for cell nuclei. Intense brown staining shows the presence of Ki67. Images represent mid-sections through the spheroids at 20x magnification. Scale bars = 100 µm.

Characterisation of a functional primary rat hepatocyte spheroid model

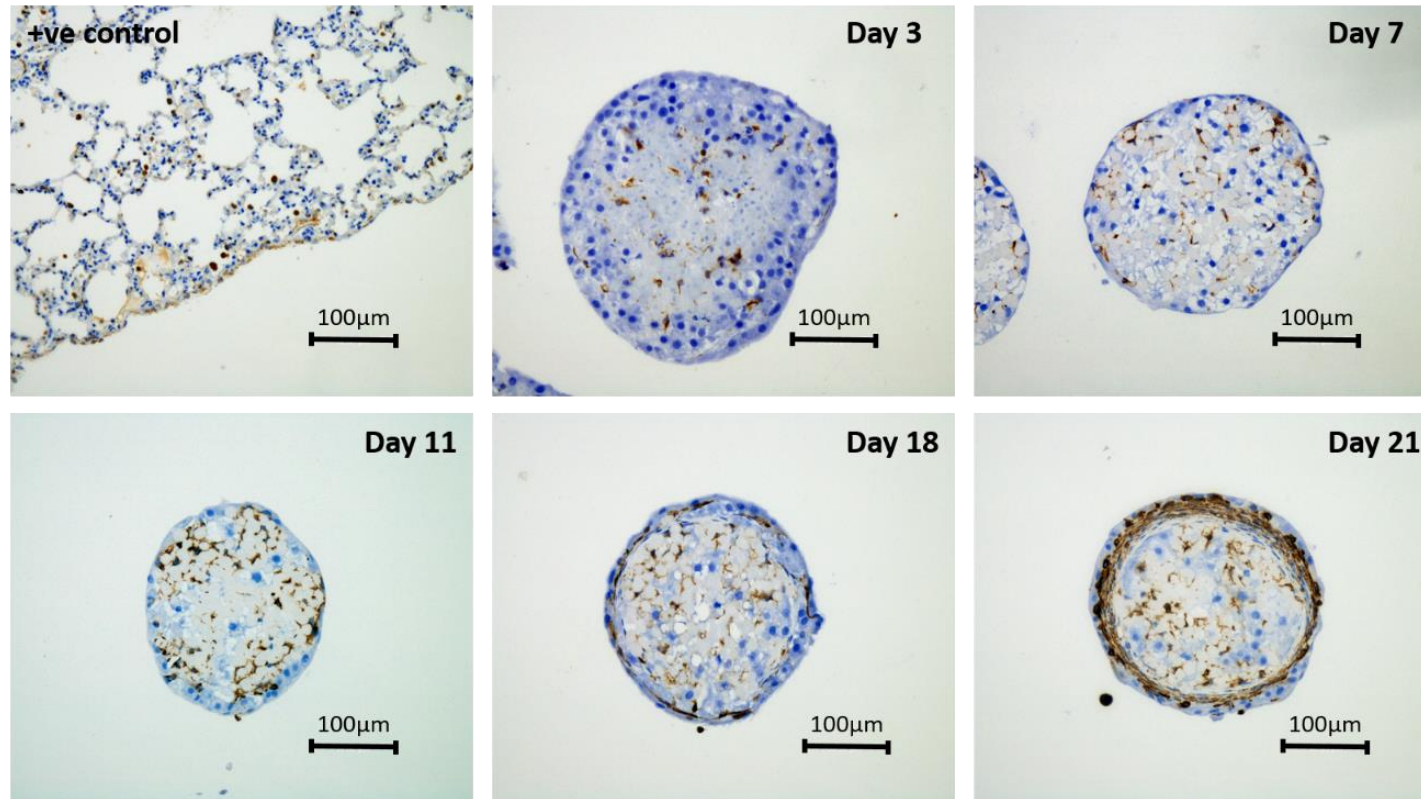


Figure 2-12 - Vimentin staining for boundary cell characteristic analysis. Spheroids were created on liquid-overlay plates from 5000 cells per well and fixed at day 3, 7, 11, 18 and 21 of culture, paraffin embedded, sectioned and stained with Vimentin. Slides were counterstained with haematoxylin (blue) to stain for cell nuclei. Intense brown staining shows the presence of mesothelial cells. Images represent mid-sections through the spheroids at 20x magnification. Scale bars = 100 µm.

Characterisation of a functional primary rat hepatocyte spheroid model

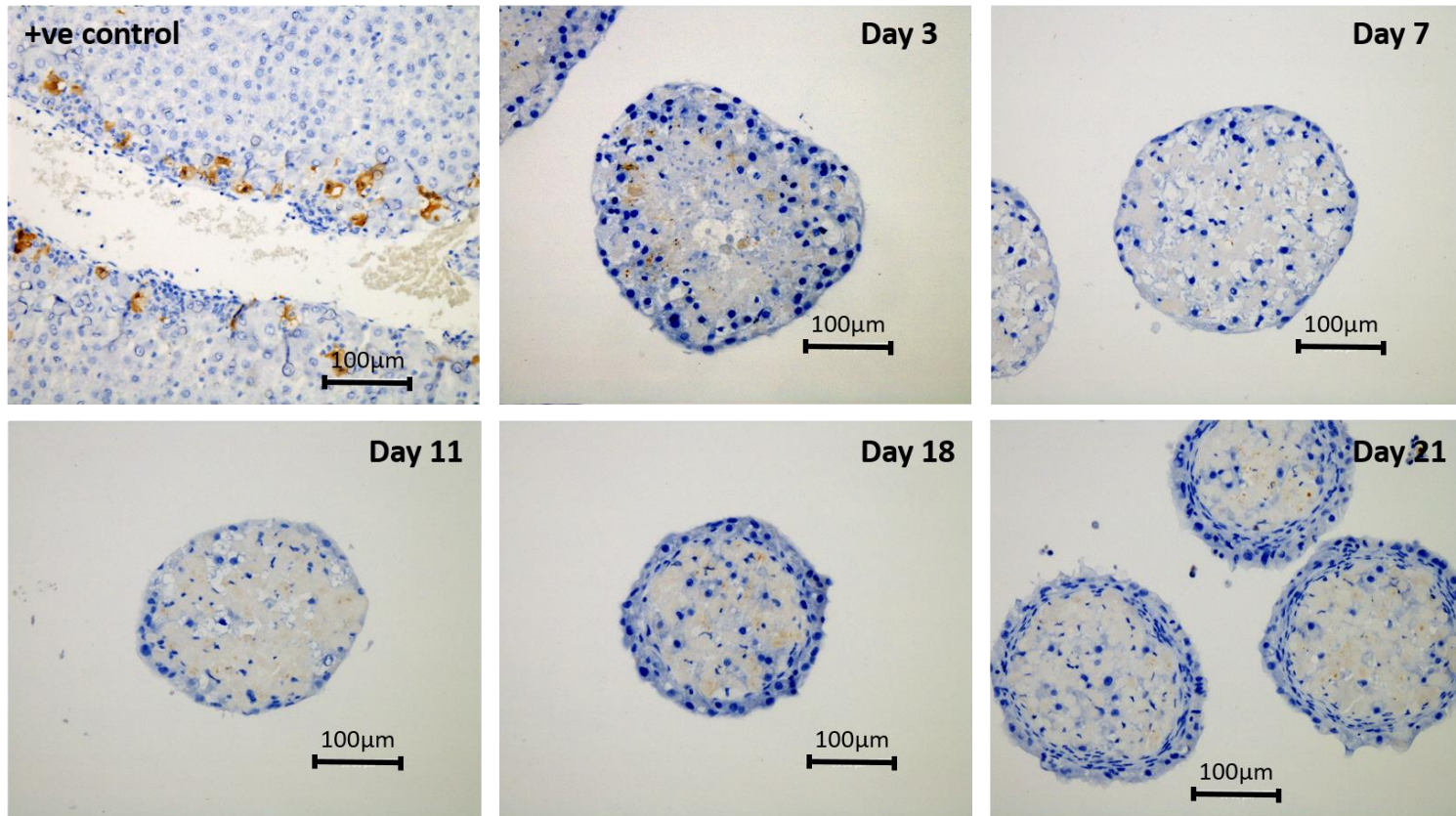


Figure 2-13- Cleaved caspase 3 staining for analysis of apoptotic cell death. Spheroids were created on liquid-overlay plates from 5000 cells per well and fixed at day 3, 7, 11, 18 and 21 of culture, paraffin embedded, sectioned and stained with cleaved-caspase 3. Slides were counterstained with haematoxylin (blue) to stain for cell nuclei. Brown staining shows the presence of apoptosis. Images represent mid-sections through the spheroids at 20x magnification. Scale bars = 100 μm.

2.3.6 Ultrastructural analysis of hepatocytes

Cellular ultrastructure was analysed utilising transition electron microscopy (TEM) analysis. Upon spheroid formation (day 3), TEM images showed characteristic hepatic ultrastructures, and specialised intracellular adherent junctions could be seen clearly at day 7. Images were taken using a Gatan digital camera.

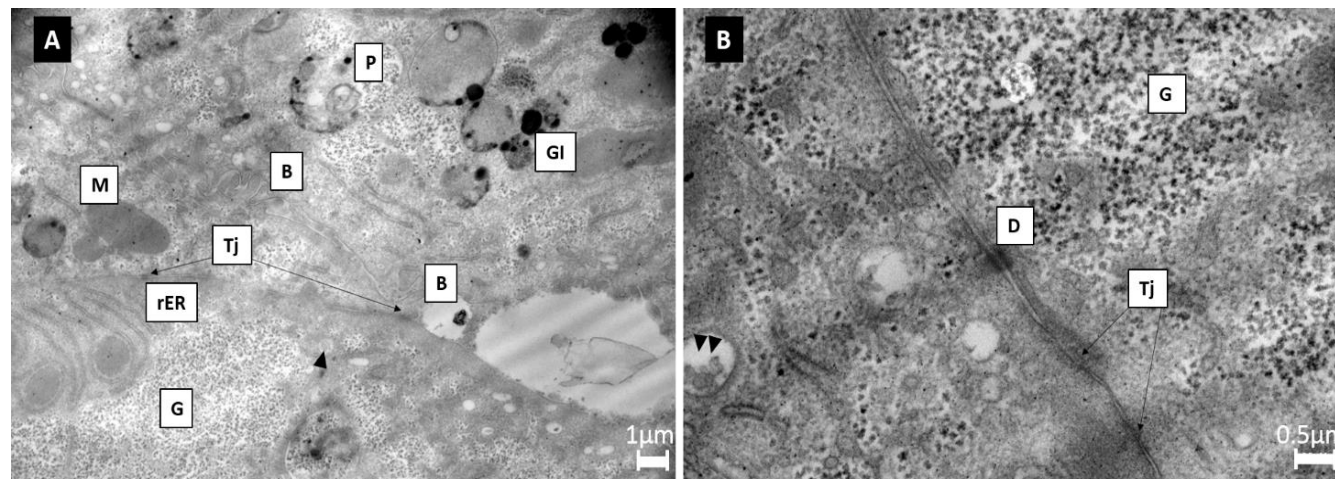


Figure 2-14 - Ultrastructural features of a 5000-cell spheroid by transmission electron microscopy (TEM) at day 3 of culture. **A** shows the presence of characteristic hepatic ultrastructures. Both glycogen vesicles (GI) and granular glycogen (G) were abundantly expressed, as well as bile canaliculi (B) forming throughout the spheroid. The PRH spheroids display a large quantity of metabolism-related organelles; including mitochondria (M), rough endoplasmic reticulum (rER), peroxisomes (P), and evidence of endocytosis or exocytosis (indicated by black arrow). There was also presence of tight junctions (Tj), indicating hepatic cell-cell interaction throughout the spheroid. **B** shows the presence of glycogen (G), desmosomes (D) and specialised intracellular adherent junctions (Tj). The paracellular space between the two hepatocytes was analysed using ImageJ software to estimate the pore radius (r_p). Scale bar = 1 μm and 0.5 μm respectively.

2.3.7 Cellular polarisation in spheroids

This experiment was conducted to analyse the formation of cytoskeletal components and ECM properties within PRH spheroids. The internal structure of spheroids was analysed by immunofluorescence (IF) utilising phalloidin (red) to stain for F-actin and Hoechst (blue) as the standard stain for cell nuclei. Visualisation was performed by confocal microscopy (**Figure 2-15**). Upon spheroid formation (day 3), F-actin filaments can be seen to form throughout the spheroid and at day 21, F-actin structures can be seen to remain throughout the spheroid body creating an intricate network. F-actin staining demonstrates the cuboidal morphology of the cells within the spheroid.

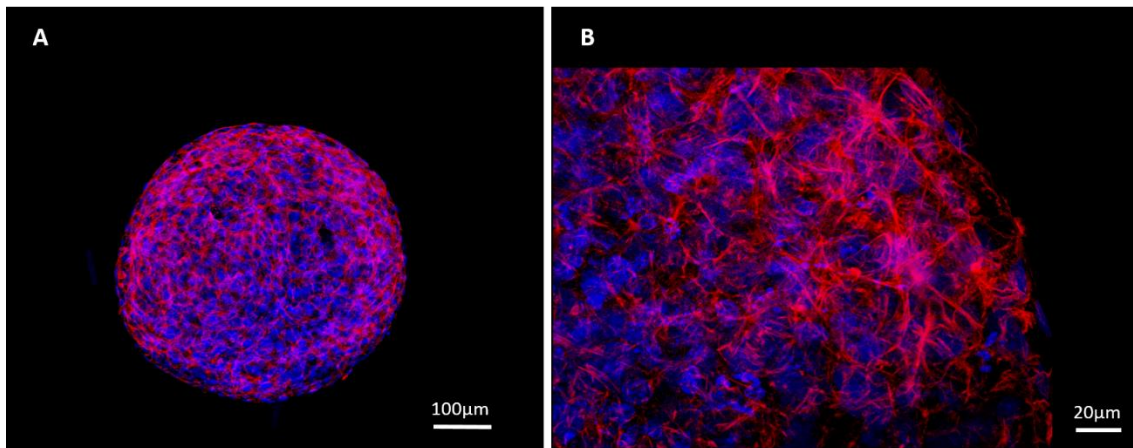


Figure 2-15 – Formation of cytoskeletal F-actin throughout spheroids. 5000-cell Spheroids were cultured on liquid-overlay plates for 3 days (A) or 21 days (B), fixed and stained with phalloidin (red) to stain F-actin and Hoechst (blue) to stain the cell nuclei. A single plane snap shot was taken for (A) at 10x magnification whilst a maximum intensity projection image was taken for (B) at 40x magnification. Scale bars = 100 µm and 20 µm, respectively.

2.3.8 Secondary structure formation in spheroids

Secondary structure formation (structural polarisation of hepatocytes) was determined via IF analysis. P-gp and MRP2 transporters are isolated to the apical/canalicular membrane of polarised hepatocytes. The expression of these two canalicular transporters was analysed to affirm the structural polarisation of the PRH within the spheroid and to confirm the formation of bile canalicular-like structures. Spheroids were analysed for up to 18 days for P-gp expression (**Figure 2-16**). The staining pattern of the P-gp transporter was consistent with the staining seen with the phalloidin (**Figure 2-15**). The secondary structures could be seen forming from day 3 of culture until at least day 18.

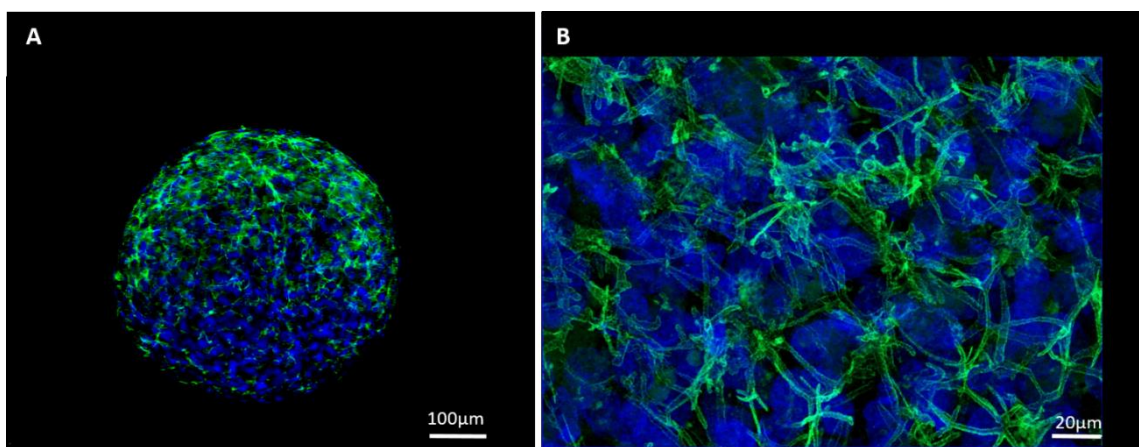


Figure 2-16 – P-gp staining of bile canalicular formation throughout spheroids. 5000-cell Spheroids were cultured on liquid-overlay plates for 3 days (A) or 18 days (B), fixed and stained with P-gp (green) and Hoechst (blue) to stain the cell nuclei. A single plane snap shot was taken for (A) at 10x magnification whilst a maximum intensity projection image was taken for (B) at 40x magnification. Scale bars = 100 μm and 20 μm respectively.

Characterisation of a functional primary rat hepatocyte spheroid model

Spheroids were analysed for up to 11 days for MRP2 expression (see **Figure 2-17**). This figure demonstrates the co-localisation of the canalicular transporter MRP2 (green) with the cytoskeletal F-actin (red) resulting in the yellow overlay image.

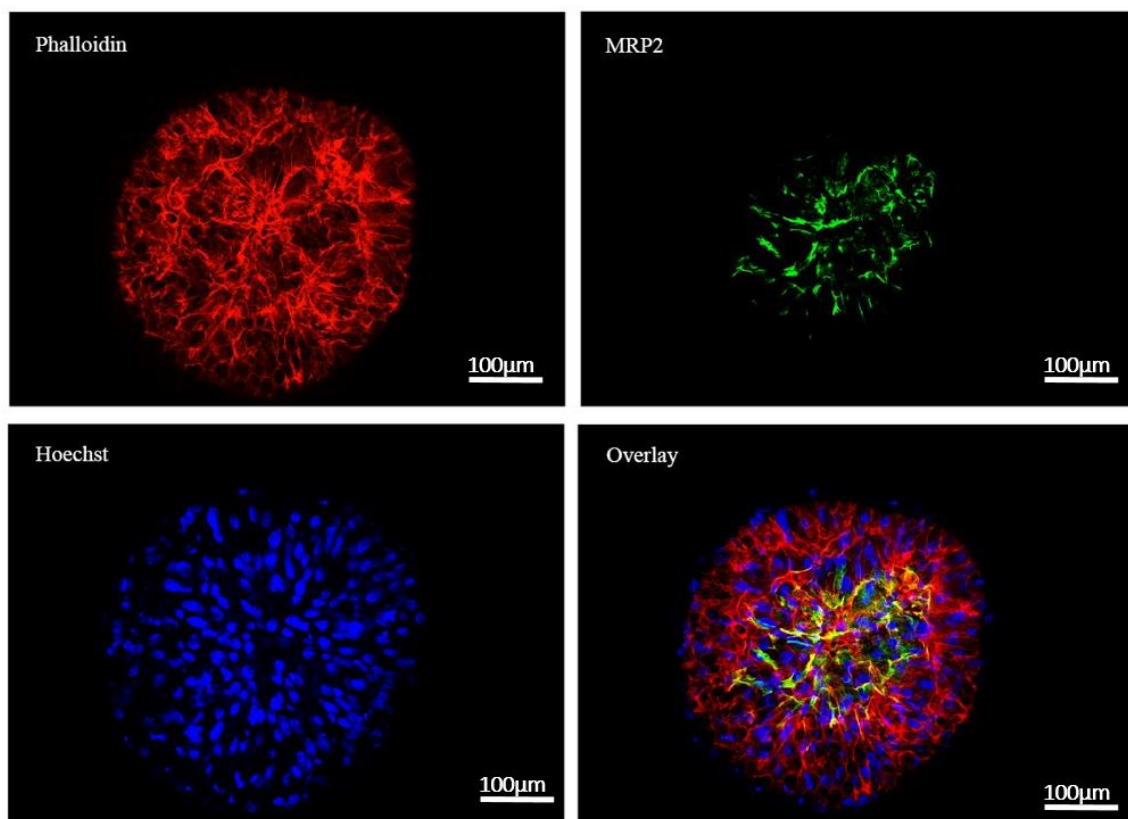


Figure 2-17 – MRP2 staining of bile canalicular formation throughout spheroids. Spheroids were cultured on liquid-overlay plates for 7 days, fixed and stained with pahlloidin (red), MRP2 (green) and Hoechst (blue) to stain the cell nuclei. 16 maximum intensity projection images were taken for **Figure 2-17** at 40x magnification using a Zeiss Axio Observer microscope, and stitched together utilising a moving platform. Scale bars = 100 µm.

2.3.9 Analysis of transporter functionality

Functionality of secondary structures was assessed using a fluorescently labelled dye. Spheroids were incubated with 5 μ M 5-chloromethylfluorescein diacetate (CMFDA- Thermo Fisher Scientific) for 1 hour (**Figure 2-18**). Spheroids were washed in PBS and prepared for IF as previously described (**2.2.8**). PRH spheroids exhibited some limited retention of CMFDA substrates within the cell cytoplasm, but also and an accumulation and co-localisation of the CMFDA substrates within the secondary bile canalicular-like structures, shown by MRP2 staining (white) and complementary F-actin staining (red).

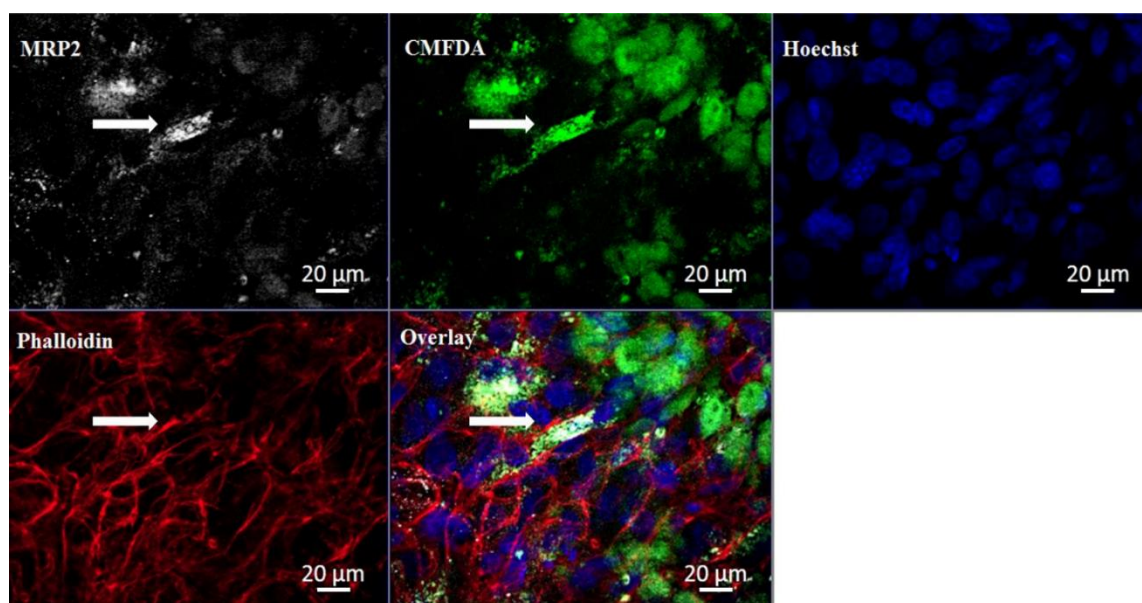


Figure 2-18 – Functional transport of CMFDA by MRP2 into secondary structures. Spheroids were cultured on liquid-overlay plates for up to 21 days. 5000-cell spheroids were cultured on liquid-overlay plates for up to 21 days. Spheroids were incubated with CMFDA (green) for 1 hour, fixed and then stained with MRP2 (white), phalloidin (red) (to stain F-actin) and Hoechst (blue) to stain the cell nuclei. A maximum projection image was taken for at 40x magnification. White Arrows represent the overlay of the canalicular-like structures and substrate along with F-actin indicating co-localisation within the secondary structures. A Zeiss Axio Observer microscope was used for both images. Scale bars = 20 μ m.

2.3.10 Urea quantification

In order to assess hepatocyte functionality, both urea and albumin secretion was analysed as these end point analyses are demonstrative of liver-specific functionality. Urea synthesis from 5000-cell spheroids was quantified over 28 days of culture (**Figure 2-19**). Urea synthesis decreased from 10.71 ± 1.79 nmol/ μ l to 1.32 ± 0.42 nmol/ μ l for 5000-cell spheroids from day 3 to day 11. Urea synthesis was at its lowest at day 11 for the 5000-cell spheroids but then increased over time to 2.63 ± 0.52 nmol/ μ l at day 28 of culture.

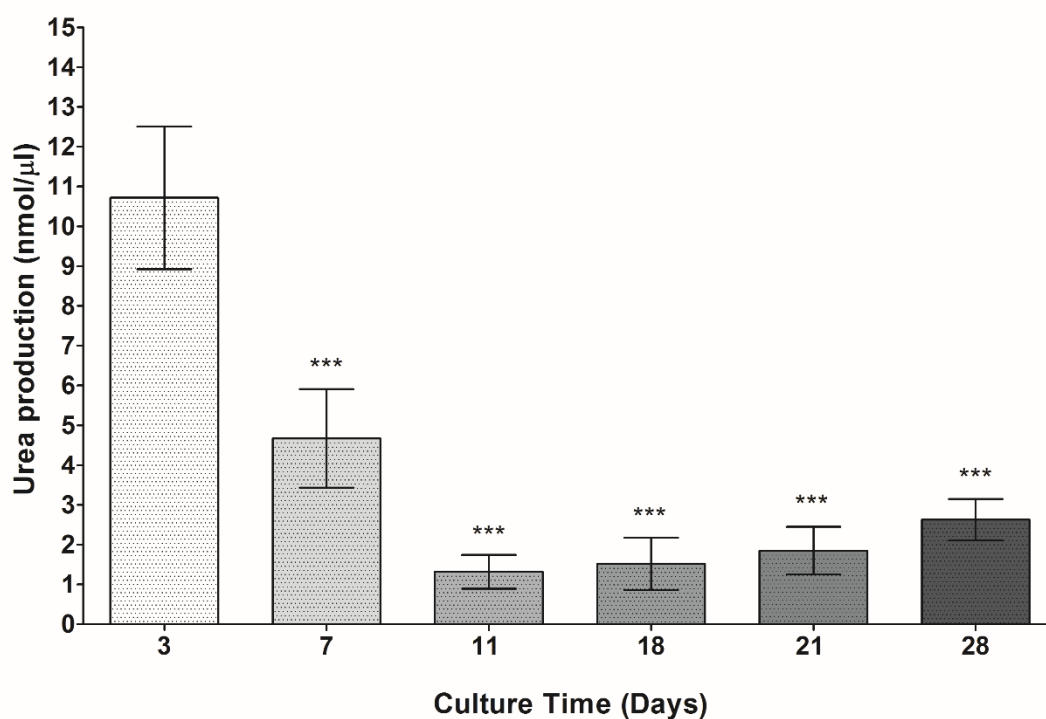


Figure 2-19 – Urea synthesis in the spheroids. Spheroids were produced from on liquid-overlay plates. Urea secretion was quantified in 5000-cell spheroid supernatant samples and plotted again culture time (days). Data are represented as mean \pm SD (n=3 in triplicate). Urea production was considered statistically significantly lower for all other time points compared to day 3 by One-way ANOVA, * $p < 0.001$.**

2.3.11 Albumin quantification

Albumin production from the 5000-cell spheroids was quantified over 28 days of culture period (**Figure 2-20**). Albumin production initially decreased but stabilised and then increased over the culture period. Albumin production decreased from 146.02 ± 17.48 ng/ml to 64.14 ± 17.62 ng/ml from day 3 to day 11. From day 11 until day 28, albumin production steadily increased from the observed low of 64.14 ± 17.62 ng/ml to 175.23 ± 42.02 ng/ml.

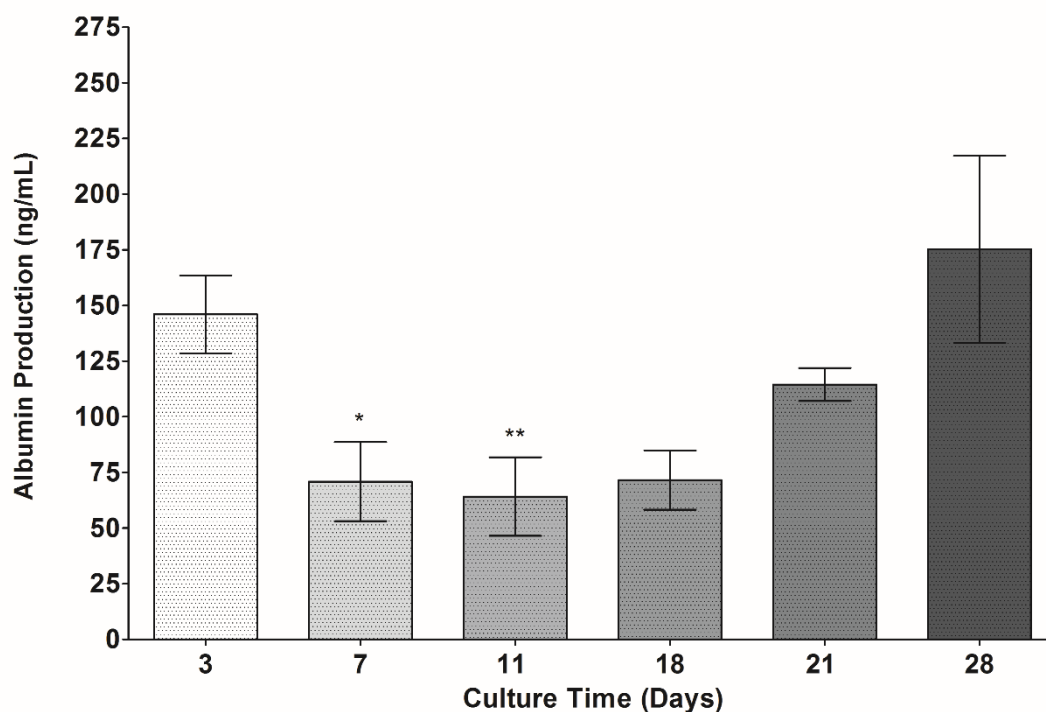


Figure 2-20 – Albumin production from spheroids. Spheroids were produced from 5000 cells on liquid-overlay plates. Albumin production was quantified in supernatant samples over a 28 day period. Data are represented as mean \pm SD ($n=3$ in triplicate). Albumin production was considered statistically significantly lower for day 7 and 11 time points compared to day 3 by One-way ANOVA, ** $p<0.01$, * $p<0.05$. There was no statistically significant difference in albumin production between day 3 and day 18, 21 or day 28.

2.3.12 Oxygen consumption rate analysis

The oxygen consumption rate of spheroids was analysed at day 7 and day 11 (**Figure 2-21**). At day 7, 2000-cell spheroids had an oxygen consumption rate of $0.0189 \pm 0.0039 \text{ mol s}^{-1} \text{ m}^{-3}$ and this decreased to $0.0133 \pm 0.0018 \text{ mol s}^{-1} \text{ m}^{-3}$ by day 11. For 3000- and 4000-cell spheroids, OCR decreased from $0.0132 \pm 0.0028 \text{ mol s}^{-1} \text{ m}^{-3}$ to $0.0157 \pm 0.0038 \text{ mol s}^{-1} \text{ m}^{-3}$, and $0.0140 \pm 0.002 \text{ mol s}^{-1} \text{ m}^{-3}$ to $0.0133 \pm 0.0018 \text{ mol s}^{-1} \text{ m}^{-3}$ respectively from day 3 to day 11. Finally, 5000-cell spheroid OCR increased from $0.0051 \pm 0.0018 \text{ mol s}^{-1} \text{ m}^{-3}$ on day 7 to $0.012 \pm 0.0017 \text{ mol s}^{-1} \text{ m}^{-3}$ by day 11.

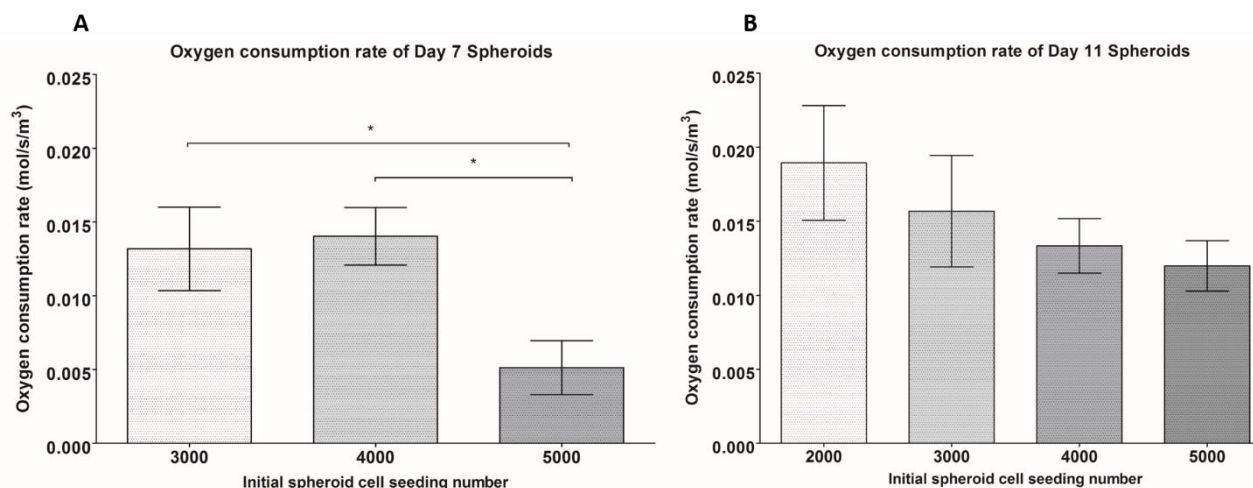


Figure 2-21 – The oxygen consumption rate (OCR) of spheroids was quantified in live spheroids on day 7 and 11 of culture. Data are represented as mean \pm SEM ($n \geq 6$). Oxygen consumption rate was considered statistically significantly lower for 4000- and 5000-cell spheroids at day 7 when compared to 3000-cell spheroids by One-way ANOVA, * $p < 0.05$. There was no statistically significant difference in oxygen consumption rate between 2000-, 3000-, 4000- and 5000-cell spheroids at day 11 of culture.

2.4 Chapter discussion

Previous research has shown 3D liver spheroids to be an improved *in vitro* model when compared with 2D cultures [43, 76, 109], so much so that there are now a number of companies that sell ‘ready-made’ spheroids as platforms for xenobiotic toxicity assessments [125]. Hepatocyte spheroid models have been shown to maintain liver-specific functions for extended periods of time in culture [81, 126]. However, some of the key characteristics previously discussed needed to be evaluated more comprehensively. This more extensive characterisation represented an area that required more attention within the field of *in vitro* liver models. In particular, functional polarisation of primary hepatocytes within liver spheroid systems was an area that required more in-depth investigation.

In this study, I have developed a cost-effective and reproducible method for producing PRH spheroids. PRH used in combination with the LOT had not previously been investigated. However, much interest had previously been given to the hanging-drop method, as implemented by Messner *et al.* [125], and the utilisation of ready-made ULA plates [126]. PRH were chosen because primary cells demonstrate a number of inherently advantageous characteristics when compared to the more utilised hepatic derived cell lines.

Firstly, primary cells do not proliferate *ex vivo* and as an initial hypothesis, it was speculated that the resultant spheroid sizes would be more stable when compared with a proliferative hepatic cell line. It has previously been reported that C3A hepatocarcinoma cells display contact inhibited growth characteristics when compared with their parent HepG2 cells and as a result do not proliferate to the same extent when cultured in a spheroid conformation [73]. However, histological and image analysis has demonstrated that the C3A cells within the microtissue do proliferate considerably over the duration of the culture time to the point where extensive areas of necrosis form [76]. The formation of necrosis within 3D liver models over extended culture periods is one of the key difficulties that remains to date.

The literature has previously reported that the physiologically occurring oxygen gradient was considered to be crucial for zonation within the liver lobule [118]. However, more recent investigations have reported that the oxygen gradient within the liver lobule is a regulator of zonation [12]. This is important when discussing the formation of necrotic regions within 3D liver models as this apparent lack of oxygen diffusion throughout the entirety of the microtissue will inevitably negatively impact on the zoned properties of the 3D model, as well as gene expression and subsequent functionality.

Within the liver lobule blood coming from the portal triad flows through the sinusoids to the central vein. Due to uptake, metabolism and elimination of xenobiotics along the sinusoid, the composition of this blood changes. Gradients of substrates, and in particular oxygen, are formed as a result. Consequently, there has been a drive in recent years to produce viable long-term 3D liver models that remain devoid of necrosis throughout the entirety of the culture period. With this in mind, I have conducted experimental ORC analysis in order to parametrise my mathematical model for the investigation of oxygen gradient formation with PRH spheroids. These experimentally-derived values along with spheroid growth characteristics will be invaluable to validate my *in silico* approach.

Phase contrast imagery (**Figure 2-4**) demonstrated that over the course of our culture period the spheroid diameter decreased in size. The literature has reported this phenomenon previously with other primary isolated spheroid cultures [127] and up-regulation in key ECM components and cytoskeletal elements such as E-cadherin and beta-1 integrin etc. have been attributed to this observation. Histological analysis (**Figure 2-6** and **Figure 2-8**) demonstrated the compact morphology of the hepatocytes within the spheroids and highlighted tight cell-cell interactions comparable with the morphology hepatocytes exhibit *in vivo*. This is in contrast with conventional monolayer cultures whereby the cellular morphology is altered to a flattened state, and cells have relatively few cell-cell and cell-ECM interactions. This has previously been reported for HepG2 spheroids and monolayer cultures by Li *et al.* [43]. Our PRH spheroids show no visible sign of the characteristic central necrotic zones often observed in multicellular

tumour spheroids. This may be partly due to the non-proliferative properties of primary hepatocytes *ex vivo*.

The literature has previously reported that spheroids with a diameter greater than 150 μm form necrotic cores due to hypoxia and lack of nutrient penetration [32]. However, little quantitative research has focused on the factors and specific conditions that may contribute to the formation of these necrotic zones. These factors may include the cell type being cultured, the initial size of the spheroids upon formation, the specific oxygen consumption rate (OCR) of the cells and the culture conditions themselves. A much more robust analysis of these factors required for the adequate characterisation of 3D liver microtissues and its applications are needed. It is for this reason that in Chapter 3 I will focus on answering this question applying a number of the experimental parameters taken from this initial characterisation work. Although I was unable to investigate necrotic markers specifically in my PRH spheroids, immunohistochemical analysis with cleaved-caspase 3 (**Figure 2-13**) confirmed small areas of apoptotic cells at early time points such as day 3, however, there were no central regions of necrosis within the PRH spheroids contrary to that reported previously with other hepatic-derived spheroids. This result along with the histological (**Figure 2-6**), IF (**Figure 2-9**) and TEM (**Figure 2-14**) results increasingly suggest that this spheroid model remains devoid of necrosis for extended periods of culture.

Immunohistochemical analysis demonstrated the presence of another cell type, namely mesothelial cells as shown via Vimentin staining (**Figure 2-12**). These results confirm the formation of a mesothelial lining/capsule surrounding the spheroids similar to the Glisson membrane seen encapsulating the exterior of the liver *in vivo*. It is important to note that the formation of the capsule becomes extremely apparent by day 21. On day 18, we can see a thin cell layer lining the spheroid boundary, however, this rapidly thickens to a stratified outer membrane by day 21.

Specific transporters are expressed on the canalicular, and sinusoidal membranes of the hepatocytes [207]. Due to this transporter expression, bile canaliculi form between

adjacent hepatocytes. The formation and maintenance of hepatocyte polarity is essential for a multitude of functions and I have been able to recapitulate this *in vivo*-like characteristic within my *in vitro* spheroid model. The establishment of structural polarisation was confirmed via IF analysis where the canalicular membrane transporters P-gp and MRP2 were stained and visualised (**Figure 2-16** and **Figure 2-17**). This analysis has previously been carried out with HepG2 and C3A spheroids [76]. However, the bile canalicular networks present in the PRH spheroids are much finer, more extensive and complete when compared to the more globular-like secondary structures of HepG2 and C3A spheroids.

As well as identifying the formation of these networks, I have been able to observe the functionality of these structures (functional polarisation) utilising CMFDA, a cell tracker that is passively taken up by hepatocytes (**Figure 2-18**). CMFDA substrates were actively transported out of the hepatocytes via MRP2. IF analysis revealed that this cell tracker substrate co-localised with the MRP2 transporter showing functionality within our spheroids.

I was also able to demonstrate that PRH spheroids were able to produce albumin and secrete urea consistently over the duration of the culture period (**Figure 2-19** and **Figure 2-20**). Urea secretion was seen to be significantly higher in PRH spheroids when compared to the previously characterised C3A and HepG2 spheroids [76]. Albumin production was also seen to be stable over the culture period. Urea secretion was significantly lower compared to day 3 for all other time points. After an initial decline in albumin production, functional stability was achieved from the point of spheroid formation until day 28. Albumin production and urea secretion are well defined physiological functions of hepatocytes *in vivo* [15, 208] and therefore, the analysis of the production of these two functional end points provides an indicative measure of liver-specific functionality in our spheroid model. These findings help to assert that the culturing of cells in 3D provides a more representative model that recapitulates a number

of *in vivo*-like characteristics that are not apparent in more commonly used monolayer cultures [81].

2.5 Conclusion

3D liver models have long been acknowledged as an improved platform for toxicological investigations due to the more representative morphology, improved functionality and increased viability for the duration of culture when compared with 2D methods. The technique described in Chapter 2 for the formation of PRH spheroids allows for a high-throughput platform with the potential for repeat-dose investigations. A key attribute of this spheroid system, particularly when compared with other spheroid models that utilise hepatic-derived cell lines, is the ability to be cultured over a 31-day period without the formation of necrotic regions as demonstrated via multiple histological and IF analyses. However, this is an area of research that requires further investigation with a view to characterise more precisely the causative factors for the formation of these necrotic regions. It may be that oxygen is unable to diffuse more than 150 μm within spheroid models, or it could be due to other specific factors such as the oxygen usage by cells, their proliferative characteristics and cellular functional output, or a combination of all of these factors.

In conclusion, I have successfully developed a reproducible technique for creating uniform, size controllable, PRH spheroids, and characterised their growth characteristics over a culture period of 31 days. The resultant spheroids exhibit an *in vivo*-like morphology, intricate cell-cell and cell-ECM interactions, as well as structural and functional polarisation. I additionally confirmed liver-specific functionality by analysing albumin production and urea secretion. I was also able to demonstrate that the canalicular transporters were functional. The culmination of these analyses further affirm that 3D liver spheroids provide a model that recapitulate the *in vivo* liver more closely than currently utilised 2D cultures.

Characterisation of a functional primary rat hepatocyte spheroid model

In Chapter 3, I will utilise experimental data from my characterisation work and look at how oxygen diffuses through the *in vitro* spheroid system. I will look at mathematically modelling the diffusion and consumption of oxygen within my spheroids, and analyse the subsequent oxygen profiles in order to determine the representativeness of the experimental model. Seahorse OCR results will be used from Chapter 2 to parameterise the mathematical model in order to develop a PRH-specific oxygen diffusion model.

Chapter 3: Mathematical modelling of oxygen diffusion through primary rat hepatocyte spheroids

3.1 Biological motivation

Hypoxia occurs when the amount of oxygen within a tissue decreases to a level lower than the physiological amount required and this may be caused by, increased demand, decreased supply or abnormal utilisation by the cells [208]. In much of the current literature regarding liver 3D microtissues, including spheroids, oxygen consumption rate (OCR) and oxygen diffusion remain poorly characterised. When using tumour spheroids and other tumour 3D models, oxygen distribution is an important factor to consider as it has been shown that, tumours that exhibit hypoxia tend to be associated with a poor prognosis [209]. It is, for this reason, that hypoxia within tumour spheroids may be a desirable characteristic to replicate *in vitro*, as it is more representative of the *in vivo* situation. However, for an *in vitro* liver model that attempts to recapitulate the native liver microenvironment, this is an undesirable characteristic as necrosis and hypoxia are features of liver disease states and not the healthy liver [210].

Oxidative respiration in standard 2D cell culture models has been widely studied. However, as 2D cell cultures fail to acquire the intricacies of the 3D microenvironment, the findings from these 2D investigations may not provide the required information when looking at 3D liver microtissue models. In particular, how the 3D microenvironment will impact on the diffusion of oxygen into the microtissues and the subsequent OCR of the cells [123]. An important aspect to consider regarding 3D hepatocellular models, is that with an improvement in functional output by the cells, there is potential for an increase in OCR. Cho *et al.* [129] demonstrated that albumin and urea production increased in line with an increased OCR by hepatocytes. These researchers evaluated the effect of cell seeding densities on OCR and the subsequent expression of liver-specific functions. In this study, PRH were co-cultured with mouse 3T3-J2 fibroblasts at varying hepatocyte to fibroblast (H-F) seeding ratios. A 1:9 H-F seeding density was considered to be a low hepatocyte density, 1:3 H-F was a medium hepatocyte density, and 9:1 H-F was a high hepatocyte density. For all of these experiments, the total number of cells seeded remained constant. Results from these investigations showed that there was an inverse

Mathematical modelling of oxygen diffusion through primary rat hepatocyte spheroids

relationship between the hepatocyte density and OCR of hepatocytes in the co-culture systems. That is, PRH seeded at lower densities exhibited much higher OCR compared to those seeded at higher densities. It was noted that the increase in OCR correlated well with increased liver-specific functionality [129]. However, detailed investigations of oxygen supply to cell cultures *in vitro* is challenging and still remains an issue [211].

Regarding spheroids, the wider literature discusses the maximal size of these 3D microtissues based on the ability of oxygen to diffuse through the cellular aggregates. Generally, the literature states that spheroids that have a radius of greater than 150 μm will become necrotic due to the inability of oxygen to diffuse beyond this point [32]. Clearly, it is also the case that the specific OCR of the cells will also impact greatly on the diffusion distance of oxygen, along with the amount of oxygen available in the medium. There have been some investigations conducted in an attempt to answer the question of optimal liver spheroid size utilising simple mathematical modelling [178, 212]. These previous investigations have provided useful outcomes as the increasing use of experimental data alongside *in silico* modelling has provided better means of prediction validation. Aleksandrova *et al.* [178] concluded that, according to their mathematical model, the necrotic core is absent in spheroids consisting of 5,000 and 10,000 HepaRG cells, and the threshold size of HepaRG spheroids is 12,000 cells. However, there is still a clear need to improve the specificity of these *in silico* models by utilising cell specific and model specific parameters derived from experimental investigations.

It is important to note that there are a number of variables that need to be taken into account when assessing cellular necrosis and the potential for hypoxia. OCR may vary between cell types, and the same cells may have varying OCR depending on the way in which they are cultured [213]. The utilisation of more commonly used proliferative hepatic-derived cell lines, such as HepG2 and C3A cells, means that the subsequent *in vitro* 3D model will increase in size over the duration of the culture period. Non-proliferative cells, such as primary isolated hepatocytes, do not proliferate *ex vivo* and as a result the size of the 3D microtissue reduces over the culture period due to the impact

of the upregulation of key extracellular matrix (ECM) components. In this case, the number of hepatocytes within an *in vitro* 3D model will not increase over the culture time and this, coupled with increasing ECM and cytoskeletal components whereby the interactions between cells becomes more stable, causes the 3D microtissues to become more compact.

Unlike conventional tumour spheroid models for example, spheroids produced from isolated hepatocytes can be thought as being quiescent with no proliferative outer rim. Initial work that we have carried out with PRH spheroids and C3A spheroids has shown that the size of spheroids can be controlled via the initial seeding density of cells [76]. With this in mind, it is reasonable to assume that the specific OCR of the cells, (whether the cells are proliferative or non-proliferative), and initial size of the 3D spheroid model will both have an impact upon the formation of necrotic zones within the spheroids. There are a number of researchers that have analysed OCR of cells in various 3D liver models. However, with these values being taken from a variety of different models (spheroids, sandwich cultures, co-cultures, bioartificial livers (BAL) etc.), the OCR values published tend to vary considerably.

3.1.1 Aims of the chapter

These studies seek to establish a more definitive answer for the optimal spheroid size for PRH based on a combined *in vitro* and mathematical modelling approach. Using this approach, I will propose optimised cell culture operating conditions to mimic *in vivo* characteristics, such as the maintenance of sinusoidal oxygen tensions, for as long as possible.

With the ability to control the initial size of PRH spheroids via cell seeding density, and the fact that primary hepatocytes are non-proliferative *ex vivo*, I hypothesise that I can produce a mathematically-optimised 3D spheroid liver model, cultured for an extended period of up to 31 days that remains devoid of necrosis. I suggest that the formation of these necrotic regions is ultimately determined by, (i) the model-specific OCR of the cells

and the availability of oxygen in culture and; (ii) the stability of spheroids in terms of their size during the culture period.

Previous work with tumours has demonstrated that the presence of vasculature does not necessarily translate to a well-oxygenated tissue and thus, to first understand oxygen diffusion and transport, an avascular *in vitro* model is desirable [123].

I have analysed oxygen diffusion and OCR utilising PRH spheroids produced using the LOT as previously described [8]. To investigate OCR in PRH spheroids, I derive a mathematical model which describes the diffusion and consumption of oxygen through a homogenous, avascular PRH spheroid.

3.1.2 Modelling background

When modelling the movement of a dynamic variable, we must consider how that variable changes over time and space. Such modelling has been previously applied to a number of applications such as population dynamics [214], the modelling of disease states [215] and the proliferation and metastatic processes of cancer [216]. One standard method for analysing these types of problems involves the use of partial differential equations (PDEs). In the case of using PDE models, we can describe the movement of biological variables such as chemicals or solutes.

I define $c(\underline{x}, t)$ as a chemical concentration at position \underline{x} and time t , contained within an arbitrary volume V , enclosed by a surface S , that contains c where $d\underline{S}$ is the outer unit normal to S (**Figure 3-1**).

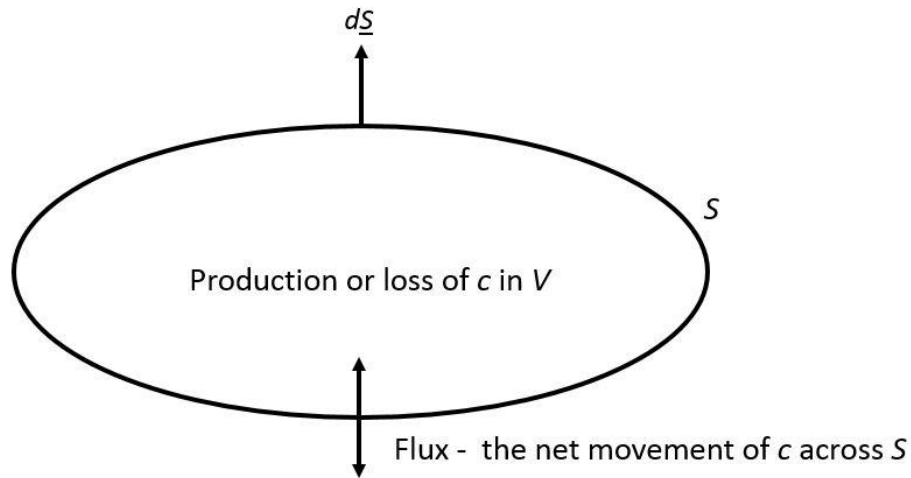


Figure 3-1 – Schematic representation of biological movement. The oval represents some arbitrary volume with S representing the surface area. $d\underline{S}$ is the outward facing norm (note that $d\underline{S}$ is short hand for $\underline{n}dS$, where \underline{n} is the outward pointing normal of the boundary S) and flux represents the movement of a drug, for example, in or out of the volume. Changes in the variable also occur due to production or loss e.g. birth and death rates within a population.

A change in the concentration of c within the volume V can occur due to the processes of production or consumption of c . We also need to account for the flux, $\underline{J}(\underline{x}, t)$, which describes the net movement of c across the surface, S , at position \underline{x} . The biological movement of c can now be formulated mathematically as a conservation law,

$$\frac{\partial}{\partial t} \int_V c(\underline{x}, t) dV = - \int_{S^-} \underline{J} d\underline{S} + \int_V f(c) dV, \quad (3-1)$$

where f is a function that describes the growth or decay of c depending on its current concentration.

$$\int_{S^-} \underline{J} d\underline{S} = \int_V \nabla \cdot \underline{J} dV, \quad (3-2)$$

applied to equation (3-1) we therefore obtain;

$$\int_V \left(\frac{\partial c}{\partial t} + \nabla \cdot \underline{J} - f(c) \right) dV = 0. \quad (3-3)$$

Because the volume V is arbitrary, equation (3-3) can only be satisfied if the integrand is zero, namely;

$$\frac{\partial c}{\partial t} = -\nabla \cdot \underline{J} + f(c). \quad (3-4)$$

Equation (3-3) is for a general n-dimensional volume V . In one spatial dimension this becomes,

$$\frac{\partial c}{\partial t} = -\frac{\partial J}{\partial x} + f(c). \quad (3-5)$$

In this case (e.g. oxygen diffusion), I assume Fickian diffusion where D is the diffusion coefficient and net movement is assumed to be down the gradient of c .

This is described by the following equation (Fick's first law) in 1 dimension,

$$\underline{J} = -D\nabla c = -D \frac{\partial c}{\partial x}. \quad (3-6)$$

If I now substitute equation (3-6) in to equation (3-5) I derive the following equation,

$$\frac{\partial c}{\partial t} = -D \frac{\partial^2 c}{\partial x^2} + f(c). \quad (3-7)$$

3.1.3 Modelling oxygen diffusion

Mathematical models of oxygen transport tend to be based on a simple diffusive process through a homogeneous medium governed by the equation,

$$\frac{\partial c}{\partial t} = D\nabla^2 c - K, \quad (3-8)$$

where c is the oxygen concentration within the tissue, D is the diffusion coefficient of oxygen within the tissue, and K describes the constant oxygen consumption rate. In the original model described by Krogh [217], which describe how oxygen diffuses from capillaries in to muscle tissue, a Dirichlet boundary condition was imposed upon a blood vessel wall where the concentration of oxygen was fixed. The constant uptake rate assumption for K requires that equation (3-8) needs an additional assumption stating that, when the concentration is equal to zero, the consumption rate is also equal to zero. This assumption prevents the equations from providing solutions with negative concentrations.

A more comprehensive form for the oxygen consumption term K in equation (3-8) is the Michaelis-Menten form,

$$K = \frac{V_{max}c}{K_m + c}. \quad (3-9)$$

With this nonlinear consumption rate, as $c \rightarrow \infty$, the consumption asymptotes to the constant value $K = V_{max}$, so that when oxygen is abundant, consumption is approximately constant [218]. However, when oxygen is limiting, oxygen consumption is linearly proportional to the available oxygen. K_m indicates the concentration of oxygen required to achieve 50% saturation with these values being negatively correlated with substrate affinity. By using equations (3-8) and (3-9) I can derive a reaction diffusion equation to model the diffusion of oxygen within my spheroids.

3.2 Mathematical methods

My experimental PRH spheroid system is a 3D in vitro model composed of multiple cells. To mathematically describe the spatio-temporal dynamics of oxygen in my system, a partial differential equation (PDE) model is required. I therefore suggest that the changes in oxygen distribution within the spheroid model are driven by two factors. Firstly, the diffusion of oxygen into the spheroid from an external source (namely, the media), and secondly the consumption of oxygen by the hepatocytes under normal respiratory conditions. For my initial simulations, I assume the diffusion coefficient is constant. My mathematical model of oxygen tensions in PRH spheroids assumes that the medium is continuously renewed and oxygen concentration around the spheroid can be considered to be constant. The rate of oxygen consumption by cells is described by Michaelis–Menten kinetics (3-9).

Since I will be considering oxygen transport and consumption dynamics, which varies on a much quicker timescale than normal cell reorganisation, growth and division, I make the assumption that the radius of the spheroid, R , is constant.

Because I am dealing with spheroids, I write the Laplacian operator with respect to spherical coordinates, (r, ϕ, θ) and can re-write (3-8) as follows:

$$\begin{aligned} \frac{\partial c}{\partial t} = D \left(\frac{1}{r^2} \frac{\partial}{\partial r} \left(r^2 \frac{\partial c}{\partial r} \right) + \frac{1}{r^2 \sin(\theta)} \frac{\partial}{\partial \theta} \left(\sin \theta \frac{\partial c}{\partial \theta} \right) \right. \\ \left. + \frac{1}{r^2 \sin^2 \theta} \frac{\partial^2 c}{\partial \phi^2} \right) - \frac{V_{max} c}{K_m + c}, \end{aligned} \quad (3-10)$$

where,

$$\theta \in [0, \pi], \phi \in [0, 2\pi], \text{ and } r \in [0, R]. \quad (3-11)$$

Mathematical modelling of oxygen diffusion through primary rat hepatocyte spheroids

For my purposes of modelling within 3D spheroids, I assume radial symmetry so that the problem is reduced to a 1D equation in variable r , the radial coordinate. With this assumption, the terms $\frac{\partial}{\partial \theta}$ and $\frac{\partial}{\partial \phi}$ are taken to be zero. I therefore obtain;

$$\nabla^2 = \frac{1}{r^2} \frac{\partial}{\partial r} \left(r^2 \frac{\partial}{\partial r} \right), \quad (3-12)$$

and my specific PDE can therefore be written as,

$$\frac{\partial c}{\partial t} = \frac{D}{r^2} \frac{\partial}{\partial r} \left(r^2 \frac{\partial c}{\partial r} \right) - \frac{V_{max}c}{K_m + c}. \quad (3-13)$$

I use the initial condition,

$$c(r, 0) = c_R, \quad (3-14)$$

where c_R is the oxygen concentration in the media.

I also use the boundary conditions,

$$\frac{\partial c}{\partial r} = 0, \quad \text{at } r = 0, \quad (3-15)$$

$$c = c_R, \quad \text{at } r = R,$$

The first condition is due to spherical symmetry and the second is where I fix the oxygen at the spheroid perimeter to that of the media.

3.2.1 Numerical methods

The Matlab function, *pdepe*, numerically integrates PDE systems using finite difference approximations in the spatial dimension to reduce the problem to an ordinary differential equation (ODE) problem. Using my PDE as an example, the spatial dimension can be appropriately discretised to derive the following finite difference approximations,

$$\frac{\partial c(r, t)}{\partial r} = \frac{c(r + \Delta r, t) - c(r - \Delta r, t)}{2\Delta r},$$

$$\frac{\partial^2 c(r, t)}{\partial r^2} = \frac{c(r + \Delta r, t) - 2c(r, t) + c(r - \Delta r, t)}{(\Delta r)^2}.$$

Therefore, I can re-write my PDE model as;

$$\frac{\partial c}{\partial t} = \frac{D}{r^2} \frac{\partial}{\partial r} \left(r^2 \frac{\partial c}{\partial r} \right) - \frac{V_{max}c}{c + K_m} = D \left(\frac{\partial^2 c}{\partial r^2} + \frac{2}{r} \frac{\partial c}{\partial r} \right) - \frac{V_{max}c}{c + K_m}, \quad (3-16)$$

$$\Rightarrow \frac{dc_i}{dt} = \frac{D}{\Delta r} \left(\frac{c_{i+1} - 2c_i + c_{i-1}}{\Delta r} + \frac{c_{i+1} - c_{i-1}}{r} \right) - \frac{V_{max}c_i}{c_i + K_m}, \quad (3-17)$$

for $i = 1..N + 1$ ($r = 0..R$) where I use notation $c_{i+1} = c(r + \Delta r, t)$ such that an increase by 1 in subscript i corresponds to a radial increment in Δr as defined by the discretisation of the mesh (spatial domain). I must also now consider the boundary conditions in order to determine special case boundary values.

In the case where $i = 1$ I have

$$\frac{dc_1}{dt} = \frac{1}{\Delta r} \left(\frac{c_2 - 2c_1 + c_0}{\Delta r} + \frac{c_2 - c_0}{r} \right) - \frac{V_{max}c_1}{c_1 + K_m},$$

and therefore, I need to determine the value of the ghost node c at $i = 0$, i.e. $r = 0 - \Delta r$. In order to do this I apply the Neumann boundary condition, $\partial c / \partial r = 0$, for the sphere centre boundary:

$$\frac{\partial c_1}{\partial r} = \frac{c_2 - c_0}{2\Delta r} = 0, \quad r = 0, \quad (3-18)$$

$$\Rightarrow c_0 = c_2. \quad (3-19)$$

Therefore,

$$\frac{dc_1}{dt} = \frac{2}{(\Delta r)^2} (c_2 - c_1) - \frac{V_{max}c_1}{c_1 + K_m}. \quad (3-20)$$

When $i = N$ I have

$$\frac{dc_N}{dt} = \frac{D}{\Delta r} \left(\frac{c_{N+1} - 2c_N + c_{N-1}}{\Delta r} + \frac{c_{N+1} - c_{N-1}}{r} \right) - \frac{V_{max}c_N}{c_N + K_m}$$

and I determine the value of c at $i = N + 1$, i.e. $r = R$. In order to do this, I apply the Dirichlet boundary condition, $c = c_R$, at the sphere outer boundary.

$$c = c_R = c_{N+1} \quad r = R \quad (3-21)$$

Therefore,

$$\frac{dc_N}{dt} = \frac{D}{\Delta r} \left(\frac{c_R - 2c_N + c_{N-1}}{\Delta r} + \frac{c_R - c_{N-1}}{r} \right) - \frac{V_{max}c_N}{c_N + K_m} \quad (3-22)$$

The time integration is done with ode15s, which is a variable-step, variable-order (VSVO) solver based on the numerical differentiation formulas (NDFs) of orders 1 to 5 [219].

Convergence to steady state was confirmed by using a stopping condition in the Matlab file which halted the code when the least squares difference between solutions at successive time points was less than the relative error tolerance of the ode15s solver (RelTol=10⁻⁵).

3.3 Fixed boundary oxygen profile simulations

3.3.1 Parameter values

Table 3 – Initial parameter values used for oxygen simulations.

<u>Simulation parameters</u>	<u>Values</u>
Spheroid radius	150 μm
Boundary oxygen concentration	9%
Diffusion coefficient	$1.6 \times 10^{-9} \text{ m}^2 \text{ s}^{-1}$
V_{max}	$1.22 \times 10^{-16} \text{ mol s}^{-1} \text{ cell}^{-1}$
K_m	$6.24 \times 10^{-3} \text{ mol m}^{-3}$

The spheroid radius, R was set at 150 μm as this has been previously reported to be the maximal distance that oxygen is able to diffuse through *in vitro* spheroids before the onset of necrosis [116, 220]. The external concentration of oxygen at the spheroid boundary, c_R , was fixed at 9%, based on values obtained from estimated liver periportal tensions in the literature [118, 221]. The diffusion coefficient of oxygen, D , through the homogenous spheroid was taken to be the $1.6 \times 10^{-9} \text{ m}^2 \text{ s}^{-1}$ [222]. The reaction diffusion coefficient value was calculated from spheroids produced from human S-type neuroblastoma cells (SK-N-AS). Mathematical modelling and fitting of experimental observations of the oxygen uptake rate and diffusion inside the spheroid allowed for the estimation of this parameter. This value for the diffusion coefficient seems to be a plausible estimate when compared to the mean diffusion rate of oxygen in water ($2 \times 10^{-9} \text{ m}^2 \text{ s}^{-1}$) [223]. The V_{max} of the cells was taken to be $1.22 \times 10^{-16} \text{ mol s}^{-1} \text{ cell}^{-1}$ for initial simulations [181]. This value is an experimentally derived parameter for the oxygen uptake rate of freshly isolated PRH cultured on a single layer of collagen. I will initially use a literature-derived OCR value that has been well accepted and this will allow for a direct comparison to my experimental seahorse values which will be implemented in the model.

Mathematical modelling of oxygen diffusion through primary rat hepatocyte spheroids

Finally, the value for the half maximal consumption rate (K_m) was taken to be 6.24×10^{-3} mol m⁻³ [224]. This value was calculated from experimental observations for primary rat hepatocytes in a hollow fibre bioreactor setting [225, 226].

3.3.2 Oxygen concentration conversion

Oxygen was converted to % O_2 using the following relationship;

$$O_2 \text{Concentration} = K \times PO_2(\text{mmHg}) \quad (3-23)$$

Where (K is the solubility of oxygen in water at standard pressure and temperature);

$$K = 1.39 \times 10^{-3} \text{ mol m}^{-3} \text{mmHg}^{-1}$$

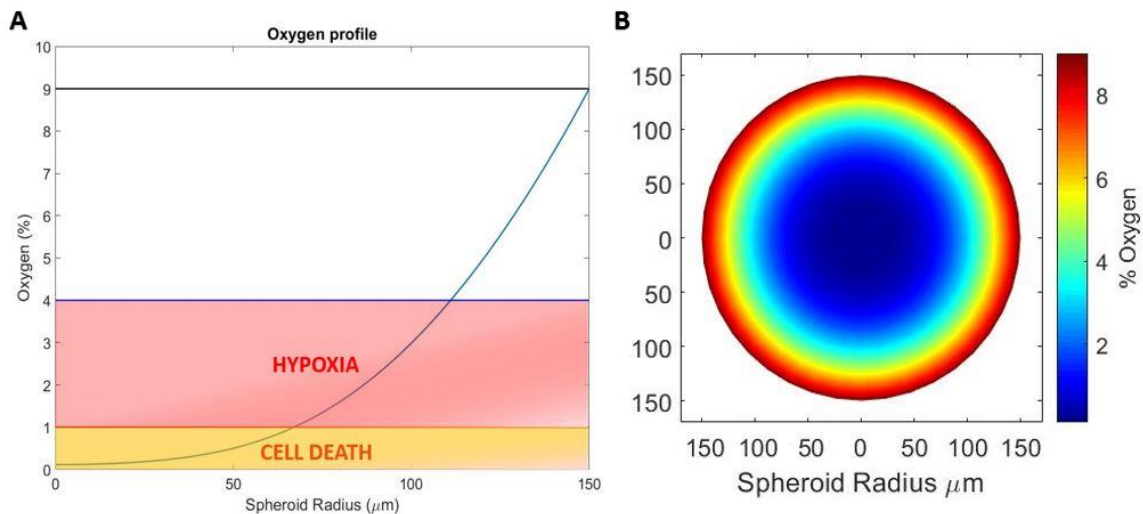
and,

$$\frac{\%O_2}{100} \times 760 = PO_2 \text{ mmHg} \quad (3-24)$$

The concentration of oxygen (mol m⁻³) is therefore approximately, the % O_2 divided by 100.

3.3.3 Single parameter value simulations

Figure 3-2 – Simulation of oxygen profile with single parameter estimates. The curve from (A) shows the decreasing oxygen profile from the boundary of the spheroid, (150 μm) to the core of the spheroid (0 μm). (B) describes the same oxygen profile as (A) assuming spherical symmetry. This figure provides a representative visualisation for the oxygen profile described in my spheroid system.



In **Figure 3-2 (A)**, the horizontal black line at 9% represents the oxygen tension at the spheroid boundary. The horizontal blue line at 4% O_2 represents the pericentral O_2 tension *in vivo* and below this threshold cellular hypoxia is observed [118]. The red line at 1% O_2 is demonstrative of this hypoxia threshold for cellular survival, i.e. cell death. When using these parameters the model predicts that a PRH spheroid with a radius of 150 μm will be hypoxic and that the central oxygen tension is close to zero. Although the model does predict hypoxia, it is important to note that this is not for the entire spheroid body. The oxygen tension falls below the 4% threshold at around 120 μm , and below the 1% threshold at around 70 μm . **Figure 3-2 (B)** has been rotated round 360° in order to plot the same information as a heat plot where the changing oxygen concentrations are represented by the change in colour.

Mathematical modelling of oxygen diffusion through primary rat hepatocyte spheroids

These initial simulations demonstrate the need for a better understanding of some of the initial parameters as, when comparing this result to some of the previously characterised experimental work, it is clear that my PRH spheroids do not exhibit zones of necrosis, whereas this initial simulation does (i.e. $O_2 < 1\%$). Although OCR analysis had been conducted in Chapter 2, a literature search for OCR values for rat hepatocytes was conducted in order to assess the potential variability within the reported values and to determine the potential validity of our Seahorse experimental results.

Table 4 – Literature reported rat hepatocyte oxygen consumption rates

<u>Ranges for OCR (mol s⁻¹cell⁻¹)</u>	<u>Reference</u>
1.25×10^{-16} to 3.5×10^{-16}	Wagner <i>et al.</i> 2011 [213]
2×10^{-16}	Guarino <i>et al.</i> 2004 [227]
3.8×10^{-16} to 4.3×10^{-16}	Foy <i>et al.</i> 1994 [182]
1.0395×10^{-16} to 8.162×10^{-17}	Rotem <i>et al.</i> 1992 [181]
1×10^{-15} to 7×10^{-16}	Smith <i>et al.</i> 1996 [211]
2.4×10^{-16} to 3.3×10^{-16}	Cho <i>et al.</i> 2007 [129]

3.3.4 Literature OCR value simulations

From **Table 4**, it is clear that there is wide variability of OCR for rat hepatocytes and this is largely down to the particular *in vitro* model in which the cells have been cultured. The method by which cellular OCR values have been evaluated also differs between publications, and hence there are a wide range of reported values. I was subsequently able to utilise this range of OCR values (8.162×10^{-17} to 1×10^{-15} mol s⁻¹ cell⁻¹) from the literature within my simulations to understand the effects of these different OCR (V_{max}) values on the oxygen profiles (see **Figure 3-3**).

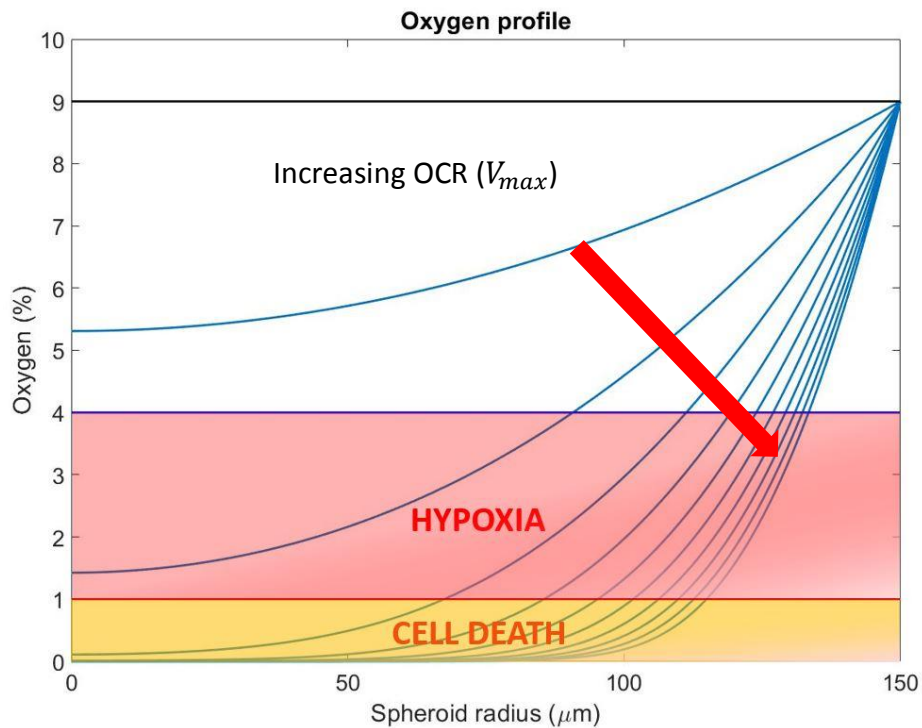


Figure 3-3 – Oxygen tension simulations for 150 μm radius spheroids for multiple literature OCR values. The wide variability in OCR values from the literature produces huge variation in predicted oxygen profiles for the spheroid system. As the OCR increases by the cells, the core oxygen tension decreases dramatically from around 5% to 0%. With some of the higher literature OCR values, hypoxia is predicted at around 140 μm, and the cell survival threshold is reached at around 120 μm.

Mathematical modelling of oxygen diffusion through primary rat hepatocyte spheroids

Simulations utilising the range of literature values provide useful information with regards to estimating the OCR of my PRH spheroids. From previous experimental analyses (**Figure 2-6** and **Figure 2-9**) I have been able to show that my PRH spheroids do not show signs of classic necrosis. Consequently, the model seems to suggest that the OCR for the PRH within my spheroid model must be close to the lower end of the values identified in the literature.

3.3.5 Experimentally-derived spheroid radii simulations

In order to incorporate this experimental data, a single OCR value was chosen from the literature values ($8.162 \times 10^{-17} \text{ mol s}^{-1} \text{ cell}^{-1}$) and simulations were conducted implementing the range of spheroid radii as described in **Figure 2-4**. From my experimental work, observations from histological analysis were not consistent with the formation of necrosis. As I do not visualise these necrotic cores, I made the assumption that the cells within our spheroid may be consuming oxygen at a rate similar to the lower end of my initial estimates from the literature. Hence, the lowest values for the oxygen consumption rate was used in subsequent simulations.

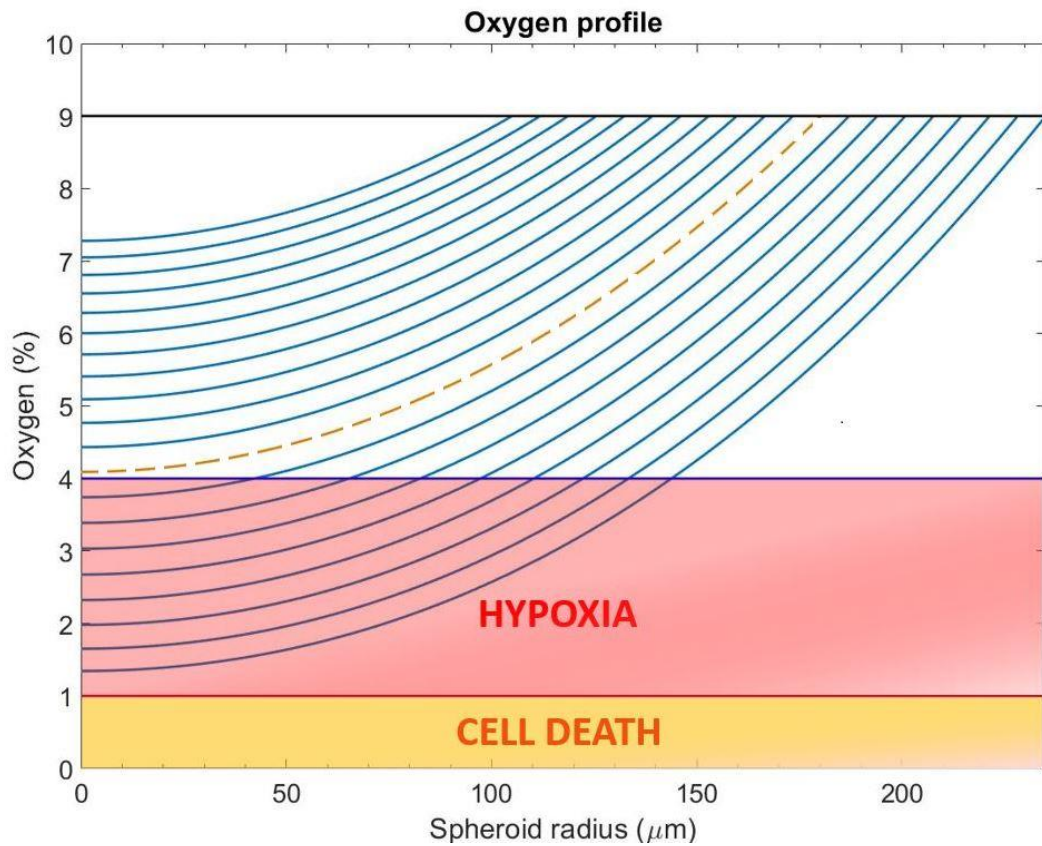


Figure 3-4 – Oxygen profile for fixed OCR with varying spheroid radii from experimental data. The steady state oxygen profiles for this range of spheroid sizes shows that the larger spheroids ($R > 180 \mu\text{m}$) become hypoxic where the core oxygen falls below the 4% pericentral oxygen value. However, none of the spheroids fall below the critical 1% cell survival threshold. This simulation suggests that the critical size of spheroid before the onset of necrosis is just over 180 μm . This is larger than the literature reported 150 μm value, but the simulation provides an extremely plausible value at this radius.

Figure 3-4 shows simulations for the oxygen profiles with a fixed OCR for my experimental spheroid sizes relevant to ranges observed in my experiments. From these simulations, and utilising literature-derived parameter values for V_{max} ($8.162 \times 10^{-17} \text{ mol s}^{-1} \text{ cell}^{-1}$), I demonstrate that spheroids of around 180 μm radius (orange dashed line) recapitulate the liver oxygen tension of 9% at the boundary and 4% in the core (as seen in the *in vivo* liver sinusoid). However, the main limitation that arises from **Figure 3-4** is that simulations predict that PRH spheroids with a radius $>180 \mu\text{m}$ may be necrotic in the central regions due to hypoxia, which is contrary to the experimental characterisation. In order to investigate this more robustly, the experimental analyses of PRH spheroid OCR that was carried out in Chapter 2 was implemented for subsequent simulations.

Mathematical modelling of oxygen diffusion through primary rat hepatocyte spheroids

Table 5 – Seahorse OCR readings for spheroids of different initial cell seeding numbers with unit conversions.

<u>Spheroids cell seeding number (Day 7)</u>	<u>Mean OCR Seahorse readings</u>	<u>Conversion</u>	<u>Spheroid Radius</u>	<u>Spheroid volume</u>	<u>Cell density</u>	<u>OCR values for Matlab</u>
	($\mu\text{mol min}^{-1}$)	($\text{mol s}^{-1} \text{cell}^{-1}$)	(μm)	(m^3)	(cell m^{-3})	($\text{mol s}^{-1} \text{m}^{-3}$)
3000	21.52	1.1958×10^{-16}	186.5	2.717×10^{-11}	1.10407×10^{14}	0.0132
4000	22.15	9.2272×10^{-17}	191	2.919×10^{-11}	1.37048×10^{14}	0.0126
5000	17.08	5.6933×10^{-17}	208.75	3.810×10^{-11}	1.31221×10^{14}	0.0075
<u>Spheroid cell seeding number (Day 11)</u>	<u>OCR Seahorse readings</u>	<u>Conversion</u>	<u>Spheroid Radius (μm)</u>	<u>Spheroid volume</u>	<u>Cell density</u>	<u>OCR values for Matlab</u>
	($\mu\text{mol min}^{-1}$)	($\text{mol s}^{-1} \text{cell}^{-1}$)		(m^3)	(cell m^{-3})	($\text{mol s}^{-1} \text{m}^{-3}$)
2000	20.39	1.6991×10^{-16}	169	2.022×10^{-11}	9.89194×10^{13}	0.0168
3000	21.64	1.202×10^{-16}	181.75	2.515×10^{-11}	1.19291×10^{14}	0.0143
4000	23.38	9.7429×10^{-17}	195.5	3.129×10^{-11}	1.278×10^{14}	0.0125
5000	23.20	7.7333×10^{-17}	200.75	3.388×10^{-11}	1.47542×10^{14}	0.0114
Total average OCR (day 7 and 11)						0.0126

3.3.6 Spheroid-specific OCR value simulations

Table 5 shows the results from my Seahorse analysis which were used to determine the OCR of the cells within my PRH spheroids. As with previous studies, I will utilise the mean OCR value calculated from the values in **Table 5** (spheroids at day 7 and 11 of the culture period).

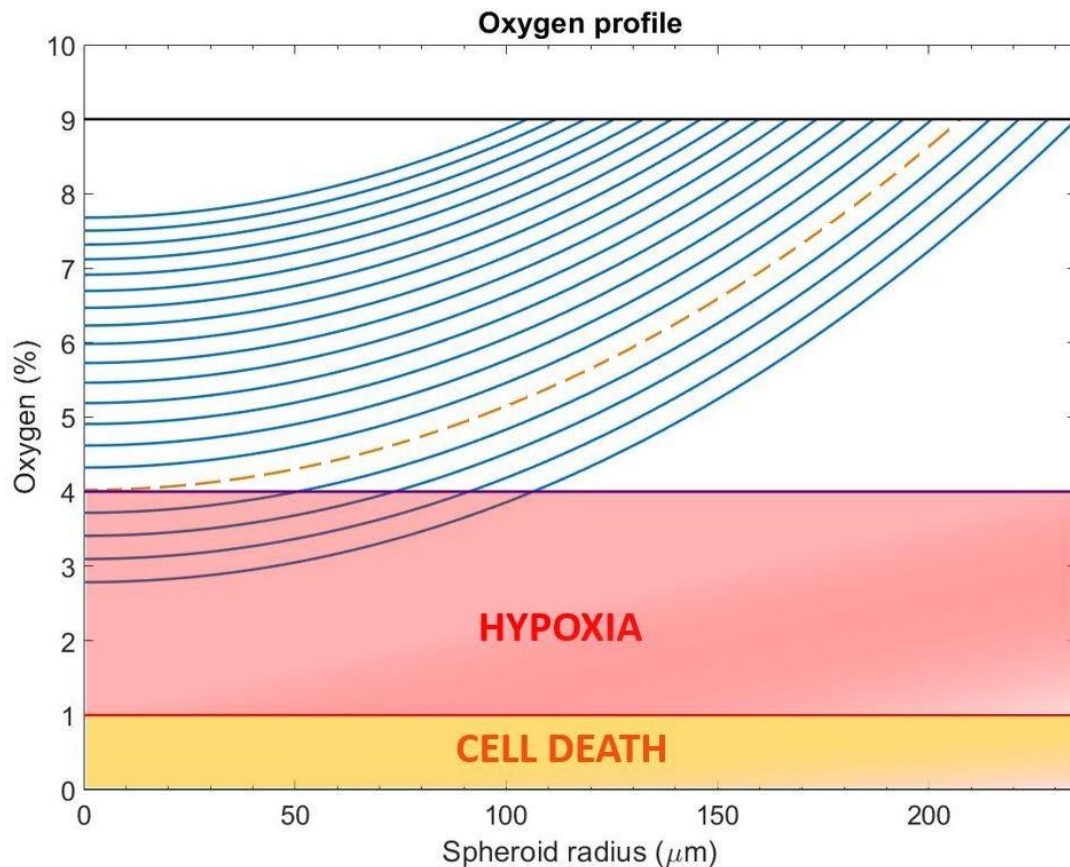


Figure 3-5 Oxygen profiles for average experimental OCR with varying spheroid radii from experimental data. The oxygen profiles for my experimental spheroid radius ranges look very similar to the profiles utilising the lowest literature OCR value (see **Figure 3-4**). None of the profiles for this spheroid radius range fall below the critical cell survival threshold of 1%, and the simulation predicts an increase in spheroid radius threshold for oxygen diffusion from 180 μm in **Figure 3-4** to approximately 210 μm (orange dotted line).

Figure 3-5 shows simulations for the oxygen profiles with a fixed average OCR based on the experimental Seahorse analysis (**Table 5**). The simulation implies that spheroids with a radius of approximately 210 μm (orange dashed line) best recapitulates the sinusoidal oxygen tension of 9% at the boundary and 4% in the core. These simulations display similar qualitative results to that of **Figure 3-4**. However, the issue remains that even though my spheroids are devoid of classical necrosis staining as demonstrated by previous experimental work and characterisation (**Figure 2-6**, **Figure 2-9**, **Figure 2-13** and **Figure 2-14**), these simulations suggest that hypoxia may be present within the larger spheroids ($>210 \mu\text{m}$). The fact that the larger spheroids correspond with early culture times in my experiments, (i.e. the largest spheroids are at day 3), poses an interesting question as to the representativeness of taking the average OCR value for all of the simulations. It is therefore important to take a more in-depth look at how OCR varies against spheroid size.

3.3.7 Analysis of experimental OCR measurements

The experimental OCR values obtained from the Seahorse XF analysis (see **Table 5**) were scrutinized in more detail to determine if there was a relationship between the initial cell seeding density, or the size of the spheroids, and the OCR values. As I had analysed the OCR of spheroids for 2 separate time points, I could also look at the effect of spheroid compaction to see if this had any effect on OCR.

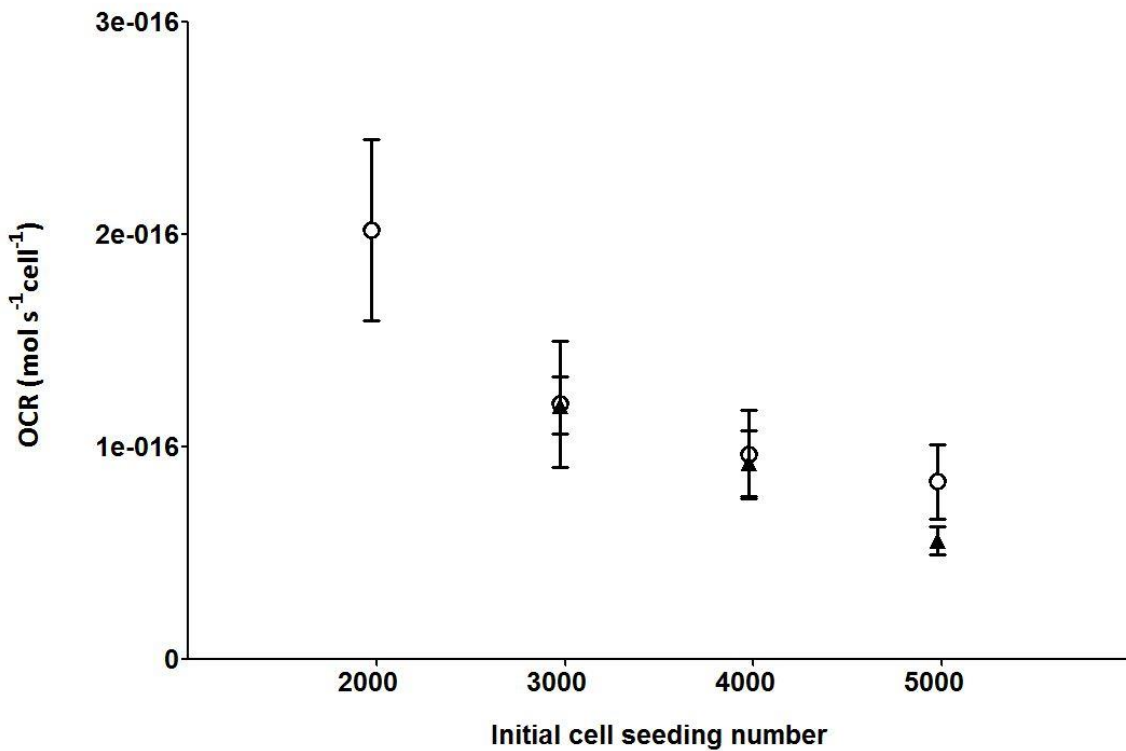


Figure 3-6 – OCR of PRH spheroids on days 7 and 11 of culture. OCR of PRH spheroids were analysed on day 7 of culture for 3000-, 4000- and 5000-cell spheroids denoted by black triangles, and for 2000-, 3000-, 4000- and 5000-cell spheroids on day 11 denoted by clear circles. OCR measurements were normalized to initial cell seeding density to provide an OCR value per cell. Results are mean \pm standard deviation (SD).

From **Figure 3-6** we can see that spheroids with smaller initial cell seeding densities seem to have an increased OCR. The OCR values from day 11 (clear circles) are slightly higher than the values for day 7 (black triangles) but there is no significant difference between the values for spheroids of the same cell number between time points. The original OCR data from **Figure 3-6** was plotted against spheroid radius to take into account the effect of spheroid compaction during the culture period (again for day 7 and day 11 time points).

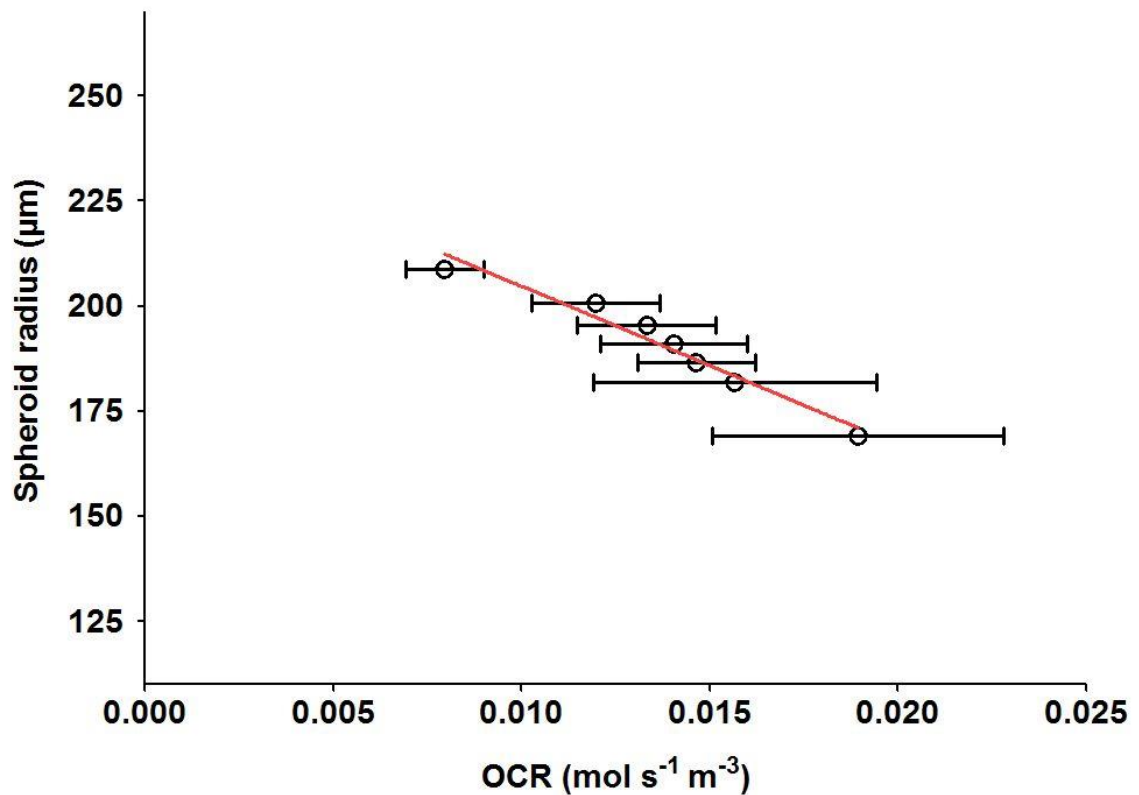


Figure 3-7 – Seahorse OCR measurements plotted against spheroid radius. Smaller spheroids have an increased OCR. The red line is from linear regression analysis ($R^2=0.93$) and represents the relationship by which subsequent OCR-radius coupled simulations were carried out. Results are mean \pm standard deviation (SD).

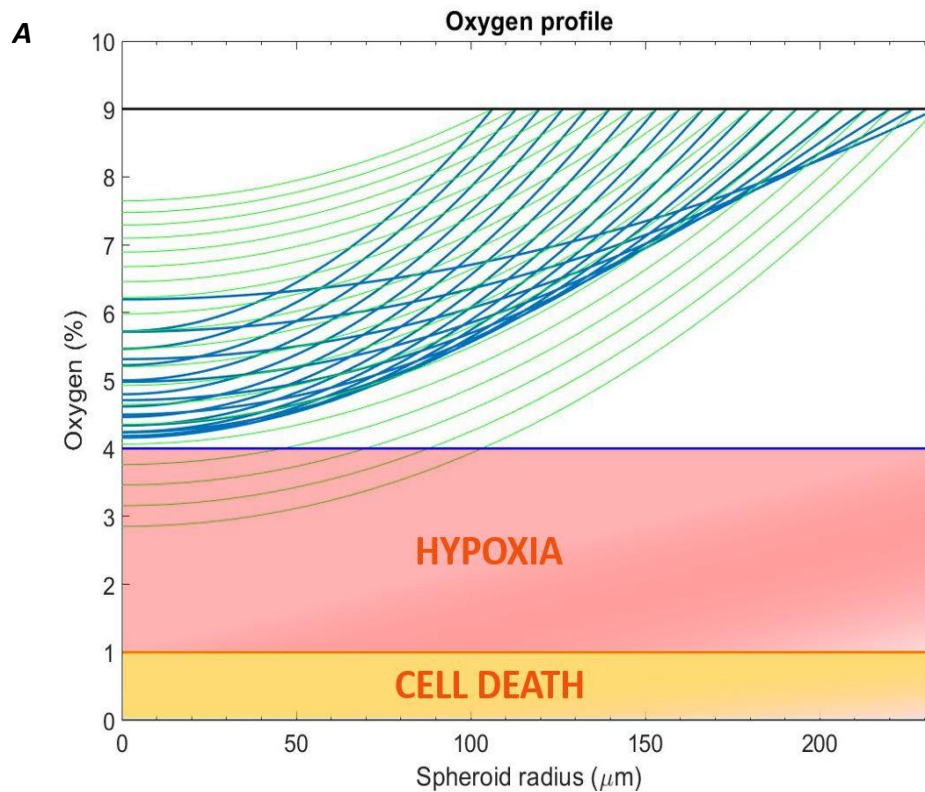
Interestingly, from **Figure 3-7** I was able to determine a definitive relationship between the experimentally-derived OCR values from the Seahorse analysis, and spheroid radius. The data shows that as spheroid radius decreases (due to compaction over the culture period), the OCR of the component cells increases. Assuming a linear relationship between OCR and spheroid radius we obtain,

$$V_{max} = 260.78 - \frac{R}{4977.5} \quad (3-25)$$

Within the mathematical model, I can now determine the OCR parameter (V_{max}) based on the relevant spheroid radius (R) according to this relationship. Therefore, instead of using the fixed average OCR value as in **Figure 3-5**, this radius-dependant OCR variable was introduced. To evaluate the effects of this relationship, the simulations corresponding to the plots in **Figure 3-5** were repeated with both the fixed average OCR ($1.26 \times 10^{-2} \text{ mol s}^{-1} \text{ m}^{-3}$), and with OCR as a radius-dependent parameter for the range of my observable spheroid radii given by equation (3-25).

3.3.8 Radially-coupled OCR simulations

Figure 3-8 (A) shows the new oxygen profiles with the radius-coupled OCR values, as indicated by the blue lines. The green lines are the same profiles as seen in **Figure 3-5**. This result suggests that the largest spheroids have higher core oxygen tensions than the smallest spheroids. We can visualise the results of these two cases more clearly by plotting the core oxygen tensions in the cases where OCR (V_{max}) is fixed at the average value versus OCR being a function of spheroid size (R).



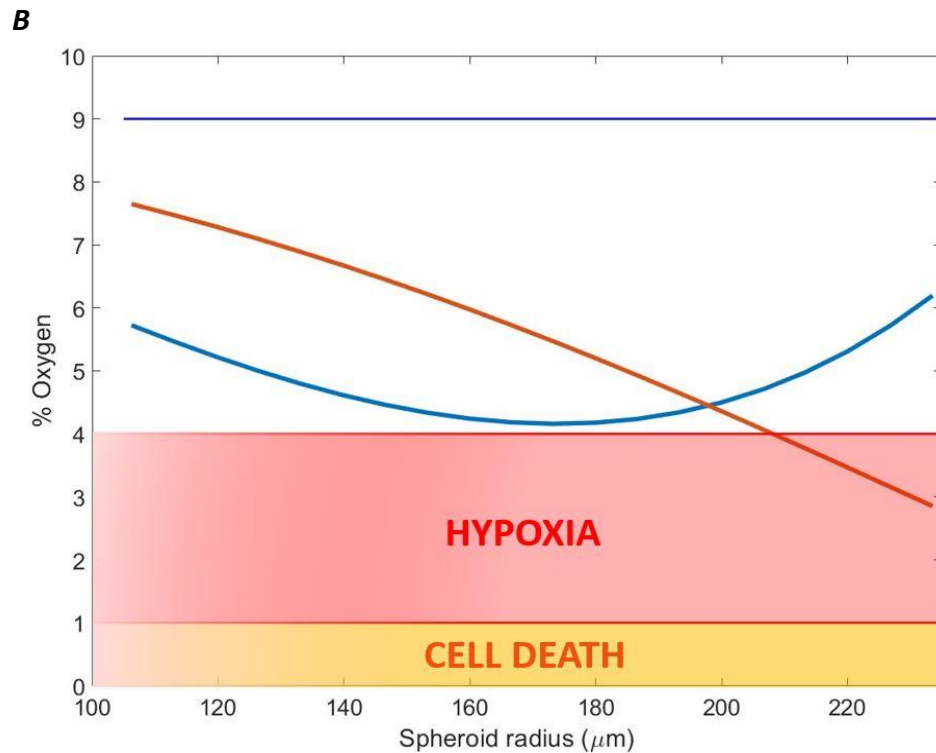


Figure 3-8 – (A) Oxygen profiles for both average experimental OCR, and spheroid-radius-dependent OCR with varying spheroid radii. (B) Boundary oxygen tensions plotted with core oxygen tensions for varying spheroid radii. The orange line shows the core oxygen tensions when I assume OCR is fixed at $1.26 \times 10^{-2} \text{ mol s}^{-1} \text{ m}^{-3}$. The blue line shows the core oxygen tensions where OCR is coupled with spheroid radius (R).

These results indicate that it is the intermediate sized PRH spheroids that most closely resemble the *in vivo* oxygen tension found within the liver sinusoid and that with OCR taken to be a function of the radius, spheroids stay devoid of necrosis. This is due to the effect of the reduction in OCR within the larger spheroids.

The main aim of my modelling efforts was to aid in the characterisation of the PRH spheroid system. The possibility of maintaining appropriate *in vivo* oxygen gradients and conditions for as long as possible would implicate the model as highly appropriate in its utility. One main limitation with the relevance of these initial simulations is the principle

Mathematical modelling of oxygen diffusion through primary rat hepatocyte spheroids

assumption that the boundary tension of oxygen at the spheroid periphery is fixed at 9%, when this may not be necessarily accurate. Within my experimental set-up, the spheroid is observed at the bottom of the well within the culture plate. Spheroids are cultured under standard conditions whereby the incubator oxygen levels are at 21%. Therefore, I can assume that there is 21% oxygen at the media-air interface. Oxygen consequently has to diffuse through 100 μl of culture media to reach the cells within the spheroid, which is referred to as the media-cell interface. Oxygen is subsequently consumed via cellular respiration. With these observations, and for my modelling efforts, it is important to discern the actual oxygen tension experienced at this media-cell interface. It may also be important to note that the physical dimensions of the spheroid in the well may impact on the oxygen tension experienced at the very bottom of the well.

3.4 Oxygen profile simulations with non-fixed boundary conditions

In order to be able to better understand the spheroid perimeter oxygen condition within the PDE model, further work is needed to ascertain the oxygen tension experienced by the cells at the media-cell interface within the experimental setup. To more accurately model the oxygen diffusion and consumption, I take into account the amount of media that is in the well (100 μl), and what effect this will have on the diffusion profile of the oxygen. This requires an extension of the mathematical model in order to more accurately determine the relevant spatial parameters of the spheroid system and the dimensions of the wells in which the spheroids are cultured. However, it is not possible to exactly model the geometries of the LOT plates due to the variability in production, therefore I have utilised the geometry of the ULA plates originally used for initial comparative characterisation work (**Figure 2-3**). I subsequently approximate the LOT well dimensions with the ULA ones. The spatial and dimensional parameters of the ULA plate wells are inferred in **Figure 3-9**.

Mathematical modelling of oxygen diffusion through primary rat hepatocyte spheroids

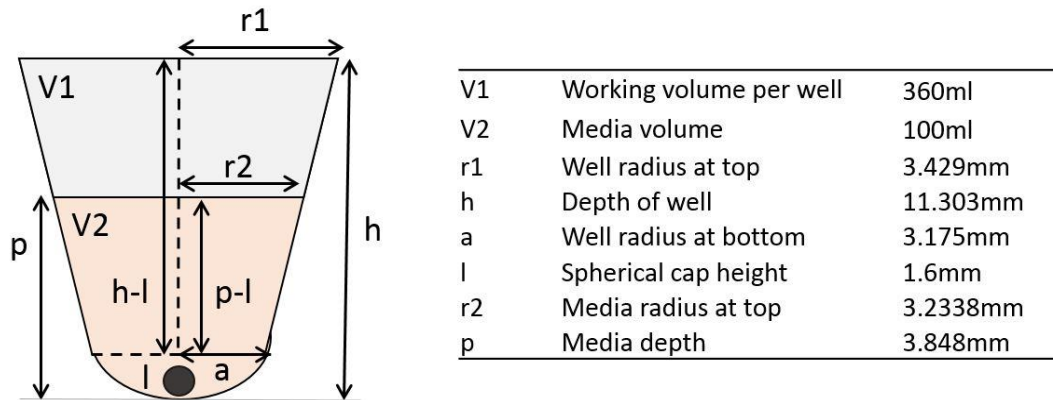


Figure 3-9 – Typical dimensions of ULA plates and volume of medium. As LOT well dimensions were not attainable, I approximate the dimensions from the ULA plates as appropriate parameters for my experimental system. The spheroids tend to sit at the very bottom of the well, and do move slightly as they are not stuck down to the substratum. Understanding the total depth of the media in the well provides relevant information regarding the distance over which oxygen must diffuse to reach the cells.

For simplicity, I retain the assumption of radial symmetry within the model, and assume that the physical liver spheroid sits within a larger sphere of media. I assume that the radius of this sphere of media is representative of the typical media depth in the ULA plate well (3.848mm).

The oxygen tension at the media-spheroid interface is unknown. However, PRH spheroids in my experiments were cultured under normal cell culture conditions where there is 21% oxygen in the incubator (i.e. the media-air interface). In order to account for this, within the model a new equation is added to account for the diffusion of oxygen in the media, namely,

$$\frac{\partial c}{\partial t} = D_2 \frac{\partial^2 c}{\partial r^2} \quad \text{where } h > r > R, \quad \text{(i.e. the media)} \quad (3-26)$$

$$\frac{\partial c}{\partial t} = D_1 \frac{\partial^2 c}{\partial r^2} - \frac{V_{max}c}{K_m + c} \quad \text{where } 0 \leq r \leq R, \quad \text{(i.e. the spheroid)} \quad (3-27)$$

where R is the spheroid radius and h is the well depth.

In order to calculate D_2 , I utilised the Stokes-Einstein equation for a spherical particle diffusing through a liquid with a low Reynold's number, which states,

$$D = \frac{K_B T}{6\pi\eta r}, \quad (3-28)$$

where K_B is the Boltzmann constant value, T is the temperature value (Kelvin), η is the viscosity of the medium, and r is the size of the diffusing particle value which was taken to be 2 Å (for oxygen). The viscosity of Williams' medium E was taken to be same as for DMEM/F12 media as described by Wang *et al.* [228]. From these parameters, the diffusion coefficient of oxygen in Williams' medium E was taken to be $1.456 \times 10^{-9} \text{ m}^2 \text{ s}^{-1}$.

The well depth was set to $3.848 \times 10^{-3} \text{ m}$ which corresponds to the total depth of 100 µm of culture media within the dimensions of the ULA plates. I vary the spheroid radius from 106.5 µm to 233.5 µm in line with the sizes observed in my experiments.

The boundary condition at $r = h$ (the media-air interface) was set to be 21% in line with my experimental culture conditions, and, for an initial simulation, a single spheroid radius of 106.5 µm (representing the smallest spheroid radius for 2000-cell initial seeding density) was used along with the appropriate OCR given by equation (3-25) (see **Figure 3-10**).

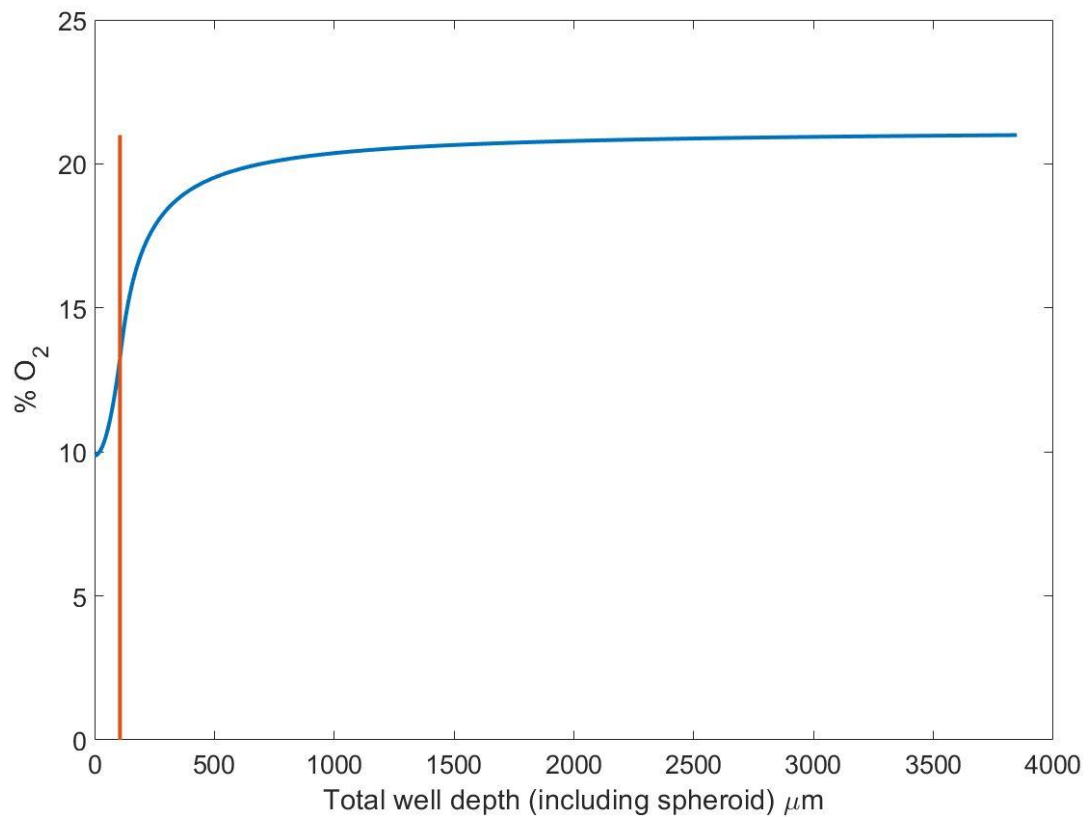


Figure 3-10 – Steady state oxygen profile for 106.5 μm spheroid utilising diffusion coefficients D_1 and D_2 and the cellular OCR term coupled with spheroid radius. The vertical orange line represents the boundary of the spheroid (R), and the media-spheroid interface. In the model, the oxygen concentration in the media is 21% initially, the same concentration as in the incubator.

In **Figure 3-10**, the blue line represents the oxygen profile, which varies over space, and the vertical orange line indicates the position of the spheroid boundary (106.5 μm). As previously stated, for $r > R$, the change in oxygen profile is driven by the diffusion of oxygen only, and for $r \leq R$ the change in the oxygen profile is driven by both the diffusion of oxygen through the spheroid and consumption of oxygen by the cells through the process of respiration. We can see from the curve that, in this case, the boundary oxygen tension for this spheroid is around 14% with a corresponding core oxygen tension

Mathematical modelling of oxygen diffusion through primary rat hepatocyte spheroids

of around 10%. The simulation was repeated for the whole range of spheroid radii observed with the initial cell seeding density of 2000 cells, with OCR (V_{max}) again given by equation (3-25) (see **Figure 3-11**).

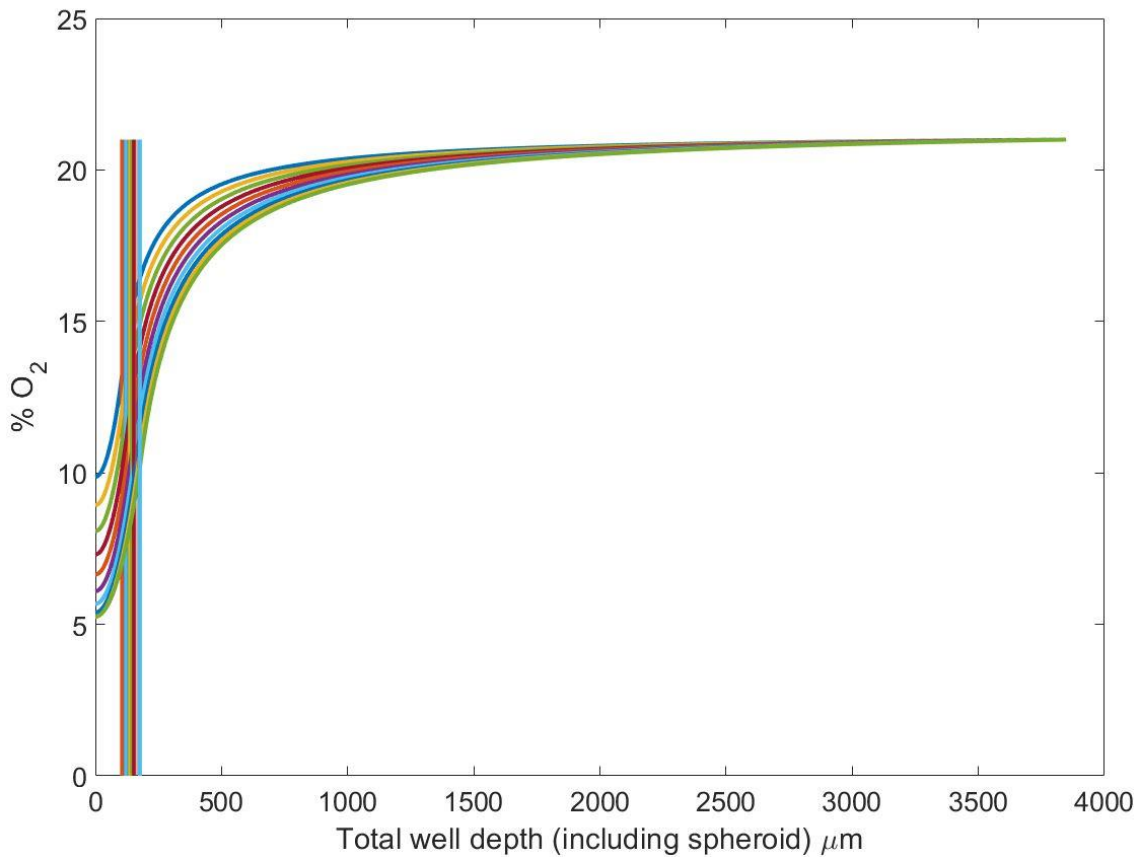


Figure 3-11 – *Oxygen profiles for spheroid radii corresponding to 2000-cell initial seeding density with OCR coupled with spheroid radius. Vertical lines represent the spheroid boundary for the range of spheroid sized observed in my experiments. Y axis values shows the end solutions corresponding with the core oxygen tensions.*

Figure 3-11 shows the oxygen profiles for all the spheroid radii observed over the culture period for spheroids with an initial seeding density of 2000 cells (i.e. 106.5 μm to 176.5 μm). The coloured vertical lines denote the respective spheroid boundaries.

As the boundary and core oxygen tensions are difficult to visualise, I present the data in a clearer format whereby I show the boundary and core oxygen tensions only, and how these values vary with regards to spheroid radius. In **Figure 3-12**, the results were plotted as boundary and core oxygen tensions for these varying spheroid radii. For completeness, I also show the results for spheroid radii corresponding with 3000-, 4000- and 5000-cell initial seeding densities in later results (see **Figure 3-13** and **Figure 3-14**).

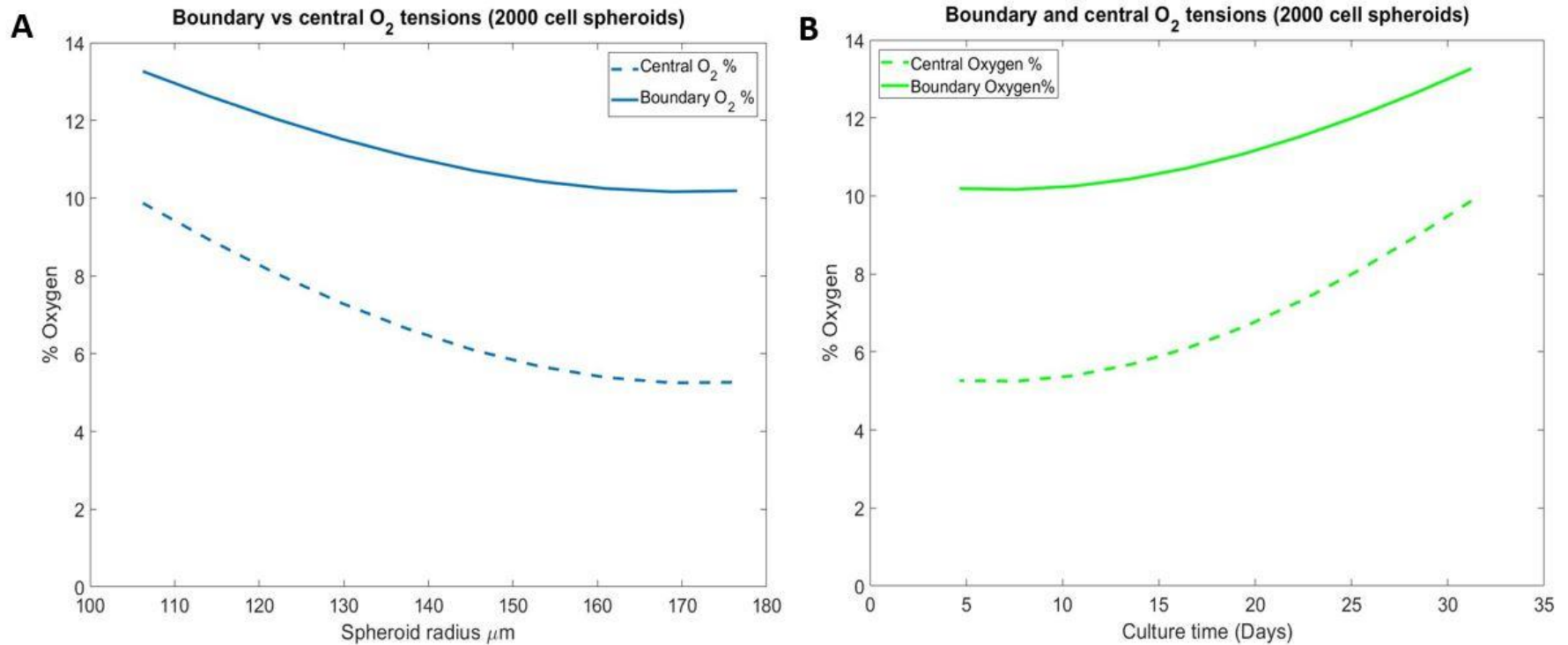


Figure 3-12- Boundary and core oxygen tensions for radii corresponding to spheroids with 2000 cell initial seeding density. Solid lines represent boundary oxygen values and the dashed lines represent the core oxygen tension. (A) shows spheroid boundary and core oxygen steady state profiles plotted against varying spheroid radii; (B) shows the equivalent oxygen profiles but this time plotted against culture time using the simple linear regression relationship shown by the straight lines in **Figure 2-4**.

Mathematical modelling of oxygen diffusion through primary rat hepatocyte spheroids

For the simulation in **Figure 3-12 (B)** the spheroid radii corresponding to the initial cell seeding density of 2000 cells were converted to time using the following relationship ($R^2 = 0.96$);

$$time = \frac{377.4 - 2R}{5.273}. \quad (3-29)$$

Figure 3-12 provides us with extremely important information regarding the oxygen profile within my *in vitro* model. When I fixed the spheroid perimeter oxygen to 9% I can predict that the PRH spheroids remain devoid of necrosis. This information can go some way to validate the observations made with the experimental characterisation, and the fact that central zones of necrosis were not observed within the experimental model.

Similarly to the 2000 cell seeding density spheroids, to assess the effect of the varying the initial cell seeding densities, 3000-, 4000- and 5000-cell spheroid radii were converted to culture time using the following relationships;

For 3000-cell spheroids ($R^2 = 0.96$),

$$time = \frac{416.6 - 2R}{5.722}. \quad (3-30)$$

For 4000-cell spheroids ($R^2 = 0.95$),

$$time = \frac{436.7 - 2R}{5.719}. \quad (3-31)$$

For 5000-cell spheroids ($R^2 = 0.97$),

$$time = \frac{473.4 - 2R}{6.788}. \quad (3-32)$$

These values are again derived from the straight lines fitted through my experimental data (see **Figure 2-4**) using the inbuilt linear regression analysis in Graphpad Prism.

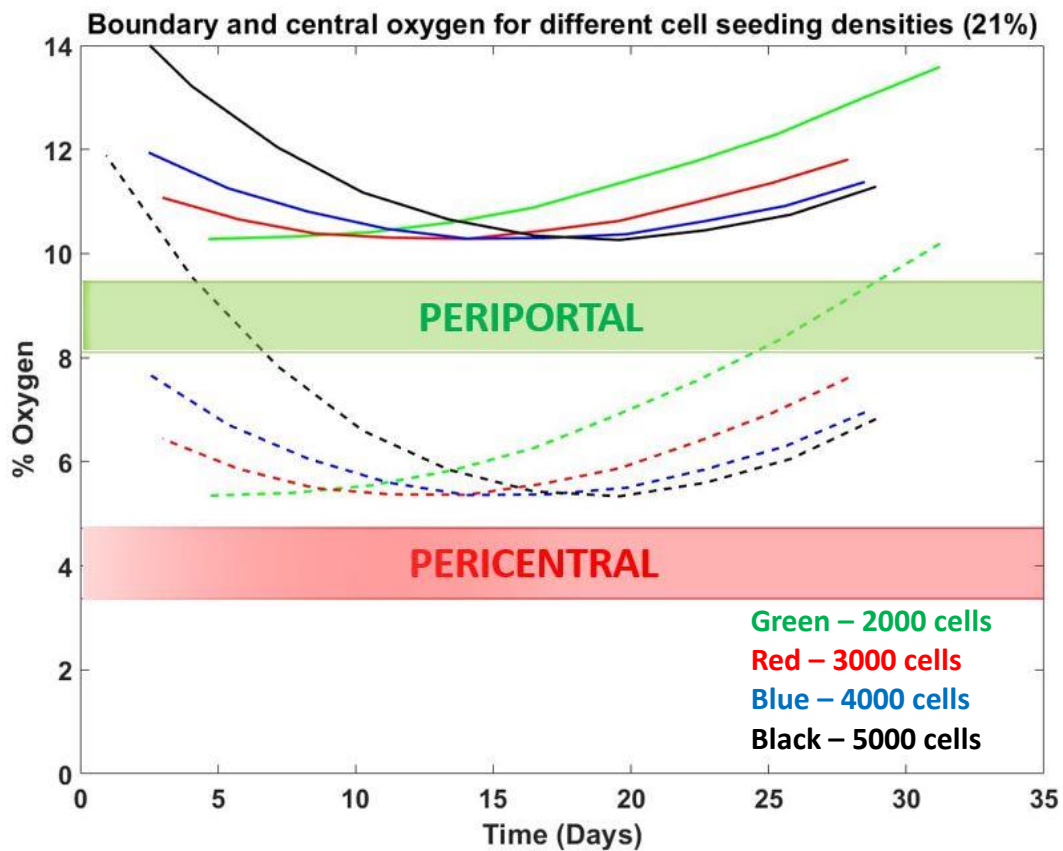


Figure 3-13 – Boundary and core oxygen tensions for 2000-, 3000-, 4000- and 5000-cell seeding densities plotted against culture time (days). Solid lines represent boundary oxygen whilst dashed lines represent core oxygen tensions.

Figure 3-13 illustrates the oxygen profiles for all of my experimental spheroids with segregated initial cell seeding densities. Periportal and pericentral oxygen tensions ranges were taken from the literature [118, 120, 221]. That is, periportal oxygen tensions have been describes as ranging from 60-70 mmHg (8.10 - 9.45%), and pericentral oxygen tensions have been reported in the range of 25-35 mmHg (3.37 - 4.72%). These simulations demonstrate a number of key points. Firstly, by incorporating the specific rat hepatocyte OCR for the cells cultured as a spheroid, the phenomenon of spheroidal contraction over time, and the conversion of the spheroid radius to culture time, I can assert that the PRH spheroids have the potential to remain devoid of necrosis for the

duration of the culture period (31 days). The formation of necrosis within *in vitro* systems can represent a major limitation to their utility, and physiological relevance to liver studies in particular. Therefore, the characterisation of a 'healthy' *in vitro* liver model would have a significant impact. From these simulations, however, we can see that the model does not capture either the desired periportal or pericentral tensions at any point during the culture period. Although I would have liked to have seen my experimental spheroid systems exhibiting core and boundary oxygen tensions within these ranges, a number of interesting questions are raised. Can I recapitulate these liver oxygen tensions by varying the concentration of oxygen within the incubator? And if so, what fixed incubator oxygen concentration is the most suitable to attain the desired *in vivo* oxygen tensions? Also, if I can continually change the external oxygen at source, can I replicate these tensions for the entirety of the culture period? Note that in my model, the incubator oxygen corresponds to the boundary condition $c(h, t) = 21\%$.

3.4.1 Oxygen profile simulations with varying incubator oxygen supply

In order to see how the external oxygen availability impacts upon the simulations and subsequent boundary and core oxygen tensions, the initial boundary oxygen concentration was reduced by 2% (from 21% to 19%), and then further reduced to 17%, and all other parameters within the model remained the same as for **Figure 3-13**. Thus, I can make a direct comparison between the original profiles where I have 21% incubator O₂, and the profiles for the spheroids in 19% and 17% O₂ within the incubator.

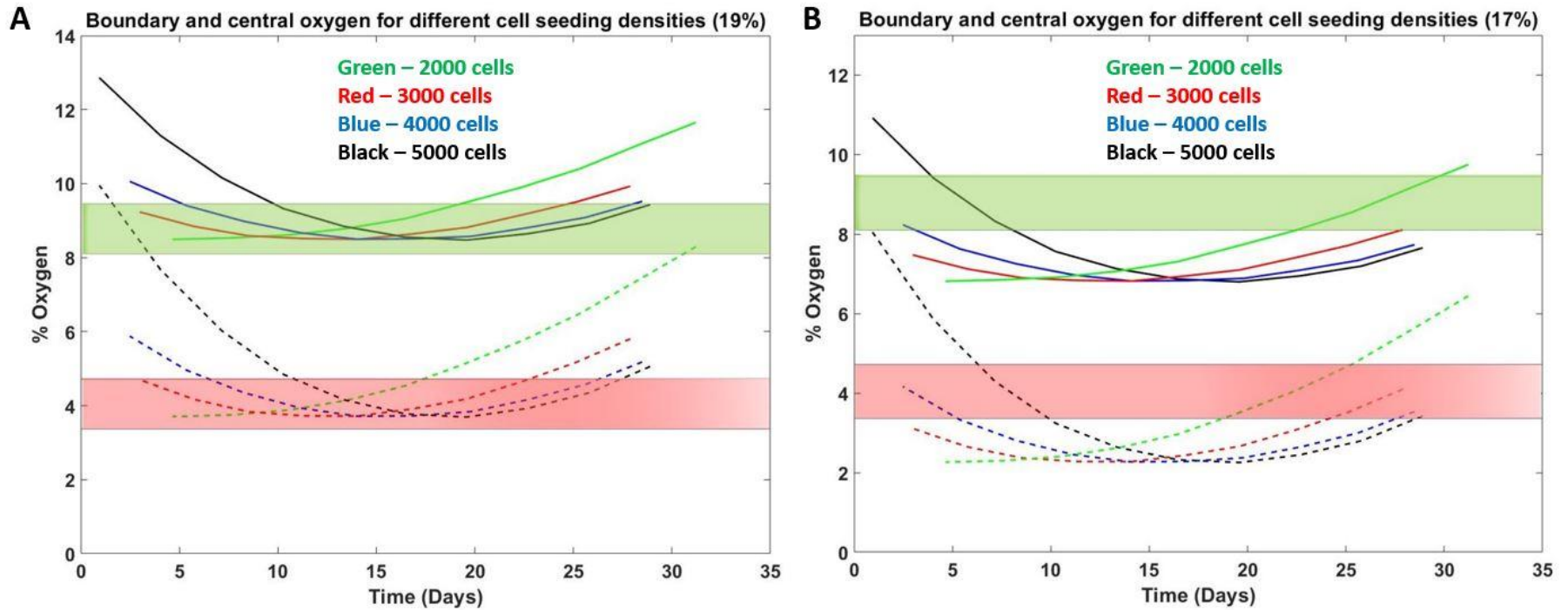


Figure 3-14 – Boundary and core oxygen profiles of spheroids (2000- to 5000-cell seeding densities) plotted against culture time (days), with (A) 19% incubator oxygen, and (B) 17% incubator oxygen. The green box represents the periportal oxygen tension ranges described in the literature and the red box represents the corresponding pericentral oxygen tension ranges. Dotted lines represent spheroid core oxygen tensions whilst solid lines represent spheroid boundary oxygen tensions.

Figure 3-14 (A) shows the profound impact that changing the incubator oxygen concentration to 19% has on the oxygen profiles of the spheroids. When the initial oxygen concentration was at 21%, none of the spheroids captured either the desired periportal or pericentral oxygen tensions. However, by reducing the incubator oxygen to 19% we can see that the 3000- and 4000-cell spheroids are exhibiting periportal oxygen tensions for most of the 31-day culture period as indicated by the green box (8.10-9.45%). It is interesting to note that there is a difference between the boundary and core oxygen profiles as both curves are not parallel, and thus, although the periportal oxygen tension may be achieved at this external oxygen concentration, this does not necessarily mean that the pericentral oxygen tension will also be achieved at the same time. **Figure 3-14 (B)** shows the spheroid oxygen profiles with the external oxygen set at 17%. This figure demonstrates that the periportal oxygen tensions may be achieved within the spheroids, however, spheroids may not be able to recapitulate the pericentral oxygen tensions simultaneously. This can be seen for the 2000-cell spheroids (green lines), where the boundary oxygen values are within the limits of the periportal range from approximately day 22 to day 30. However, the pericentral oxygen tension is only maintained until approximately day 25.

This has implications for the utility of the spheroid model for hepatotoxicity assessments because different xenobiotics exhibit toxicity in different ways. For example, hepatocytes within the pericentral zone of the sinusoid are susceptible to toxicity caused by APAP overdose due to enzymatic gradients along the sinusoid. Consequently, it can be implied that if these gradients are not maintained, toxicity may not be adequately represented within these models. However, when compared with other models that are currently being utilised within the battery of experimental tools for hepatotoxicity investigations, the maintenance of specific gradients, including oxygen, is often overlooked. The fact that hepatic-derived cell lines proliferate means that the subsequently derived models increase in size over time, and inevitably form areas of necrosis. Currently there is insufficient literature with regards to the effect of cellular necrosis on the functionality, gene-expression, and microarchitecture of *in vitro* 3D liver microtissues. It would be fair

to assume that areas of necrosis will have a negative influence on these functional aspects of the model, and clearly *in vitro* liver models that exhibit necrotic regions are not representative of the healthy liver *in vivo* [210].

My simulations suggest that for the PRH spheroid model, if we are able to control the external oxygen within the culture incubator, 19% external oxygen would confer the best results in terms of recapitulation of both the periportal and pericentral oxygen tensions for the longest period possible. The simulations provided by the mathematical model indicate that 2000-cell spheroids may be used for repeat-dose investigations from initial formation (day 3) to approximately day 15, whilst 5000-cell spheroids may be used from approximately day 10 to day 31 of the culture period.

3.5 Proposed optimal culture conditions for maintenance of sinusoidal oxygen gradients

Whilst this information is extremely useful for experimental applications, I now want to see if I can use the mathematical modelling to determine a specific incubator oxygen concentration that would allow the *in vitro* system to maintain the periportal and pericentral oxygen tensions for the duration of the culture period. In order to do this, I separated the boundary and core oxygen tensions for the discrete seeding densities, and examine more closely the effect of varying incubator oxygen concentrations on these levels (see **Figure 3-15**). For subsequent simulations, the mean values from the ranges of the periportal and pericentral oxygen tensions were used for fitting. The required mean periportal oxygen tension was taken to be 8.7%, whilst the mean pericentral oxygen tension was taken to be 4.05%. I want to determine the optimal incubator oxygen concentration that tolerably satisfy both the mean periportal and pericentral oxygen tensions. Simulations were initially optimised for 2000-cell spheroids.

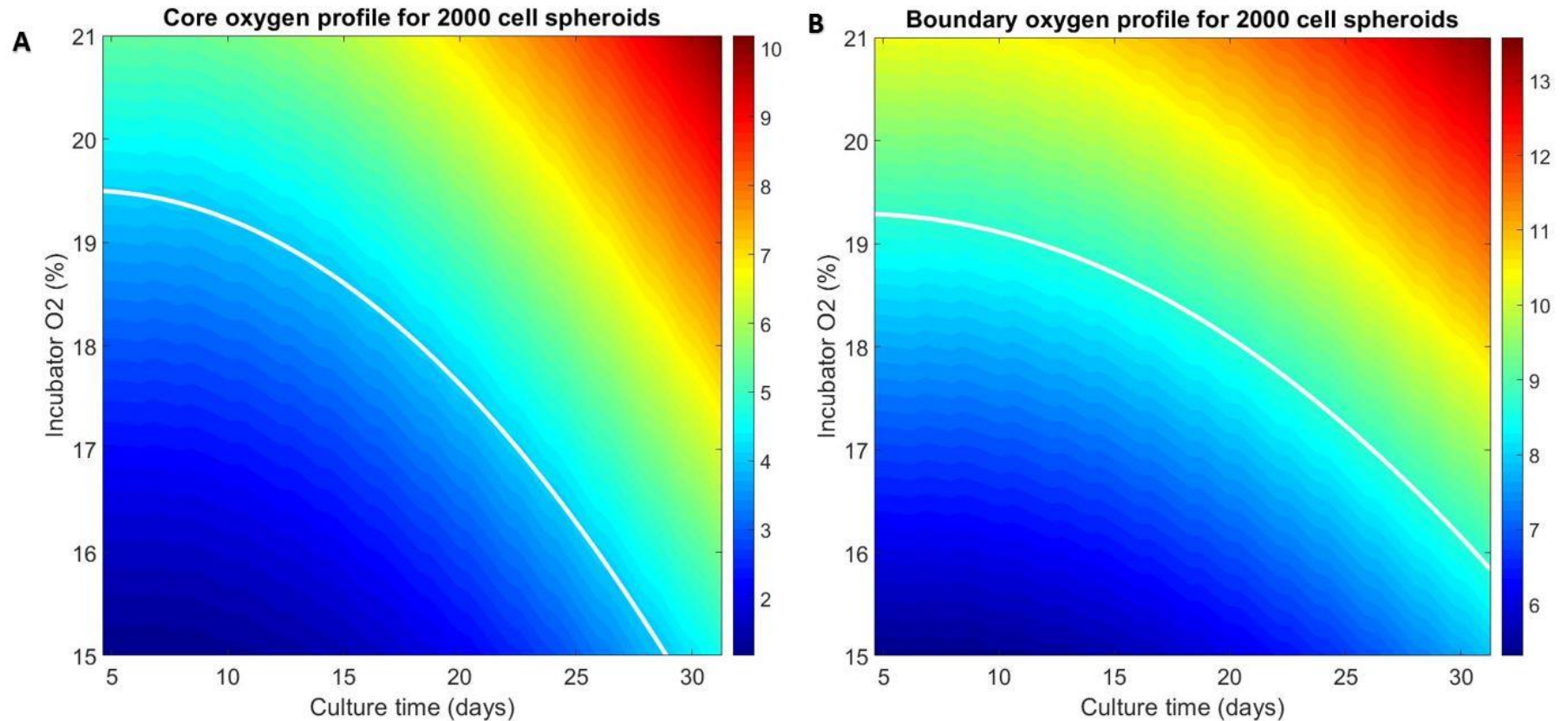


Figure 3-15 – Required incubator oxygen concentration to achieve (A) mean periportal, and (B) mean pericentral oxygen tensions. The white contour lines demonstrate this required incubator oxygen concentration. We can see that the lines are not parallel curves and therefore different oxygen concentrations are required in order to achieve the required periportal or pericentral oxygen tensions.

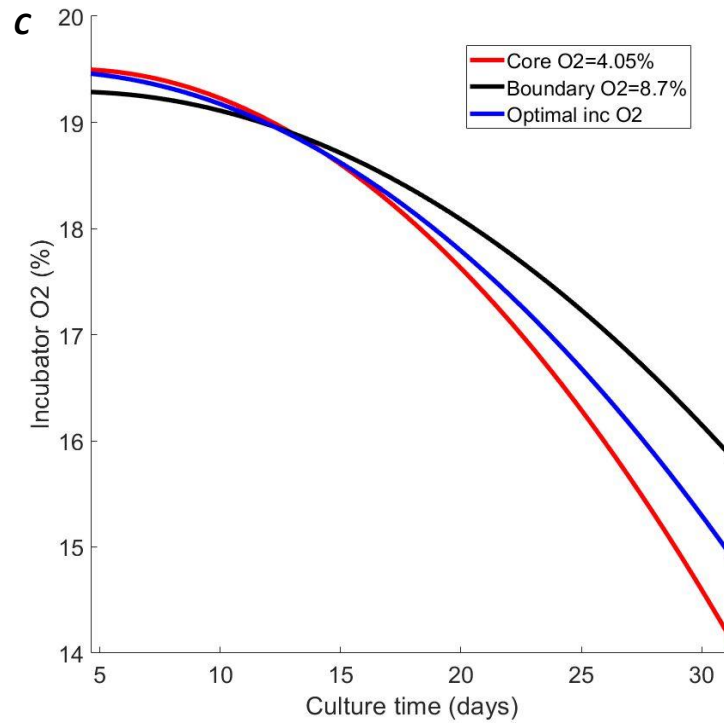


Figure 3-16 -Overlay of both core (red curve) and boundary (black curve) curves from Figure 3-15 (A) and (B) with an optimally fitted curve (blue) to capture both sinusoidal zones.

3.5.1 Normalised error function for optimisation fitting

In order to determine the optimised incubator oxygen profile to recapitulate both the required boundary and core oxygen tensions (blue line **Figure 3-16** and **Figure 3-17**), I utilised normalised error functions. Namely, the error for the simulated boundary and core oxygen tensions from **Figure 3-15 (A)** and **(B)** were calculated as,

$$Error\ Bd = \frac{(Bd - 8.7\%)^2}{Bd}, \quad (3-33)$$

$$\text{Error } Cr = \frac{(Cr - 4.05\%)^2}{Cr}, \quad (3-34)$$

where,

$$Bd \equiv bd(\text{culture time, incubator } O_2), \quad (3-35)$$

and,

$$Cr \equiv Cr(\text{culture time, incubator } O_2), \quad (3-36)$$

are the boundary and core oxygen levels given in **Figure 3-15 (B)** and **(A)** respectively.

From these calculated normalised errors I calculated the total error function,

$$\text{Total error} = \text{Error } Bd + \text{Error } Cr. \quad (3-37)$$

Figure 3-16 plots both the incubator oxygen values required to recapitulate a boundary oxygen tension of 8.7%, denoted by the contour line from **(A)**, the required external oxygen required to recapitulate a core oxygen tension of 4.05%, denoted by the contour line from **(B)**, and the optimally fitted curve to best satisfy both conditions.

The blue line in **Figure 3-17** is the optimally fitted curve and represents the minimum of this total error from the normalised error function. It is also important to note that these simulations were based on optimisation for the mean observed periportal and pericentral oxygen tensions. By nature, these two zones of the *in vivo* sinusoid have oxygen tension ranges as previously described. This implies that there may already be some acceptable error already built in to the simulation as a result of this mean fitting.

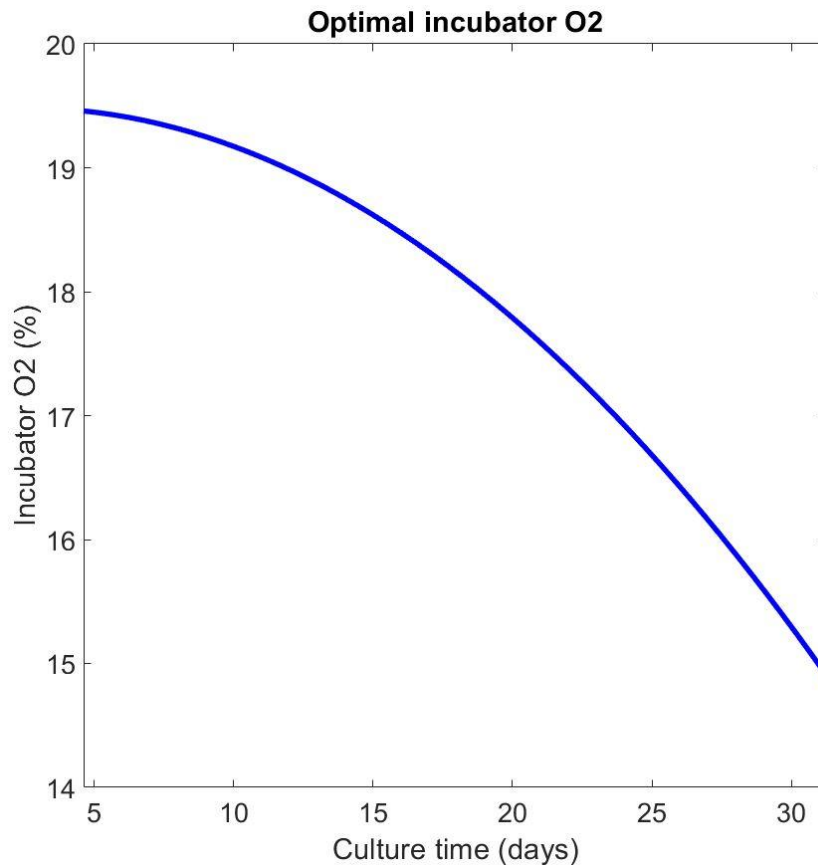


Figure 3-17 – Optimal culture operating conditions for 2000-cell spheroids to recapitulate *in vivo* periportal and pericentral oxygen tensions. The optimally fitted line demonstrates the required incubator oxygen concentration to maintain *in vivo*-like liver oxygen tensions.

The aim of this aspect of my mathematical modelling was to ascertain the optimal *in vitro* culturing conditions (i.e. incubator oxygen levels) to replicate the *in vivo* sinusoidal oxygen profiles. By further extending the model to incorporate varying external oxygen concentrations, I have now been able to discern the most appropriate operating conditions for my PRH spheroids with an initial cell seeding density of 2000 cells as given by **Figure 3-17**. This figure shows that in order to capture the required periportal and pericentral oxygen tensions, the incubator oxygen concentration needs to be reduced continually over the duration of the culture period. The initial incubator concentration

Mathematical modelling of oxygen diffusion through primary rat hepatocyte spheroids

starts at around 19.5% and by day 31 the incubator oxygen needs to be decreased to around 15%. As I have been able to mathematical model the optimised operating conditions for 2000-cell spheroids, I wanted to see if there was a difference between the cell seeding densities and how the spheroid radius-coupled OCR (V_{max}) and compaction characteristics may have affected these operating conditions. That is, the final aim of this part of the mathematical modelling was to develop optimised operating conditions for all of the cell seeding densities that I have used throughout the experimental characterisation work. Currently there is no work within the literature that has used mathematical modelling to optimise an *in vitro* liver system to recapitulate *in vivo* oxygen tensions in this way. Therefore, my aim is to provide experimentalists with appropriate operating conditions in order to achieve these desired characteristics. The premise of this kind of mathematical optimisation allows potential end users to culture PRH spheroids in different oxygen conditions depending on their application.

Mathematical modelling of oxygen diffusion through primary rat hepatocyte spheroids

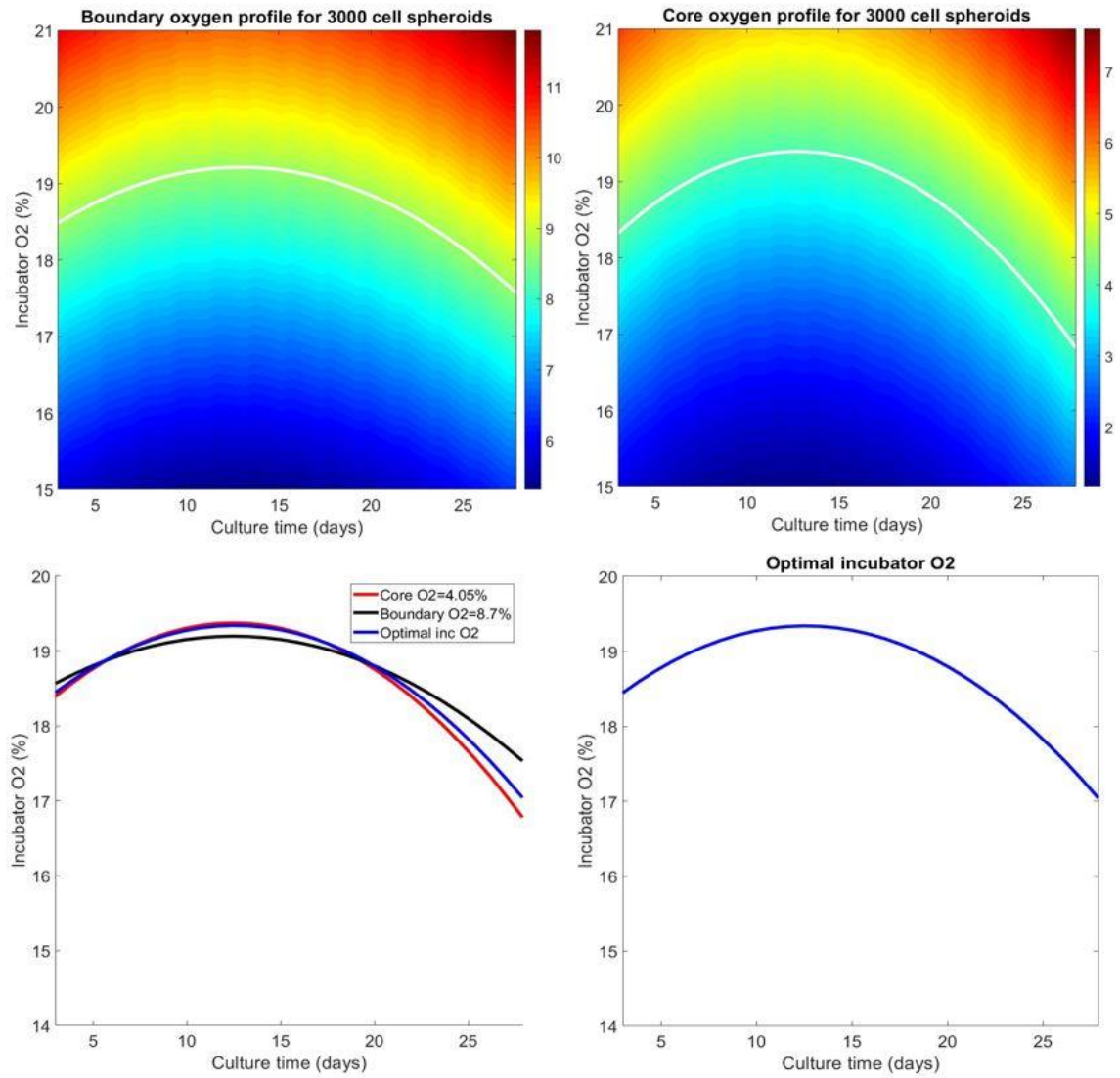


Figure 3-18 - Required external oxygen concentration to achieve (A) mean periportal, (B) mean pericentral oxygen tensions, (C) both core and boundary curves with a best fit curve for both hepatic zones and (D), the optimal operating conditions for 3000-cell spheroids over the duration of the culture period.

Mathematical modelling of oxygen diffusion through primary rat hepatocyte spheroids

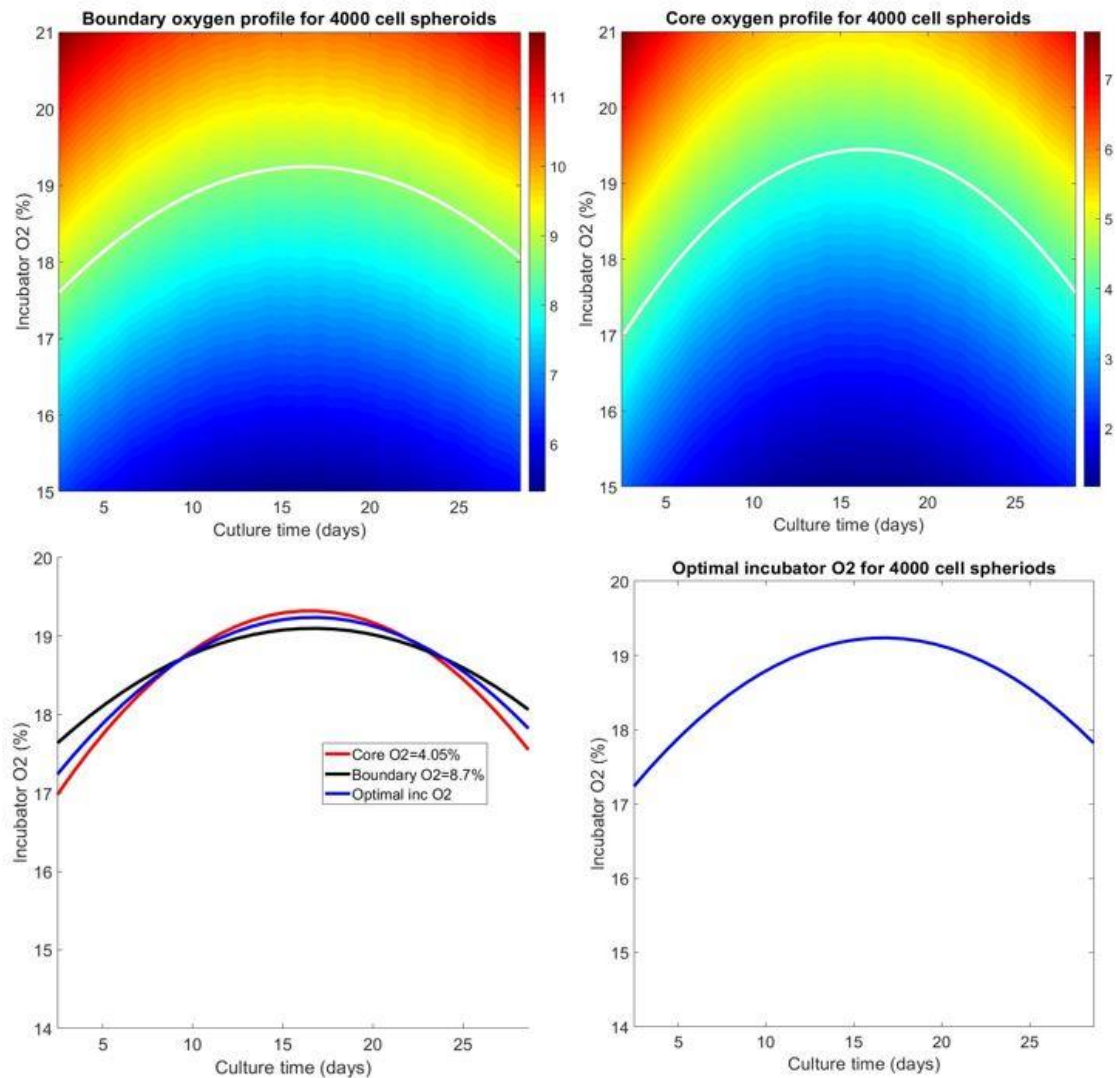


Figure 3-19 – Required external oxygen concentration to achieve (A) mean periportal, (B) mean pericentral oxygen tensions, (C) both core and boundary curves with a best fit curve for both hepatic zones and (D), the optimal operating conditions for 4000-cell spheroids over the duration of the culture period.

Mathematical modelling of oxygen diffusion through primary rat hepatocyte spheroids

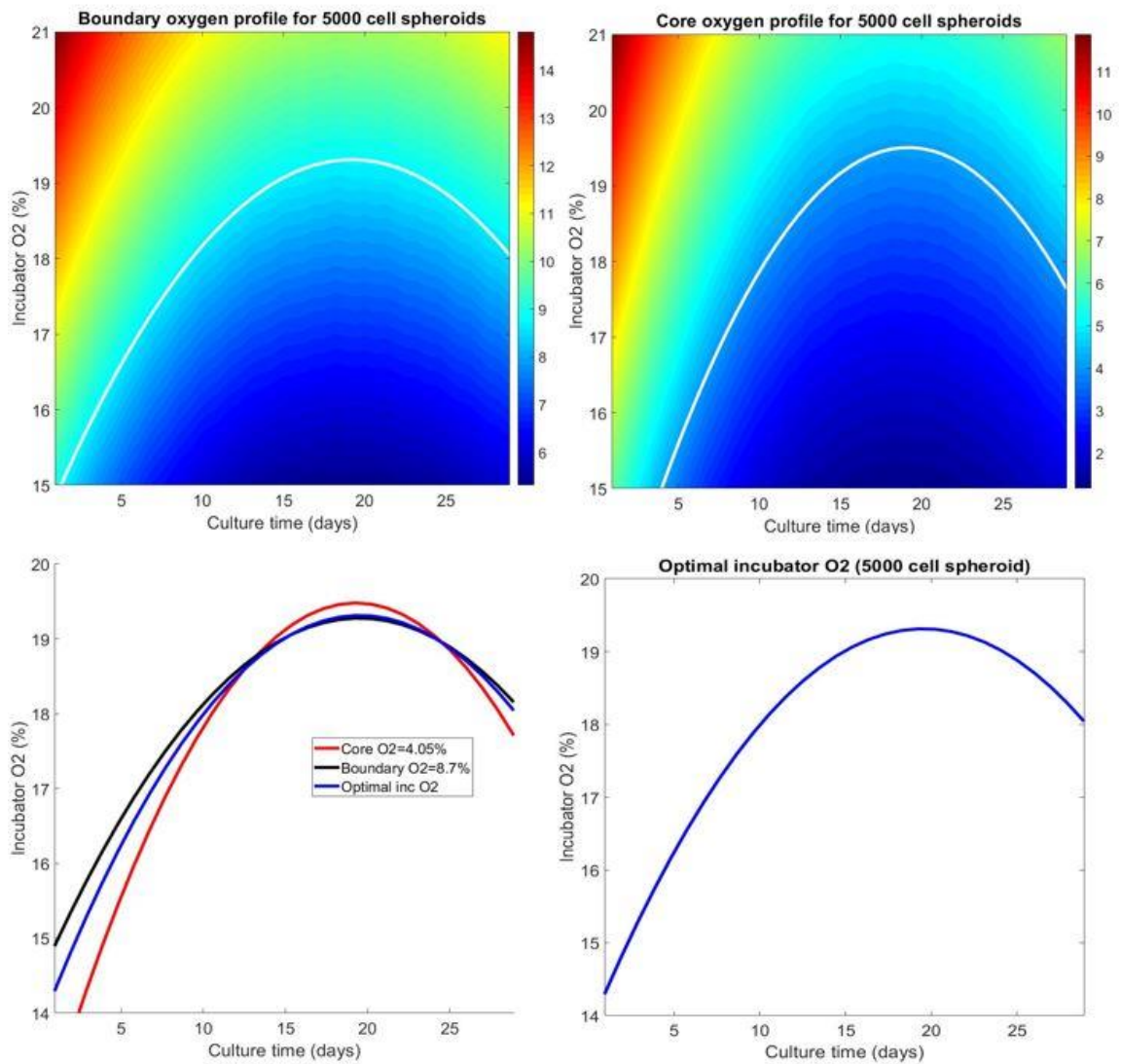


Figure 3-20 - Required external oxygen concentration to achieve (A) mean periportal, (B) mean pericentral oxygen tensions, (C) both core and boundary curves with a best fit curve for both hepatic zones and (D), the optimal operating conditions for 5000-cell spheroids over the duration of the culture period.

Figure 3-18, Figure 3-19 and **Figure 3-20**, demonstrate the external oxygen concentration regimes required to achieve recapitulation of observable *in vivo* oxygen tension for 3000-, 4000- and 5000- initial cell seeding densities respectively over the duration of the culture period. We can see from these figures that the required incubator oxygen concentrations vary dramatically depending on the initial cell seeding density. This observation is clearly influenced by the relationship between OCR (V_{max}) and spheroid radius.

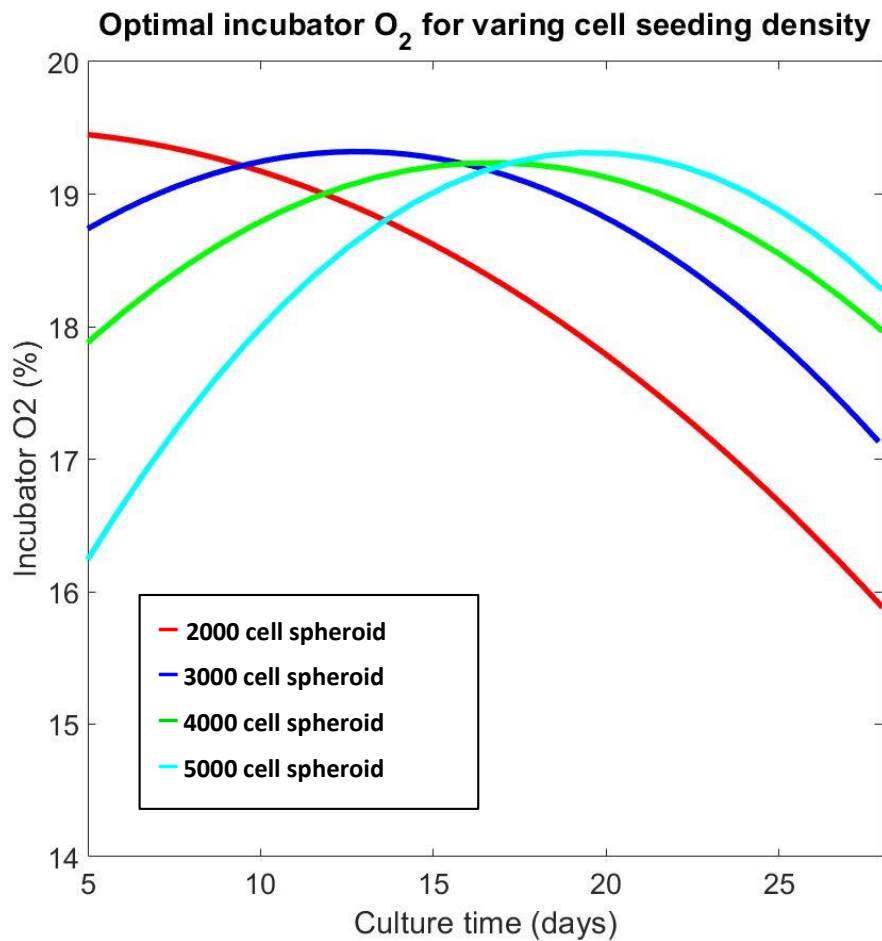


Figure 3-21 – Overlay of optimal operating conditions (the required incubator oxygen %) for all PRH cell seeding densities. The red curve represents the optimally fitted curve for 2000-cell spheroids, the blue curve is for 3000-cell spheroids, the green curve is for 4000-cell spheroids and the cyan curve is for 5000-cell spheroids.

Figure 3-21 shows all of the optimised incubator operating conditions (in terms of the % oxygen required in the incubator) needed to capture both the periportal and pericentral oxygen tension as seen *in vivo*. From these results, the 2000-cell spheroids require a continual reduction in incubator oxygen levels (%) to achieve the desired oxygen profiles, as previously discussed. 3000-cell spheroids require an initial incubator oxygen of approximately 18.7% on day 3 of culture, and then a steadily increase in % oxygen to approximately 19.5% at day 15. Finally, a gradual decrease to approximately 17% oxygen is required for the remainder of the culture period. 4000-cell spheroids require the initial oxygen levels in the incubator to be just under 18%. A gradual increase is then required to approximately 19.2% oxygen by day 17, and then a gradual reduction back to approximately 18% is required for the duration of the culture period. Interestingly, the 5000-cell spheroids require a completely different incubator oxygen profile when compared to the other seeding densities. At day 3, 5000-cell spheroids initially require approximately 16.2% oxygen inside the incubator. The oxygen needs to be gradually increased to approximately 19.3% by day 20, and finally a gradual decrease to approximately 18.5% is required for the remainder of the culture period.

3.6 Chapter discussion

The principle aim of my mathematical modelling in this chapter was to be able to optimise the *in vitro* PRH spheroid model, previously characterised experimentally in Chapter 2, to display sinusoidal oxygen gradients that are characteristic of the healthy *in vivo* liver sinusoid. The premise of modelling oxygen diffusion within spheroid models has a long history and has been investigated and published by several authors (e.g. see [229, 230]). The diffusion of oxygen into a spheroid containing oxygen-consuming cells has been investigated with results indicating that the oxygen profile can be determined by the OCR per cell and the diffusion coefficient [231]. As such, it was imperative that reliable values for each of these parameters could be identified within my own model.

There has been some recent work undertaking a similar aim. For example, a recent publication looked at the determination of oxygen gradients within HepaRG spheroids

[178]. In this paper, the authors cultured HepaRG spheroids and utilised image analysis from fluorescence staining of propidium iodide (PI) to determine the degree of necrosis within the spheroids. The cellular OCR was described by a Michaelis–Menten term and numerical values were taken from reported literature on HepG2 cells, as the specific OCR values for HepaRG cells are unknown. A principle limitation of this study is that the mathematical modelling of optimal spheroid size is based on the assumption that the HepaRG spheroids will have a similar OCR to HepG2 cells. There have been numerous studies that have demonstrated that HepaRG cells (in 2D and 3D), have improved liver-specific functionality when compared with HepG2 cells [87, 232, 233]. This improved cellular output is highly likely to have an effect on cell-specific OCR. However, this mathematical modelling approach, with analysis of fluorescent images to determine levels of necrosis throughout the spheroids, does allow for a robust investigation in terms of validating simulations against known oxygen profiles within the *in vitro* model.

In a similar way, I took cellular OCR values from the literature and observed the vast variation in these parameter values. Thus, it was vitally important to determine not only cell-specific OCR, but also experimental model-specific OCR. Utilisation of the Seahorse platform to undertake these investigations provided us with a more comprehensive understanding of the process of oxygen usage by the cells within the spheroid, and also the interesting dynamics between the consumption of oxygen and its relationship spheroid radius. For most of the previous investigations of oxygen consumption rates by spheroids, the derived consumption rates are treated as mean values. The literature has previously reported the interesting phenomenon of OCR being a function of spheroid radius [231, 234]. These previous investigations with tumour spheroids describe OCR of spheroids decreasing as the spheroid radius increases. Experimental OCR values have shown that as spheroids increase in size (radius) due to cell proliferation, the cells tend to turn over less oxygen. This relationship has been seen when normalising to spheroid radius and, in the case where necrotic cores are observed, OCR values have been normalised to viable rim size, and the data still demonstrates the same trend. However, to my knowledge, there have been no studies that have implemented this relationship

Mathematical modelling of oxygen diffusion through primary rat hepatocyte spheroids

within a mathematical model to simulate relevant oxygen profiles. Furthermore, there has been no research that use these profiles to subsequently propose optimised culture conditions in order to mimic sinusoidal-specific gradients.

Additional experimental work, similar to that of Aleksandrova *et al.* [178], would have provided further means to validate my mathematical modelling predictions. There have been numerous ways in which experimentalists have attempted to utilise image analysis to derive oxygen profiles for spheroids including the use of hypoxyprobe analysis [235, 236] and fluorescence lifetime imaging analysis [222]. This type of supplementary experimental assessment would provide an appropriate benchmark from which to compare my predictions. Although this potential future work would strengthen and potentially improve the validity of my modelling efforts, the previously undertaken histological, IHC and IF analysis does imply that my PRH spheroids produced using the LOT are devoid of necrosis.

In direct comparison with hepatic-derived cell lines (C3A, HepG2 etc.) the growth characteristics of spheroids produced from proliferative cell lines limits their utility for toxicological investigations. It is entirely probable that proliferative HepG2 and C3A cells have an increased OCR when compared with isolated primary hepatocytes, as this aspect of the cell cycle requires a much-increased turnover in ATP and thus, increased consumption of oxygen. A recent publication described the effects of octyl gallate (OG) in HepG2 cells and the intrinsic mechanisms involved [237]. They reported that treatment with OG for 24 hours inhibited HepG2 cell growth by decreasing mitochondrial activity and mass, which subsequently led to the reduction of ATP levels. This reduction in the ATP supply initiated a decrease in Ki67 protein expression (a marker of cell proliferation), leading to cell-cycle arrest [237]. From this study, it is clear that cell proliferation requires increased levels of ATP, and consequently an increased oxygen consumption demand on the cells. It is possible that hepatic-derived cell line spheroids are increasingly limited in terms of radius expansion due to the presence of these proliferating cells.

From **Figure 1-7 (B)**, we can see that there are three distinct zones within a classic tumour spheroid and it is the proliferative rim that has an increased OCR when compared with the quiescent zone [234]. This may be partly responsible for the formation of necrotic regions due to hypoxia. In my spheroid model, the isolated hepatocytes do not proliferate *ex vivo* and consequently these cells behave much more similarly to the quiescent zone of a tumour spheroid. Also, the effect of spheroidal compaction due to upregulation of ECM elements and components of the cytoskeleton leads to an overall reduction in spheroid size during culture. The size stability of these 3D microtissues may facilitate oxygenation of the spheroids over the entire culture time. However, analysis of PRH spheroid OCR shows that there is an increase in the consumption of oxygen in line with this decrease of overall spheroid size. This may be caused by an increase in the liver-specific functionality of the cells within spheroids over the duration of the culture period. It may be the case that by altering the concentration of the incubator oxygen supply, instead of capturing the normal sinusoidal oxygen tensions of a healthy liver, it may be possible to produce an *in vitro* system that is representative of various liver disease states. Although simple recapitulation of oxygen tensions seen in liver disease manifestations may not be wholly representative of a liver disease, an oxygen gradient replicating this unhealthy sinusoidal gradient will certainly affect the potential zonation of the cells and subsequent enzyme and gene expression. The normal oxygen gradient of the liver sinusoid previously described by [118, 120] plays a vital role in liver zonation. This normalised oxygen supply and subsequent sinusoidal gradient, also known as 'normoxia', results in hepatocytes displaying specific functional and structural characteristics [120, 238]. Hypoxia of the liver would describe an oxygen tension that falls below the normoxic pericentral oxygen tension (around 4%), and conversely 'hyperoxia' would describe an oxygen tension greater than that of the normoxic periportal region (around 9%). Despite the variation in oxygen tensions within the liver sinusoid for both periportal and pericentral regions, hypoxia is not observed in the normal healthy liver *in vivo* [239, 240]. Modest changes in liver oxygen tensions occur due to a number of disease manifestations, such as, infection with viral hepatitis, metabolic disorders, steatohepatitis, inflammation

and carcinogenesis [240-242]. In other studies looking at the effects of oxygen supplementation for patients with poorly functioning lungs, hyperoxia has been shown to alter mitochondrial thiol status in the liver [243].

The ability to recapitulate oxygen tensions for specific liver diseases may allow the *in vitro* model to capture required end points in order to investigate how novel xenobiotics and compounds with unknown outcomes are converted and metabolised for diseased liver models.

3.7 Conclusion

The results from my mathematical modelling show the potential to optimise *in vitro* liver models by recapitulating specific gradients as seen within the liver sinusoid. My initial aim was to establish guidance for viable spheroid size limitations based on a combined *in vitro* and *in silico* approach. In this work, I have been able to propose optimised cell culture operating conditions in order to replicate *in vivo* characteristics. The next stage of characterisation would be to now test my optimised spheroid system with known liver toxicants.

Finally, further experimental investigations, whereby I could look at controlling the external oxygen concentration at source, would provide vital validation for my modelling predictions. The use of hypoxypromes or other immunofluorescent imaging would be able to provide vital information with regards to the formation of necrosis due to hypoxia. This additional experimentation would be able to attest to the validity of the mathematical model and its subsequent utility, not only for the testing of novel xenobiotics for hepatotoxic investigations, but also its potential for recapitulating the sinusoidal oxygen tensions displayed with various forms of liver injury or disease.

The aim of this chapter was to better understand the limitations of spheroid sizes due to the effects of oxygen diffusion and consumption. I have been able to answer this question for my specific experimental model, and I have further developed the mathematical model to optimise operating conditions. The changing spatio-temporal dynamics of

Mathematical modelling of oxygen diffusion through primary rat hepatocyte spheroids

oxygen are relatively straight forward due to the fact that oxygen is a relatively small diffusing particle. I wanted to be able to understand how other molecules and solutes are transported in my experimental model, and develop a mathematical model to see how the transport of other solutes is different when compared with oxygen. As oxygen diffuses through cells and across cellular membranes, I do not need to account for diffusion barriers and other transport routes within the model. However, when considering other solutes including xenobiotics, because these particles are much larger than oxygen, it is highly likely that the cellular microenvironment will affect the ability of these solutes to be transported.

The aim of Chapter 4 is to develop a mathematical model to better understand how larger molecules are transported within my experimental spheroid system. I aim to incorporate PRH spheroid-specific parameters pertaining to features of paracellular transport (and potential barriers of diffusion) in to the model and analyse how these may impede the ability of solutes to be transported.

Chapter 4: Mathematical modelling of xenobiotic transport through hepatocyte spheroids

4.1 Biological motivation

Much of our understanding regarding the effects of xenobiotics on cells *in vitro* is based on investigations using conventional monolayer cultures, and until recently this was due to limitations of experimentation. More recent studies have utilised 3D models including spheroid systems to investigate xenobiotic effects, however, many of these 3D platforms are relatively poorly characterised [187]. Previous investigations using spheroids derived from tumour cell lines have shown promise with regards to assessing the effects of xenobiotics. These investigations have provided some insight into the potential efficacy of xenobiotics on tumours *in vivo* [231, 244, 245]. Classic tumour spheroids are characterised by three specific zones as described previously (see **Figure 1-7**). As a direct result of the 3D microenvironment, specific solute gradients exist from the boundary to the core of spheroids. Limitations in the diffusion potential of these solutes results in the formation of zones of proliferation, quiescence and necrosis within the spheroid, recapitulating the specific heterogeneity of tumours as observed *in vivo* [122, 246]. The implication that the 3D cellular microenvironment may affect the diffusive capabilities of nutrients and solutes within the spheroids also raises the same question for the ability of xenobiotics to penetrate into the entirety of the microtissue. This concern regarding drug penetration in 3D microtissue models has also been noted in various studies utilising tumour spheroids [247, 248]. Additionally the extracellular space between cells is permeated by a network of cross-linked proteins which make up the ECM. This matrix provides both structural and biochemical support to the surrounding cells *in vivo* and also *in vitro*. External forces exerted on these cellular structures and proteins within the network results in cellular migration and proliferation. The ECM is also continually remodelled by cells within the tissue, as multiple cell signals result in the production of matrix-degrading enzymes, whilst other signals result in the formation of new filaments [249]. These physical phenomena, and the continuous motile characteristics of cells and other constituent cellular elements within tissues (both *in vivo* and *in vitro*) makes mathematical modelling approaches to describe these characteristics difficult.

Mathematical modelling of xenobiotic transport through hepatocyte spheroids

3D cell culture has been generally described as superior to 2D monolayer cell culture with respect to physiological relevance [250]. Specifically, 3D *in vitro* liver models are increasingly being acknowledged as an advanced platform for hepatotoxicity assessments due to the preservation of *in vivo* characteristics and liver-specific functionality [7]. Cells cultured in a 2D conformation are exposed to a nutrient-rich environment in which all cells experience the same oxygen tension and a homogenous amount of nutrients and growth factors from the medium during growth [250]. Waste products from these cells are also freely expelled into the culture medium. This cellular situation is certainly not representative of the *in vivo* situation. 2D cell cultures have previously been useful in determining drug action kinetics, and more recently at developing our understanding of chemical processes and kinetics of drug action at the single cell level [251]. However, the limitations of 2D cell culture systems have moved the research into exploring whether 3D cell culture platforms can provide more accurate *in vitro* tools that can bridge the gap between *in vitro* and *in vivo*.

There have been numerous publications that demonstrate that spheroids display increased resistance to a number of xenobiotics when compared with monolayer cultures [250, 252]. This increased resistance to xenobiotics displayed by spheroid cultures is likely to be a result of the complex 3D microenvironment, including upregulated ECM and cytoskeletal components. The inherent physicochemical properties of xenobiotics may also affect the ability of specific compounds to penetrate the cultures effectively, as compounds with a higher propensity to adhere to cells may have increased binding affinity with the peripheral cells of the spheroid [189].

Previously described mathematical models for drug penetration into tumours have provided insightful information in predicting therapeutic efficacy [253, 254]. The majority of research in this specific area has involved the modelling of cancer therapeutic drugs [187, 194, 255]. Mathematical modelling of transport properties in spheroid systems has described the delivery and movement of macromolecules in tumours, with most publications implicating the assumption of radial symmetry in order to facilitate

the modelling efforts [256]. A key conclusion from these previous works has been the demonstration of micro-architectural diffusional impediments to these molecules. However, relatively few investigations have attempted to model the penetration of larger molecules including nanoparticles and other xenobiotics. As these relatively smaller macromolecules have transport limitations within 3D microenvironments, it is clear that this effect may be more prominent for larger compounds.

One notable publication that has implemented experimentally derived spheroid-specific (tumour) parameters into a mathematical diffusion model is that of Goodman *et al.* [245]. This publication provides a useful insight into the diffusion, penetration and transport properties of nanoparticles in a 3D spheroid system. The model parameterises spatial features in the spheroid microarchitecture including, the volume fraction of the accessible routes for paracellular diffusion, and the changing tortuosity of these routes with respect to spheroid radius. Other parameters, such as nanoparticle binding and accessible volume fraction were determined experimentally. This combined experimental and mathematical modelling approach has improved our understanding of the efficiency of nanoparticle delivery, and the effect of tumour architecture on nanoparticle transport.

4.1.1 Background on porous media modelling

Previously published models of porous media transport provide a useful basis for the derivation of a new mathematical framework for modelling paracellular solute transport. In general terms, porous media refers to a material or biomaterial that contains voids that are subsequently filled with a fluid. A porous medium is most often characterised by its porosity, which is defined as the fraction of the volume of pores over the total volume of the medium. For example, such porosity calculations for the *in vivo* liver have been explored by Bonfiglio *et al.* [257] and Siggers *et al.* [258]. Porous media may also be characterised by other features such as permeability, tensile strength etc. However, a key feature for my *in silico* modelling is tortuosity i.e. the directness of the paracellular path.

Tortuosity can be defined as the ratio of the length of the curved path to the Euclidian distance between the two ends of the path.

Tortuosity has been utilised and described in far more detail with regards to chemical engineering [259] and in the field of medicine [260]. However, there have been some publications regarding the liver that utilise this parameter. Izadifar *et al.* [261] described a mechanistic modelling approach for drug elimination by the liver where the porosity, tortuosity and physicochemical properties were derived to describe the transient drug transfer and elimination across the liver following intravenous (IV) dosing. I want to be able to apply this method, and adapt it to investigate the transport and uptake of various molecules and xenobiotics in my experimental PRH spheroid model.

My initial modelling will investigate the diffusivity of xenobiotics, of varying sizes and physicochemical properties, to determine whether or not they will penetrate the entirety of the spheroid. I will also analyse the heterogeneous microarchitecture of the experimental system and translate these physical properties into the model.

4.1.2 Aims of mathematical modelling of solute diffusion in PRH spheroids

The main aim of my mathematical modelling approach is to better understand the implications of the liver microtissue cellular microarchitecture on the diffusion of xenobiotics of varying sizes with different physicochemical properties. In particular, I aim to gain a more comprehensive understanding of how different compounds are transported into the 3D microtissue liver models.

The experimental work in Chapter 2 has demonstrated the in-depth functional characterisation of my *in vitro* system and the mathematical modelling in Chapter 3 has provided prospective operating conditions for the recapitulation of *in vivo* oxygen gradients. The next step is to develop our understanding of how larger solutes (e.g. xenobiotics) are transported into the spheroid system, and how the microarchitecture of the spheroids impacts on the transport profiles of these molecules. I propose a mathematical model, based on porous media modelling, to investigate xenobiotic

Mathematical modelling of xenobiotic transport through hepatocyte spheroids

penetration into PRH spheroids. This model incorporates experimentally derived parameters for radially dependent changes in spheroid microarchitecture, as represented by the volume fraction of paracellular space available for transport, and the tortuosity of the paracellular paths. These changes in microarchitecture have been correlated with my experimental spheroid growth characteristics to provide an *in silico* model that closely resembles my *in vitro* model.

4.2 Porous media modelling equations

The mathematical equations I use for porous media modelling are derived from Fick's law and the previously identified Laplacian symmetry equations. The principle equations were derived in previous work by Goodman *et al.* [245], namely;

$$\frac{\partial c}{\partial t} = \frac{1}{r^2} \frac{\partial}{\partial r} \left[D \epsilon r^2 \frac{\partial}{\partial r} \left(\frac{c}{\epsilon} \right) \right] - k_u \frac{c}{\epsilon}. \quad (4-1)$$

Where r is the radial coordinate ($r = 0$ is the centre of the spheroid and $r = R$ is the outer spheroid boundary), t is time, ϵ is the volumetric porosity of the spheroid (the volume fraction of paracellular space), c is the molar concentration of xenobiotic (e.g. mol/m³), c/ϵ is the concentration of the xenobiotic in the accessible paracellular volume, k_u is the passive diffusion rate of the xenobiotic into the cells, and, D is the effective diffusion coefficient of the xenobiotic in the spheroid.

In Goodman *et al.* [245] the effective diffusion coefficient is expressed by the following equation;

$$D = D_0 \frac{L(\lambda)}{\tau(\epsilon)}, D_0 = \frac{k_B T}{6\pi\mu\alpha}, \quad (4-2)$$

$$L(\lambda) = (1 - \lambda)^2 * (1 - 2.1044\lambda + 2.089\lambda^3 - 0.948\lambda^5),$$

$$\lambda = \frac{\alpha}{r_p}, \quad \tau(\epsilon) = \frac{1}{1 - \frac{2}{3}(1 + \epsilon)(1 - \epsilon)^{\frac{2}{3}}}. \quad (4-3)$$

Where D_0 is the diffusion coefficient of the xenobiotic in the liquid medium, $L(\lambda)$ is a factor responsible for hydrodynamic and steric reduction of the diffusion coefficient in the pore due to the size of the xenobiotic (α) and that of the pore (r_p), λ is the ratio of the particle size to pore radius, $\tau(\epsilon)$ is the tortuosity of the paracellular paths, k_B is Boltzmann's constant, T is the absolute temperature (in Kelvin), μ is the viscosity of the

liquid medium, α is the radius of the diffusing xenobiotic, and r_p is the radius of the paracellular pores within the spheroid. The equations for $L(\lambda)$ and $\tau(\epsilon)$ have been empirically defined by Saltzman [262], whereby transport rates of particles have been examined in multiple tissues. These equations are based on the idea that a spherical particle travels along the centre line of a cylindrical tube. Equation (4-3) describes how $L(\lambda)$ is a decreasing function of λ , and that the tortuosity, $\tau(\epsilon)$, is a function of the volumetric porosity, ϵ (see **Figure 4-2**).

4.3 Model parameterisation

In the initial model by Goodman and colleagues, a number of the key variables, including volumetric porosity and pore radius, were determined via the use of brightfield microscopy image analysis (e.g. see **Figure 4-1**). In this example, spheroids are produced from monodispersed cells (FaDu human hypopharyngeal carcinoma cells) where they form into a 3D microtissue via self-reaggregation. FaDu spheroids were produced utilising the LOT as previously described (**2.2.1** and **2.2.3**). Spheroids were washed in PBS, fixed for 1 hour in 4% paraformaldehyde (PFA) and embedded in 2% agarose (low EEO) in 4% PFA before being subjected to routine histological processing and finally resin embedded. 5 μ m sections were cut using a Leica RM2235 microtome (Leica microsystems) and stained with toluidine blue. These spheroids contain clear paracellular spaces that can be easily identified and dimensions quantified. FaDu spheroids were chosen for comparison with PRH spheroids as both microtissue models were produced utilising the same culture technique. This allows for direct comparison of cellular organisation between the proliferative tumour cell line and the non-proliferative PRH cells as all other culture and microtissue processing protocols were equivalent.

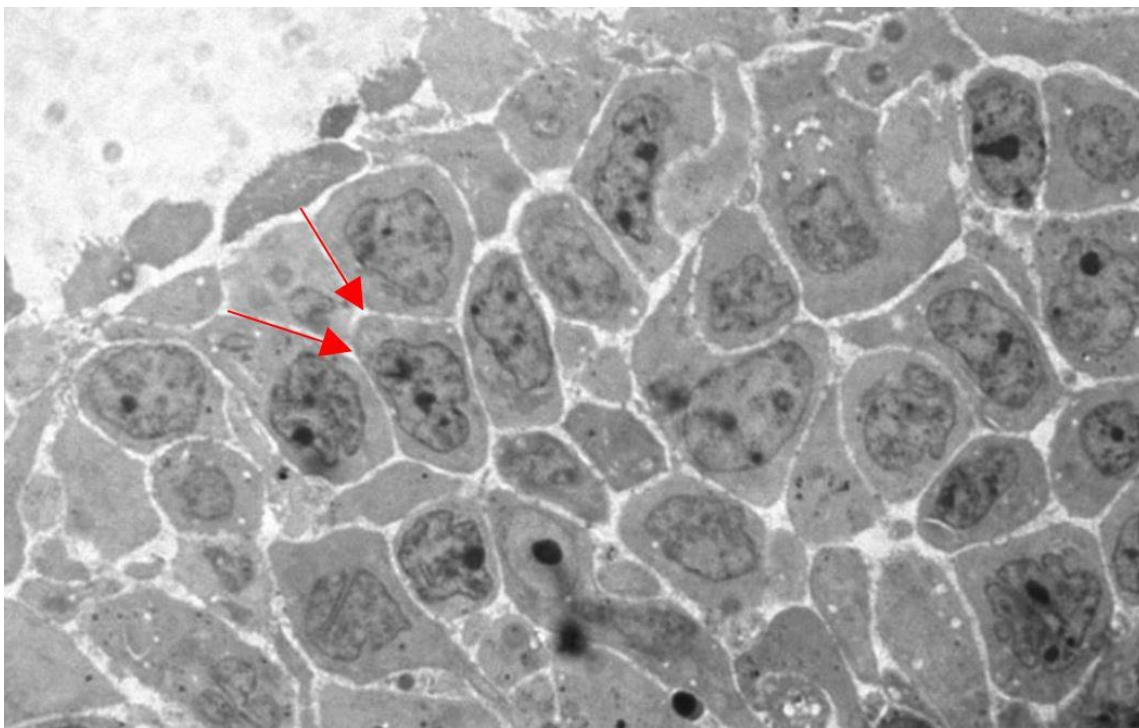


Figure 4-1 – A brightfield microscopy image of the edge of a fixed, stained section of a **FaDu spheroid slice (5 μm) imaged at 100x magnification**. Pores between cells show up as unstained areas in the microscope image and were measured with MetaMorph software to obtain an estimate of pore size. Dark black staining shows cell nuclei.

Goodman *et al.* [245] used these types of images (**Figure 4-1**) to calculate the volumetric porosity (ε), and the pore radius (r_p) (for graphical representation of ε and r_p see **Figure 4-2**).

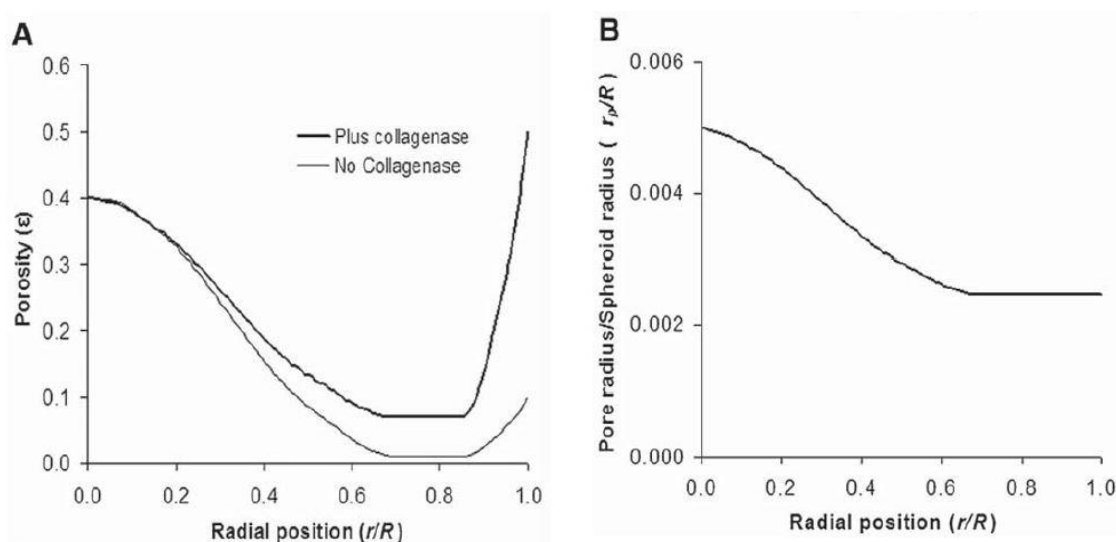


Figure 4-2 – (A) shows the porosity, ε , based on structural measurements of spheroid sections, as a function of the scaled radial position (where 0 is the centre of the spheroid, and 1 is the spheroid boundary). (B) shows the ratio of pore size, r_p , to spheroid radius, R , as a function of scaled radial position [245].

For my PRH spheroids, the analysis of brightfield microscopy images of toluidine blue stained slices was ineffectual for determining these parameters. This was due to the much higher levels of ECM and cytoskeletal components within the PRH spheroids when compared to tumour spheroids. Standard cellular staining and image analysis could not elucidate the distinct paracellular spaces (as seen for the FaDu cell spheroids **Figure 4-1**), and similarly I was unable to determine the size of the pores or the tortuosity from the initial image analysis.

Figure 4-3 demonstrates the tight cell-cell interactions within the spheroid and the presence of large amounts of ECM.

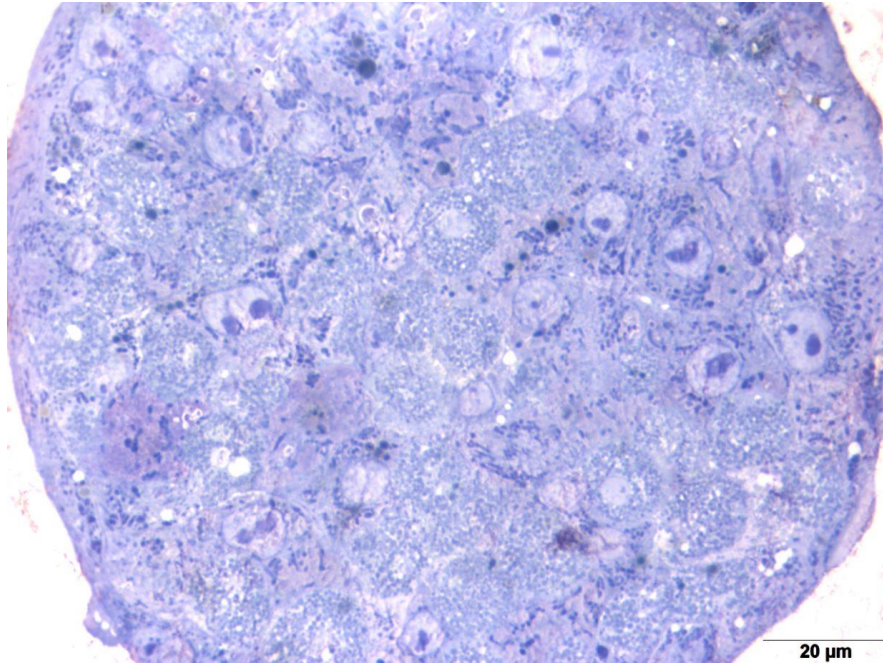


Figure 4-3 – 5 μm slice of a PRH spheroid stained with toluidine blue, demonstrating that paracellular spaces are not visible under this magnification using brightfield microscopy. Scale bar = 20 μm.

Therefore, the first parameter that I need to obtain is the size of the paracellular spaces between the cells (r_p). In order to calculate this I utilise transition electron microscopy (TEM) images and ImageJ analysis from the experimental characterisation in Chapter 2 (see 2.2.7).

Figure 2-14 (B) shows the paracellular space between two adjacent hepatocytes. By magnifying the image, analysing the width of the space between the cells and comparing this to the known scale bar size, the average width of the paracellular spaces was determined. There were slight variations in the size of the paracellular pores but for my subsequent mathematical modelling I assume the average pore size for the entire spheroid. The average pore size (r_p) from this analysis was taken to be 0.05 μm .

Having determined the average size of the pores within the experimental model, I now want to calculate values for the volumetric porosity. In essence, this refers to the proportion of the spheroid that is composed of paracellular space. From my initial characterisation work in Chapter 2, brightfield images and histological analysis demonstrates spheroid compaction over the duration of the culture period and also cellular stratification on the periphery of the spheroid. I want to be able to assess what impact these changes may have on the diffusion and transport of xenobiotics, by quantifying how these observed variations impact on the values of volumetric porosity, and over the duration of the culture period.

In order to determine the volumetric porosity I need to be able to visualise the paracellular spaces for the entire spheroid. Clearly, using TEM images to assess this is inappropriate due to the size of the spheroids relative to the scale of the TEM images, therefore I implement the use of a novel mathematical modelling approach in order to determine this parameter.

One such method that may facilitate the derivation of the volumetric porosity (ε) parameter has been described in the literature, and is referred to as Voronoi tessellation (VT). VT is a mathematical description where cells within a tissue are regarded as tiles

tessellating space. This mathematical description is commonly used for estimating the morphology of cells in epithelial tissues [263] and, as hepatocytes are essentially specialised epithelial cells, the implementation of this mathematical technique to provide morphological estimates for PRH spheroid models seems appropriate. An example of the use of VT to define cellular morphologies was done in 1978 by Honda *et al.* [264], which describes cellular morphologies by Dirichlet domains (convex polygons) which cover a plane without leaving any gaps or overlaps. These Dirichlet domains were shown to accurately describe cellular patterns including monolayer cells, and epithelial cells in tissue.

4.3.1 Voronoi tessellation

VT will be implemented to determine the boundary of cells within my spheroids. A key constituent element to a VT is a set of discrete points around which the VT is organised. In my work, this set of points will be described by the individual cell nuclei. The theory of VT as applied to this problem is as follows.

I suppose there are n cell nuclei p_1, \dots, p_n . Modelling the slice of our spheroid as a planar region, p_1, \dots, p_n are given as points in the \mathbb{R}^2 plane. This set of cell nuclei is then defined by,

$$P = \{p_1, \dots, p_n\} \text{ is a set in } \mathbb{R}^2. \quad (4-4)$$

For point p_i , I associate its Voronoi region $V(p_i)$ where;

$$V(p_i) = \{q \in \mathbb{R}^2: |q - p_i| \leq |q - p_j|, \forall j \leq n\}. \quad (4-5)$$

The region $V(p_i)$ is therefore the intersection of $n - 1$ half-spaces. This half-space contains p_i and is bounded by the bisector of p_i and another point of P . For example, for $p_i, p_j \in P$, this region is bounded by the bisector of p_i and p_j , that is, the set of points which have the same distance to both p_i and p_j (see **Figure 4-4**).

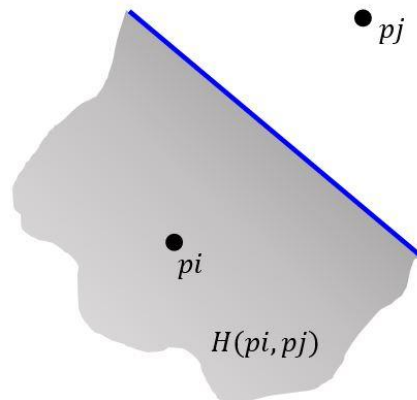


Figure 4-4 – shows a schematic illustration of p_i and p_j where these points are separated by a bisector.

$H(p_i, p_j)$ denotes the closed halfspace bounded by the bisector of p_i and p_j that contains p_i . In \mathbb{R}^2 , $H(p_i, p_j)$ is a halfplane. The Voronoi Diagram $VD(P)$ of a set $P = \{p_1 \dots p_n\}$ of points in \mathbb{R}^2 is the subdivision of the plane caused by the Voronoi cells $V(p_i)$, for $i = 1, \dots, n$.

Voronoi can also be thought of in terms of another form of computational geometry called Delaunay triangulation. The premise of the approach is that for $P = \{p_1 \dots p_n\}$ in \mathbb{R}^2 , a triangulation of these points is a collection, T , of triangles. Every set in \mathbb{R}^2 , with $n \geq 3$ points has a triangulation, unless all points in P are collinear. Using this method, Delaunay triangulation connects all points in P with straight lines. For an example, I take the simplest case where I have 3 points within the plane (see **Figure 4-5**).

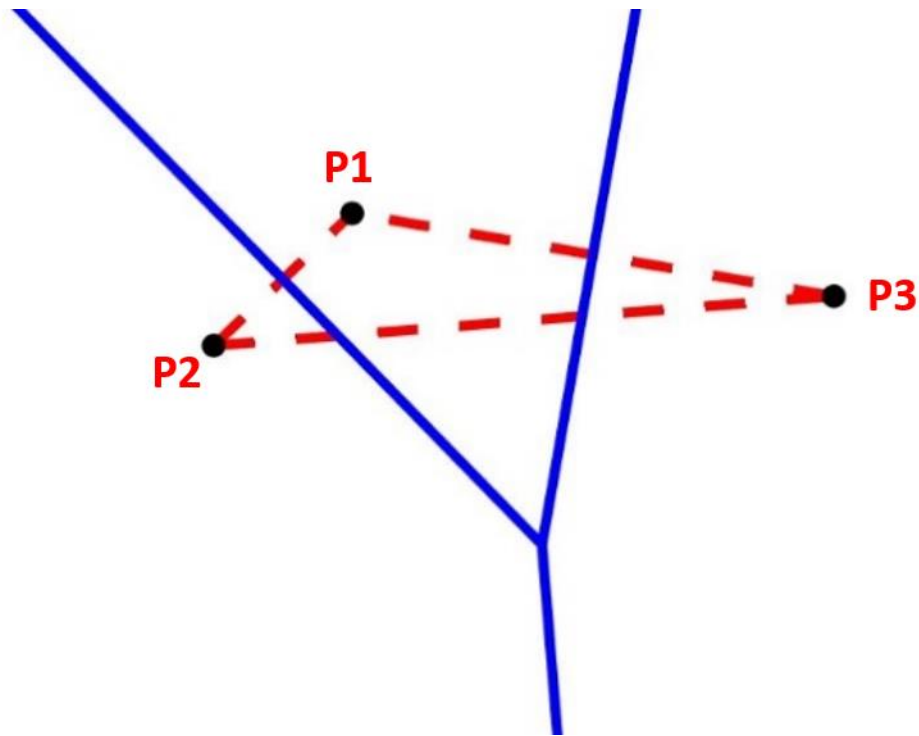


Figure 4-5 – Voronoi diagram and Delaunay triangulation of 3 discrete points (P1, P2 and P3). The blue lines describe the boundaries of the Voronoi cells which are bisectors of the Delaunay triangulation shown by the red dashed lines.

Figure 4-5 demonstrates the simplest example of Voronoi diagram with accompanying Delaunay triangulation. The dashed red line shows the Delaunay triangulation of these points, where all the points are simply connected with each other. The blue lines show the bisectors between the points which converge towards each other to produce the Voronoi cells. For illustrative purposes **Figure 4-6** shows the effect of increasing the number of points within the plane.

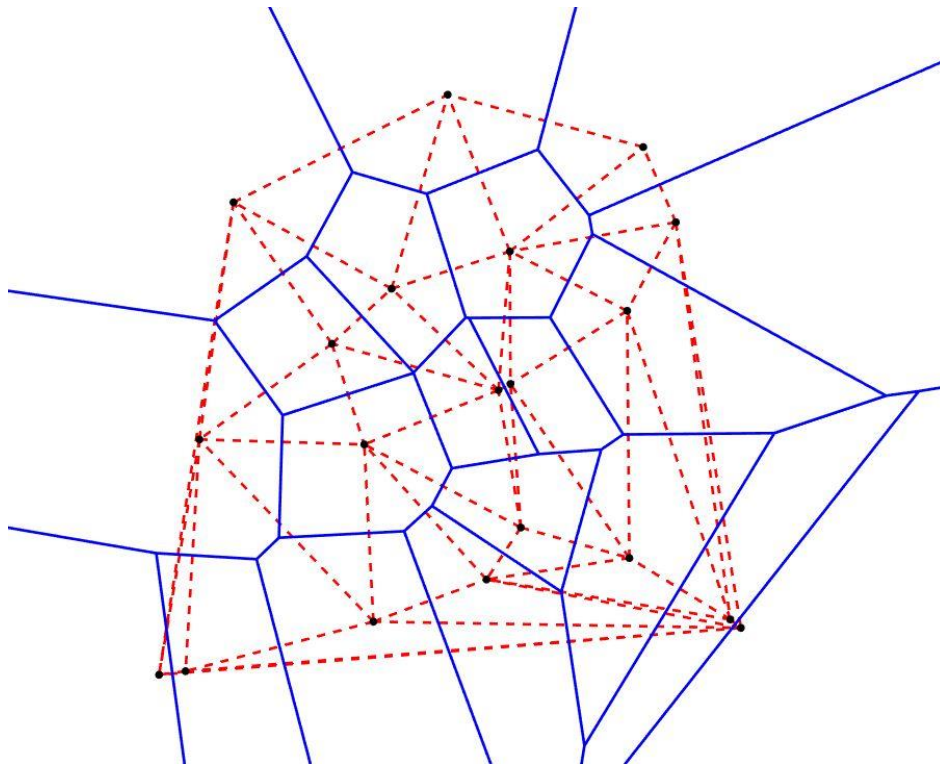


Figure 4-6 – Voronoi diagram and Delaunay triangulation of 20 randomly generated points. We can see now with a larger number of points that a number of Voronoi cells have been produced in the centre of the figure. These mathematically predicted cells have been reported to be a good estimation for epithelial cell membranes/boundaries in both monolayer and 3D culture [263].

In this figure, we can see the interconnected points (Delaunay triangulation), again shown by the dashed red lines, with the bisecting blue lines to produce the Voronoi diagram. This approach to model epithelial cell boundaries has been found to be effective in capturing the morphological features of biological cells due to the natural cuboidal morphology of these biological cells, especially in 3D [263]. It is now accepted that these tessellations predict the observed morphological characteristics of epithelial cells with good accuracy. I therefore implement this same mathematical modelling approach to

distinguish the cell boundaries within IHC and histological images of our own spheroid slices.

Firstly, I describe how I generate our Voronoi diagrams from my IHC and histology images. I utilise a publically available web-based application called WEBPLOTDIGITIZER, to extract the positions of the cell nuclei from the IHC images. The IHC images represent 2D slices of the 3D spheroids so that the cell nuclei represent points in the \mathbb{R}^2 plane.

The corresponding Voronoi tessellations can be generated using the Matlab Voronoi function. In some cases (i.e. cell nuclei near the cell boundary) the corresponding Voronoi cells are not closed. To close these cells, an additional tool was utilised called VoronoiLimit (<https://uk.mathworks.com/matlabcentral/fileexchange/34428-voronolimit-varargin->) which constrains the Voronoi vertices to a given boundary domain. This means that I was able to limit the Voronoi tessellations to the region of \mathbb{R}^2 space bounded by the spheroid boundaries.

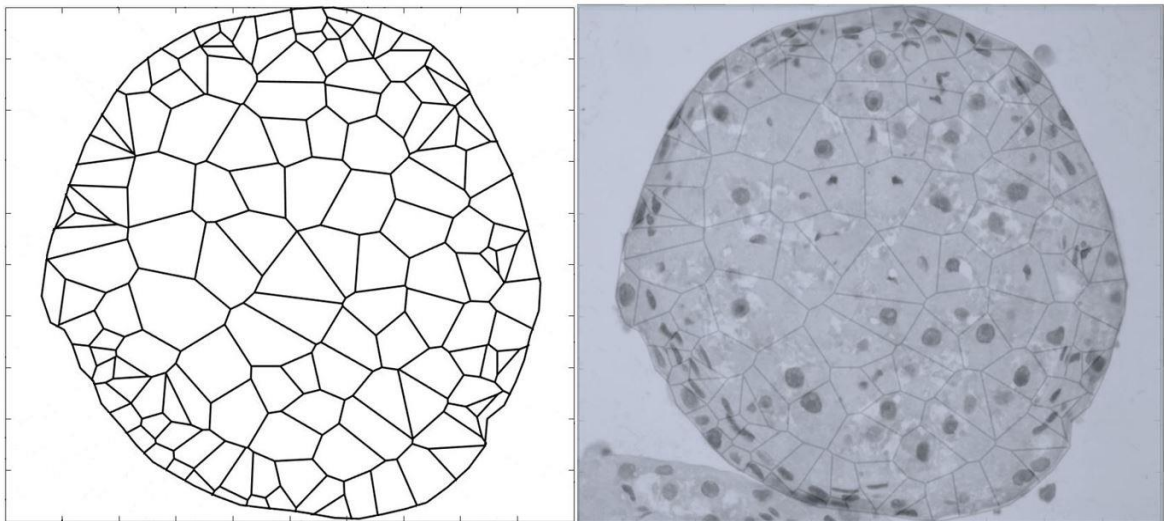


Figure 4-7 – (Left) Voronoi diagram for a day-11, 3000-cell spheroid. (Right) overlay of mathematically derived cell boundaries from VT and original microscopy image of IHC stained spheroid section (5 μm slice).

Mathematical modelling of xenobiotic transport through hepatocyte spheroids

The left-hand image of **Figure 4-7** shows the generated Voronoi diagram for an example spheroid slice. The right-hand image shows an overlay image of the IHC microscopy image and the generated Voronoi diagram. The large cell nuclei are visible in the right-hand image and we can see that the computed cellular geometry provides a convincing representation of the cell-cell boundaries. I repeat this approach to all cell seeding densities, for days 3, 7, 11, 18 and 21 (*in triplicate*) (see **Figure 4-8**).

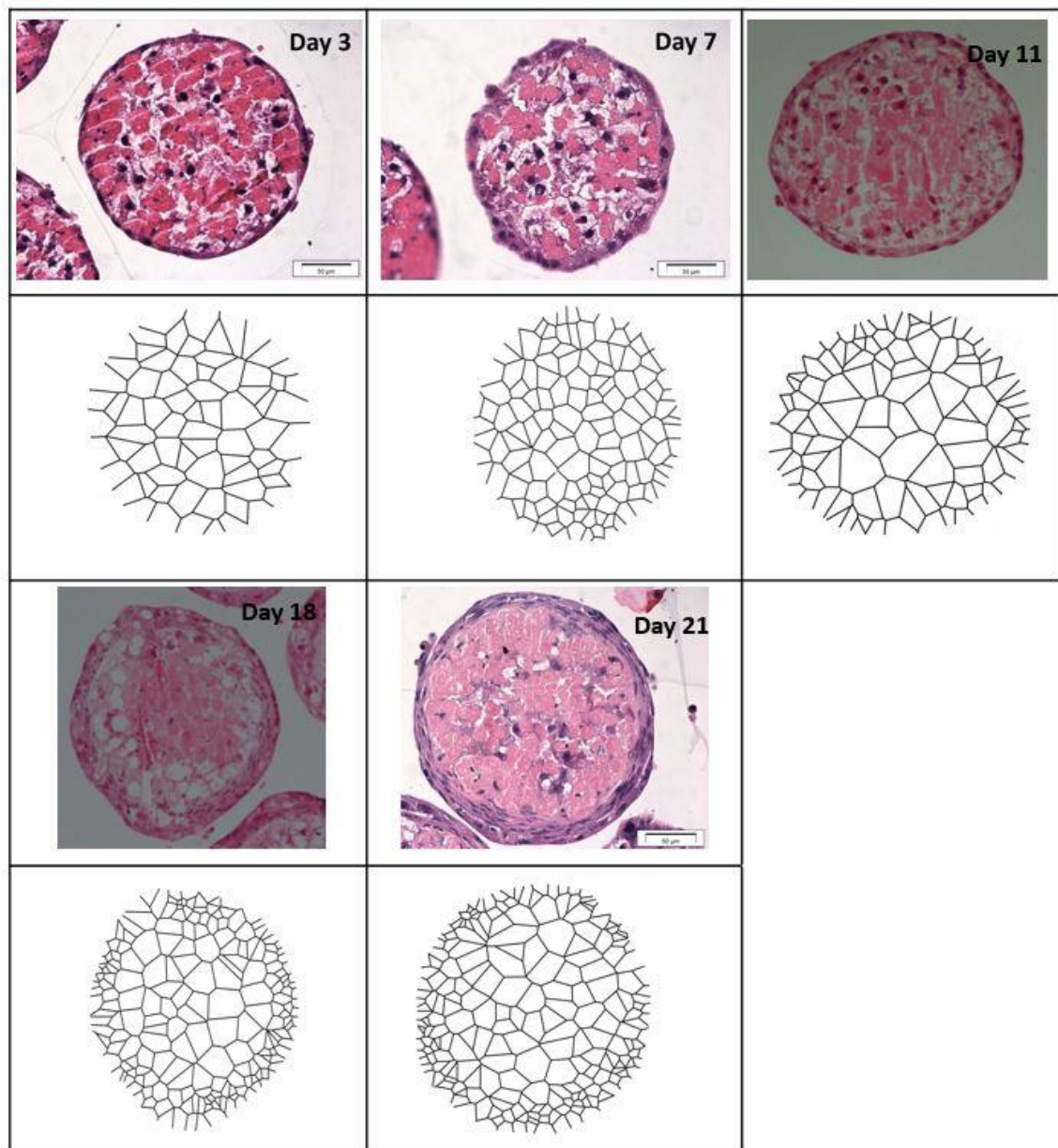


Figure 4-8 – Histology images for days 3, 7, 11, 18 and 21 with corresponding mathematically computed Voronoi diagrams. H&E stained histology samples show distinct nuclear staining in purple. Scale bars = 50 μm.

Mathematical modelling of xenobiotic transport through hepatocyte spheroids

In order to determine how the volumetric porosity changes with regards to radius and time, the next step of analysis was to spatially categorise the Voronoi diagram and subsequently establish the volumetric porosity of separate annuli. Values for volumetric porosity (ε) can then be calculated for the separate annuli of decreasing radius and a function, $\varepsilon(r)$, can be determined.

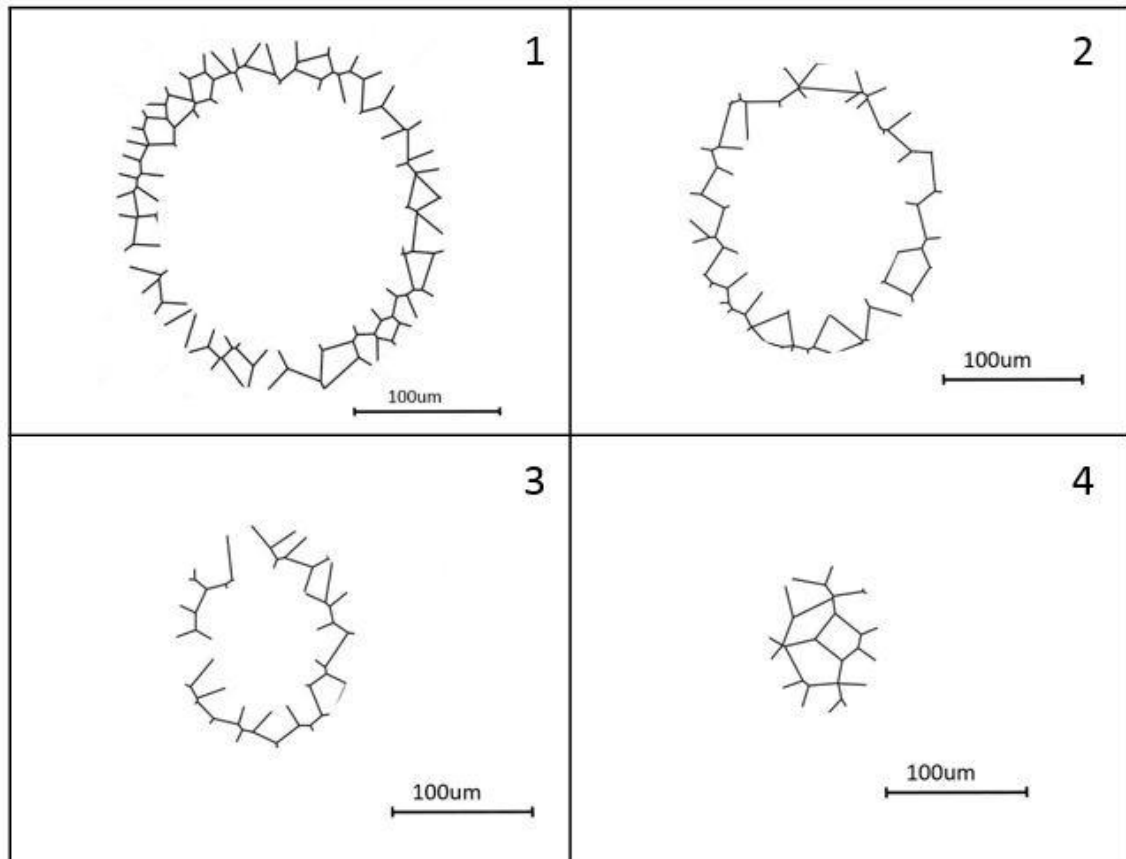


Figure 4-9 – Separated annuli for a day-7, 4000-cell spheroid Voronoi tessellation. (Each annulus represented a thickness of 25 µm).

Figure 4-9 shows an example of the method utilised to partition the Voronoi diagram into separate annuli. For example, annulus 1 shows the outer most section of my day 7 spheroids, where the radius of the annulus is 25 μm . From this outer most annulus, the inner edge was taken to be the outer most edge for the subsequent annuli section. This was repeated for the additional annuli of the Voronoi diagram with each annulus taken to be 25 μm . The method of partitioning the Voronoi images was implemented for all time points.

ImageJ analysis was then utilised to produce a binary image of the different spheroid annuli. For each annuli image, the percentage of the area that is made up from paracellular lines was determined by using a threshold function, which quantified the area of the black lines. The % area of paracellular lines was converted to area (μm^2). The width of the black lines (i.e. pixel width) produced from the VT was subsequently measured. This paracellular line area was then divided by this width and multiplied by the calculated pore size (0.05 μm) to give an estimate of area for the paracellular space in the annuli.

This area value was then expressed as a fraction of the annulus area to give an estimate of volumetric porosity (ε) (see **Table 6** for the full calculations). For each time point (day 3, 7, 11, 18 and 21), 3 spheroids were analysed, and all of the normalised volumetric porosity values were plotted.

Mathematical modelling of xenobiotic transport through hepatocyte spheroids

	DAY 7	DAY 7	DAY 7	DAY 7
Annulus #	1	2	3	4
X AXIS LENGTH (μm)	251.03	219.66	206.55	152.05
Y AXIS LENGTH (μm)	263.1	228.97	207.59	156.51
TOTAL AREA (μm^2)	6.605×10^4	5.030×10^4	4.288×10^4	2.380×10^4
Background area %	96.66%	96.72%	97.54%	97.83%
VT area %	3.34%	3.28%	2.46%	2.17%
Total area of scale bar%	0.30%	0.40%	0.47%	0.84%
VT area % - scale bar %	3.04%	2.88%	1.99%	1.33%
Corrected area of VT (μm^2)	2.01×10^3	1.45×10^3	8.53×10^2	3.17×10^2
Width of line (average) (μm)	1.147	0.993	1.100	1.073
Width of line(1) (μm)	1.01	0.96	1.12	1.04
Width of line(2) (μm)	1.03	0.98	1.31	1.33
Width of line(3) (μm)	1.4	1.04	0.87	0.85
Total length of VT (μm)	1.751×10^3	1.458×10^3	7.757×10^2	2.949×10^2
Circle diameter (average) (μm)	225.33	170.9933333	116.2433333	65.97333333
Circle diameter (1) (μm)	238.19	181.77	128.98	73.9
Circle diameter (2) (μm)	206.09	155.09	101.84	50.95
Circle diameter (3) (μm)	231.71	176.12	117.91	73.07
Area of circle [r] (μm^2)	3.988×10^4	2.296×10^4	1.061×10^4	3.418×10^3
Area of inner circle ([r-r] (μm^2))	3.152×10^4	1.674×10^4	6.539×10^3	N/A
Area of annulus [r] (μm^2)	8.358×10^3	6.224×10^3	4.074×10^3	N/A
Gap size (μm)	0.05	0.05	0.05	0.05
Area of gaps (μm^2)	87.54933956	72.91167009	38.78484175	14.74400754
ϵ	0.010475147	0.011714565	0.009520109	0.004313093
(%)	1.05%	1.17%	0.95%	0.43%
Normalised radius(R-12.5)/R	0.944525807	0.703383186	0.460406219	0.073196349

Table 6 - Table of volumetric porosity calculations as described in Figure 4-9 for 4000-cell spheroids at day 7 of culture. These values were calculated for 3 spheroids for each time point. Normalised radius is subsequently plotted against volumetric porosity values.

Mathematical modelling of xenobiotic transport through hepatocyte spheroids

In order to understand how the values for volumetric porosity change radially, these calculated porosity values were plotted against the normalised spheroid radius for all time points. Note that I use the mid-points of the annuli as the relevant radial points for the subsequent plot (**Figure 4-10**). Using non-linear regression analysis, a power function was fitted through the data for each time point.

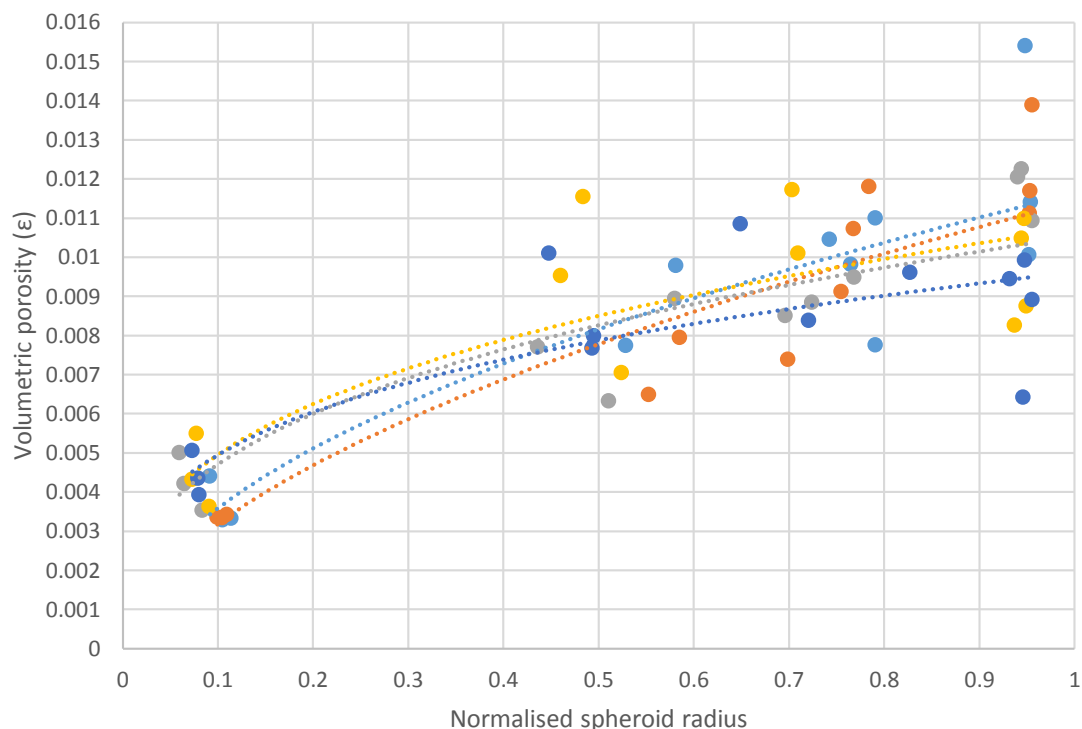


Figure 4-10 – Volumetric porosity values for day 3, 7, 11, 18 and 21 spheroids, plotted against normalised spheroid radius. Where 0 is the spheroid core and 1 is the spheroid boundary. Dark blue dots show day 3, yellow dots show day 7, grey dots show day 11, orange dots show day 18 and light blue dots show day 21. Non-linear regression analysis was used to fit power curves through the data points (the line colour corresponds to the data of that colour). R^2 values for these lines were 0.75, 0.76, 0.86, 0.93 and 0.89 for days 3, 7, 11, 18 and 21 respectively. ($n=3$ for each time point).

Figure 4-10 shows the relationship between volumetric porosity and normalised spheroid radius to take into account the observation of spheroid compaction. For all time points, the volumetric porosity (ε) increases as we move out radially from the spheroid centre. This relationship becomes more apparent for later time points as there is an increase in cellular stratification on the periphery of the spheroid. The nuclear staining as seen in **Figure 2-9** demonstrates this relationship. However, utilising the Voronoi method and subsequent ImageJ analysis I have been able to quantify this relationship. I want to implement this data for volumetric porosity and how it depends against radius in my mathematical model. **Table 7** shows the fitted ε versus r curves for the different spheroids (shown in **Figure 4-10**).

Table 7 – Calculated volumetric porosity values from power fits shown in Figure 4-10.

Culture time (days)	Calculated volumetric porosity (ε)
3	$0.0096 r^{0.2889}$
7	$0.0107 r^{0.3359}$
11	$0.0105 r^{0.3493}$
18	$0.0114 r^{0.5536}$
21	$0.0116 r^{0.5103}$

Mathematical modelling of xenobiotic transport through hepatocyte spheroids

I now need to be able to determine the values for tortuosity and again look at how these values change with respect to spheroid radius and culture time. Again, as I am unable to use my microscopy images and simply measure the path lengths, I will utilise the previously generated Voronoi diagrams to estimate the relevant values for tortuosity.

In order to properly derive values for tortuosity, I need to know the positions of where the lines intersect, subsequently referred to as nodes, within the Voronoi diagrams. These nodes represent the points at which multiple cell boundaries meet. This is to enable me to determine the routes of the paracellular spaces and the lengths of these paracellular routes between these nodes.

As part of the construction of the Voronoi diagram, the spatial $(x, y) \in \mathbb{R}^2$ positions of the Voronoi nodes are calculated. From these, I calculate the lengths of all the edges of each Voronoi cell (i.e. the distances between connected Voronoi nodes). These Voronoi nodes and the associated edges therefore define a weighted, connected graph (e.g. see **Figure 4-11**). To calculate the tortuosity of this resulting network, I follow the following procedure;

1. For a given node, identify all nearby nodes within a given Euclidean radius (I take this distance to be 0.2, relative to the normalised radius), that are not directly adjacent to the given node.
2. Calculate the shortest graph path length between the selected node and all nodes within the given Euclidean radius.
3. Calculate the corresponding Euclidean distance between these points.
4. Divide the path lengths calculated in step 3 by the distance calculated in step 4 to give the individual tortuosities of the paths from the selected node to its adjacent/nearby nodes.
5. Record the average of these individual tortuosities to give an estimate of the 'local' tortuosity of the tessellation structure at this radial position.
6. Repeat for each Voronoi node.

Mathematical modelling of xenobiotic transport through hepatocyte spheroids

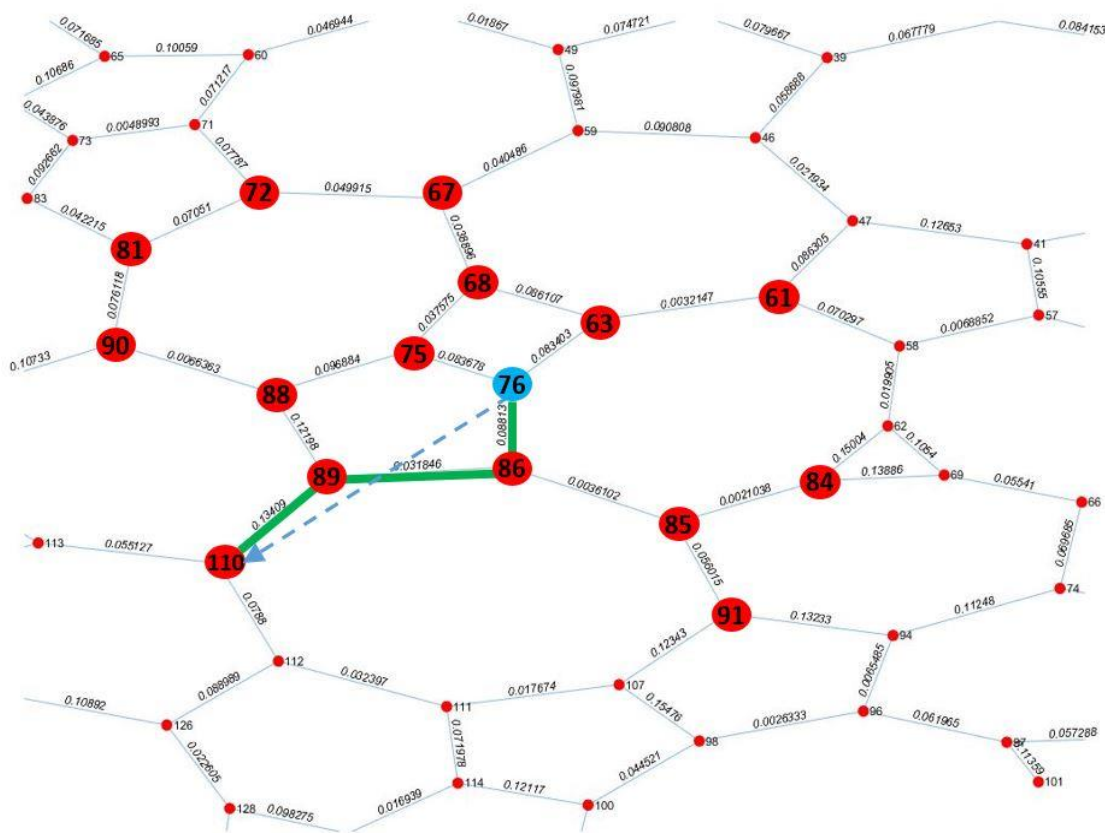


Figure 4-11 – Weighted Voronoi to determine the tortuosity within PRH spheroids. Red circles denote the nodes where the Voronoi edges meet. The green lines represent the total path length between nodes 76 and 110, whilst the blue dashed line denotes the Euclidean distance between the two points.

Figure 4-11 demonstrates this methodology. For example, the tortuosity is calculated by looking at a specific node, in this case uniquely identified by the number 76, and looking at the total path length between neighbouring nodes e.g. node 110. This is the cumulative sum of the straight-line distances between these nodes within a specified region (not including direct neighbours). The tortuosity is therefore calculated by the ratio of the total path length, to the Euclidian between the two points. For my model, these calculations were determined for every node of the Voronoi with a specified

Mathematical modelling of xenobiotic transport through hepatocyte spheroids

neighbourhood range. These calculations were repeated for all of the original Voronoi diagrams as used for the volumetric tortuosity calculations ($n=3$). Again, in order to compare the contraction of the spheroids over the duration of the culture time, and the effect of the cellular stratification on the spheroid boundary, the values for tortuosity were normalised to experimental spheroid radius, providing us with the scaled radial distance for all time points (i.e. r/R , where R is the spheroid radius).

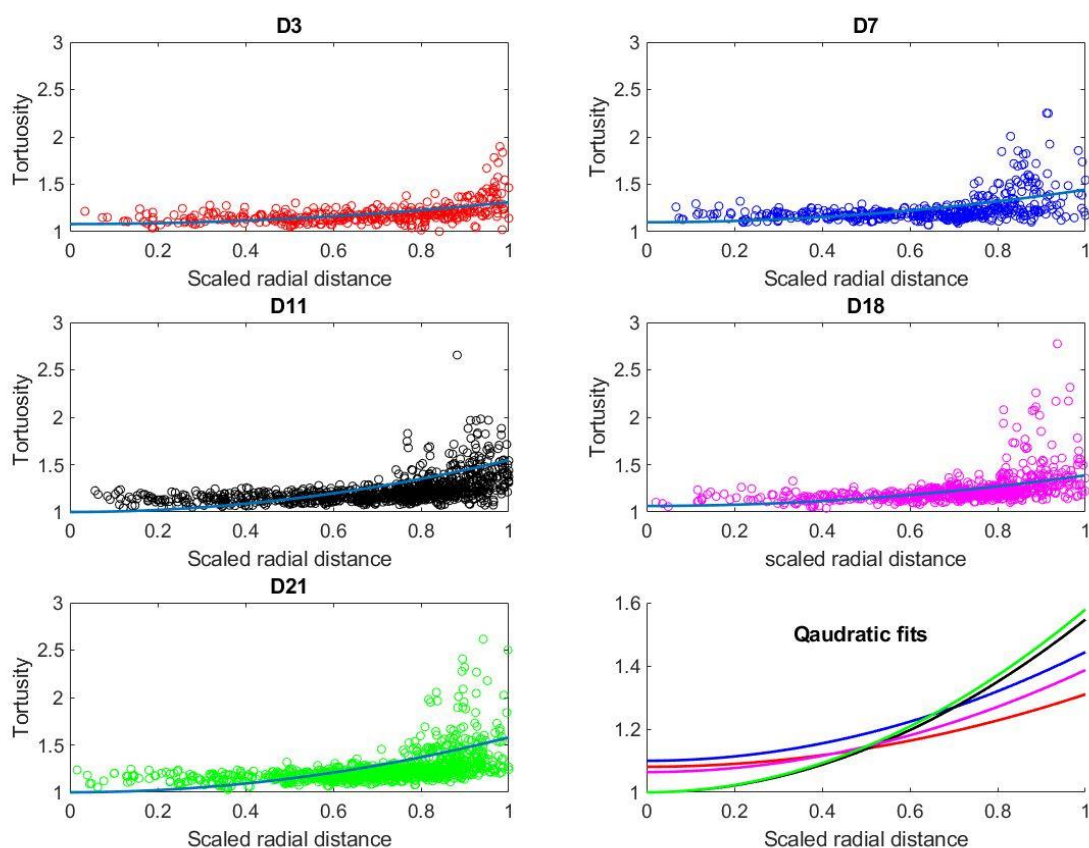


Figure 4-12 – Calculated tortuosity values plotted against scaled spheroid radius. Red circles show the tortuosity values for day 3, blue for day 7, black for day 11, magenta for day 18 and green for day 21. Non-linear regression analysis was used to fit these data points. The bottom right-hand subplot shows the resulting quadratic fits. R^2 values for the quadratic fits were 0.90, 0.81, 0.82, 0.8437 and 0.80 for days 3, 7, 11, 18 and 21 respectively. ($n=3$ for each im point).

Figure 4-12 shows the tortuosity values from my calculations for each node within the Voronoi diagrams. The coloured circles describe the individual tortuosity calculations for each node within the Voronoi tessellation ($n=3$). The scaled radial distance takes into account the variations in the spheroid sizes and allows a comparison of the tortuosities to be made. The lines on the subplots represent quadratic fits through the data points. For all time points we can see that the tortuosity increases as you move out from the spheroid core (scaled radius of 0), to the spheroid boundary (scaled radius of 1). This relationship can be seen to generally increase with respect to culture time i.e. day 21 spheroids have a greater tortuosity at the boundary than the day 3 spheroids, and also have a much smaller tortuosity at the spheroid core than those from day 3.

The quadratic fits through the calculated tortuosity values have the following relationships, where r is the scaled radial distance (see **Table 8**);

Table 8 – Calculated tortuosity values from quadratic fits through the data points. For these values, r represents the scaled radial distance.

Culture time (days)	Calculated tortuosity (τ)
3	$0.2293 r^2 + 1.0808$
7	$0.3439 r^2 + 1.0998$
11	$0.5469 r^2 + 1.0000$
18	$0.3229 r^2 + 1.0640$
21	$0.5787 r^2 + 1.0000$

I have now been able to derive a number of the key parameters that are required for my mathematical model. From the TEM microscopy images I have been able to determine the average size of the paracellular gaps within the spheroid, namely (r_p). By implementing the Voronoi tessellation method, I have been able to derive appropriate estimates for both the volumetric porosity, $\varepsilon(r)$, and the tortuosity, $\tau(r)$, and how both these parameters change with respect to culture time. In the original model by Goodman *et al.* [245] they found tortuosity to be a function of volumetric porosity. I did not see this relationship and instead implement both ε and τ as functions of the scaled spheroid radius (r).

Finally, I need to describe the range of particle sizes that I want to investigate with regards diffusion within the model. For this, I develop a list of xenobiotics and a number of important characteristics for each of these including, the size of the particle, LogP, LogD_{7.4}, etc.

4.3.2 Physicochemical characteristics of chosen xenobiotics

Here I will present a list of compounds chosen to investigate with regards to application to my spheroid model, and describe the methods by which I have generated the characteristics required for the mathematical model. As previously described by Goodman *et al.* [245], I require the size of the diffusing particle (namely, its radius, α , see (4-3)). In Chapter 3, I looked at the diffusion of oxygen, which is a relatively small diffusing particle. Goodman *et al.* [245] looked at the diffusion of nanoparticles with a size range of up to 200nm, predicting that particles greater than 100nm experience restricted transport. I want to be able to quantify the particle size from a list of applicable xenobiotics.

It is important to note that I calculate the spherical radius of xenobiotics, where the spherical radius is calculated as,

$$\alpha = \sqrt[3]{\frac{3M_w \cdot n}{4\pi N_A \rho}}, \quad (4-6)$$

where α is the spherical radius of the xenobiotic, M_w is the molecular weight, n is the number of moles, N_A is Avogadro's number, and ρ is the density.

An extensive list of over 270 compounds was compiled including specific physicochemical properties based on a list previously described by Separham *et al.* [265]. Although these compounds are not specific hepatotoxins, they have been selected due to the diversity in physicochemical parameters. Due to the mathematical modelling approach taken whereby I assume a spherical particle travels down the centre line of a cylinder (representing the paracellular space), the spherical radius of the compound is highlighted as a key parameter that will impact on transport potentials. Online databases such as www.drugbank.ca and the national chemical database services (cds.rsc.org) were used to obtain values for density, LogP, pKa, and molecular weight for each of the compounds. Structural files pertaining to each of the xenobiotics from the list were also sourced. The key information obtained from these searches were used to calculate xenobiotic-specific parameters (see Appendix).

Table 9 – Selected xenobiotics show the range of calculated spherical radii from equation (4-6). APAP is shown as a xenobiotic of interest. Fluorouracil has the smallest calculated spherical radius and vinblastine has the largest calculated spherical radius.

Name of xenobiotic	Density (g/cm ³)	Molecular weight (Da)	Calculated spherical radius (nm)
Fluorouracil	1.557	130.08	0.321
APAP	1.26	151.16256	0.362
Etomidate	1.11	244.29	0.444
Methotrexate	1.536	454.45	0.490
Diclofenac Sodium	0.63	318.13	0.585
Vinblastine	1.37	810.99	0.617

From **Table 9** we can see that the size of the diffusing particles for my model will range from 0.321nm to 0.617nm. I can use this range within the model to see what effect varying these values have on xenobiotic transport.

A key parameter that I need to calculate is the passive diffusion rate of these compounds from the paracellular space into the cell interiors (defined by k_u in equation (4-1)). Such

Mathematical modelling of xenobiotic transport through hepatocyte spheroids

passive diffusion has been shown to be related to $\text{Log}D_{7.4}$ by Menochet *et al.* [266] with the following formula,

$$\text{Log } k_u = 0.5977 \times \text{Log}D_{7.4} - 0.0437. \quad (4-7)$$

These values for passive diffusion have the units; $\mu\text{l}/\text{min}/10^6$ cells so in order to convert this passive uptake rate to the required units (s^{-1}), I implemented the following;

$$V = \frac{4}{3}\pi r^3 = 2.5882 \times 10^{-11} \text{ m}^3 \quad (4-8)$$

Where r is taken to be the average radius of 4000-cell spheroids for all time points (183.5 μm). V , is the total volume of the spheroid. I correct this value by subtracting the average value for the volumetric porosity of the 4000-cell spheroid ($\varepsilon = 0.008307$).

$$1 - \varepsilon = 1 - 0.008307 = 0.9917$$

$$\therefore V_{\text{cells}} = 2.5882 \times 10^{-11} \times 0.9917 = 2.5667 \times 10^{-11} \text{ m}^3 \quad (4-9)$$

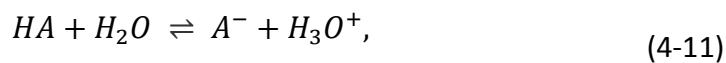
$$\therefore 0.025667 \mu\text{l}^{-1} 4000 \text{ cells} = 6.4167 \mu\text{l}^{-1} 10^6 \text{ cells},$$

where 0.9917 is the fraction of the spheroid that is made up of cells, and V_{cells} is the total volume occupied by the cells. The original k_u values have the units $\mu\text{l}/\text{min}/10^6$ cells. I convert these values to rates (s^{-1}) by calculating the volume per cell, dividing the V_{cells} value by the known number of cells in the spheroid and then multiplying this value by 10^6 . This value represents the total volume of 10^6 cells (6.4167 $\mu\text{l}/10^6$ cells). As a comparison, Menochet *et al.* [266] described this value being 3.9 $\mu\text{l}/10^6$ cells. To obtain our passive uptake terms for the specific xenobiotics I rearrange the original equation (4-7) and divide this by 6.4167 $\mu\text{l}/10^6$ cells to cancel the units of μl and cells. Finally, I divide this value by 60 to convert the time from minutes to seconds (see equation (4-10)).

$$k_u = \frac{1}{60} \frac{10^{(0.5977 \times \text{LogD}_{7.4} - 0.0437)}}{6.4167} \quad (4-10)$$

Menochet *et al.* [267] looked at the simultaneous uptake and metabolism of compounds in rat hepatocytes and therefore the relationship described in (4-7) between $\text{LogD}_{7.4}$ and passive diffusion is highly appropriate for the mathematical modelling of an experimental PRH spheroid. In order to calculate the values for k_u I first use ACD/labs software (ACD/Structure Elucidator, version 15.01, Advanced Chemistry Development, Inc., Toronto, ON, Canada, www.acdlabs.com, 2015) which uses the corresponding structural SMILES (simplified molecular-input line-entry system) files to calculate the appropriate $\text{LogD}_{7.4}$ values based on the pKa values of the compounds. SMILES files are a specific line notation which describes the structure of a chemical species using short ASCII strings. SMILES strings can subsequently be imported into molecule editing software for conversion back into 2D drawings or 3D models of the molecules. From these molecular structural files, various physicochemical properties can be predicted depending on the specific reactive groups of the chemical.

pKa refers to the acid dissociation constant which is a quantitative measure of the strength of an acid in solution. In aqueous solution, the equilibrium of acid dissociation can be written as,



where HA is a generic acid that dissociates into A^- (conjugate base), and the hydrogen ion combines with a water molecule to produce a hydronium ion.

Mathematical modelling of xenobiotic transport through hepatocyte spheroids

The concept of LogD is derived from an understanding of the partition coefficient which is itself is a constant. The partition coefficient is defined as the ratio of concentration of compound in aqueous phase to the concentration in an immiscible solvent. The LogP will vary according to the conditions under which it is measured and the choice of partitioning solvent were,

$$\text{Partition coefficient, } P = \frac{[\text{Organic}]}{[\text{Aqueous}]}, \quad (4-12)$$

where []= concentration.

$$\text{Log}P = \log_{10} (\text{Partition coefficient}). \quad (4-13)$$

LogD is the log distribution coefficient at a certain pH. LogD at pH 7.4 (LogD_{7.4}) is said to give an indication of the lipophilicity of a drug at the pH of blood plasma.

$$\text{Distribution coefficient, } D = \frac{[\text{Unionised}](o)}{[\text{Unionised}](aq) + [\text{Ionised}](aq)}, \quad (4-14)$$

$$\text{Log}D = \log_{10} (\text{Distribution coefficient}). \quad (4-15)$$

The LogD_{7.4} value refers to lipophilicity at pH 7.4 which is a measure of how well a compound dissolves in fats, and is therefore a key physicochemical characteristic when considering the transport and diffusion of the compound within my list. The passive diffusion rates for the xenobiotics introduced in **Table 9** are derived from equation (4-7) and by utilising the ACD/labs generated LogD_{7.4} values (see **Table 10**).

Table 10 – Previously selected xenobiotics and calculated passive diffusion rates. These rates have been calculated using equation (4-7) and ACD/labs generated $\text{Log}D_{7.4}$ values.

Name of xenobiotic	Passive diffusion rate k_u (1/s)
Fluorouracil	1.0708×10^{-6}
APAP	0.0038
Etomidate	0.2086
Methotrexate	2.7676×10^{-6}
Diclofenac Sodium	0.0087
Vinblastine	0.3770

4.4 Xenobiotic transport simulations

The principle equation used for the modelling of xenobiotic transport is described by the following equation;

$$\frac{\partial c}{\partial t} = \frac{1}{r^2} \frac{\partial}{\partial r} \left[D \varepsilon r^2 \frac{\partial}{\partial r} \left(\frac{c}{\varepsilon} \right) \right] - k_u \frac{c}{\varepsilon}, \quad (4-16)$$

I use the initial condition,

$$c(r, 0) = 0, \quad (4-17)$$

I also use the boundary conditions,

$$\frac{\partial c}{\partial r} = 0, \quad \text{at } r = 0, \quad (4-18)$$

$$c = 0, \quad \text{at } r = R, \quad (4-19)$$

where c is the molar concentration of the xenobiotic in the spheroid volume. I will look at normal dose ranges for known compounds e.g. 50mM for APAP. k_u is the calculated passive diffusion rate based on LogD_{7.4}, D is the effective diffusion coefficient expressed by equation (4-2). In this case the diffusion coefficients of each xenobiotic will be compound specific. Recall that in Goodman *et al.* [245], the diffusion coefficient was calculated using the following formula:

$$D = D_0 \frac{L(\lambda)}{\tau(\varepsilon)}, D_0 = \frac{k_B T}{6\pi\mu\alpha},$$

where the researchers describe tortuosity as being a function of the volumetric porosity, $\tau(\varepsilon)$. I did not observe this relationship within my spheroid model and instead explicitly calculated tortuosity as a function of spheroid radius, $\tau(r)$. Similarly with volumetric porosity, ε , I explicitly calculated tortuosity as a function of spheroid radius $\varepsilon(r)$.

Where D_0 is the diffusion coefficient in unbounded liquid medium (in this case I assume it to be culture medium), $\tau(r)$ is the calculated tortuosity, k_B is Boltzmann's constant, T

Mathematical modelling of xenobiotic transport through hepatocyte spheroids

is the absolute temperature (in Kelvin), μ is the viscosity of the liquid (water), α is the calculated spherical radius of the diffusing xenobiotic as shown in **Table 9**, r_p is the calculated radius of the pores within the spheroid (0.05 μm), $\lambda = \alpha/r_p$, and $L(\lambda)$, as described above, is the factor responsible for hydrodynamic and steric reduction of the diffusion coefficient in the pore.

The spheroid radius is fixed for my simulations and the PDE is solved for,

$$r \in [0, R] \text{ and } t \in [0, 3] \text{ (minutes)},$$

where R is the spheroid radius. For these simulations I assume that the radius of the spheroid and spatial features don't vary in this short three minute time frame, and only the concentration of the xenobiotic varies.

I will show the results for the 4000-cell spheroids (days 3, 7, 11, 18 and 21). The results for the remaining spheroids are similar.

I will now describe the initial simulation results where I use APAP as an example xenobiotic. These steady state simulations will show the paracellular transport of the xenobiotic where there is no passive uptake term for the cells, and I will compare this to the same simulation where I have both the paracellular transport as well as a passive uptake term. I will also look at the effect of the spatially varying porosity and tortuosity (**Table 7** and **Table 8**).

The key aim of my simulations is to quantify how long it takes for the initial dose concentration to accumulate in the centre of the spheroid, assuming that I have a constant source of xenobiotic at the boundary (i.e. the media). By simulating for both paracellular transport and passive uptake, I can better discern the effect that the specific lipophilicity of the xenobiotic has on its transport within the microtissue. Also I will look at how the spatially varying volumetric porosity and tortuosity effects the transport of the xenobiotics and if the observed stratification effects xenobiotic penetration into the microtissue.

4.5 Simulation results

4.5.1 Transport of APAP

In this section, I show the *in silico* predicted transport profiles for APAP, and how variations in the volumetric porosity (ε) and tortuosity (τ) effect this transport. I will utilise the explicitly calculated values for volumetric porosity and tortuosity that change with respect to radius, $\varepsilon(r), \tau(r)$, and I will also investigate the effect of these parameters in the cases where;

- ε is constant and $\tau(r)$,
- $\varepsilon(r)$ and τ is constant,
- ε is constant and τ is constant.

For the simulations where ε is constant I will use the mean $\varepsilon(r)$ over all sample considered (i.e. 0.008307). For the simulations where τ is constant I will utilise the corresponding mean tortuosity value, $\tau = 1.272$.

I solve the reaction diffusion equation (4-16) utilising the Matlab pdepe solver which solves PDEs using finite differences on the spatial derivatives to generate a system of coupled ODEs, which are then solved using an in-built Matlab ODE solver (ODE15s). (See **3.2.1** for numerical methods).

APAP transport profiles

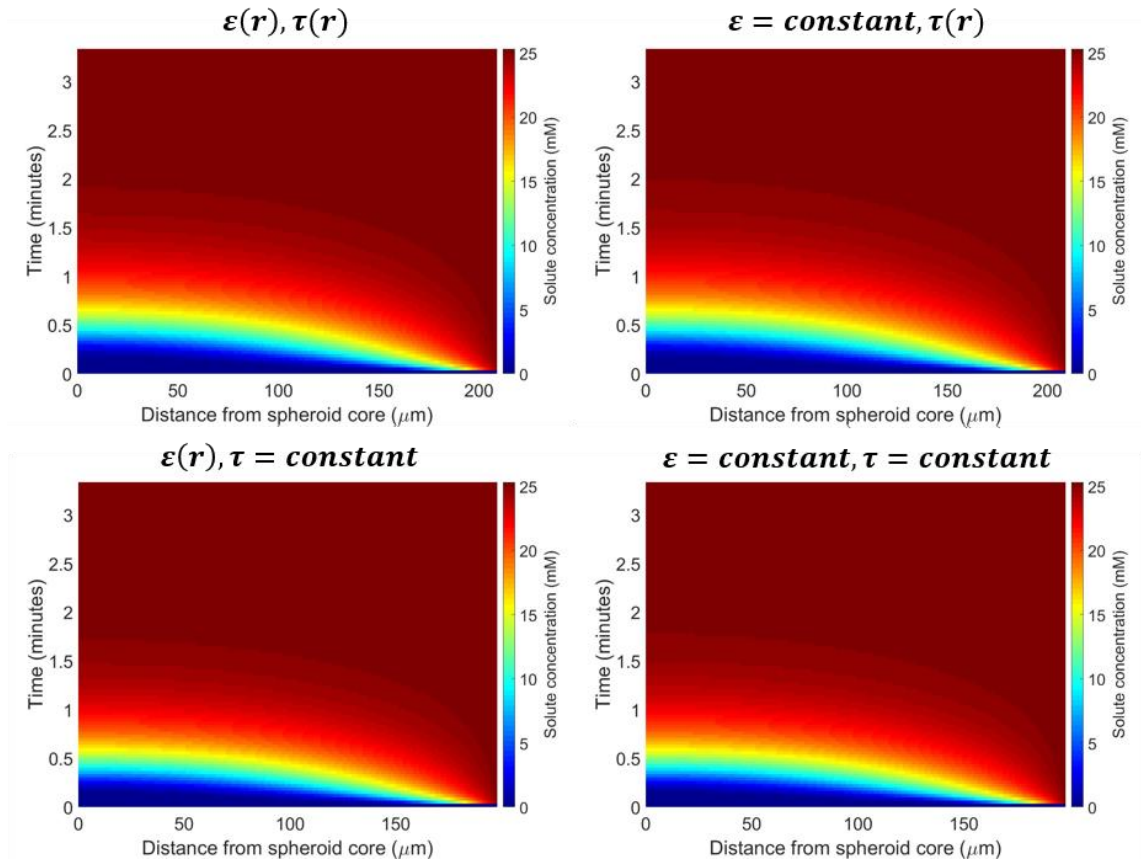


Figure 4-13 - APAP transport where we assume paracellular transport only (i.e. $k_u = 0$) where we have; top left where $\varepsilon(r)$ and $\tau(r)$, top right where ε is a constant term and $\tau(r)$, bottom left where $\varepsilon(r)$ and τ is a constant, and bottom right where ε and τ are both constant terms. The y axis represents time (minutes), the x axis describes the scaled radial distance from the spheroid core to the boundary, and the colour bar represents concentration of the xenobiotic. All cases use the spatial profiles and radius corresponding to that of a day 3 spheroid with 4000 cells.

Figure 4-13 demonstrates the transport profile for APAP when we assume paracellular transport with no uptake into the cells (i.e. $k_u = 0$). I have solved the PDE with the previously described variations in ε and τ to see if these radially coupled values cause changes in the transport profiles of APAP. I.e. I test the effect of the aggregation of the cells at the spheroid boundary. The results from this simulation show that there is no discernible difference when we have $\varepsilon(r)$ and $\tau(r)$, or when we utilise constant values for these, i.e. when we assume paracellular transport only ($k_u = 0$), my simulations show that APAP will accumulate in the core of the spheroids within 2 minutes of dosing at 50mM at day 3.

APAP transport profiles

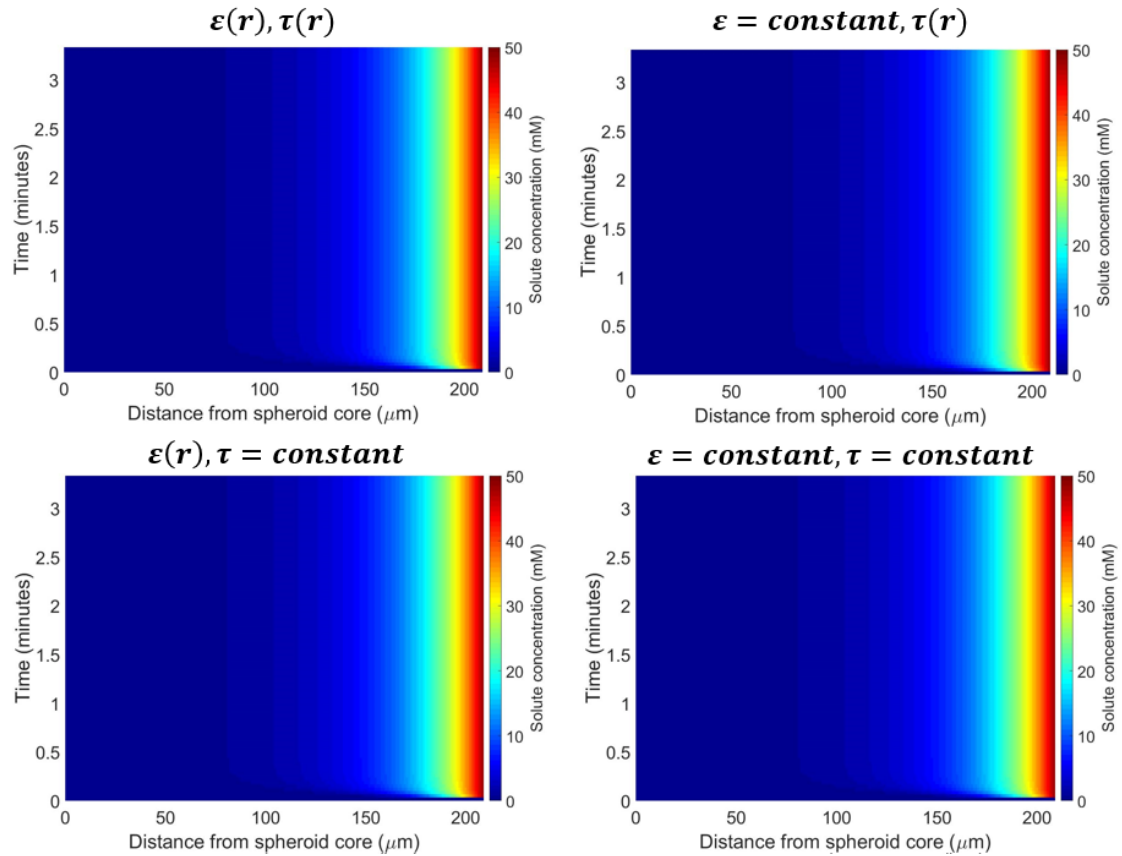


Figure 4-14 APAP transport where we assume paracellular transport and passive uptake where we have; top left $\epsilon(r)$ and $\tau(r)$, top right ϵ is a constant term and $\tau(r)$, bottom left $\epsilon(r)$ and τ is a constant, and bottom right ϵ and τ are both constant terms. The y axis represents time (minutes), the x axis describes the scaled radial distance from the spheroid core to the boundary, and the colour bar represents concentration of the xenobiotic. In each case, I take $k_u = 0.0038 \text{ (s}^{-1}\text{)}$.

Figure 4-14 shows the same transport profiles for APAP as **Figure 4-13**, however, with the implementation of the passive uptake term as calculated from equation (4-10) and given in **Table 10** ($k_u = 0.0038 \text{ s}^{-1}$ for APAP). From these results we can see that when I incorporate passive uptake into the cells, the transport profiles for APAP are distinctly different to paracellular transport only. Initially, when we assume paracellular transport only, APAP fully accumulates in the core at the same concentration as the initial dose within approximately 2 minutes. However, **Figure 4-14** shows that when we include paracellular transport of APAP into the cells, APAP does not fully penetrate the spheroid, independent of the spatial effects of ε and/or τ , and is instead rapidly taken up by the cells on the periphery of the spheroid.

These simulations were also repeated for APAP at day 7, 11, 18 and 21 (data not shown). However, there was no discernible difference between these transport profiles and that of the original simulations at day 3 (**Figure 4-14**). Therefore, for all other subsequent simulations I will look at day 3 as we do not observe any difference between transport profiles as culture time increases.

From these initial simulations I therefore conclude that, for a diffusing particle of this size (0.362nm), the discrete radial changes in spheroid microarchitecture ($\varepsilon(r)$ and $\tau(r)$) makes little difference to the transport profiles. What can clearly be seen from the simulations is that when we only assume paracellular transport, APAP accumulates in the spheroid core rapidly. However, when we incorporate the calculated passive uptake term, very little of the drug penetrates to the centre of the spheroid.

I will now look at vinblastine, a chemotherapeutic drug commonly used to treat breast cancer. This xenobiotic had the largest calculated spherical radius in my list of compounds, and therefore I can investigate the effect of a larger diffusing particle within the model structure.

4.5.2 Transport of vinblastine

These subsequent simulations will show the transport of vinblastine with both transport scenarios, where we have paracellular transport only and both paracellular diffusion with passive uptake. I will again investigate the effects of changing the values for ε and τ , to see if changes in the microarchitecture of the mathematical spheroid model may impede the transport of this xenobiotic. In this instance I will implement a therapeutic dose of vinblastine (10^{-6} mol/l) as previously described [268].

Vinblastine transport profiles

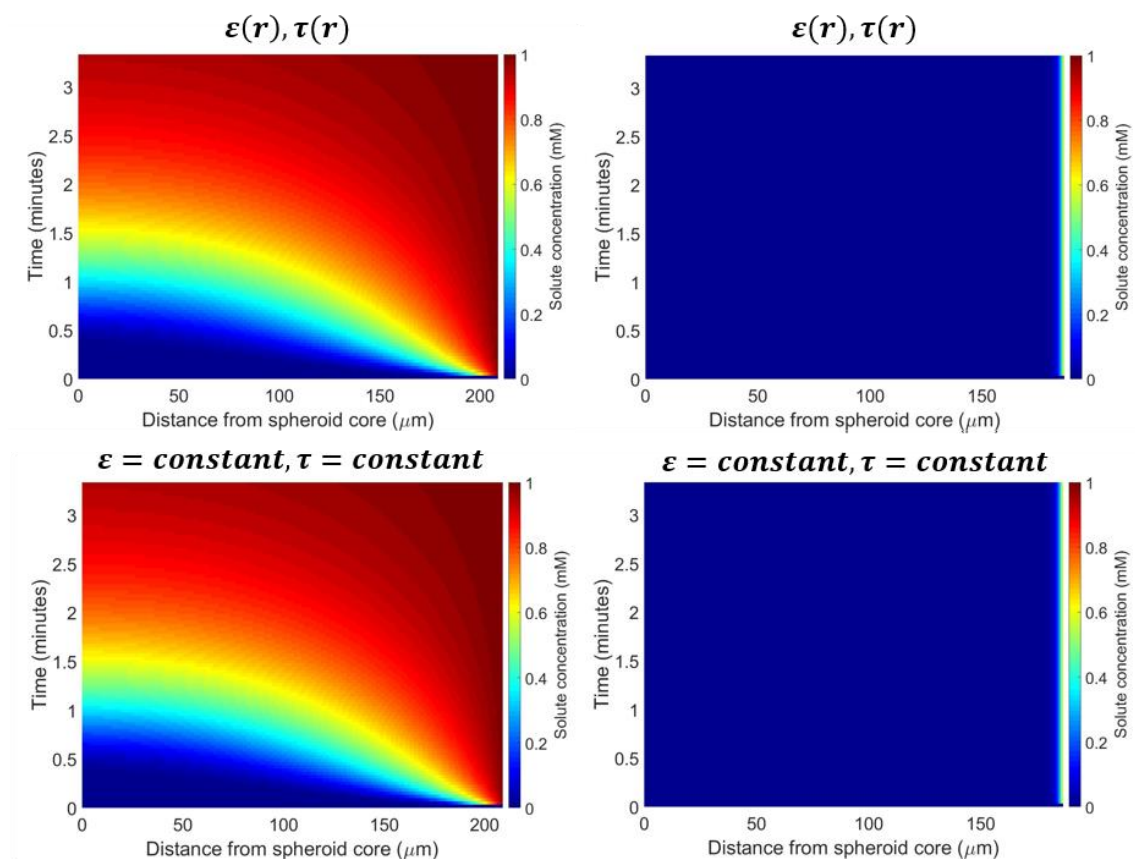


Figure 4-15 - Vinblastine transport where we assume; top left where we have paracellular transport only and $\varepsilon(r)$ and $\tau(r)$; top right we have both paracellular transport and passive uptake, with $\varepsilon(r)$ and $\tau(r)$; bottom left where we have paracellular transport only and ε, τ are both constants; and, bottom right we have both paracellular transport and passive uptake and ε, τ are both constant terms. In this case we take $k_u = 0.3770 \text{ (s}^{-1}\text{)}$.

Figure 4-15 demonstrates the transport profiles for vinblastine. The simulations show the difference between transport via paracellular routes only, versus combined paracellular transport and passive uptake of the xenobiotic. When we assume paracellular transport only, the simulations show that vinblastine will almost fully accumulate in the core of the

spheroids of dosing at 10^{-6} mol/l at day 3. Also, there is no discernible difference between the transport profiles for vinblastine when we assume spatially dependent or constant values for ε and τ . When we look at the same simulations but include passive uptake, we instead see that vinblastine is not transported to the spheroid interior and instead the simulations suggest that the dose of the drug is taken up by the cells on the periphery of the spheroid. Again, by varying ε and τ , we see no changes in this result. From these simulations and the previous result for APAP, I conclude that for the transport of small molecule xenobiotics, the spatial variations in volumetric porosity and tortuosity makes little difference to the drug transport profiles.

As a comparison, I will now look at the transport profiles of fluorouracil, another chemotherapeutic drug commonly used to treat colorectal cancer. This xenobiotic had the smallest calculated spherical radius in my list of compounds. The previous simulations with the largest xenobiotic vinblastine, showed that spatial variations in ε and τ had no effect on its transport profile. As I am now looking at the smallest xenobiotic from my list, I can postulate that radial changes in ε and τ will similarly have little effect on the resulting transport profiles for fluorouracil. Interestingly, when compared to APAP and vinblastine, fluorouracil has a much smaller passive uptake rate as calculated as a function of its $\text{LogD}_{7.4}$ ($1.0708 \times 10^{-6} \text{ s}^{-1}$). This is because, fluorouracil has a relatively low lipophilicity when compared to APAP and vinblastine. I therefore expect to see more penetrance of this xenobiotic into the core of the spheroid, as it will be less likely to diffuse across the cell membranes (i.e. lower k_u).

4.5.3 Transport of fluorouracil

Figure 4-16 shows the transport of fluorouracil where I will again compare the cases of paracellular transport only, versus the combined transport of fluorouracil with passive uptake. For completeness, I will again investigate the spatial effects of ε and τ . Fang *et al.* [269] describe an optimised dose of fluorouracil of between 28-38mg/L/h. In line with this, I use a therapeutic dose of 33mg/L/h.

Fluorouracil transport profiles

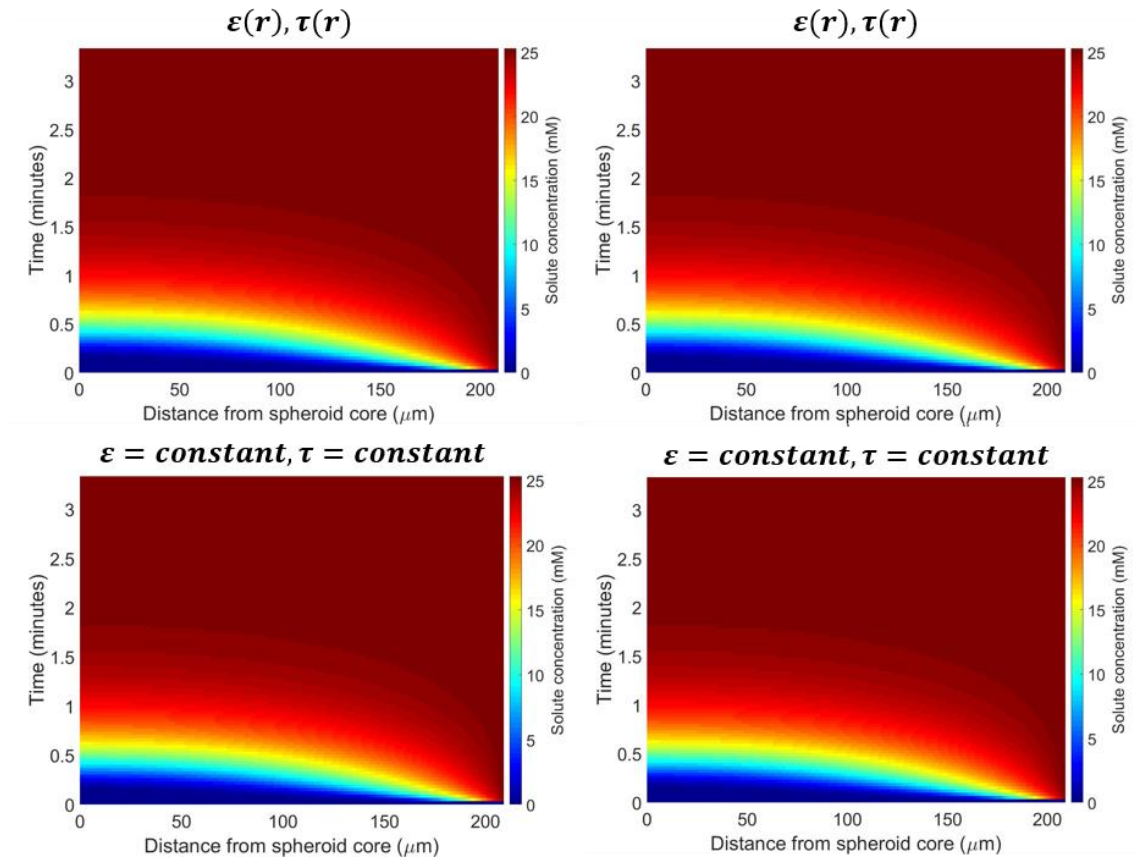


Figure 4-16 - Fluorouracil transport where we assume; top left, we have paracellular transport only with $\epsilon(r)$ and $\tau(r)$; top right, we have both paracellular transport and passive uptake with $\epsilon(r)$ and $\tau(r)$; bottom left, we have paracellular transport only and ϵ and τ are both constants; and bottom right, we have both paracellular transport and passive uptake and ϵ and τ are both constant terms. In this case, we take $k_u = 1.0708 \times 10^{-6} (s^{-1})$.

Figure 4-16 demonstrates the transport profiles for fluorouracil. These simulations show the similarity between transport profiles when I assume paracellular transport only (i.e. $k_u=0$), compared with paracellular transport coupled with passive uptake into the cells (i.e. $k_u=1.0708 \times 10^{-6} \text{ s}^{-1}$). This result is completely different for the simulations for APAP and vinblastine where the rapid rate of passive uptake into the cells is predicted to impede the transport of the xenobiotic into the spheroid core. The result for fluorouracil demonstrates the importance of the lipophilicity ($\text{LogD}_{7.4}$) of the compound, and how this physicochemical property will affect the potential transport within my *in vitro* model. Xenobiotics that have a low $\text{LogD}_{7.4}$ values are less likely to be taken up into the cells as they have a relatively low lipophilicity. These simulations may help to determine what the likely penetration profiles will be, based on physicochemical properties of the xenobiotic and calculated values for cellular passive uptake. The simulations for fluorouracil, where ε and τ are taken to be constant values, show that the inclusion of these spatial changes do not appear to affect the transport of this small molecule xenobiotic as I have demonstrated above.

The results from all of my simulations so far have demonstrated that the spatial variations in ε and τ do not appear to impact on the subsequent transport profiles of these compounds considered. For these simulations, I have looked at both the smallest and largest xenobiotics from my list (0.321-0.617nm), compounds with different $\text{LogD}_{7.4}$ values, and subsequently different cellular uptake rates (**Table 10**). I can conclude that for xenobiotics that fall into this size range, the major impactor on spheroid penetration is lipophilicity. Where xenobiotics are highly lipophilic (e.g. such as vinblastine), they are more likely to be transported by passive diffusion into the cells and therefore appear not to accumulate in the centre of the microtissue. Conversely, if the xenobiotic has a relatively low lipophilicity (e.g. such as fluorouracil), they are more likely to be transported via the paracellular routes and therefore are predicted to accumulate in the spheroid core.

Mathematical modelling of xenobiotic transport through hepatocyte spheroids

To further investigate the effects of $\text{LogD}_{7.4}$, I now look at the transport profiles of fluorouracil again. I run the simulations for day 3 only, and I again look at paracellular transport only ($k_u = 0$) versus combined transport with passive uptake ($k_u \neq 0$). I use the same therapeutic dose of 33mg/L/h. However, for these simulations I now choose 3 limiting values for $\text{LogD}_{7.4}$, namely;

1. $\text{LogD}_{7.4} = -5$, as a value representative for low lipophilicity (similar to the original value -5.59),
2. $\text{LogD}_{7.4} = 5$, as a value representative for high lipophilicity (similar to that of felodipine 4.83),
3. $\text{LogD}_{7.4} = 0.74$, as the average $\text{LogD}_{7.4}$ value from my list of approximately 270 compounds.

Fluorouracil transport profiles

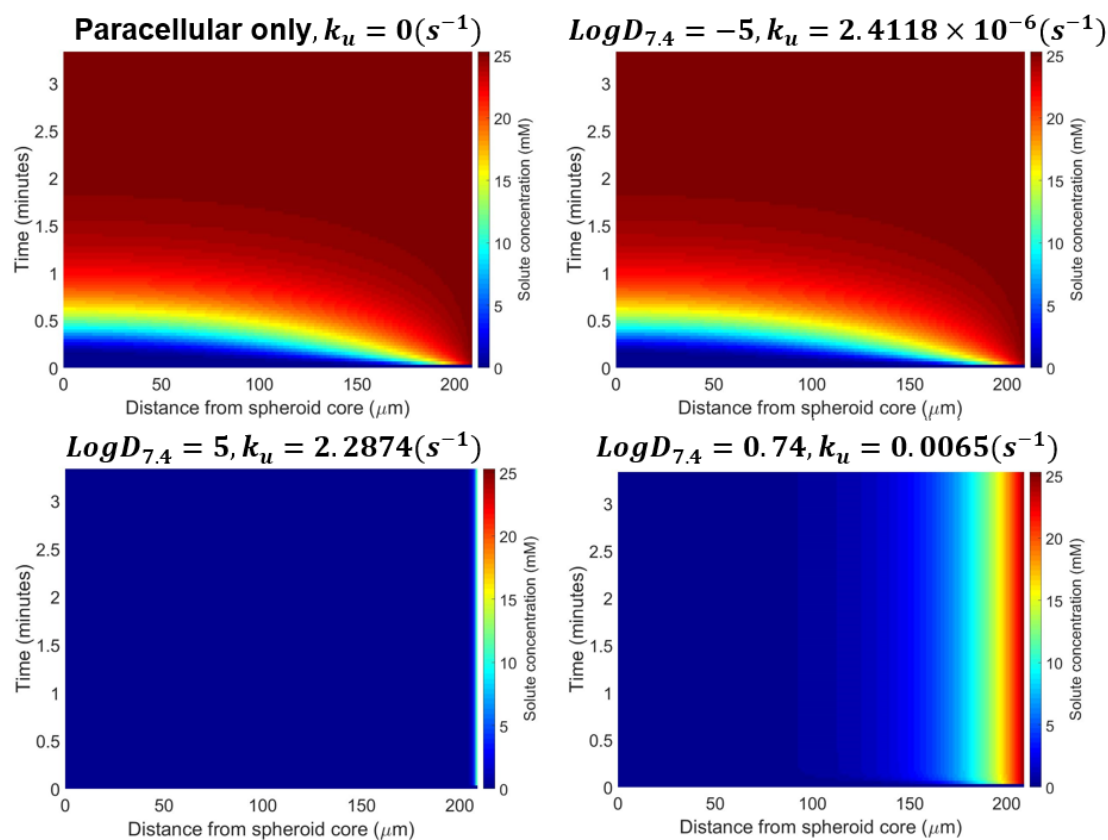


Figure 4-17 - Fluorouracil transport for day 3 where we assume only paracellular transport for the top left simulation; we assume both paracellular transport and passive uptake for top right simulations with a $\text{Log}D_{7.4} = -5$; we assume both paracellular transport and passive uptake for bottom right simulation with a $\text{Log}D_{7.4} = 0.74$; we assume both paracellular transport and passive uptake for bottom left simulations with a $\text{Log}D_{7.4} = 5$. In all simulations, ε and τ are assumed to be spatially varying, as described above.

Figure 4-17 shows the transport profiles for fluorouracil on day 3 where I vary the values of the $\text{Log}D_{7.4}$ parameter to account for high, low or mean (calculated) lipophilicity. Here I have used $\varepsilon(r)$ and $\tau(r)$ as with my initial simulations in **Figure 4-16** to include the

spatial variations in spheroid microarchitecture. The results show that changing the $\text{LogD}_{7.4}$ has a profound effect on the predicted transport profiles. When we look at implementing the calculated mean value for $\text{LogD}_{7.4}$ (i.e. 0.74), the compound is now readily taken up by the cells. There is some penetrance of the xenobiotic into the, but only to around 50 μm . When we use a relatively high value for $\text{LogD}_{7.4}$ (i.e. 5), we see that none of the xenobiotic is transported into the spheroid core as all of the initial dose is taken up into the periphery cells. These simulations further support the idea that the xenobiotic $\text{LogD}_{7.4}$ is a key parameter when determining the spheroid transport profile, as this value dramatically affects the ability of the compound to be taken up passively by the cells.

4.5.4 Transport of larger particles

So far, I have looked at particles that range between 0.321nm and 0.617nm. I will now finally investigate the profiles of larger particles, similar to those investigated by Goodman *et al.* [245]. The size of the pores within the mathematical model are 0.05 μm , and therefore, particles of this size will not be transported through the paracellular spaces. Goodman *et al.* [245], identify the size of the pores within their tumour spheroid non-necrotic regions as being 1.23 μm , 25 times larger than the pores in my spheroid model. The researchers also describe transport being impeded when the diffusing particles are 100-200nm. If we consider the same particle to pore size ration, this is equivalent to a particle of size 4nm diffusing in my system. As this is a hypothetical, I assume paracellular transport only with no given $\log\text{D}_{7.4}$ ($k_u = 0$). As a comparison, the dose of the 4nm particle is assumed to be the same as that of APAP (50mM). I will look at day 3 and day 21 profiles to see if the compaction of the spheroids over time, impedes the transport of this larger particle. I select the appropriate calculated $\varepsilon(r)$, $\tau(r)$ profiles for these respective (day3 and 21) spheroids.

4nm particle transport profiles

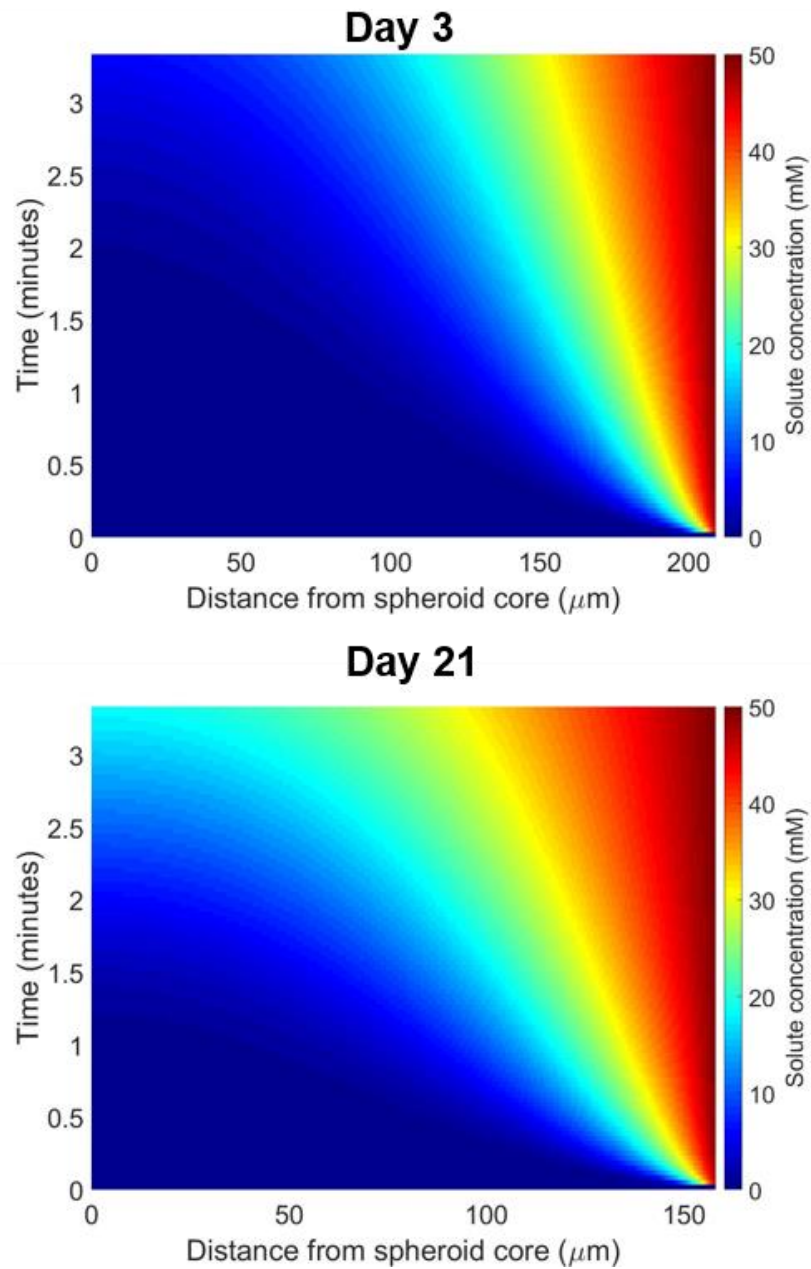


Figure 4-18 – Transport profile for 4nm particle for day 3 and day 21 where we assume only paracellular transport ($k_u = 0$), where $\varepsilon(r)$ and $\tau(r)$ as described in Table 7 and Table 8.

Figure 4-18 shows the transport of a 4nm particle. We can see that for paracellular transport of the particle on day 3, we do not get full penetrance of the particle. Instead, approximately 10 mM concentration accumulates in the spheroid core under steady state conditions. However for the same simulation on day 21, approximately 20 mM concentration reaches the core of the spheroid. These simulations indicate that the spheroidal compaction may impact on the transport profiles for larger particles. To investigate this more thoroughly, I now look at the transport profiles of a range of particle sizes (0.1 nm – 10 nm) for day 3, 7, 11, 18 and 21 spheroids to take into account the compaction as described previously. I will look at the concentration of the accumulated particle in the spheroid core under steady state conditions, and determine the proportion of the initial particle dose that penetrates to the core of the spheroids.

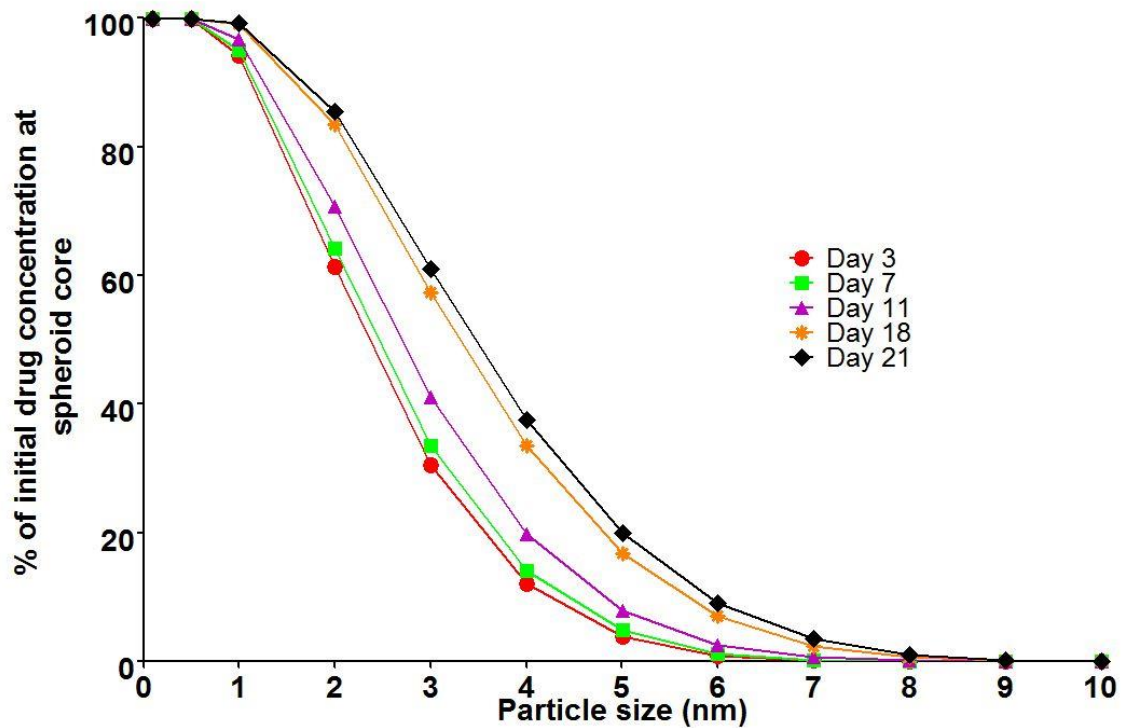


Figure 4-19 shows the percentage of the initial dose concentration (50 mM) that accumulates in the spheroid core under steady state conditions. Red circles represent spheroids at day 3, green squares represent spheroids at day 7, purple triangles represent spheroids at day 11, orange stars represent spheroids at day 18 and the black diamonds represent spheroids at day 21. In all cases, $k_u = 0$. For these simulations, spheroid radii are as follows; Day 3, $R = 209 \mu\text{m}$; day 7, $R = 198 \mu\text{m}$; day 11, $R = 186.7 \mu\text{m}$, day 18, $R = 166.7 \mu\text{m}$; day 21, $R = 158 \mu\text{m}$.

Figure 4-19 shows the transport profiles for hypothetical particles of varying sizes with no specific $\text{LogD}_{7.4}$ (i.e. no cellular passive uptake, where $k_u = 0$). The percentage of the initial particle dose concentration that accumulates in the centre of the spheroids under steady state conditions is plotted against particle size. For these simulations, R varies as previously described for 4000-cell spheroids (**Figure 2-4**), and the volumetric porosity and tortuosity also vary with respect to spheroid radius, $\varepsilon(r), \tau(r)$. From these results we can see that the compaction of the spheroids makes little difference when looking at the commonly used small molecule xenobiotics (0.321 - 0.617 nm). However, if we take a particle size of 2 nm for example, the PDE model predicts that at day 3, approximately 60% of the initial 50 mM dose will accumulate in the spheroid core. Compare that to day 18 and 21, and the PDE model predicts that approximately 80-85% of the initial 50 mM dose will accumulate in the spheroid core. This same trend can be seen for particles of between 3 nm and 6 nm. For example, for a 3 nm particle the model predicts that approximately 30% of the initial 50 mM dose concentration will penetrate to the spheroid core at day 3, and at day 18 and 21, the model predicts that approximately 60% of the initial 50 mM dose will penetrate to the spheroid core. The difference in predicted particle penetrance for varying culture times significantly reduces when we look at the particles of 6 nm or greater, and also for particles of 1 nm or smaller.

This result suggest that if we assume paracellular transport only and no passive uptake (i.e. $k_u = 0$), the compaction of the spheroids and/or the spatially varying values for ε and τ , significantly affect the transport profiles of these particles. In order to determine if this result is predominantly due to spheroid compaction, or due to spatial variations in $\varepsilon(r), \tau(r)$, we will use the PDE model to simulate the same transport scenarios as seen in **Figure 4-19**. However, we will use a fixed spheroid radius of 183.7 μm (representative of the mean value for 4000-cell spheroids over the culture period) (see **Figure 4-20**).

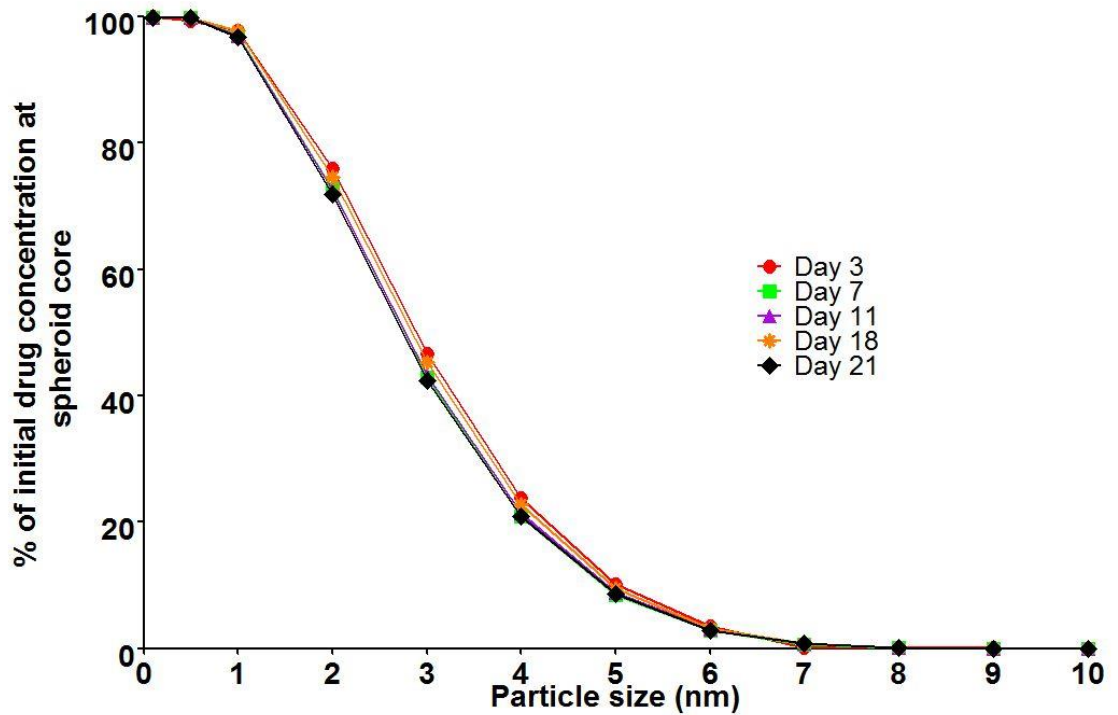


Figure 4-20 shows the percentage of the initial dose concentration (50mM) that accumulates in the spheroid core under steady state conditions. Red circles represent spheroids at day3, green squares represent spheroids at day 7, purple triangles represent spheroids at day 11, orange stars represent spheroids at day 18 and the black diamonds represent spheroids at day 21. In all cases, $k_{u} = 0$. For these simulations, the spheroid radii for all time points are fixed at, $R = 183.7 \mu\text{m}$.

Figure 4-20 shows the transport profiles for hypothetical particles of varying sizes (0.1 - 10 nm) with no specific $\text{LogD}_{7.4}$ and no passive uptake rate, ($k_u = 0$). The percentage of the initial particle dose concentration that accumulates in the centre of the spheroids under steady state conditions is again plotted against particle size. For these simulations, R is fixed at the mean value of 185.7 μm for 4000-cell spheroids. For these simulations, volumetric porosity and tortuosity are the only parameters that vary ($\varepsilon(r), \tau(r)$), as described in **Table 7** and **Table 8**.

These results show that, when we assume the spheroid radius is constant for all time points, and where porosity and tortuosity are both functions of spheroid radius, there is little difference between the transport profiles when we vary the size of the particle. If we take the 2 nm particle for example, the model predicts that approximately 70-75% of the initial dose concentration will accumulate in the spheroid core for all time points. This trend is observed for all of the particle sizes and therefore confirms that, whilst there may be slight variation in the % dose accumulation in the spheroid cores due to spatial variations in ε and τ , it is the compaction of the spheroids that impacts on the transport profiles with the most significance.

4.6 Chapter discussion

The aim of this chapter was to better understand the effects of cellular microarchitecture variations on the transport of xenobiotics. Previous studies that have investigated similar transport profiles of larger nanoparticles within tumour spheroids [187, 245] have provided some insight into the dynamics of transport within spheroid systems. However, an understanding of how small molecule xenobiotics are transported within liver spheroids has not been undertaken previously.

There are currently no studies that investigate the impact of spheroid volumetric porosity or tortuosity on the potential transport profiles of xenobiotics. Additionally, there are no studies that explore the effects of passive uptake rates, based on lipophilicity, as a means of assessing modes of xenobiotic transport.

Mathematical modelling of xenobiotic transport through hepatocyte spheroids

Initially, I identified changes in the microarchitecture of the experimental system (specifically ε and τ) (see **Figure 2-6** and **Figure 2-9**), where we see stratification of cells on the boundary of the spheroid producing an encapsulated model. Additionally there was cellular reorganisation and distribution, where we have more cells distributed at the periphery and fewer cells populating the spheroid core. I hypothesised that these micro-architectural features in the experimental model could impede the transport of xenobiotics.

I have previously described a mathematical diffusion model of oxygen. As oxygen is a small diffusing particle, it is known to readily and rapidly cross the cell membrane. However, for larger particles such as drugs and other compounds, they can be transported between cells, as well as into cells via passive uptake. I also wanted to be understand the importance of the xenobiotic-specific physicochemical characteristics, such as lipophilicity and what effect variations in these parameters may have had on transport into the microtissue.

Goodman *et al.* [245] previously described a mathematical model for nanoparticle diffusion into tumour spheroids. They explored the effect of the increasing particle size on transport profiles, whilst also considering the changing microarchitecture within the experimental system. They concluded that the size of the particle, particle binding rate and the porosity of the tissue, were key parameters to take into account when designing nanoparticles as carriers for drugs. Ward *et al.* [187] looked at the potential for spheroid cellular death as a result of modelling the penetrance of compounds with varying initial dose concentrations. Clearly this kind of modelling is extremely useful for developing an understanding of drug action on tumours. However, this approach has not yet been translated to an *in vitro* liver system.

I have developed a mathematical model based on porous media modelling, specifically applied to my experimental PRH spheroid, to investigate the effect of particle size, porosity and tortuosity, and physicochemical properties on the penetrance of xenobiotics into the *in vitro* liver system. I was able to develop this model and incorporate

Mathematical modelling of xenobiotic transport through hepatocyte spheroids

experimentally derived parameters for tortuosity and volumetric porosity and identify that these two parameters vary spatially against spheroid radius. A number of xenobiotics were considered in order to comprehensively determine the effects of the microtissue architecture on transport profiles. Additionally the intrinsic xenobiotic physicochemical characteristics were also investigated as a means to discern the likely transport profiles.

In particular, I analysed the transport profiles of APAP, vinblastine and fluorouracil to see if the varying sizes of these commonly utilised xenobiotics effected the transport profile characteristics. I chose APAP initially as this drug has been intensively investigated in terms of its pharmacology and toxicology and therefore I could benchmark my findings against the current literature. Vinblastine and fluorouracil were chosen as these were the smallest and largest xenobiotics from my list of commonly used small molecule compounds. Additionally, they both had distinctly different physicochemical properties based on their $\text{LogD}_{7.4}$ values and therefore the subsequent calculated cellular passive uptake rates were also different, providing a good comparison.

My results shown in **Figure 4-13** describe, firstly, the transport profiles of APAP for paracellular diffusion only and, secondly, with the additional assumption of passive uptake. The effect of passive uptake of APAP significantly effects the initial prediction of xenobiotic penetration. When assuming passive uptake, little APAP is transported to the spheroid core. This is an interesting point to discuss because toxicity caused by APAP overdose, for example, is experienced by hepatocytes within the pericentral zone of the sinusoid. If we look at the simulations where we assume passive uptake of APAP, none of the drug penetrates the entirety of the spheroid body. Therefore, the pericentral-like hepatocytes within the spheroid core may not be exposed to the drug and manifestations of known toxicity may not be captured accurately in this *in vitro* system.

I also investigated the effect of varying the values for both tortuosity and porosity to see if these radially coupled functions affect compound transport profiles. **Figure 4-13**, **Figure 4-14**, **Figure 4-15**, and **Figure 4-16** show the results when assuming that these

parameters are constant or functions of the spheroid radius. My results demonstrated that when considering the range of small molecule compounds from my list of xenobiotics (0.321 nm - 0.617 nm), we do not see an effect from these spatial variations in these micro-architectural features.

Figure 4-16 describes the transport profiles for fluorouracil. These simulations demonstrate the difference in transport profiles for xenobiotics that are highly lipophilic (such as APAP) versus those that have a low lipophilicity. I was able to show that the transport of fluorouracil was dominated by the paracellular route due to its low $\text{LogD}_{7.4}$, and subsequently low cellular uptake. I therefore conclude that the favoured transport route of xenobiotics within my *in vitro* model is determined mostly by its lipophilicity. When xenobiotics have high $\text{LogD}_{7.4}$ values, (i.e. highly lipophilic), calculated passive uptake rates are high which leads to more transport by passive uptake. This passive uptake into cells means that the xenobiotics will therefore not accumulate as readily in the centre of my spheroids. On the other hand, when xenobiotics have a relatively low $\text{LogD}_{7.4}$, (i.e. low lipophilicity), these low $\text{LogD}_{7.4}$ values result in subsequently calculated low passive uptake rates and therefore are more likely to be transported via the paracellular routes.

4.7 Conclusion

The results from my mathematical modelling have shown that the transport profiles of xenobiotics in my spheroid system are dependent on the specific physicochemical parameters as well as particle size. I have shown that spatial variations in volumetric porosity and tortuosity have little impact on the transport of larger molecules (see **Figure 4-20**), or that of commonly used small molecule compounds. I have also demonstrated that the size of the spheroids i.e. spheroidal compaction effects the transport profiles of larger molecules (see **Figure 4-19**).

A limitation of my *in silico* model system is that I did not include active transporter kinetics or other routes for xenobiotic transport, such as the bile canaliculi or cellular

endocytosis. If I was to include these other modes of cellular transport, I could potentially develop a more comprehensive model to assess the transport of these compounds. Within my model, cellular passive uptake refers to the movement of compounds down the concentration gradient, and therefore this process does not require cellular energy. In contrast, active transport requires the expenditure of ATP in order to pump molecules against the concentration gradient. Thus, the transport of molecules occurs from a low concentration to high concentration, or up the concentration gradient. The addition of this type of transport in my *in silico* system may well impact on the transport properties of certain xenobiotics. However, active transport seems to be limited to xenobiotics that are structurally similar to endogenous substances. Despite this, there are some drug compounds that have been shown to be absorbed via active transport mechanisms, namely equilibrative nucleoside transporters, which include s-adenosylmethionine, fludarabine, arabinosylcytosine and azidothymidine [270]. I can therefore assert that, the specific physicochemical properties of xenobiotics will determine their likely transport profiles. Additional experimental work to try and elucidate some of the key transport parameters would therefore further strengthen my modelling efforts.

My initial aim for this chapter was to develop a mathematical model to assess xenobiotic transport and penetration into a PRH spheroid. I have used novel mathematical techniques to derive parameters that would be extremely difficult to achieve experimentally. I have demonstrated that the changes in τ and ε with respect to culture time have little affect the transport profiles of the compounds that are commonly tested in these systems. From experimental observations of cellular reorganisation, I hypothesised that the uptake and transport of drugs may have been impeded by the spatial variations in microarchitecture. However, my mathematical modelling demonstrates that these features do not affect the xenobiotic transport profiles. Furthermore, the most sensitive parameters regarding transport into the microtissue is the lipophilicity of the molecule and the compaction of the spheroid.

Chapter 5: Concluding discussion

Our understanding of xenobiotic safety is continually developing due to improvements in the predictive capabilities of both experimental *in vitro* and *in silico* platforms. However, xenobiotic safety still remains a complicated area of research due to the wide variation in population susceptibility and also due to our limited understanding in the pharmacology of some novel xenobiotics. To elucidate this unknown pharmacology and toxicological potential, there is a requirement of more representative *in vitro* and *in silico* liver models. The implementation of the 3R's has also driven the process of accelerated *in vitro* model development and optimisation, leading to the progression of microtissue and fluid-flow, systems such as bioreactor technologies, microfluidic devices and 3D spheroid models. The literature has demonstrated that these more complex *in vitro* models are able to recapitulate more of the intricate physiological aspects of the liver as seen *in vivo* and therefore are considered more representative when compared to classical 2D and sandwich culture models [43, 54, 76, 81, 109, 250]. Despite the major developments in 3D and more complex *in vitro* systems, it is clear that the requirement of animal studies for toxicological investigations remains within the process of research and development. As a result, researchers are continually advancing methods by which the number of animals used in these studies is in compliance with the 3R's principles. The incorporation of more refined and representative 3D *in vitro* liver models that are able to successfully capture appropriate toxicity endpoints at early stage investigations, will inevitably facilitate the reduction of many potential compounds reaching later stage testing in animal trials.

Hepatocytes within the liver sinusoid are exposed to multiple solute gradients such as; oxygen, nutrients, hormones, and metabolites. These gradients are caused by successive cellular uptake along the sinusoid which reduces the concentrations of these solutes for subsequent cells. The variation in the cellular exposure to these solutes results in zonation, whereby cells along the sinusoid have varying levels of metabolic competence and gene expression. Recent *in vitro* and *in silico* models have attempted to replicate the oxygen gradients as seen *in vivo*, as the literature has reported that specific oxygen tensions are a key physiological characteristic that modulates liver zonation [12, 13, 118,

120]. It may be the case that the replication of these appropriate *in vivo*-like oxygen gradients results in appropriate zonation within the *in vitro* model.

In order for these systems to be utilised in industry for hepatotoxicity assessments, a comprehensive programme of evaluation and validation is required to demonstrate that these models add value with regards to exhibiting the relevant and appropriate experimental end points. Of the vast number of 3D models, microfluidic devices and bioreactor platforms available, spheroids in particular have been investigated with intensity over the last decade. The implementation of such relatively simplistic experimental methodologies for the production of a highly functional and representative high-throughput system illustrates the potential for the application of this model.

5.1 Chapter summaries

Chapter 2 in this thesis details the extensive experimental characterisation of a primary isolated rat hepatocyte spheroid model. My aim was to implement a method by which to produce a spheroid model that is relatively simple in terms of culture and laboratory manipulation, and also and cost-effective. Additionally I wanted to develop an *in vitro* model that would circumvent other limitations that have previously been described, such as the formation of necrosis. Size controllability of spheroids was an area initially highlighted as a limitation of numerous spheroid production techniques. Commercially available systems, like that of Insphero, utilise the hanging-drop method to produce size controllable spheroids, however, they are extremely expensive when compared to other systems [7].

I have implemented the application of the liquid-overlay technique (LOT) as a culture platform for PRH, as a means to produce size controllable cost-effective spheroids based on the initial seeding density of the cells. This novel combination of the LOT method and culturing PRH results in the formation of viable and reproducible spheroids. This is advantageous when compared with hepatic-derived cell lines, which tend to proliferate abundantly when cultured with the LOT. This proliferation results in spheroids that rapidly increase in size, resulting in the inability of oxygen to diffuse through the entirety

of the microtissue, culminating in the formation of centralised necrotic zones [230]. The formation of necrosis subsequently affects gene expression and the expression of metabolising enzymes and, as a consequence, the system is no longer representative of a healthy liver [271]. This brings in to question the appropriateness of such cell systems as tool for reliable hepatotoxicity investigations. By comparison, my PRH spheroid model shows no signs of central necrosis and the fact that these spheroids actually compact during the culture time, means that it is much more likely that oxygen will be able to penetrate the entirety of the microtissue.

Experimental characterisation has demonstrated the structural and functional polarisation of the hepatocytes within the spheroid via immunofluorescent analysis, and also confirmed the functionality of the apical membrane transport MRP2 via incubation with CMFDA. The demonstration of CMFDA transport via MRP2 is a key output from this research as this has never been carried out with primary isolated hepatocytes previously.

Interestingly, histological analysis of my PRH spheroid model has shown that the cells at the periphery of the spheroid seem to become distinctly different in morphology when compared with the more centralised hepatocytes. Only one other paper within the literature makes comment of the formation of a similar feature and identifies this to be the mesothelial lining of the liver *in vivo*, namely the Glisson's capsule [42]. Immunohistochemical analysis has confirmed that these peripheral cells are likely to be mesothelial and therefore the formation of this *in vivo*-like feature further strengthens my assertion that this spheroid model is representative of the *in vitro* liver.

My objective for Chapter 3 was to develop a mathematical model of oxygen diffusion, utilising experimental derived parameters, with the aim of establishing a prediction for optimal spheroid size before the onset of necrosis. To appropriately model this, I highlighted the need for model-specific parameters due to the extensive variability of OCR values in the literature. Appropriate oxygen delivery to cells is a critical component *in vivo* and consequently it is just as important a consideration for *in vitro* cell models. However, many cell culture protocols do not take into account the fundamental

properties of oxygen diffusion [179]. Many of the previously described culture models are used by a number of research laboratories and they are dependent on oxygen exchange at the air-medium interface [179]. Oxygen then travels by diffusion through the culture medium to the underlying cells. Distances from the air-medium interface to the cells vary between *in vitro* devices. For example, in my spheroid system, oxygen has to diffuse over 3.5mm from the air-medium interface to the top of the spheroid. Information regarding the determination of oxygen tensions experienced at the cell surface are extremely limited and this is often an overlooked feature [179].

My mathematical model was able to predict the oxygen tensions experienced by the cells at the spheroid boundary as well as the spheroid core and I subsequently used this to propose optimised operating conditions in order to recapitulate sinusoidal oxygen tensions. The optimisation of these operating conditions was firstly based on the size of the spheroids at specific times of the culture period, as a result of the initial cell seeding densities, and secondly on experimentally derived oxygen consumption rates (OCR).

Previous modelling approaches for oxygen diffusion within 3D microtissue models have utilised average OCR values for all cells within the spheroid [178]. However, after scrutinizing the experimental results from Seahorse analysis, I was able to demonstrate that OCR is a function of the spheroid radius. It is important to note that this relationship has previously been reported in the literature with tumour spheroids [231]. By incorporating this radius dependent OCR rate, I demonstrate that larger spheroids actually consume less oxygen than smaller ones, and this means that there is a higher oxygen potential to diffuse further into the spheroid core. My *in vitro* and *in silico* results demonstrate that when attempting to optimise a spheroid model, the specific OCR of the cells and the size stability of the spheroids over the course of the culture period are the important characteristics to determine. Size stability in particular will be dependent on the proliferative characteristics of the cells.

Chapter 4 describes the construction of a mathematical model, based on porous media modelling, to predict the diffusion of xenobiotics that vary in size and lipophilicity. The

key aim of this work was to improve our understanding of how xenobiotics are potentially transported within my spheroid model, and also to discern the effects of microarchitectural variations on the transport profiles of these xenobiotics. I incorporated experimental model-specific features including variations in cellular microarchitecture into my *in silico* model. My mathematical model incorporates solute transport route characteristics, namely tortuosity and pore fraction properties, in order to understand if changes in the microarchitecture of the experimental model would impact on the transport potential of xenobiotics. I have previously described a number of other publications that had investigated the transport potential of nanoparticles and other solutes in tumour spheroid models. Goodman *et al.* [245] investigated the diffusion, penetration and transport properties of nanoparticles in a tumour spheroid model and used experimental parameters for changes in the spheroid microarchitecture including, the volume fraction and tortuosity. Binding affinity and accessible volume fraction were also determined experimentally. Although this particular publication provided good insight into the potential transport profiles of nanoparticles in tumour spheroids, a more comprehensive understanding of how xenobiotics are transported within liver spheroids was required.

I was able to demonstrate that the transport profiles for small molecule xenobiotics were unchanged when I implemented my radially coupled terms for volumetric porosity and tortuosity. I was able to conclude that for the size of particles I was interested in, the subtle temporal changes in the cellular microarchitecture did not impact on their transport potential. I was, however, able to show that the most sensitive parameter that effected the transport profiles for the xenobiotics of interest, was the calculated $\text{LogD}_{7.4}$ values, which is a measure of particle lipophilicity. In particular, my findings demonstrated that for a wide range of dosing regimen, not all of the compounds penetrate the entirety of the spheroid due to uptake into peripheral cells.

I have demonstrated that microarchitectural changes within my spheroid model, do not affect the transport profiles of xenobiotics despite the concern from experimental observations. I have also shown that for my model the most sensitive parameter is the

lipophilicity/ $\text{LogD}_{7.4}$ value of the molecule for commonly used small molecule xenobiotics. Furthermore, when I consider larger molecules, I have been able to highlight that spheroidal compaction significantly effects the transport profiles of these particles.

These kinds of studies would be extremely difficult and costly to undertake experimentally, and therefore the mathematical modelling approaches taken in this research demonstrate the added value and appropriateness of my reciprocal *in vitro* and *in silico* modelling approach. Additionally, these results show that mathematical modelling with verifiable and model-specific parameters provides a more accurate model than those previously described in the literature.

5.2 Key research outputs

The overall aim of this research was develop a 3D microtissue model, suitable for repeat-dose hepatotoxicity testing. My extensive experimental characterisation and *in silico* modelling demonstrates that this system may be well placed as *in vitro* platform to assess hepatotoxicity after repeat-dose exposure to xenobiotics. I have been able to produce a novel *in vitro* liver spheroid model that can be cultured for extended periods (up to 31 days) that remain devoid of central regions of necrosis. Additionally, these spheroids display structural and functional polarisation of transporters with CMFDA transport via MRP2. The formation of the potential mesothelial lining surrounding the PRH spheroids is also something that has rarely been mentioned in the literature and strengthens the apparent *in vivo*-like morphology of my microtissue model.

I have also implemented numerous novel mathematical techniques and computational modelling approaches to allow for better utilisation of experimental results. The proposed optimised operating conditions for the recapitulation of sinusoidal oxygen gradients is perhaps the most impactful result from my research. Not only has the experimental characterisation shown that the PRH spheroids can be utilised for long-term investigations, but also that it may be possible to maintain healthy oxygen gradients for the duration of the culture period. Additionally, I have implemented mathematical models to derive microarchitectural properties of an experimental model, in way that

has never been utilised before for *in vitro* liver models. I concluded from my xenobiotic transport modelling that microarchitectural properties of the model would not affect the transport properties of selected compounds, further enhancing the utility of mathematical modelling in order to address concerns that would have been extremely difficult and costly to address experimentally.

5.3 Future work

In order to fully determine the application of my *in vitro* and *in silico* models, additional experimental work would help strengthen the conclusions from my research. In particular, further insight into the oxygen tensions experienced by spheroids in the culture set-up would help validate the mathematical modelling approaches. The use of an oxygen probe/dye could potentially be used to demonstrate the oxygen gradients within the spheroids. However, it is important to state that the mathematical modelling approach was taken because experimental determination of these parameters is extremely difficult to achieve. Seahorse analysis was chosen to determine spheroid OCR as this is considered an appropriate means of analysis when compared with other techniques such as immunofluorescent dyes etc.

A better understanding of the mechanisms driving the PRH spheroidal compaction during the culture period may also be warranted, however, numerous publications have previously focussed on, and attributed this compaction to the upregulation of key ECM and cytoskeletal components. A quantitative analysis of the spheroidal compaction along with improved cellular viability analysis may facilitate the mathematical modelling findings with regards to OCR values over culture time.

Finally, considering the characterisation work that has been undertaken and the complimentary mathematical modelling alongside this experimental work, I believe that the outlook for future work would be in testing compounds with known hepatotoxic potential utilising the PRH spheroid model. As I have demonstrated that this model is amenable in the laboratory and both cost-effective with high-throughput potential, it

may prove beneficial within the early compound screening tools already utilised across industry as well as academia.

5.4 Concluding statement

Hepatic-derived spheroid models have recently been incorporated into a number of industry sectors as tools for early-stage hepatotoxicity investigations. Although these spheroid models may be superior in predictive capabilities when compared with other more simplistic cultures and testing platforms, I suggest that the implementation of a primary cell line spheroid model that remains devoid of necrosis would be a further improvement to the battery of tools already utilised. In terms of the literature, although primary spheroid models have been developed and characterised for many years, there have been no investigations that have been able to detail experimental operating conditions for the maintenance of healthy liver oxygen gradients, and none that have critically evaluated size-dependent OCR analysis of spheroids I can conclude that using a combined research approach, both the *in vitro* and *in silico* modelling facilitates the development of these systems in a reciprocal fashion. I have shown that mathematical modelling of oxygen diffusion within my spheroid model, has allowed for the prediction of incubator oxygen levels required to recapitulate *in vivo* liver oxygen gradients for as long as possible. The maintenance of these *in vivo*-like gradients may therefore facilitate repeat-dose toxicological studies as the model is more representative of the *in vivo* organ. This research demonstrates that a combined quantitative systems pharmacology approach will pave the way for the development of more representative *in vitro* systems to be used for repeat-dose, and long-term toxicological investigations.

Chapter 6: Appendix

6.1 Appendix

Appendix shows the full list of xenobiotic compounds described in Chapter 4. I describe a number of key physicochemical parameters that were required for the modelling of xenobiotic transport. Xenobiotics are shown from smallest calculated radius to largest. This list of compounds is based on a list previously described by Separham *et al* [265]. Online databases including www.drugbank.ca, the national chemical database services (cds.rsc.org) etc. were used to obtain values for density and molecular weight. The calculated spherical radius was determined by implementing equation (4-6). LogD_{7.4} values were determined via computational analysis using ACD/labs software which uses structural SMILES files to calculate the appropriate LogD_{7.4} values based on pKa values. The passive uptake rates of these compounds were calculated by implementing equation (4-10).

<u>Name of xenobiotic</u>	<u>Density (g/cm³)</u>	<u>Molecular weight (Da)</u>	<u>Spherical Radius (cm)</u>	<u>LogD_{7.4}</u>	<u>Passive uptake rate (s⁻¹)</u>
Fluorouracil	1.557	130.08	3.21E-08	-5.59	1.07076E-06
Benzyl alcohol	1.047	108.14	3.45E-08	1.03	0.009693219
Ancitabine	2.01	225.20	3.54E-08	-3.25	2.68109E-05
Creatinolfosfate	1.65	197.13	3.62E-08	-6.29	4.08605E-07
APAP	1.26	151.16256	3.62E-08	0.34	0.003750205
Sulfanilamide	1.427	172.20	3.63E-08	-0.72	0.000871953
Dacarbazine	1.486	182.18	3.65E-08	-0.28	0.001597648
Norfenefrine	1.249	153.18	3.65E-08	-1.92	0.000167206
Penicillamine	1.204	149.21	3.66E-08	-1.58	0.000266975
Mizoribine	2.06	259.22	3.68E-08	-0.9	0.000680624
Acetylcysteine	1.294	163.19	3.68E-08	-2.73	5.48423E-05
Thiotepa	1.5	189.22	3.68E-08	0.52	0.004804421
Aciclovir	1.77	225.21	3.70E-08	-5.85	7.48673E-07
Aminocaproic acid	1.03	131.17	3.70E-08	-2.61	6.46904E-05
Vidarabine	2.08	267.24	3.71E-08	-1.02	0.00057701

<u>Name of xenobiotic</u>	<u>Density (g/cm³)</u>	<u>Molecular weight (Da)</u>	<u>Spherical Radius (cm)</u>	<u>LogD7.4</u>	<u>Passive uptake rate (s⁻¹)</u>
Flopropione	1.372	182.18	3.75E-08	2.32	0.057213829
Triaziquone	1.727	231.25	3.76E-08	-1.79	0.000199965
Minoxidil	1.521	209.25	3.79E-08	0.35	0.003802174
Tegafur	1.45	200.17	3.80E-08	-0.96	0.000626679
Tranexamic acid	1.096	157.21	3.85E-08	-2.18	0.00011691
Chlorothiazide	2.04	295.72	3.86E-08	-0.37	0.001411523
Amrinone	1.277	187.20	3.87E-08	-0.55	0.001101798
Chlorazanyl	1.483	221.65	3.90E-08	0.77	0.006777445
Bemegride	1.024	155.20	3.92E-08	1.53	0.019289369
Ethinamate	1.1	167.21	3.92E-08	-0.77	0.000813969
Caffeine	1.23	194.19	3.97E-08	-0.13	0.001963975
Mephesisin	1.152	182.22	3.97E-08	1.21	0.012418067
Cinoxacin	1.64	262.22	3.99E-08	-3.38	2.24187E-05
Diprophylline	1.57	254.25	4.00E-08	-1.1	0.000516853
Proxiphylline	1.46	238.24	4.01E-08	-0.2	0.001783598
Sulfathiazole	1.561	255.31	4.02E-08	-0.33	0.001491406
Carbromal	1.445	237.10	4.02E-08	-1.87	0.000179117
Cyclobutyrol	1.128	186.25	4.03E-08	-1.23	0.000432181
Guaifenesin	1.195	198.22	4.04E-08	0.57	0.005146666
Baclofen	1.285	213.66	4.04E-08	-0.94	0.000644168
Sulfadiazine	1.496	250.27	4.05E-08	-0.84	0.000739212
Doxofylline	1.59	266.26	4.05E-08	-0.7	0.000896287
Captopril	1.272	217.28	4.08E-08	-3.18	2.95224E-05
Nikethamide	1.042	178.23	4.08E-08	0.33	0.003698946
Sulfamethizole	1.562	270.32	4.09E-08	-1.17	0.000469384
Nalidixic acid	1.331	232.24	4.11E-08	-0.37	0.001411523
Glyconiazide	1.679	295.25	4.12E-08	-1.52	0.000289957
Orciprenaline	1.199	211.26	4.12E-08	-1.77	0.000205546
Trifluridine	1.646	296.20	4.15E-08	-0.22	0.001735174

<u>Name of xenobiotic</u>	<u>Density (g/cm³)</u>	<u>Molecular weight (Da)</u>	<u>Spherical Radius (cm)</u>	<u>LogD7.4</u>	<u>Passive uptake rate (s⁻¹)</u>
Busulfan	1.35	246.29	4.17E-08	-0.52	0.001148241
Mexiletine	0.979	179.26	4.17E-08	0.96	0.008802966
Sulfamerazine	1.439	264.30	4.18E-08	-0.02	0.002284983
Imipenem	1.62	299.34	4.18E-08	-5.28	1.64052E-06
Lofexidine	1.39	259.14	4.20E-08	1.73	0.025401421
Epirizole	1.25	234.26	4.20E-08	1.4	0.016129356
Propofol	0.948	178.27	4.21E-08	4.16	0.719894763
Metricrane	1.464	275.34	4.21E-08	-0.15	0.001910654
Phenobarbital	1.234	232.24	4.21E-08	-3.11	3.2508E-05
Methypylon	0.969	183.25	4.22E-08	0.23	0.003223354
Dichlorophen	1.419	269.13	4.22E-08	4.61	1.337315919
Sulfaethidole	1.499	284.35	4.22E-08	-0.66	0.000947011
Sulfalene	1.465	280.30	4.23E-08	-0.13	0.001963975
Meprobamate	1.139	218.25	4.24E-08	0.7	0.006154985
Ranimustine	1.69	327.72	4.25E-08	0.58	0.005217987
Bamethan	1.079	209.29	4.25E-08	-0.65	0.000960134
Chlorphenesin carbamate	1.365	265.09	4.25E-08	1.41	0.016352871
Ozagrel	1.17	228.25	4.26E-08	-1.09	0.000524015
Cyclophosphamide	1.33	261.09	4.27E-08	0.23	0.003223354
Ifosfamide	1.326	261.09	4.27E-08	0.23	0.003223354
Beclamide	1.145	225.72	4.28E-08	0.91	0.008217581
Aminophenazone	1.17	231.30	4.28E-08	0.76	0.006684809
Morphine	1.44	285.34	4.28E-08	-0.4	0.001354431
Cimetidine	1.27	252.34	4.29E-08	-0.25	0.001664991
Phenylbutazone	1.542	308.38	4.30E-08	0.85	0.007566273
Khellin	1.301	260.25	4.30E-08	1.78	0.027210907
Etamivan	1.115	223.27	4.30E-08	1.45	0.01727834
Mefenamic acid	1.203	241.29	4.30E-08	2.37	0.061289491

<u>Name of xenobiotic</u>	<u>Density (g/cm³)</u>	<u>Molecular weight (Da)</u>	<u>Spherical Radius (cm)</u>	<u>LogD7.4</u>	<u>Passive uptake rate (s⁻¹)</u>
Flufenamic acid	1.396	281.23	4.31E-08	2.57	0.080709752
Suprofen	1.29	260.31	4.31E-08	-0.77	0.000813969
Piromidic acid	1.4	288.31	4.34E-08	-2	0.000149774
Furosemide	1.606	330.74	4.34E-08	-0.03	0.002253751
Chlorpropamide	1.334	276.74	4.35E-08	0.94	0.008563968
Salbutamol	1.152	239.31	4.35E-08	-2.12	0.000126973
Chloramphenicol	1.547	323.13	4.36E-08	0.82	0.007260241
Ibudilast	1.09	230.31	4.38E-08	3.34	0.232892238
Ketoprofen	1.198	254.29	4.38E-08	-0.26	0.001642234
Pentoxifylline	1.31	278.31	4.38E-08	0.32	0.003648388
Carbuterol	1.248	267.33	4.40E-08	-1.99	0.00015185
Mitomycin	1.56	334.33	4.40E-08	-2.73	5.48423E-05
Tazanolast	1.343	289.29	4.40E-08	0.35	0.003802174
Pindolol	1.152	248.32	4.41E-08	-0.21	0.001759219
Trichlormethiazide	1.748	380.65	4.42E-08	0.13	0.002808911
Methylphenidate	1.07	233.31	4.42E-08	0.47	0.004484934
Flumazenil	1.39	303.29	4.42E-08	0.67	0.005906035
Procaine	1.077	236.31	4.43E-08	0.52	0.004804421
Pipemidic acid	1.38	303.32	4.43E-08	-2.72	5.56023E-05
Etomidate	1.11	244.29	4.44E-08	3.26	0.208611869
Secobarbital	1.079	238.28	4.44E-08	2.04	0.038917507
Carbutamide	1.226	271.33	4.44E-08	0.31	0.003598521
Procainamide	1.06	235.37	4.45E-08	-0.8	0.000781047
Bendazac	1.27	282.30	4.45E-08	-0.62	0.001000606
Azosemide	1.661	370.83	4.46E-08	1.3	0.014055523
Viloxazine	1.061	237.30	4.46E-08	0	0.002348751
Benzoctamine	1.114	249.36	4.46E-08	1.29	0.013863408
Nalorphine	1.38	311.38	4.47E-08	0.65	0.005745688
Sulfaphenazole	1.39	314.36	4.48E-08	0.98	0.009048634

<u>Name of xenobiotic</u>	<u>Density (g/cm³)</u>	<u>Molecular weight (Da)</u>	<u>Spherical Radius (cm)</u>	<u>LogD7.4</u>	<u>Passive uptake rate (s⁻¹)</u>
Ketobemidone	1.092	247.34	4.48E-08	1.18	0.011915795
Ciprofloxacin	1.461	331.35	4.48E-08	-1.29	0.000397928
Clorexolone	1.447	328.81	4.48E-08	0.71	0.006240279
Riboflavin	1.65	376.37	4.49E-08		0.002348751
Lidocaine	1.026	234.34	4.49E-08	2.31	0.056431814
Chlordiazepoxide	1.3	299.75	4.51E-08	2.16	0.045905954
Melphalan	1.32	305.20	4.51E-08	-0.7	0.000896287
Indobufen	1.275	295.34	4.51E-08	0.42	0.004186692
Azapropazone	1.29	300.36	4.52E-08	-0.75	0.000836685
Iopanoic acid	2.426	570.94	4.54E-08	1.42	0.016579484
Atenolol	1.125	266.34	4.54E-08	-1.99	0.00015185
Norfloxacin	1.344	319.34	4.55E-08	-1.61	0.000256177
Ajmaline	1.373	326.44	4.55E-08	0.08	0.002622123
Aztreonam	1.83	435.43	4.55E-08	-5.47	1.26304E-06
Ethylmorphine	1.31	313.40	4.56E-08	0.8	0.007063127
Gliclazide	1.35	323.41	4.56E-08	-0.18	0.001833374
Trofosfamide	1.35	323.59	4.56E-08	1.77	0.02683898
Oxaprozin	1.222	293.32	4.57E-08	1.13	0.011123412
Ampicillin	1.45	349.40	4.57E-08	-1.91	0.000169524
Midazolam	1.35	325.77	4.57E-08	3.92	0.517393555
Atropine	1.194	289.37	4.58E-08	-0.94	0.000644168
Pipradrol	1.103	267.37	4.58E-08	1.01	0.00943005
Nortriptyline	1.084	263.38	4.58E-08	3.17	0.184308776
Prothipendyl	1.168	285.41	4.59E-08	0.91	0.008217581
Dextromethorphan	1.11	271.40	4.59E-08	2.39	0.062999922
Propentofylline	1.25	306.36	4.60E-08	1.38	0.015691448
Pilsicainide	1.11	272.39	4.60E-08	0.53	0.004870999
Pimobendan	1.36	334.38	4.60E-08	1.81	0.028357897
Zimeldine	1.286	317.23	4.61E-08	4	0.577613074

<u>Name of xenobiotic</u>	<u>Density (g/cm³)</u>	<u>Molecular weight (Da)</u>	<u>Spherical Radius (cm)</u>	<u>LogD7.4</u>	<u>Passive uptake rate (s⁻¹)</u>
Clozapine	1.319	326.83	4.61E-08	1.96	0.034860131
Doxepin	1.122	279.38	4.62E-08	2.09	0.041689819
Diphenhydramine	1.025	255.36	4.62E-08	2.29	0.054899705
Chloropyramine	1.158	289.81	4.63E-08	1.53	0.019289369
Promazine	1.133	284.42	4.63E-08	2.67	0.092618131
Perlapine	1.16	291.40	4.64E-08	1.48	0.018006654
Thenalidine	1.14	286.43	4.64E-08	3.01	0.147881557
Zopiclone	1.54	388.81	4.64E-08	-0.41	0.001335919
locetamic acid	2.416	613.96	4.65E-08	0.18	0.003009006
Desipramine	1.047	266.69	4.66E-08	1.43	0.016809238
Protirelin	1.421	362.38	4.66E-08	-5.56	1.1159E-06
Piretanide	1.415	362.40	4.67E-08	-1.01	0.000585006
Maprotiline	1.081	277.41	4.67E-08	1.65	0.022753175
Nipradilol	1.27	326.35	4.67E-08	0.17	0.002967878
Benzthiazide	1.66	431.93	4.69E-08	0.94	0.008563968
Nadolol	1.189	309.41	4.69E-08	-0.81	0.000770371
Dibenzepin	1.134	295.37	4.69E-08	0.55	0.005006936
Zotepine	1.27	331.86	4.70E-08	5.24	3.182621662
Griseofulvin	1.35	352.77	4.70E-08	3.53	0.30249487
Fleroxacin	1.409	369.34	4.70E-08	-0.59	0.001042783
Tetracaine	1.004	264.37	4.71E-08	2.61	0.085277412
Methylergometrine	1.28	339.44	4.72E-08	1.39	0.015908895
Nizatidine	1.249	331.45	4.72E-08	0.98	0.009048634
Ranitidine	1.184	314.40	4.72E-08	0.23	0.003223354
Rebamipide	1.394	370.79	4.72E-08	-0.68	0.0009213
Quinidine	1.218	324.42	4.73E-08	1.6	0.021240122
Salazosulfapyridine	1.488	398.39	4.74E-08	0.03	0.002447755
Imipramine	1.041	280.41	4.74E-08	2.79	0.10924964
Mefruside	1.417	382.88	4.75E-08	1.76	0.026472138

<u>Name of xenobiotic</u>	<u>Density (g/cm³)</u>	<u>Molecular weight (Da)</u>	<u>Spherical Radius (cm)</u>	<u>LogD7.4</u>	<u>Passive uptake rate (s⁻¹)</u>
Tetracycline	1.644	444.43	4.75E-08	-4.26	6.67782E-06
Doxycycline	1.639	444.44	4.76E-08	-3.36	2.30444E-05
Tetroxoprim	1.232	334.38	4.76E-08	0.34	0.003750205
Quazepam	1.42	386.79	4.76E-08	4.06	0.627334272
Vinpocetine	1.28	350.46	4.77E-08	4.54	1.214492996
Dimetindene	1.065	292.42	4.78E-08	1.95	0.034383653
Pentazocine	1.036	285.43	4.78E-08	3	0.14586027
Oxyphenbutazone	1.241	342.38	4.78E-08	0.45	0.004363169
Sulpiride	1.236	341.43	4.78E-08	-1.39	0.000346764
Periciazine	1.32	365.49	4.79E-08	2.5	0.073297138
Trazodone	1.33	371.87	4.80E-08	1.49	0.018256184
Oxytetracycline	1.645	460.43	4.81E-08	-4.43	5.28477E-06
Etofenamate	1.317	369.34	4.81E-08	4.15	0.71005504
Chlortetracycline	1.704	478.89	4.81E-08	-2.75	5.33534E-05
Nitrendipine	1.28	360.37	4.82E-08	3.5	0.290259882
Floctafenine	1.437	406.36	4.82E-08	3.63	0.347126696
Penbutolol	1.03	291.43	4.82E-08	2	0.036832993
Binedaline	1.03	293.41	4.83E-08	2.26	0.052679181
Miconazole	1.451	416.13	4.84E-08	5.86	7.470660738
Chloroquine	1.111	319.18	4.85E-08	1.86	0.030377989
Terbinafine	1.007	291.43	4.86E-08	6.49	17.7791099
Bifonazole	1.07	310.40	4.86E-08	4.78	1.689829994
Budipine	1.009	293.45	4.87E-08	1.92	0.03299294
Piperidolate	1.11	323.43	4.87E-08	3.77	0.420887487
Fencarbamide	1.127	328.47	4.87E-08	2.97	0.139960671
Papaverine	1.161	339.39	4.88E-08	3.71	0.387528828
Clebopride	1.27	373.88	4.89E-08	1.99	0.03632955
Perazine	1.149	339.50	4.89E-08	3.43	0.263601583
Bentiromide	1.367	404.42	4.90E-08	0.61	0.005437935

<u>Name of xenobiotic</u>	<u>Density (g/cm³)</u>	<u>Molecular weight (Da)</u>	<u>Spherical Radius (cm)</u>	<u>LogD7.4</u>	<u>Passive uptake rate (s⁻¹)</u>
Methotrexate	1.536	454.45	4.90E-08	-4.9	2.76762E-06
Adiphenine	1.052	311.42	4.90E-08	3.14	0.176854052
Isradipine	1.249	371.39	4.90E-08	3.59	0.328533768
Risperidone	1.38	410.49	4.90E-08	2.1	0.042267544
Nilvadipine	1.29	385.38	4.91E-08	1.72	0.025054227
Fosfestrol	1.433	428.32	4.91E-08	-2.36	9.12568E-05
Kanamycin	1.62	484.50	4.91E-08	-6.84	1.91677E-07
Bufetolol	1.081	323.43	4.91E-08	-0.5	0.001180285
Thioridazine	1.237	370.57	4.92E-08	3.72	0.392899082
Felodipine	1.277	384.26	4.92E-08	4.83	1.81020606
Haloperidol	1.239	375.87	4.94E-08	2.18	0.04718707
Azelastine	1.25	381.90	4.95E-08	1.81	0.028357897
Dinoprost	1.153	354.49	4.96E-08	-0.47	0.001230037
Urapidil	1.26	387.48	4.96E-08	1.87	0.030798957
Tobramycin	1.52	467.52	4.96E-08	-8.72	1.44176E-08
Benperidol	1.24	381.45	4.96E-08	3.06	0.15841599
Propanidid	1.087	337.42	4.97E-08	2.3	0.055660489
Fluanisone	1.146	356.44	4.98E-08	3.14	0.176854052
Bevantolol	1.11	345.44	4.98E-08	1.77	0.02683898
Bromperidol	1.336	420.32	5.00E-08	2.36	0.060451769
Nemonapride	1.23	387.91	5.00E-08	2.02	0.037860907
Vesnarinone	1.246	395.46	5.01E-08	1.71	0.024711779
Domperidone	1.341	425.92	5.01E-08	1.75	0.026110309
Pipamperone	1.174	375.49	5.02E-08	1.45	0.01727834
Opipramol	1.129	363.55	5.04E-08	3.23	0.20017416
isoldipine	1.205	388.42	5.04E-08	4.38	0.974457751
Perphenazine	1.253	403.97	5.04E-08	4	0.577613074
Sisomicin	1.387	447.53	5.04E-08	-7.55	7.21443E-08
Trifluperidol	1.26	409.42	5.05E-08	2.29	0.054899705

<u>Name of xenobiotic</u>	<u>Density (g/cm³)</u>	<u>Molecular weight (Da)</u>	<u>Spherical Radius (cm)</u>	<u>LogD7.4</u>	<u>Passive uptake rate (s⁻¹)</u>
Moracizine	1.315	427.52	5.05E-08	2.29	0.054899705
Carvedilol	1.25	406.48	5.05E-08	3.09	0.165093515
Plaunotol	0.936	306.45	5.06E-08	5.75	6.421138159
Talinolol	1.11	363.50	5.06E-08	1.03	0.009693219
Cinnarizine	1.125	368.52	5.06E-08	4.46	1.087875045
Glisoxepide	1.37	449.52	5.07E-08	-1.63	0.000249222
Nicergoline	1.47	484.39	5.07E-08	4.3	0.872864869
Sulforidazine	1.221	402.57	5.08E-08	2.16	0.045905954
Tofisopam	1.15	382.46	5.09E-08	2.03	0.038385572
Cloricromen	1.189	395.88	5.09E-08	1.83	0.029149292
Nimodipine	1.25	418.45	5.10E-08	3.85	0.469874649
Doxorubicin	1.61	543.53	5.12E-08	1.11	0.010821414
Budesonide	1.27	430.54	5.12E-08	3.14	0.176854052
Daunorubicin	1.554	527.53	5.13E-08	1.23	0.012764624
Dehydrocholic	1.172	402.53	5.15E-08	-0.86	0.000719143
Suxibuzone	1.265	438.48	5.16E-08	0.17	0.002967878
Chenodeoxycholic acid	1.129	392.58	5.17E-08	2.05	0.039456814
Pivampicillin	1.33	463.55	5.17E-08	1.8	0.027970293
Netilmicin	1.32	461.56	5.18E-08	-6.84	1.91677E-07
Dextromoramide	1.121	392.54	5.18E-08	3.68	0.371854477
Etodroxizine	1.175	418.96	5.21E-08	1.59	0.020949806
Thiopropazine	1.237	446.63	5.23E-08	2.56	0.079606589
Oxatomide	1.175	426.56	5.24E-08	3.29	0.217405243
Buprenorphine	1.26	467.65	5.28E-08	2.46	0.069371169
Acarbose	1.7	631.58	5.28E-08	-4.18	7.45506E-06
Piritramide	1.15	430.59	5.30E-08	3.8	0.438628669
Dipyridamole	1.347	504.63	5.30E-08	-1.24	0.000426274
Pimozide	1.224	461.55	5.31E-08	2.91	0.128867681

<u>Name of xenobiotic</u>	<u>Density (g/cm³)</u>	<u>Molecular weight (Da)</u>	<u>Spherical Radius (cm)</u>	<u>LogD7.4</u>	<u>Passive uptake rate (s⁻¹)</u>
Etoposide	1.555	588.56	5.31E-08	0.3	0.003549335
Astemizole	1.2	458.58	5.33E-08	4.41	1.015532939
Ketoconazole	1.38	531.44	5.35E-08	3.43	0.263601583
Convallatoxin	1.41	550.65	5.37E-08	0.81	0.007161006
Carpipramine	1.143	446.64	5.37E-08	2.46	0.069371169
Calcitriol	1.063	416.64	5.38E-08	6.12	10.68466757
Sofalcone	1.149	450.53	5.38E-08	3.03	0.152008549
Ergotamine	1.47	581.67	5.39E-08	3.63	0.347126696
Proscillaridin	1.33	530.66	5.41E-08	3.9	0.503346455
Loperamide	1.187	477.04	5.42E-08	3.73	0.398343756
Meproscillaridin	1.29	544.69	5.51E-08	3.09	0.165093515
Mupirocin	1.183	500.63	5.52E-08	0.85	0.007566273
Verapamil	1.058	454.61	5.54E-08	2.33	0.058006681
Pantethine	1.277	554.72	5.56E-08	-1.4	0.000342024
Deserpidine	1.32	578.66	5.58E-08	3.72	0.392899082
Gefarnate	0.9	400.64	5.61E-08	10.53	4619.74511
Reserpine	1.329	608.69	5.66E-08	3.82	0.450869663
Iotroxic acid	2.648	1215.82	5.67E-08	-2.41	8.51883E-05
Iocarmic acid	2.57	1253.87	5.78E-08	-4.27	6.58655E-06
Ioxaglic acid	2.545	1268.89	5.83E-08	-4.04	9.03918E-06
Itraconazole	1.4	705.64	5.85E-08	4.29	0.860934307
Diclofenac Sodium	0.63	318.13	5.85E-08	0.95	0.008682644
Hexobendine	1.147	592.69	5.90E-08	3.52	0.298360286
Inositol nicotinate	1.5	810.73	5.98E-08	6.37	15.07252505
Oleandomycin	1.21	687.87	6.09E-08	0.48	0.004547084
Vincristine	1.406	824.97	6.15E-08	2.27	0.053409193
Vinblastine	1.37	810.99	6.17E-08	3.69	0.377007521

Bibliography

1. Park, B.K., et al., *Drug bioactivation and protein adduct formation in the pathogenesis of drug-induced toxicity*. *Chemico-Biological Interactions*, 2011. **192**(1–2): p. 30-36.
2. Heidari, R., et al., *Factors affecting drug-induced liver injury: antithyroid drugs as instances*. *Clin Mol Hepatol*, 2014. **20**(3): p. 237-48.
3. Williams, D.P., et al., *Novel in vitro and mathematical models for the prediction of chemical toxicity*. *Toxicology research*, 2013. **2**(1): p. 40-59.
4. Taylor, K., et al., *Estimates for worldwide laboratory animal use in 2005*. *Altern Lab Anim*, 2008. **36**(3): p. 327-42.
5. Hackam, D.G. and D.A. Redelmeier, *Translation of research evidence from animals to humans*. *Jama*, 2006. **296**(14): p. 1731-2.
6. Schechtman, L.M., *Implementation of the 3Rs (refinement, reduction, and replacement): validation and regulatory acceptance considerations for alternative toxicological test methods*. *ILAR J*, 2002. **43 Suppl**: p. S85-94.
7. Kyffin, J.A., et al., *Impact of cell types and culture methods on the functionality of in vitro liver systems – A review of cell systems for hepatotoxicity assessment*. *Toxicology in Vitro*, 2018. **48C**: p. 262-275.
8. Yuhas, J.M., et al., *A Simplified Method for Production and Growth of Multicellular Tumor Spheroids*. *Cancer Research*, 1977. **37**(10): p. 3639-3643.
9. Kmiec, Z., *Cooperation of liver cells in health and disease*. *Adv Anat Embryol Cell Biol*, 2001. **161**: p. III-XIII, 1-151.

10. Michalopoulos, G.K., *Liver Regeneration*. Journal of cellular physiology, 2007. **213**(2): p. 286-300.
11. Oinonen, T. and K.O. Lindros, *Zonation of hepatic cytochrome P-450 expression and regulation*. Biochemical Journal, 1998. **329**(Pt 1): p. 17-35.
12. Kietzmann, T., *Metabolic zonation of the liver: The oxygen gradient revisited*. Redox Biology, 2017. **11**: p. 622-630.
13. Kietzmann, T., et al., *Oxygen: modulator of physiological and pathophysiological processes in the liver*. Z Gastroenterol, 2006. **44**(1): p. 67-76.
14. Hofmann, A.F. and L.R. Hagey, *Bile acids: chemistry, pathochemistry, biology, pathobiology, and therapeutics*. Cell Mol Life Sci, 2008. **65**(16): p. 2461-83.
15. Godoy, P., et al., *Recent advances in 2D and 3D in vitro systems using primary hepatocytes, alternative hepatocyte sources and non-parenchymal liver cells and their use in investigating mechanisms of hepatotoxicity, cell signaling and ADME*. Arch Toxicol, 2013. **87**(8): p. 1315-530.
16. Tacke, F., T. Luedde, and C. Trautwein, *Inflammatory pathways in liver homeostasis and liver injury*. Clin Rev Allergy Immunol, 2009. **36**(1): p. 4-12.
17. Senoo, H., *Structure and function of hepatic stellate cells*. Med Electron Microsc, 2004. **37**(1): p. 3-15.
18. Ahmad, A. and R. Ahmad, *Understanding the mechanism of hepatic fibrosis and potential therapeutic approaches*. Saudi J Gastroenterol, 2012. **18**(3): p. 155-67.
19. Wisse, E., *An ultrastructural characterization of the endothelial cell in the rat liver sinusoid under normal and various experimental conditions, as a contribution to the distinction between endothelial and Kupffer cells*. Journal of Ultrastructure Research, 1972. **38**(5): p. 528-562.

20. Elvevold, K., B. Smedsrod, and I. Martinez, *The liver sinusoidal endothelial cell: a cell type of controversial and confusing identity*. Am J Physiol Gastrointest Liver Physiol, 2008. **294**(2): p. G391-400.
21. Gale, R.P., R.S. Sparkes, and D.W. Golde, *Bone marrow origin of hepatic macrophages (Kupffer cells) in humans*. Science, 1978. **201**(4359): p. 937-8.
22. Roberts, R.A., et al., *Role of the Kupffer cell in mediating hepatic toxicity and carcinogenesis*. Toxicol Sci, 2007. **96**(1): p. 2-15.
23. Larusso, N.F., *Morphology, Physiology, and Biochemistry of Biliary Epithelia*. Toxicologic Pathology, 1996. **24**(1): p. 84-89.
24. Rao, R.K. and G. Samak, *Bile duct epithelial tight junctions and barrier function*. Tissue Barriers, 2013. **1**(4): p. e25718.
25. Moore, K.L. and A.M.R. Agur, *Essential clinical anatomy*. 2007.
26. Raunio, H., et al., *Modeling of interactions between xenobiotics and cytochrome P450 (CYP) enzymes*. Frontiers in Pharmacology, 2015. **6**: p. 123.
27. Xu, C., C.Y. Li, and A.N. Kong, *Induction of phase I, II and III drug metabolism/transport by xenobiotics*. Arch Pharm Res, 2005. **28**(3): p. 249-68.
28. Awasthi, Y.C., S. Awasthi, and P. Zimniak, *Multiple transport proteins involved in the detoxification of endo-and xenobiotics*. Frontiers Biosc, 1997. **2**: p. d427-d437.
29. Brouwer, K.R., et al., *The Importance of In Vitro Liver Models: Experts Discuss Whole-Cell Systems, Transporter Function, and the Best Models for Future In Vitro Testing*. Applied In Vitro Toxicology, 2016. **2**(1): p. 1-7.
30. Moscato, S., et al., *Poly(vinyl alcohol)/gelatin Hydrogels Cultured with HepG2 Cells as a 3D Model of Hepatocellular Carcinoma: A Morphological Study*. J Funct Biomater, 2015. **6**(1): p. 16-32.

31. Knight, E., et al., *Alvetex®: Polystyrene Scaffold Technology for Routine Three Dimensional Cell Culture*, in *3D Cell Culture: Methods and Protocols*, J.W. Haycock, Editor. 2011, Humana Press: Totowa, NJ. p. 323-340.
32. Funatsu, K., et al., *Hybrid artificial liver using hepatocyte organoid culture*. *Artif Organs*, 2001. **25**(3): p. 194-200.
33. Huch, M., et al., *Long-term culture of genome-stable bipotent stem cells from adult human liver*. *Cell*, 2015. **160**(1-2): p. 299-312.
34. Domansky, K., et al., *Perfused multiwell plate for 3D liver tissue engineering*. *Lab Chip*, 2010. **10**(1): p. 51-8.
35. Tostoes, R.M., et al., *Human liver cell spheroids in extended perfusion bioreactor culture for repeated-dose drug testing*. *Hepatology*, 2012. **55**(4): p. 1227-36.
36. Gomez-Lechon, M.J., et al., *Competency of different cell models to predict human hepatotoxic drugs*. *Expert Opin Drug Metab Toxicol*, 2014. **10**(11): p. 1553-68.
37. Gomez-Lechon, M.J., et al., *Human hepatocytes in primary culture: the choice to investigate drug metabolism in man*. *Curr Drug Metab*, 2004. **5**(5): p. 443-62.
38. Knobloch, D., et al., *Human Hepatocytes: Isolation, Culture, and Quality Procedures*, in *Human Cell Culture Protocols*, R.R. Mitry and R.D. Hughes, Editors. 2012, Humana Press: Totowa, NJ. p. 99-120.
39. Rodriguez-Antona, C., et al., *Cytochrome P450 expression in human hepatocytes and hepatoma cell lines: molecular mechanisms that determine lower expression in cultured cells*. *Xenobiotica*, 2002. **32**(6): p. 505-20.
40. Bhogal, R.H., et al., *Isolation of primary human hepatocytes from normal and diseased liver tissue: a one hundred liver experience*. *PLoS One*, 2011. **6**(3): p. e18222.

41. Abu-Absi, S.F., et al., *Structural polarity and functional bile canaliculi in rat hepatocyte spheroids*. *Exp Cell Res*, 2002. **274**(1): p. 56-67.
42. Landry, J., et al., *Spheroidal aggregate culture of rat liver cells: histotypic reorganization, biomatrix deposition, and maintenance of functional activities*. *J Cell Biol*, 1985. **101**(3): p. 914-23.
43. Li, C.L., et al., *Survival advantages of multicellular spheroids vs. monolayers of HepG2 cells in vitro*. *Oncol Rep*, 2008. **20**(6): p. 1465-71.
44. LeCluyse, E.L., et al., *Organotypic liver culture models: meeting current challenges in toxicity testing*. *Crit Rev Toxicol*, 2012. **42**(6): p. 501-48.
45. Nakamura, S., et al., *Kaposi's sarcoma cells: long-term culture with growth factor from retrovirus-infected CD4+ T cells*. *Science*, 1988. **242**(4877): p. 426-30.
46. Bhandari, R.N., et al., *Liver tissue engineering: a role for co-culture systems in modifying hepatocyte function and viability*. *Tissue Eng*, 2001. **7**(3): p. 345-57.
47. Riccalton-Banks, L., et al., *Long-term culture of functional liver tissue: three-dimensional coculture of primary hepatocytes and stellate cells*. *Tissue Eng*, 2003. **9**(3): p. 401-10.
48. Thomas, R.J., et al., *The effect of three-dimensional co-culture of hepatocytes and hepatic stellate cells on key hepatocyte functions in vitro*. *Cells Tissues Organs*, 2005. **181**(2): p. 67-79.
49. Dash, A., et al., *Liver tissue engineering in the evaluation of drug safety*. *Expert Opin Drug Metab Toxicol*, 2009. **5**(10): p. 1159-74.
50. Bolt, H.M., J.G. Filser, and R.J. Laib, *Metabolic Activation and Pharmacokinetics in Hazard Assessment of Halogenated Ethylenes*, in *Industrial and Environmental Xenobiotics: Metabolism and Pharmacokinetics of Organic Chemicals and Metals Proceedings of an International Conference held in Prague, Czechoslovakia*,

- 27'30 May 1980, I. Gut, M. Cikrt, and G.L. Plaa, Editors. 1981, Springer Berlin Heidelberg: Berlin, Heidelberg. p. 161-167.
51. Cohen, S.M., et al., *Hemangiosarcoma in rodents: mode-of-action evaluation and human relevance*. Toxicol Sci, 2009. **111**(1): p. 4-18.
52. Koide, N., et al., *Formation of multicellular spheroids composed of adult rat hepatocytes in dishes with positively charged surfaces and under other nonadherent environments*. Exp Cell Res, 1990. **186**(2): p. 227-35.
53. Elsdale, T. and J. Bard, *Collagen substrata for studies on cell behavior*. J Cell Biol, 1972. **54**(3): p. 626-37.
54. Pampaloni, F., E.G. Reynaud, and E.H. Stelzer, *The third dimension bridges the gap between cell culture and live tissue*. Nat Rev Mol Cell Biol, 2007. **8**(10): p. 839-45.
55. Tazzyman, S., et al., *Inhibition of neutrophil infiltration into A549 lung tumors in vitro and in vivo using a CXCR2-specific antagonist is associated with reduced tumor growth*. Int J Cancer, 2011. **129**(4): p. 847-58.
56. Hirt, M.N., et al., *Functional improvement and maturation of rat and human engineered heart tissue by chronic electrical stimulation*. J Mol Cell Cardiol, 2014. **74**: p. 151-61.
57. Tibbitt, M.W. and K.S. Anseth, *Hydrogels as extracellular matrix mimics for 3D cell culture*. Biotechnol Bioeng, 2009. **103**(4): p. 655-63.
58. Roth, A. and T. Singer, *The application of 3D cell models to support drug safety assessment: Opportunities & challenges*. Advanced Drug Delivery Reviews, 2014. **69–70**: p. 179-189.

59. Kostadinova, R., et al., *A long-term three dimensional liver co-culture system for improved prediction of clinically relevant drug-induced hepatotoxicity*. *Toxicol Appl Pharmacol*, 2013. **268**(1): p. 1-16.
60. Lerche-Langrand, C. and H.J. Toutain, *Precision-cut liver slices: characteristics and use for in vitro pharmaco-toxicology*. *Toxicology*, 2000. **153**(1-3): p. 221-53.
61. Elferink, M.G., et al., *Gene expression analysis of precision-cut human liver slices indicates stable expression of ADME-Tox related genes*. *Toxicol Appl Pharmacol*, 2011. **253**(1): p. 57-69.
62. Soldatow, V.Y., et al., *In vitro models for liver toxicity testing*. *Toxicology research*, 2013. **2**(1): p. 23-39.
63. Toutain, H.J., et al., *Morphological and functional integrity of precision-cut rat liver slices in rotating organ culture and multiwell plate culture: effects of oxygen tension*. *Cell Biol Toxicol*, 1998. **14**(3): p. 175-90.
64. Price, R.J., et al., *Use of precision-cut rat liver slices for studies of xenobiotic metabolism and toxicity: comparison of the Krumdieck and Brendel tissue slicers*. *Xenobiotica*, 1998. **28**(4): p. 361-371.
65. Sugihara, K., S. Kitamura, and K. Tatsumi, *Strain differences of liver aldehyde oxidase activity in rats*. *Biochemistry and molecular biology international*, 1995. **37**(5): p. 861-869.
66. Kacew, S. and M.F. Festing, *Role of rat strain in the differential sensitivity to pharmaceutical agents and naturally occurring substances*. *J Toxicol Environ Health*, 1996. **47**(1): p. 1-30.
67. Olinga, P., et al., *Liver slices in in vitro pharmacotoxicology with special reference to the use of human liver tissue*. *Toxicology in Vitro*, 1997. **12**(1): p. 77-100.

68. Graaf, I.A., G.M. Groothuis, and P. Olinga, *Precision-cut tissue slices as a tool to predict metabolism of novel drugs*. *Expert Opin Drug Metab Toxicol*, 2007. **3**(6): p. 879-98.
69. Elferink, M.G.L., et al., *Gene expression analysis of precision-cut human liver slices indicates stable expression of ADME-Tox related genes*. *Toxicology and Applied Pharmacology*, 2011. **253**(1): p. 57-69.
70. Rashidi, H., et al., *Fluid shear stress modulation of hepatocyte-like cell function*. *Archives of Toxicology*, 2016. **90**: p. 1757-1761.
71. Bale, S.S., et al., *In Vitro Platforms for Evaluating Liver Toxicity*. *Experimental biology and medicine* (Maywood, N.J.), 2014. **239**(9): p. 1180-1191.
72. Donato, M.T., L. Tolosa, and M.J. Gomez-Lechon, *Culture and Functional Characterization of Human Hepatoma HepG2 Cells*. *Methods Mol Biol*, 2015. **1250**: p. 77-93.
73. Wrzesinski, K., et al., *HepG2/C3A 3D spheroids exhibit stable physiological functionality for at least 24 days after recovering from trypsinisation*. *Toxicology Research*, 2013. **2**(3): p. 163-172.
74. Guillouzo, A., et al., *The human hepatoma HepaRG cells: a highly differentiated model for studies of liver metabolism and toxicity of xenobiotics*. *Chem Biol Interact*, 2007. **168**(1): p. 66-73.
75. Sivertsson, L., et al., *CYP3A4 catalytic activity is induced in confluent Huh7 hepatoma cells*. *Drug Metab Dispos*, 2010. **38**(6): p. 995-1002.
76. Gaskell, H., et al., *Characterization of a functional C3A liver spheroid model*. *Toxicology Research*, 2016. **5**(4): p. 1053-1065.
77. Gerets, H.H., et al., *Characterization of primary human hepatocytes, HepG2 cells, and HepaRG cells at the mRNA level and CYP activity in response to inducers and*

- their predictivity for the detection of human hepatotoxins*. Cell Biol Toxicol, 2012. **28**(2): p. 69-87.
78. Hagiya, Y., et al., *Nrf2-dependent induction of human ABC transporter ABCG2 and heme oxygenase-1 in HepG2 cells by photoactivation of porphyrins: biochemical implications for cancer cell response to photodynamic therapy*. J Exp Ther Oncol, 2008. **7**(2): p. 153-67.
79. Castell, J.V., et al., *Hepatocyte cell lines: their use, scope and limitations in drug metabolism studies*. Expert Opinion on Drug Metabolism & Toxicology, 2006. **2**(2): p. 183-212.
80. Jennen, D.G.J., et al., *Comparison of HepG2 and HepaRG by Whole-Genome Gene Expression Analysis for the Purpose of Chemical Hazard Identification*. Toxicological Sciences, 2010. **115**(1): p. 66-79.
81. Chang, T.T. and M. Hughes-Fulford, *Monolayer and spheroid culture of human liver hepatocellular carcinoma cell line cells demonstrate distinct global gene expression patterns and functional phenotypes*. Tissue Eng Part A, 2009. **15**(3): p. 559-67.
82. Atienzar, F.A., et al., *Predictivity of dog co-culture model, primary human hepatocytes and HepG2 cells for the detection of hepatotoxic drugs in humans*. Toxicol Appl Pharmacol, 2014. **275**(1): p. 44-61.
83. Ramboer, E., et al., *Immortalized Human Hepatic Cell Lines for In Vitro Testing and Research Purposes*. Methods Mol Biol, 2015. **1250**: p. 53-76.
84. Sun, H., et al., *Label-free cell phenotypic profiling decodes the composition and signaling of an endogenous ATP-sensitive potassium channel*. Sci Rep, 2014. **4**: p. 4934.

85. Le Vee, M., et al., *Functional expression of sinusoidal and canalicular hepatic drug transporters in the differentiated human hepatoma HepaRG cell line*. Eur J Pharm Sci, 2006. **28**(1-2): p. 109-17.
86. Hart, S.N., et al., *A Comparison of Whole Genome Gene Expression Profiles of HepaRG Cells and HepG2 Cells to Primary Human Hepatocytes and Human Liver Tissues*. Drug Metabolism and Disposition, 2010. **38**(6): p. 988-994.
87. McGill, M.R., et al., *HepaRG cells: a human model to study mechanisms of acetaminophen hepatotoxicity*. Hepatology, 2011. **53**(3): p. 974-82.
88. Aninat, C., et al., *Expression of cytochromes P450, conjugating enzymes and nuclear receptors in human hepatoma HepaRG cells*. Drug Metab Dispos, 2006. **34**(1): p. 75-83.
89. Guguen-Guillouzo, C. and A. Guillouzo, *General review on in vitro hepatocyte models and their applications*. Methods Mol Biol, 2010. **640**: p. 1-40.
90. Langenbach, R., et al., *Maintenance of adult rat hepatocytes on C3H/10T1/2 cells*. Cancer Res, 1979. **39**(9): p. 3509-14.
91. Zinchenko, Y.S., et al., *Hepatocyte and kupffer cells co-cultured on micropatterned surfaces to optimize hepatocyte function*. Tissue Eng, 2006. **12**(4): p. 751-61.
92. Peters, S.J., et al., *Co-culture of primary rat hepatocytes with rat liver epithelial cells enhances interleukin-6-induced acute-phase protein response*. Cell Tissue Res, 2010. **340**(3): p. 451-7.
93. Kang, Y.B., et al., *Layered long-term co-culture of hepatocytes and endothelial cells on a transwell membrane: toward engineering the liver sinusoid*. Biofabrication, 2013. **5**(4): p. 045008.

94. Jemnitz, K., et al., *A transgenic rat hepatocyte - Kupffer cell co-culture model for evaluation of direct and macrophage-related effect of poly(amidoamine) dendrimers*. *Toxicol In Vitro*, 2017. **38**: p. 159-169.
95. Kegel, V., et al., *Subtoxic Concentrations of Hepatotoxic Drugs Lead to Kupffer Cell Activation in a Human In Vitro Liver Model: An Approach to Study DILI*. *Mediators Inflamm*, 2015. **2015**: p. 640631.
96. Auth, M.K., et al., *Preservation of the synthetic and metabolic capacity of isolated human hepatocytes by coculture with human biliary epithelial cells*. *Liver Transpl*, 2005. **11**(4): p. 410-9.
97. Andersson, T.B., *Evolution of Novel 3D Culture Systems for Studies of Human Liver Function and Assessments of the Hepatotoxicity of Drugs and Drug Candidates*. *Basic Clin Pharmacol Toxicol*, 2017. **121**(4): p. 234-238.
98. Dunn, J.C., R.G. Tompkins, and M.L. Yarmush, *Long-term in vitro function of adult hepatocytes in a collagen sandwich configuration*. *Biotechnol Prog*, 1991. **7**(3): p. 237-45.
99. Anthony P. Napolitano, P.C., Dylan M. Dean, and Jeffrey R. Morgan., *Dynamics of the Self-Assembly of Complex Cellular Aggregates on Micromolded Nonadhesive Hydrogels*. *Tissue Engineering.*, 2007. **13**(8): p. 2087-2094.
100. Ramaiahgari, S.C., et al., *A 3D in vitro model of differentiated HepG2 cell spheroids with improved liver-like properties for repeated dose high-throughput toxicity studies*. *Arch Toxicol*, 2014. **88**(5): p. 1083-95.
101. Gillette, B.M., et al., *Engineering extracellular matrix structure in 3D multiphase tissues*. *Biomaterials*, 2011. **32**(32): p. 8067-76.
102. van Zijl, F. and W. Mikulits, *Hepatospheres: Three dimensional cell cultures resemble physiological conditions of the liver*. *World J Hepatol*, 2010. **2**(1): p. 1-7.

103. Phung, Y.T., et al., *Rapid generation of in vitro multicellular spheroids for the study of monoclonal antibody therapy*. J Cancer, 2011. **2**: p. 507-14.
104. Kelm, J.M., et al., *Design of custom-shaped vascularized tissues using microtissue spheroids as minimal building units*. Tissue Eng, 2006. **12**(8): p. 2151-60.
105. Foty, R.A. and M.S. Steinberg, *The differential adhesion hypothesis: a direct evaluation*. Dev Biol, 2005. **278**(1): p. 255-63.
106. Rebelo, S.P., et al., *HepaRG microencapsulated spheroids in DMSO-free culture: novel culturing approaches for enhanced xenobiotic and biosynthetic metabolism*. Arch Toxicol, 2015. **89**(8): p. 1347-58.
107. Lee, B.H., et al., *Modulation of Huh7.5 spheroid formation and functionality using modified PEG-based hydrogels of different stiffness*. PLoS One, 2015. **10**(2): p. e0118123.
108. Kelm, J.M., et al., *Method for generation of homogeneous multicellular tumor spheroids applicable to a wide variety of cell types*. Biotechnol Bioeng, 2003. **83**(2): p. 173-80.
109. Sakai, Y., S. Yamagami, and K. Nakazawa, *Comparative analysis of gene expression in rat liver tissue and monolayer- and spheroid-cultured hepatocytes*. Cells Tissues Organs, 2010. **191**(4): p. 281-8.
110. Kanebratt, K.P. and T.B. Andersson, *Evaluation of HepaRG cells as an in vitro model for human drug metabolism studies*. Drug Metab Dispos, 2008. **36**(7): p. 1444-52.
111. Gunness, P., et al., *3D organotypic cultures of human HepaRG cells: a tool for in vitro toxicity studies*. Toxicol Sci, 2013. **133**(1): p. 67-78.
112. Leite, S.B., et al., *Three-dimensional HepaRG model as an attractive tool for toxicity testing*. Toxicol Sci, 2012. **130**(1): p. 106-16.

113. Sison-Young, R.L., et al., *Comparative Proteomic Characterization of 4 Human Liver-Derived Single Cell Culture Models Reveals Significant Variation in the Capacity for Drug Disposition, Bioactivation, and Detoxication*. *Toxicol Sci*, 2015. **147**(2): p. 412-24.
114. Wang, S., et al., *Three-dimensional primary hepatocyte culture in synthetic self-assembling peptide hydrogel*. *Tissue Eng Part A*, 2008. **14**(2): p. 227-36.
115. LeCluyse, E.L., K.L. Audus, and J.H. Hochman, *Formation of extensive canalicular networks by rat hepatocytes cultured in collagen-sandwich configuration*. *Am J Physiol*, 1994. **266**(6 Pt 1): p. C1764-74.
116. Mehta, G., et al., *Opportunities and Challenges for use of Tumor Spheroids as Models to Test Drug Delivery and Efficacy*. *Journal of controlled release : official journal of the Controlled Release Society*, 2012. **164**(2): p. 192-204.
117. Vadivelu, R., et al., *Microfluidic Technology for the Generation of Cell Spheroids and Their Applications*. *Micromachines*, 2017. **8**(4): p. 94.
118. Jungermann, K. and T. Kietzmann, *Oxygen: modulator of metabolic zonation and disease of the liver*. *Hepatology*, 2000. **31**(2): p. 255-60.
119. Anundi, I., et al., *Zonation of acetaminophen metabolism and cytochrome P450 2E1-mediated toxicity studied in isolated periportal and perivenous hepatocytes*. *Biochem Pharmacol*, 1993. **45**(6): p. 1251-9.
120. Jungermann, K. and T. Kietzmann, *Zonation of parenchymal and nonparenchymal metabolism in liver*. *Annu Rev Nutr*, 1996. **16**: p. 179-203.
121. Ferrigno, A., et al., *Oxygen tension-independent protection against hypoxic cell killing in rat liver by low sodium*. *Eur J Histochem*, 2017. **61**(2): p. 2798.

122. Zanoni, M., et al., *3D tumor spheroid models for in vitro therapeutic screening: a systematic approach to enhance the biological relevance of data obtained*. Sci Rep, 2016. **6**: p. 19103.
123. Grimes, D.R., et al., *A method for estimating the oxygen consumption rate in multicellular tumour spheroids*. Journal of the Royal Society Interface, 2014. **11**(92): p. 20131124.
124. Lauschke, V.M., et al., *Novel 3D Culture Systems for Studies of Human Liver Function and Assessments of the Hepatotoxicity of Drugs and Drug Candidates*. Chem Res Toxicol, 2016. **29**(12): p. 1936-1955.
125. Messner, S., et al., *Multi-cell type human liver microtissues for hepatotoxicity testing*. Arch Toxicol, 2013. **87**(1): p. 209-13.
126. Bell, C.C., et al., *Characterization of primary human hepatocyte spheroids as a model system for drug-induced liver injury, liver function and disease*. Sci Rep, 2016. **6**: p. 25187.
127. Lin, R.Z., et al., *Dynamic analysis of hepatoma spheroid formation: roles of E-cadherin and beta1-integrin*. Cell Tissue Res, 2006. **324**(3): p. 411-22.
128. Kelm, J.M. and M. Fussenegger, *Microscale tissue engineering using gravity-enforced cell assembly*. Trends Biotechnol, 2004. **22**(4): p. 195-202.
129. Cho, C.H., et al., *Oxygen uptake rates and liver-specific functions of hepatocyte and 3T3 fibroblast co-cultures*. Biotechnol Bioeng, 2007. **97**(1): p. 188-99.
130. Birgersdotter, A., R. Sandberg, and I. Ernberg, *Gene expression perturbation in vitro--a growing case for three-dimensional (3D) culture systems*. Semin Cancer Biol, 2005. **15**(5): p. 405-12.
131. Suter-Dick, L., et al., *Stem cell-derived systems in toxicology assessment*. Stem Cells Dev, 2015. **24**(11): p. 1284-96.

132. Ringel, M., et al., *Hepatocytes cultured in alginate microspheres: an optimized technique to study enzyme induction*. *Toxicology*, 2005. **206**(1): p. 153-167.
133. Iles, L.R. and G.A. Bartholomeusz, *Three-Dimensional Spheroid Cell Culture Model for Target Identification Utilizing High-Throughput RNAi Screens*, in *High-Throughput RNAi Screening: Methods and Protocols*, D.O. Azorsa and S. Arora, Editors. 2016, Springer New York: New York, NY. p. 121-135.
134. Mattei, G., et al., *Decellularized Human Liver Is Too Heterogeneous for Designing a Generic Extracellular Matrix Mimic Hepatic Scaffold*. *Artif Organs*, 2017. **41**(12): p. E347-e355.
135. Allen, A.B., et al., *Functional Augmentation of Naturally-Derived Materials for Tissue Regeneration*. *Annals of biomedical engineering*, 2015. **43**(3): p. 555-567.
136. Chan, B.P. and K.W. Leong, *Scaffolding in tissue engineering: general approaches and tissue-specific considerations*. *European Spine Journal*, 2008. **17**(Suppl 4): p. 467-479.
137. Cho, C.S., et al., *Galactose-carrying polymers as extracellular matrices for liver tissue engineering*. *Biomaterials*, 2006. **27**(4): p. 576-585.
138. Hayward, A.S., et al., *Galactose-functionalized polyHIPE scaffolds for use in routine three dimensional culture of mammalian hepatocytes*. *Biomacromolecules*, 2013. **14**(12): p. 4271-7.
139. Bokhari, M., et al., *Culture of HepG2 liver cells on three dimensional polystyrene scaffolds enhances cell structure and function during toxicological challenge*. *J Anat*, 2007. **211**(4): p. 567-76.
140. Schutte, M., et al., *Rat primary hepatocytes show enhanced performance and sensitivity to acetaminophen during three-dimensional culture on a polystyrene scaffold designed for routine use*. *Assay Drug Dev Technol*, 2011. **9**(5): p. 475-86.

141. Nantasanti, S., et al., *Concise Review: Organoids Are a Powerful Tool for the Study of Liver Disease and Personalized Treatment Design in Humans and Animals*. *Stem Cells Transl Med*, 2016. **5**(3): p. 325-30.
142. Dutta, D., I. Heo, and H. Clevers, *Disease Modeling in Stem Cell-Derived 3D Organoid Systems*. *Trends Mol Med*, 2017. **23**(5): p. 393-410.
143. Fatehullah, A., S.H. Tan, and N. Barker, *Organoids as an in vitro model of human development and disease*. *Nat Cell Biol*, 2016. **18**(3): p. 246-54.
144. Lu, W.Y., et al., *Hepatic progenitor cells of biliary origin with liver repopulation capacity*. *Nat Cell Biol*, 2015. **17**(8): p. 971-983.
145. Huch, M., et al., *In vitro expansion of single Lgr5+ liver stem cells induced by Wnt-driven regeneration*. *Nature*, 2013. **494**(7436): p. 247-50.
146. Takebe, T., et al., *Vascularized and functional human liver from an iPSC-derived organ bud transplant*. *Nature*, 2013. **499**(7459): p. 481-4.
147. Sirenko, O., et al., *High-Content Assays for Hepatotoxicity Using Induced Pluripotent Stem Cell-Derived Cells*. *Assay and Drug Development Technologies*, 2014. **12**(1): p. 43-54.
148. Gomez-Lechon, M.J. and L. Tolosa, *Human hepatocytes derived from pluripotent stem cells: a promising cell model for drug hepatotoxicity screening*. *Arch Toxicol*, 2016. **90**(9): p. 2049-61.
149. Griffin, S.J. and J.B. Houston, *Prediction of in vitro intrinsic clearance from hepatocytes: comparison of suspensions and monolayer cultures*. *Drug Metab Dispos*, 2005. **33**(1): p. 115-20.
150. Houston, J.B. and D.J. Carlile, *Prediction of hepatic clearance from microsomes, hepatocytes, and liver slices*. *Drug Metab Rev*, 1997. **29**(4): p. 891-922.

151. Ekins, S., et al., *Quantitative differences in phase I and II metabolism between rat precision-cut liver slices and isolated hepatocytes*. Drug Metabolism and Disposition, 1995. **23**(11): p. 1274.
152. Riley, R.J., D.F. McGinnity, and R.P. Austin, *A unified model for predicting human hepatic, metabolic clearance from in vitro intrinsic clearance data in hepatocytes and microsomes*. Drug Metab Dispos, 2005. **33**(9): p. 1304-11.
153. Zanelli, U., et al., *Comparison of Cryopreserved HepaRG Cells with Cryopreserved Human Hepatocytes for Prediction of Clearance for 26 Drugs*. Drug Metabolism and Disposition, 2012. **40**(1): p. 104.
154. Wang, W.W., et al., *Assessment of a micropatterned hepatocyte coculture system to generate major human excretory and circulating drug metabolites*. Drug Metab Dispos, 2010. **38**(10): p. 1900-5.
155. Sivaraman, A., et al., *A microscale in vitro physiological model of the liver: predictive screens for drug metabolism and enzyme induction*. Curr Drug Metab, 2005. **6**(6): p. 569-91.
156. Jones, H.M. and K. Rowland-Yeo, *Basic Concepts in Physiologically Based Pharmacokinetic Modeling in Drug Discovery and Development*. CPT: Pharmacometrics & Systems Pharmacology, 2013. **2**(8): p. e63.
157. Tuntland, T., et al., *Implementation of pharmacokinetic and pharmacodynamic strategies in early research phases of drug discovery and development at Novartis Institute of Biomedical Research*. Frontiers in Pharmacology, 2014. **5**: p. 174.
158. Teorell, T., *Kinetics of distribution of substances administered to the body, II : The intravascular modes of administration*. Archives internationales de pharmacodynamie et de therapie, 1937. **57**: p. 226-240.

159. Maharaj, A.R. and A.N. Edginton, *Physiologically Based Pharmacokinetic Modeling and Simulation in Pediatric Drug Development*. CPT: Pharmacometrics & Systems Pharmacology, 2014. **3**(11): p. e148.
160. Pilari, S., et al., *Development of Physiologically Based Organ Models to Evaluate the Pharmacokinetics of Drugs in the Testes and the Thyroid Gland*. CPT: Pharmacometrics & Systems Pharmacology, 2017. **6**(8): p. 532-542.
161. Veng-Pedersen, P., *Noncompartmentally-based pharmacokinetic modeling*. Advanced Drug Delivery Reviews, 2001. **48**(2): p. 265-300.
162. Upton, R.N., W.B. Runciman, and L.E. Mather, *Regional pharmacokinetics. III. Modelling methods*. Biopharm Drug Dispos, 1991. **12**(1): p. 1-15.
163. Pang, K.S. and M. Rowland, *Hepatic clearance of drugs. I. Theoretical considerations of a "well-stirred" model and a "parallel tube" model. Influence of hepatic blood flow, plasma and blood cell binding, and the hepatocellular enzymatic activity on hepatic drug clearance*. J Pharmacokinet Biopharm, 1977. **5**(6): p. 625-53.
164. Liu, L. and K.S. Pang, *An integrated approach to model hepatic drug clearance*. Eur J Pharm Sci, 2006. **29**(3-4): p. 215-30.
165. Schneider, G., P. Coassolo, and T. Lavé, *Combining in Vitro and in Vivo Pharmacokinetic Data for Prediction of Hepatic Drug Clearance in Humans by Artificial Neural Networks and Multivariate Statistical Techniques*. Journal of Medicinal Chemistry, 1999. **42**(25): p. 5072-5076.
166. Benet, L.Z. and P. Zia-Amirhosseini, *Basic principles of pharmacokinetics*. Toxicol Pathol, 1995. **23**(2): p. 115-23.
167. Gu, X. and J.E. Manautou, *Molecular mechanisms underlying chemical liver injury*. Expert reviews in molecular medicine, 2012. **14**: p. e4-e4.

168. Rowland, M., L.Z. Benet, and G.G. Graham, *Clearance concepts in pharmacokinetics*. J Pharmacokinet Biopharm, 1973. **1**(2): p. 123-36.
169. Winkler, K., Keiding, S., Tystru N., *The liver: Quantitative aspects of structure and functions*. Karger, Basel, 1973: p. p 144-155.
170. Ahmad, A.B., P.N. Bennett, and M. Rowland, *Models of hepatic drug clearance: discrimination between the 'well stirred' and 'parallel-tube' models*. J Pharm Pharmacol, 1983. **35**(4): p. 219-24.
171. Robinson, P.K., *Enzymes: principles and biotechnological applications*. Essays in Biochemistry, 2015. **59**: p. 1-41.
172. Keiding, S., *Hepatic clearance and liver blood flow*. J Hepatol, 1987. **4**(3): p. 393-8.
173. Zhuang, X. and C. Lu, *PBPK modeling and simulation in drug research and development*. Acta Pharmaceutica Sinica B, 2016. **6**(5): p. 430-440.
174. Hartmanshenn, C., M. Scherholz, and I.P. Androulakis, *Physiologically-based Pharmacokinetic Models: Approaches for Enabling Personalized Medicine*. Journal of pharmacokinetics and pharmacodynamics, 2016. **43**(5): p. 481-504.
175. Min, J.S. and S.K. Bae, *Prediction of drug-drug interaction potential using physiologically based pharmacokinetic modeling*. Arch Pharm Res, 2017. **40**(12): p. 1356-1379.
176. Wagner, C., et al., *Application of Physiologically Based Pharmacokinetic (PBPK) Modeling to Support Dose Selection: Report of an FDA Public Workshop on PBPK*. CPT: Pharmacometrics & Systems Pharmacology, 2015. **4**(4): p. 226-230.
177. Ward, J.P. and J.R. King, *Mathematical modelling of avascular-tumour growth*. IMA J Math Appl Med Biol, 1997. **14**(1): p. 39-69.

178. Aleksandrova, A.V., et al., *Mathematical and Experimental Model of Oxygen Diffusion for HepaRG Cell Spheroids*. Bull Exp Biol Med, 2016. **160**(6): p. 857-60.
179. Place, T.L., F.E. Domann, and A.J. Case, *Limitations of oxygen delivery to cells in culture: An underappreciated problem in basic and translational research*. Free Radical Biology and Medicine, 2017. **113**: p. 311-322.
180. Yu, F., et al., *A perfusion incubator liver chip for 3D cell culture with application on chronic hepatotoxicity testing*. Scientific Reports, 2017. **7**(1): p. 14528.
181. Rotem, A., et al., *Oxygen uptake rates in cultured rat hepatocytes*. Biotechnol Bioeng, 1992. **40**(10): p. 1286-91.
182. Foy, B.D., et al., *A device to measure the oxygen uptake rate of attached cells: importance in bioartificial organ design*. Cell Transplant, 1994. **3**(6): p. 515-27.
183. Mendizabal, M. and M.O. Silva, *Liver transplantation in acute liver failure: A challenging scenario*. World Journal of Gastroenterology, 2016. **22**(4): p. 1523-1531.
184. Andria, B., et al., *Liver Cell Culture Devices*. Cell Medicine, 2010. **1**(1): p. 55-70.
185. Yu, C.B., X.P. Pan, and L.J. Li, *Progress in bioreactors of bioartificial livers*. Hepatobiliary Pancreat Dis Int, 2009. **8**(2): p. 134-40.
186. Yarmush, M.L., et al., *Hepatic tissue engineering. Development of critical technologies*. Ann N Y Acad Sci, 1992. **665**: p. 238-52.
187. Ward, J.P. and J.R. King, *Mathematical modelling of drug transport in tumour multicell spheroids and monolayer cultures*. Math Biosci, 2003. **181**(2): p. 177-207.
188. Byrne, H.M., et al., *Modelling aspects of cancer dynamics: a review*. Philos Trans A Math Phys Eng Sci, 2006. **364**(1843): p. 1563-78.

189. Erlanson, M., E. Daniel-Szolgay, and J. Carlsson, *Relations between the penetration, binding and average concentration of cytostatic drugs in human tumour spheroids*. *Cancer Chemotherapy and Pharmacology*, 1992. **29**(5): p. 343-353.
190. Duchting, W. and T. Vogelsaenger, *Analysis, forecasting, and control of three-dimensional tumor growth and treatment*. *J Med Syst*, 1984. **8**(5): p. 461-75.
191. Al-Husari, M., C. Murdoch, and S.D. Webb, *A cellular automaton model examining the effects of oxygen, hydrogen ions and lactate on early tumour growth*. *Journal of mathematical biology*, 2014. **69**(4): p. 839-873.
192. Zajac, M., G.L. Jones, and J.A. Glazier, *Simulating convergent extension by way of anisotropic differential adhesion*. *J Theor Biol*, 2003. **222**(2): p. 247-59.
193. Chen, N., et al., *A parallel implementation of the Cellular Potts Model for simulation of cell-based morphogenesis*. *Comput Phys Commun*, 2007. **176**(11-12): p. 670-681.
194. Achilli, T.-M., et al., *Multilayer Spheroids To Quantify Drug Uptake and Diffusion in 3D*. *Molecular Pharmaceutics*, 2014. **11**(7): p. 2071-2081.
195. Ivascu, A. and M. Kubbies, *Diversity of cell-mediated adhesions in breast cancer spheroids*. *Int J Oncol*, 2007. **31**(6): p. 1403-13.
196. Gong, X., et al., *Generation of Multicellular Tumor Spheroids with Microwell-Based Agarose Scaffolds for Drug Testing*. *PLOS ONE*, 2015. **10**(6): p. e0130348.
197. Knöspel, F., et al., *In Vitro Model for Hepatotoxicity Studies Based on Primary Human Hepatocyte Cultivation in a Perfused 3D Bioreactor System*. *International Journal of Molecular Sciences*, 2016. **17**(4): p. 584.
198. Eichelbaum, M., M. Ingelman-Sundberg, and W.E. Evans, *Pharmacogenomics and individualized drug therapy*. *Annu Rev Med*, 2006. **57**: p. 119-37.

199. Ingelman-Sundberg, M., *Pharmacogenomic biomarkers for prediction of severe adverse drug reactions*. N Engl J Med, 2008. **358**(6): p. 637-9.
200. Yuan, L. and N. Kaplowitz, *Mechanisms of Drug Induced Liver Injury*. Clinics in liver disease, 2013. **17**(4): p. 507-518.
201. Soars, M.G., et al., *The pivotal role of hepatocytes in drug discovery*. Chem Biol Interact, 2007. **168**(1): p. 2-15.
202. Rowe, C., et al., *Proteome-wide analyses of human hepatocytes during differentiation and dedifferentiation*. Hepatology (Baltimore, Md.), 2013. **58**(2): p. 799-809.
203. Singh, S.S., *Preclinical pharmacokinetics: an approach towards safer and efficacious drugs*. Curr Drug Metab, 2006. **7**(2): p. 165-82.
204. Das, V., et al., *Reproducibility of Uniform Spheroid Formation in 384-Well Plates: The Effect of Medium Evaporation*. J Biomol Screen, 2016. **21**(9): p. 923-30.
205. Seglen, P.O., *Preparation of isolated rat liver cells*. Methods Cell Biol, 1976. **13**: p. 29-83.
206. Förster, F., A. Volz, and G. Fricker, *Compound profiling for ABCC2 (MRP2) using a fluorescent microplate assay system*. European Journal of Pharmaceutics and Biopharmaceutics, 2008. **69**(1): p. 396-403.
207. Esteller, A., *Physiology of bile secretion*. World Journal of Gastroenterology : WJG, 2008. **14**(37): p. 5641-5649.
208. McLellan, S.A. and T.S. Walsh, *Oxygen delivery and haemoglobin*. Continuing Education in Anaesthesia Critical Care & Pain, 2004. **4**(4): p. 123-126.
209. Vaupel, P., *Hypoxia and aggressive tumor phenotype: implications for therapy and prognosis*. Oncologist, 2008. **13 Suppl 3**: p. 21-6.

210. Murli, K., *Patterns of necrosis in liver disease*. Clinical Liver Disease, 2017. **10**(2): p. 53-56.
211. Smith, M.D., et al., *Techniques for measurement of oxygen consumption rates of hepatocytes during attachment and post-attachment*. Int J Artif Organs, 1996. **19**(1): p. 36-44.
212. Grimes, D.R. and F.J. Currell, *Oxygen diffusion in ellipsoidal tumor spheroids*. bioRxiv, 2018.
213. Wagner, B.A., S. Venkataraman, and G.R. Buettner, *The Rate of Oxygen Utilization by Cells*. Free radical biology & medicine, 2011. **51**(3): p. 700-712.
214. Kyogoku, D. and T. Sota, *A generalized population dynamics model for reproductive interference with absolute density dependence*. Scientific Reports, 2017. **7**(1): p. 1996.
215. Noè, U., et al. *Inference in a Partial Differential Equations Model of Pulmonary Arterial and Venous Blood Circulation Using Statistical Emulation*. in *Computational Intelligence Methods for Bioinformatics and Biostatistics*. 2017. Cham: Springer International Publishing.
216. Hartung, N., et al., *Mathematical modeling of tumor growth and metastatic spreading: validation in tumor-bearing mice*. Cancer Res, 2014. **74**(22): p. 6397-407.
217. Krogh, A., *The number and distribution of capillaries in muscles with calculations of the oxygen pressure head necessary for supplying the tissue*. J Physiol, 1919. **52**(6): p. 409-15.
218. Skeldon, A.C., et al., *Modelling and Detecting Tumour Oxygenation Levels*. PLOS ONE, 2012. **7**(6): p. e38597.

219. Shampine, L. and M. Reichelt, *The MATLAB ODE Suite*. SIAM Journal on Scientific Computing, 1997. **18**(1): p. 1-22.
220. Langan, L.M., et al., *Direct Measurements of Oxygen Gradients in Spheroid Culture System Using Electron Parametric Resonance Oximetry*. PLoS ONE, 2016. **11**(2): p. e0149492.
221. Broughan, T.A., et al., *Effects of hepatic zonal oxygen levels on hepatocyte stress responses*. J Surg Res, 2008. **145**(1): p. 150-60.
222. Leedale, J., et al., *Modeling the dynamics of hypoxia inducible factor-1alpha (HIF-1alpha) within single cells and 3D cell culture systems*. Math Biosci, 2014. **258**: p. 33-43.
223. Jamnongwong, M., et al., *Experimental study of oxygen diffusion coefficients in clean water containing salt, glucose or surfactant: Consequences on the liquid-side mass transfer coefficients*. Chemical Engineering Journal, 2010. **165**(3): p. 758-768.
224. Shipley, R.J., et al., *A strategy to determine operating parameters in tissue engineering hollow fiber bioreactors*. Biotechnology and Bioengineering, 2011. **108**(6): p. 1450-1461.
225. Sullivan, J.P., et al., *Enhanced oxygen delivery to primary hepatocytes within a hollow fiber bioreactor facilitated via hemoglobin-based oxygen carriers*. Artif Cells Blood Substit Immobil Biotechnol, 2007. **35**(6): p. 585-606.
226. Consolo, F., et al., *A computational model for the optimization of transport phenomena in a rotating hollow-fiber bioreactor for artificial liver*. Tissue Eng Part C Methods, 2009. **15**(1): p. 41-55.

227. Guarino, R.D., et al., *Method for determining oxygen consumption rates of static cultures from microplate measurements of pericellular dissolved oxygen concentration*. *Biotechnol Bioeng*, 2004. **86**(7): p. 775-87.
228. Wang, C., H. Lu, and M.A. Schwartz, *A novel in vitro flow system for changing flow direction on endothelial cells*. *Journal of Biomechanics*, 2012. **45**(7): p. 1212-1218.
229. Burton, A.C., *Rate of growth of solid tumours as a problem of diffusion*. *Growth*, 1966. **30**(2): p. 157-76.
230. Franko, A.J. and R.M. Sutherland, *Oxygen Diffusion Distance and Development of Necrosis in Multicell Spheroids*. *Radiation Research*, 1979. **79**(3): p. 439-453.
231. Mueller-Klieser, W., *Method for the determination of oxygen consumption rates and diffusion coefficients in multicellular spheroids*. *Biophys J*, 1984. **46**(3): p. 343-8.
232. Richter, L.H.J., et al., *Pooled human liver preparations, HepaRG, or HepG2 cell lines for metabolism studies of new psychoactive substances? A study using MDMA, MDBD, butylone, MDPPP, MDPV, MDPB, 5-MAPB, and 5-API as examples*. *Journal of Pharmaceutical and Biomedical Analysis*, 2017. **143**: p. 32-42.
233. Nelson Leonard, J., et al., *Human Hepatic HepaRG Cells Maintain an Organotypic Phenotype with High Intrinsic CYP450 Activity/Metabolism and Significantly Outperform Standard HepG2/C3A Cells for Pharmaceutical and Therapeutic Applications*. *Basic & Clinical Pharmacology & Toxicology*, 2016. **120**(1): p. 30-37.

234. Freyer, J.P., *Rates of oxygen consumption for proliferating and quiescent cells isolated from multicellular tumor spheroids*. Adv Exp Med Biol, 1994. **345**: p. 335-42.
235. Laurent, J., et al., *Multicellular tumor spheroid models to explore cell cycle checkpoints in 3D*. BMC Cancer, 2013. **13**(1): p. 73.
236. Jamieson, L.E., D.J. Harrison, and C.J. Campbell, *Chemical analysis of multicellular tumour spheroids*. Analyst, 2015. **140**(12): p. 3910-3920.
237. Lima, K.G., et al., *Octyl gallate reduces ATP levels and Ki67 expression leading HepG2 cells to cell cycle arrest and mitochondria-mediated apoptosis*. Toxicol In Vitro, 2018. **48**: p. 11-25.
238. Braeuning, A., et al., *Differential gene expression in periportal and perivenous mouse hepatocytes*. The FEBS Journal, 2006. **273**(22): p. 5051-5061.
239. Arteel, G.E., et al., *Chronic enteral ethanol treatment causes hypoxia in rat liver tissue in vivo*. Hepatology, 2003. **25**(4): p. 920-926.
240. Wilson, G.K., D.A. Tennant, and J.A. McKeating, *Hypoxia inducible factors in liver disease and hepatocellular carcinoma: Current understanding and future directions*. Journal of Hepatology, 2014. **61**(6): p. 1397-1406.
241. Nasimuzzaman, M., et al., *Hepatitis C virus stabilizes hypoxia-inducible factor 1alpha and stimulates the synthesis of vascular endothelial growth factor*. J Virol, 2007. **81**(19): p. 10249-57.
242. Qu, A., et al., *Hypoxia - inducible transcription factor 2 α promotes steatohepatitis through augmenting lipid accumulation, inflammation, and fibrosis*. Hepatology, 2011. **54**(2): p. 472-483.

243. Wong, Y.L., et al., *Mitochondrial thiol status in the liver is altered by exposure to hyperoxia*. Toxicol Lett, 2001. **123**(2-3): p. 179-93.
244. Jones, A.C., et al., *In vitro cytotoxic drug sensitivity testing of human tumour xenografts grown as multicellular tumour spheroids*. British Journal of Cancer, 1982. **46**(6): p. 870-879.
245. Goodman, T.T., et al., *Spatio-temporal modeling of nanoparticle delivery to multicellular tumor spheroids*. Biotechnol Bioeng, 2008. **101**(2): p. 388-99.
246. Katt, M.E., et al., *In Vitro Tumor Models: Advantages, Disadvantages, Variables, and Selecting the Right Platform*. Frontiers in Bioengineering and Biotechnology, 2016. **4**: p. 12.
247. Sha, H., et al., *Tumor-penetrating peptide fused EGFR single-domain antibody enhances cancer drug penetration into 3D multicellular spheroids and facilitates effective gastric cancer therapy*. Journal of Controlled Release, 2015. **200**: p. 188-200.
248. Lv, D., et al., *Three-dimensional cell culture: A powerful tool in tumor research and drug discovery*. Oncology Letters, 2017. **14**(6): p. 6999-7010.
249. Mascheroni, P., et al., *An avascular tumor growth model based on porous media mechanics and evolving natural states*. Mathematics and Mechanics of Solids, 2017. **23**(4): p. 686-712.
250. Edmondson, R., et al., *Three-Dimensional Cell Culture Systems and Their Applications in Drug Discovery and Cell-Based Biosensors*. Assay and Drug Development Technologies, 2014. **12**(4): p. 207-218.
251. Li, S.-S., et al., *Revealing chemical processes and kinetics of drug action within single living cells via plasmonic Raman probes*. Scientific Reports, 2017. **7**(1): p. 2296.

252. Fang, Y. and R.M. Eglen, *Three-Dimensional Cell Cultures in Drug Discovery and Development*. *Slas Discovery*, 2017. **22**(5): p. 456-472.
253. Lavezzi, S.M., et al., *Mathematical modeling of efficacy and safety for anticancer drugs clinical development*. *Expert Opin Drug Discov*, 2018. **13**(1): p. 5-21.
254. Brocato, T.A., et al., *Understanding the Connection between Nanoparticle Uptake and Cancer Treatment Efficacy using Mathematical Modeling*. *Scientific Reports*, 2018. **8**(1): p. 7538.
255. Norris, E.S., J.R. King, and H.M. Byrne, *Modelling the response of spatially structured tumours to chemotherapy: Drug kinetics*. *Mathematical and Computer Modelling*, 2006. **43**(7): p. 820-837.
256. Banerjee, R.K., et al., *Finite element model of antibody penetration in a prevascular tumor nodule embedded in normal tissue*. *J Control Release*, 2001. **74**(1-3): p. 193-202.
257. Bonfiglio, A., et al., *Mathematical modeling of the circulation in the liver lobule*. *J Biomech Eng*, 2010. **132**(11): p. 111011.
258. Siggers, J.H., et al., *Mathematical model of blood and interstitial flow and lymph production in the liver*. *Biomechanics and Modeling in Mechanobiology*, 2014. **13**(2): p. 363-378.
259. Epstein, N., *On tortuosity and the tortuosity factor in flow and diffusion through porous media*. *Chemical Engineering Science*, 1989. **44**(3): p. 777-779.
260. Diedrich, K.T., et al., *Validation of an arterial tortuosity measure with application to hypertension collection of clinical hypertensive patients*. *BMC Bioinformatics*, 2011. **12**(Suppl 10): p. S15-S15.

261. Izadifar, M., O.D. Baik, and J. Alcorn, *Mechanistic modeling of drug elimination by the liver using local volume averaging method*. Conf Proc IEEE Eng Med Biol Soc, 2011. **2011**: p. 4314-7.
262. Saltzman, W.M., *Drug delivery: engineering principles for drug therapy*. 2001: Oxford University Press, USA.
263. Kaliman, S., et al., *Limits of Applicability of the Voronoi Tessellation Determined by Centers of Cell Nuclei to Epithelium Morphology*. Frontiers in Physiology, 2016. **7**: p. 551.
264. Honda, H., *Description of cellular patterns by Dirichlet domains: The two-dimensional case*. Journal of Theoretical Biology, 1978. **72**(3): p. 523-543.
265. Separham, A., et al., *A quantitative structure - toxicity relationship of drugs on rat*. Revista Colombiana de Ciencias Químico - Farmacéuticas, 2011. **40**: p. 27-46.
266. Menochet, K., et al., *Simultaneous assessment of uptake and metabolism in rat hepatocytes: a comprehensive mechanistic model*. J Pharmacol Exp Ther, 2012. **341**(1): p. 2-15.
267. Menochet, K., et al., *Use of mechanistic modeling to assess interindividual variability and interspecies differences in active uptake in human and rat hepatocytes*. Drug Metab Dispos, 2012. **40**(9): p. 1744-56.
268. Neville Alan, J., A. Rand Carol, and D. Barr Ronald, *Vinblastine - Induced Erythrocytotoxicity*. Scandinavian Journal of Haematology, 1982. **28**(1): p. 32-38.
269. Fang, L., et al., *Determining the optimal 5-FU therapeutic dosage in the treatment of colorectal cancer patients*. Oncotarget, 2016. **7**(49): p. 81880-81887.

270. Majumdar, S., S. Duvvuri, and A.K. Mitra, *Membrane transporter/receptor-targeted prodrug design: strategies for human and veterinary drug development*. *Adv Drug Deliv Rev*, 2004. **56**(10): p. 1437-52.
271. Guicciardi, M.E., et al., *Apoptosis and Necrosis in the Liver*. *Comprehensive Physiology*, 2013. **3**(2): p. 10.1002/cphy.c120020.